Study on THz Imaging System for Concealed Threats Detection

A thesis submitted to the University of London in partial fulfilment of the
requirements for the degree of Doctor of Philosophy

By

Shaoqing Hu

Supervisors: Prof. Xiaodong Chen and Dr. Yasir Alfadhl

School of Electronic Engineering and Computer Science

Queen Mary, University of London

November 2020

Statement of originality

I, Shaoqing Hu, confirm that the research included in this thesis is my own work or that where it has been carried out in collaboration with, or supported by other, that this is duly acknowledged below and my contribution indicated. Previously published material is also acknowledged below.

I attest that I have exercised reasonable care to ensure that the work is original, and does not, to the best of my knowledge, break any UK law, infringing any third party's copyright or other Intellectual Property Right, or contain any confidential material.
I accept that the College has the right to use plagiarism detection software to check the electronic version of the thesis.

I confirm that this thesis has not been previously submitted for the award of a degree by this or any other university.
The copyright of this thesis rests with the author and no quotation from it or information derived from it may be published without the prior written consent of the author.

Signature:

Date: 05/11/2020

Acknowledgement

I would like to express my deep and sincere gratitude to my supervisor, Professor Xiaodong Chen, Dr. Yasir Alfadhl and independent assessor Dr. Robert Donnan for their invaluable encouragement, advice and supervision throughout this research work. Their continuous guidance, profound experience and keen attitude towards research have guided and kept me on the right track. It has been my great pleasure and honour to be their student and work with them.

I would like to thank all the colleagues I have worked with in the Antenna lab, Queen Mary University of London, who share their knowledge and research experiences with me. My special thanks go to my colleagues Dr. Rostyslav Dubrovka, Mr. Chao Shu, Dr. Min Zhou, Dr. Bin Deng and Dr. Qiao Cheng for valuable discussions. In addition, I would like to acknowledge the support from Mr. Ho Huen, Mr. Keith Bancroft, Dr. Jin Zhang, Dr.Xiang Li, Dr. Jiandong Lang and Dr. Tianzhong Zhang.

I am also deeply indebted to Dr. Max Munoz Torrico and Dr. Andre Andy for their patient assistance with the experimental set-up.

I wish to express my appreciation to Dr. Debbie Fellows and Torben Voigt from Altair Engineering. The technical discussions between us in the course of the imaging simulation with FEKO^{TM} are very helpful.

Last but not least, I would like to express my deep gratitude to my family and girlfriend for the support and company during my study.

Abstract

Many research groups have conducted studies on Terahertz technology for various applications in the last decades. THz imaging for personnel screening is one prospective application due in part to its superior performance compared with imaging microwave bands. Because of the demand for the accurate detection, it is desirable to devise a high-performance THz imaging system for concealed threats detection. Therefore, this thesis presents my research on the low-cost THz imaging system for security detection.

The key contributions of this research lie in investigating the linear sparse periodic array (SPA) THz imaging system for concealed threats detection, improving the traditional reconstruction algorithm of Generalized Synthetic Aperture Focusing Technique (GSAFT) to suppress the ghost images and applying the compressive sensing technique into the proposed SPA-THz imaging system to reduce the sampling data but maintain the image quality.

The first part of the work is to investigate the linear sparse periodic array (SPA) and its configuration with large element spacing in simulation, deriving the design guideline for such a SPA THz imaging system. Meanwhile, the improved GSAFT reconstruction algorithm and multi-pass interferometric synthetic aperture imaging technique have been proposed to suppress the ghost image and improve the image quality, respectively. Secondly, the compressive sensing technique has been investigated to reduce the sampling data. Therefore, we have proposed the corresponding discrete CS SPA-THz reconstruction model and verified it in simulation. Finally, we have devised a simplified experimental set-up to assess the practical imaging performance, verifying the proposed SPA-THz imaging system. The set-up only uses 1 Tx and 1 Rx scanning on two separate tracks to effectively realize the proposed imaging system. The reconstructed images by the GSAFT and CS approaches with the measured data have both shown good consistency with the simulated results, respectively. And the multi-pass interferometric synthetic aperture imaging has been experimentally proved effective in improving image SNR and contrast.

Contents

List of Figures

List of Tables

Abbreviations

BP	Basis Pursuit
BPDN	Basis Pursuit De-Noise
CCD	Charge-coupled Device
CoSaMP	Compressive Sampling Matching Pursuit
CS	Compressive/Compressed Sensing
DCT	Discrete Cosine Transform
DWT	Discrete Wavelet Transform
FFT	Fast Fourier Transformation
FIT	Finite Integration Technique
FMCW	Frequency Modulated Continuous Wave
FOV	Field of View
FPA	Focal Plane Array
GO	Geometrical Optics
GSAFT	Generalized Synthetic Aperture Focusing Technique
Haar-DWT	Haar-type Discrete Wavelet Transform
HBD	Hetero-structure Backward Diode
HDPE	High-density Polyethylene
HPBW	Half Power Beam Width
IST	Iterative Shrinkage Thresholding
JPL	Jet Propulsion Laboratory
KID	Kinetic Inductance Detector
LASSO	Least Absolute Shrinkage and Selection Operator
LEKID	Lumped Element Kinetic Inductance Detector
LEPO	Large Element Physical Optics

MIP	Maximum Intensity Projection
MLFMM	Multilevel Fast Multipole Method
MMIC	Millimeter-wave Monolithic Integrated Circuit
MOM	Methods of Moments
MP	Matching Pursuit
MRT	Minimum Resolvable Temperature
NEP	Noise Equivalent Power
NETD	Noise Equivalent Temperature Difference
OMP	Orthogonal Matching Pursuit
PHEMT	Pseudomorphic High Electron Mobility Transistor
PNNL	Pacific Northwest National Laboratory
PO	Physical Optics
PSF	Point Spread Function
PSD	Power Spectral Density
PTC	Pulse Tube Cryocooler
RAM	Random-access Memory
RLGO	Ray Launching Geometrical Optics
RMSD	Root-Mean-Square Deviation
RMSE	Root-Mean-Square Error
SAR	Synthetic Aperture Radar
SNR	Signal to Noise Ratio
SPA	Sparse Periodic Antenna Array
SPGL1	Spectral Projected-gradient for L1 Minimization
SQID	Superconducting Quantum Interference Device
TES	Transition-edge Sensor
TwIST	Two-step Iterative Shrinkage-Thresholding

Chapter 1 Introduction

1.1. Background of Security Detection

Terahertz wave is between microwaves and infrared light waves and it generally refers to the frequency band ranging from 100 GHz to 10 THz. It exhibits no health hazard due to its non-ionizing characteristic and is capable of penetrating through cloud, fog and clothing. Therefore, it has various applications in communication, material analysis and imaging. Regarding the THz imaging, it covers radio astronomy, biological research, personnel screening, and radar because it not only offers a higher spatial resolution due to its shorter wavelength but also has spectroscopic signatures for identification. Besides, personnel screening for detecting concealed threats like handguns and explosives is increasingly demanded in a variety of public gatherings such as airports, train stations and critical infrastructures due to increasing terrorist attacks. Though THz imaging has been proven to be a useful technique for the threats detection in the last decades, the challenges still exist in achieving high resolution, real-time operation and low-cost practical implementation [1-3].

There are two categories of the imaging modes: active and passive imaging. Passive imaging system only relies on emissivity or temperature differences to form images of the human body and concealed items [4-19]. This kind of system is capable of achieving high resolution either using shorter wavelengths or synthesizing/directly utilizing large aperture[20], but the key to successful target identification in such systems is having a sufficient sensitivity to detect small radiometric temperature differences [5]. Thus, a noise equivalent temperature difference (NETD or NEΔT) below 1 K is normally desirable, especially for the detection of absorbing items warmed up by body contact. However, the NETD, the actual figure of merit of the device, is proportional to $\mathrm{NEP}/\sqrt{\mathrm{n}_{\mathrm{detectors}}}$ (NEP: Noise Equivalent Power [21]; $n_{\mathrm{detectors}}$: the number of detectors) [11]. A low NETD can be achieved either by a low NEP of the detectors or by plenty of detectors [11]. However, this kind of system usually uses each detector to represent each pixel of image, so a compromise should be made between cost (number of detectors) and sensitivity (image quality) [5, 22]. The passive imaging system with high sensitive detectors like superconducting transition-edge sensor (TES) has a complex readout circuit and high system cost. A parallel superconducting quantum interference device (SQUID) readout scheme requires cooling system and sensor calibration [11, 12]. Although, recently developed Kinetic Inductance Detectors (KIDs) that are relatively simple to fabricate and read out provide a practical and cost-effective solution to the operation of the large-scale arrays, the long cooling time still prevents system continuous operation [9]. Besides, it has been proposed to use an innovative scanning mechanism such as helical scanning to achieve a fast and simple one-channel passive millimeter wave (94 GHz) imaging system for security screening. However, the experimental results in indoor environment have not reveal the shapes of plastic gun and ceramic knife properly [14]. Some state of the art techniques such as real-time calibration, automatic detection, compressive sensing, machine learning and Convolutional Neural Network (CNN) have also been applied in the latest passive security screening systems [15-19]. Regarding the active imaging system, it seeks utilizing illumination source to improve the reflection from the target area and then achieves higher image contrast primarily through differences in the orientation, shape, and reflectivity of the body or concealed objects [3]. Therefore, the active imaging system has an additional advantage over passive imaging system in forming the shape of concealed objects, which is helpful to identify the threats. Although the reflection from the ambient may cause issues like artifacts, this can be alleviated by proper system design. Furthermore, active imaging systems avoids using a cooling system to achieve the high signal-to-noise ratio operation and high contrast for detection of concealed items [23, 24]. In either passive or active imaging system, four main criteria need to be addressed: frame rate, thermal sensitivity, field of view and system cost. Capturing speed and imaging spatial resolution are two critical issues for the practical implementation. Therefore, different techniques and approaches are being explored to improve the imaging quality while reducing the cost simultaneously. THz imaging systems can also be classified into incoherent and coherent imaging system in terms of detection technology. Also, according to the scanning scheme deployed, the imaging systems can be categorized into three classes: focal plane array (FPA) imaging system [25-29], advanced quasi-optical imaging system [30-43] and interferometric array/synthetic aperture imaging system [44-50].

FPA imaging systems use lenses or curved reflectors to physically focus the signal into detectors in a focal plane array. However, the FPA technique are mainly applied in the passive imaging system and has two intrinsic drawbacks of high cost and long cooling time, as aforementioned. Therefore, the advanced quasi-optical imaging system uses specific large focusing quasi-optics to achieve a fast frame rate and reduce the cost with a fixed single transceiver [30-38, 40-43] or a compact sparse transceiver array [39]. Unfortunately, this kind of imaging system have not shown sufficient image contrast or resolution for target identification, either.

The interferometric array/synthetic aperture imaging systems addressed in this thesis remove the large-scale reflectors in quasi-optic system. So the beams directly illuminate the target, and then techniques of interferometric imaging and synthetic aperture imaging are used to mathematically form the high quality image. And 2D scanning can be achieved by either the planar array with only electronic scanning or the linear array with the combination of electronic scanning and mechanical scanning. Since it is a synthetic aperture imaging technique, the number of detectors can be reduced by rotating the array around a fixed axis [45]. However, the reported imaging systems with linear monostatic array work only below 60 GHz because it needs a large number of elements/sampling points with sub-wavelength spacing [47-49].The monostatic approximation in FFT-SAR imaging algorithm will not allow wide array element spacing. Therefore, multi-static sparse array has been proposed to reduce the number of array elements [51-55]. Nevertheless, the first kind of multi-static linear array with multiple use of each transmitter and receiver has only been demonstrated at a frequency band of 20 – 30 GHz by simulated data, the maximum sampling spacing is 0.37 wavelength [51, 52]. In terms of the second kind of linear sparse periodic array (SPA) in [53-55] , the element spacing is still small about 1.1 wavelength and operating frequency is relatively lower than 100 GHz. In terms of the multi-static planar array, however, it usually needs thousands of channels and elements that is not cost effective. So it has not been widely used yet [56, 57].

1.2. Literature Review

1.2.1. Focal Plane Array (FPA) Imaging System

FPA is similar to a standard CCD optical camera, which is mainly used in passive imaging system where each detector denotes a pixel in the image. Design considerations as well as several imaging systems of millimeter wave FPA have been generally discussed in [25]. In focal plane array imaging systems, a lens, or more commonly a mirror/reflector at millimeter wave or terahertz frequency, are usually used to focus incoming radiation onto the detector array, forming the image.

In theory, full sampling of the focal plane of the scene for incoherent illumination requires feed element spacing $\Delta x = \frac{1}{2} \cdot f \cdot \lambda / D$ where λ is radio wavelength, f is the focal length; D is the diameter of reflector-used aperture. Due to the high cost of THz detectors and limited detector packing density, it is not practical to fabricate an array of full pixels. In addition, the tight space will lead to improper illumination of antenna array so that the antenna efficiency is reduced dramatically. Therefore, space between feeds for 1-D FPA must be big enough to obtain good illumination efficiency, but that will decrease the image sampling density [25, 58]. To resolve this problem, interleaved scanning is usually carried out, which doubles the imaging time. In addition, reduced detectors causing the sensitivity drop will directly affects the success of passive imaging system [5, 59].

A broadband (0.6 – 1.2 THz) real-time THz camera using the HBD (hetero-structure backward diode)-based FPA consisting of broadband planar slot antennas, integrated sensor devices has been developed by researchers in the Ohio State University, as shown in Figure 1- 1[29]. This camera has a five frames-per-second image acquisition speed and a sub-millimeter resolution at 0.7 THz [29]. However, the central area of 31 × 31 pixels mainly contributes to the image because of the spread of THz incident power over a wide area and off-axis aberrations caused by the small extended hemispherical lens used, as shown in Figure 1- 2. So the field of view（FOV) of this camera is too small for personnel screening.

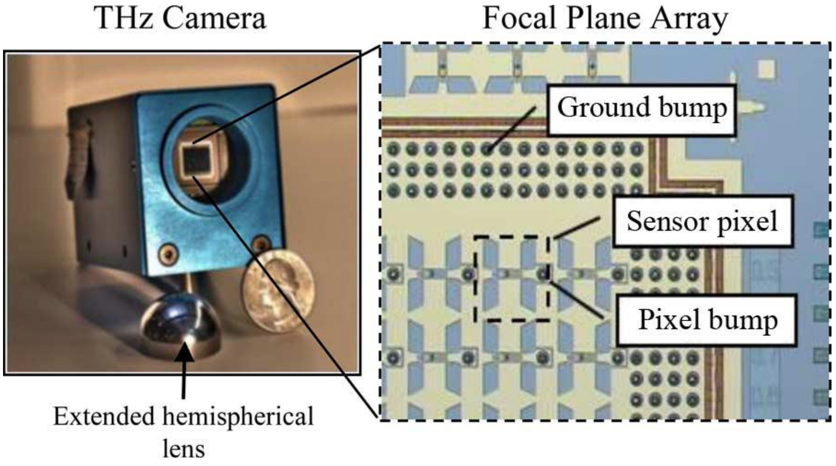

(a) (b)

Figure 1- 1. Photograph of the broadband (0.6 – 1.2 THz) real-time camera. (a) Camera with the extended hemispherical lens removed (b) Microscope image of the focal plane array [29]

Besides, Figure 1- 3 shows a passive 89 GHz (10 GHz bandwidth) millimeter wave image system for personnel screening that uses Millimeter-wave Monolithic Integrated Circuit (MMIC) technology, which has enabled the direct detection and low-noise amplification of millimeter wave signals [5]. This complete MMIC-based 89 GHz receiver has a noise figure of -5.5 dB and bandwidth of 10 GHz, consisting of low noise amplifiers that utilize pseudomorphic high electron mobility transistor (PHEMT) technology on gallium arsenide (GaAs) substrates, on-chip switches and a sensitive detector diode [5]. The high sensitivity, low-cost and power consumption of these MMIC devices have enabled NGC (Northrop Grumman Corporation) to build a 1040 receiver focal plane array (FPA) in the camera. The camera is capable of providing 17 frames-per-second with a MRT (minimum resolvable temperature) of 2K [5]. However, the results have shown that the performance is not good enough to identify the concealed threats as shown in Figure 1- 3 [5].

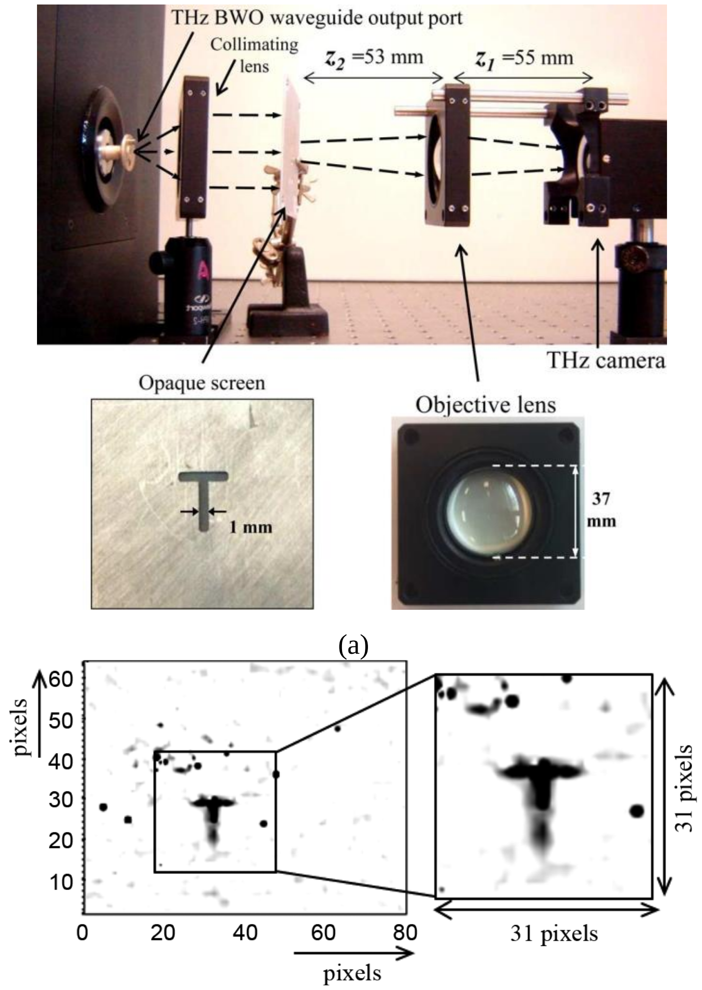

(a)

(b)

Figure 1- 2. (a) The set-up of the broadband real-time THz camera. (b) Recorded camera images at 0.7 THz. Left: THz image of a 1 mm wide ‘T’ slot. Right: Detail of 31 × 31 pixels around ‘T’ slot [29]

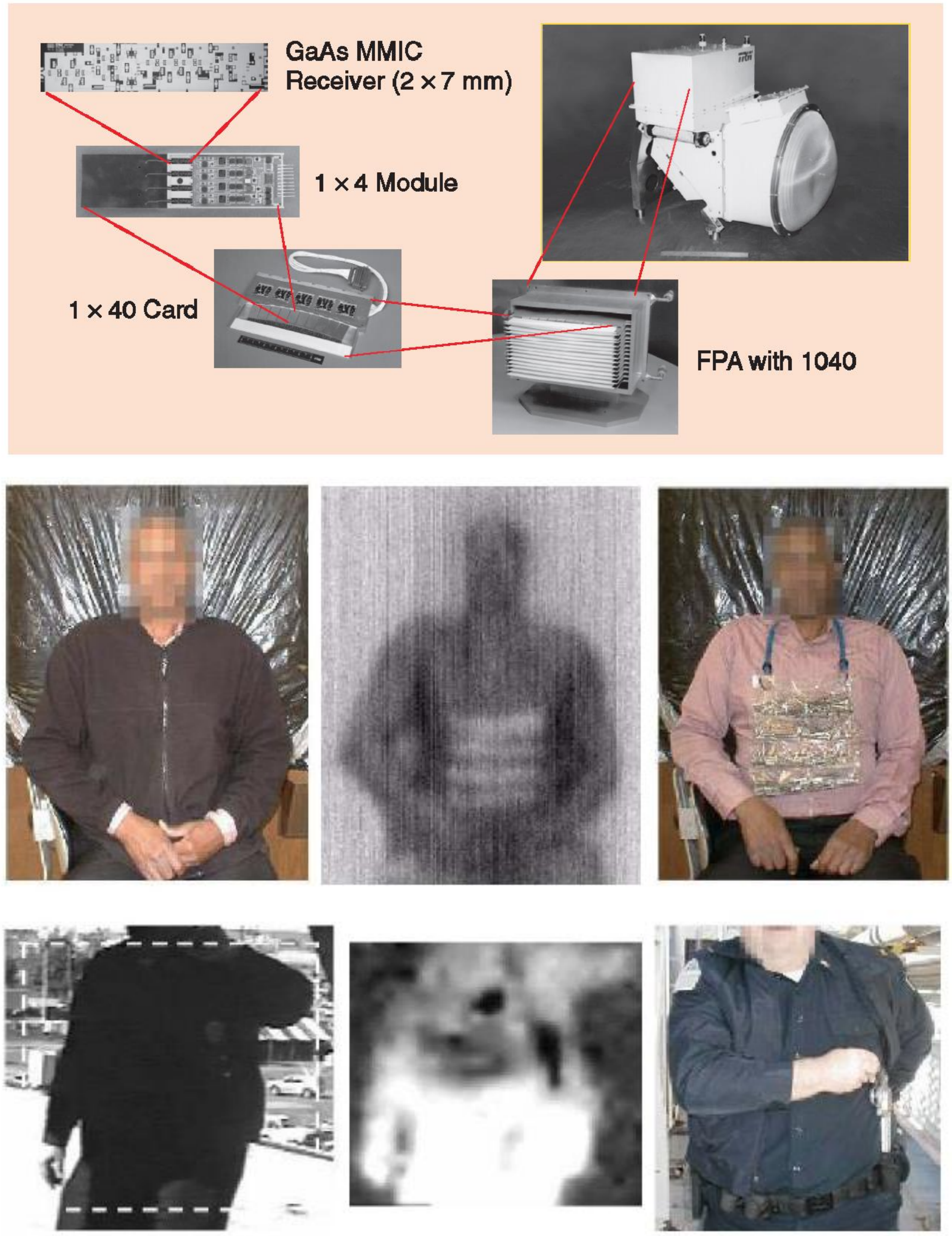

Figure 1- 3. The NGC 1040-element FPA passive millimeter wave video camera [4] and its screening images [5]

Similarly, another 350 GHz passive imaging system which uses high sensitive detectors of superconducting transition-edge sensors (TESs) to gain a high contrast has been proposed [11]. The block diagram of this system has been illustrated in Figure 1-4. The cryogenic set-up includes a commercial closed-cycle cooling system and an optical cryostat. The cooling system consists of a two-stage ^{4}He pulse tube cooler (PTC) in series with a two stage ^{4}He/^{3}He evaporation cooler. The imaging system is made up of optical reflectors based on free-form mirrors. Therefore, a field of view up to 2 m height and a diffraction limited spatial resolution in the order of 1 – 2 cm can be achieved at target distances of 3 – 25 m. The frame rate is up to 25 frames per second.

The TES signals are read out and pre-amplified by superconducting quantum interference devices (SQUIDs) acting as current sensors operating at temperature below 1K [11]. So the system with 64 detectors and its imaging result are shown in Figure 1- 5. It really shows a better image quality compared with the aforementioned passive FPA video camera. Besides the benefit from shorter wavelength, TES also helps to improve this image quality. Nevertheless, TES has issues of complexity and high cost in read out. Article states it is not economical because it has 64 detectors [11]. In addition, unlike the spiral form scanning scheme, which allows for calibration based on data redundancy [12], this linear scanning scheme has no redundancy so it does not have the problem of sensor calibration [11].

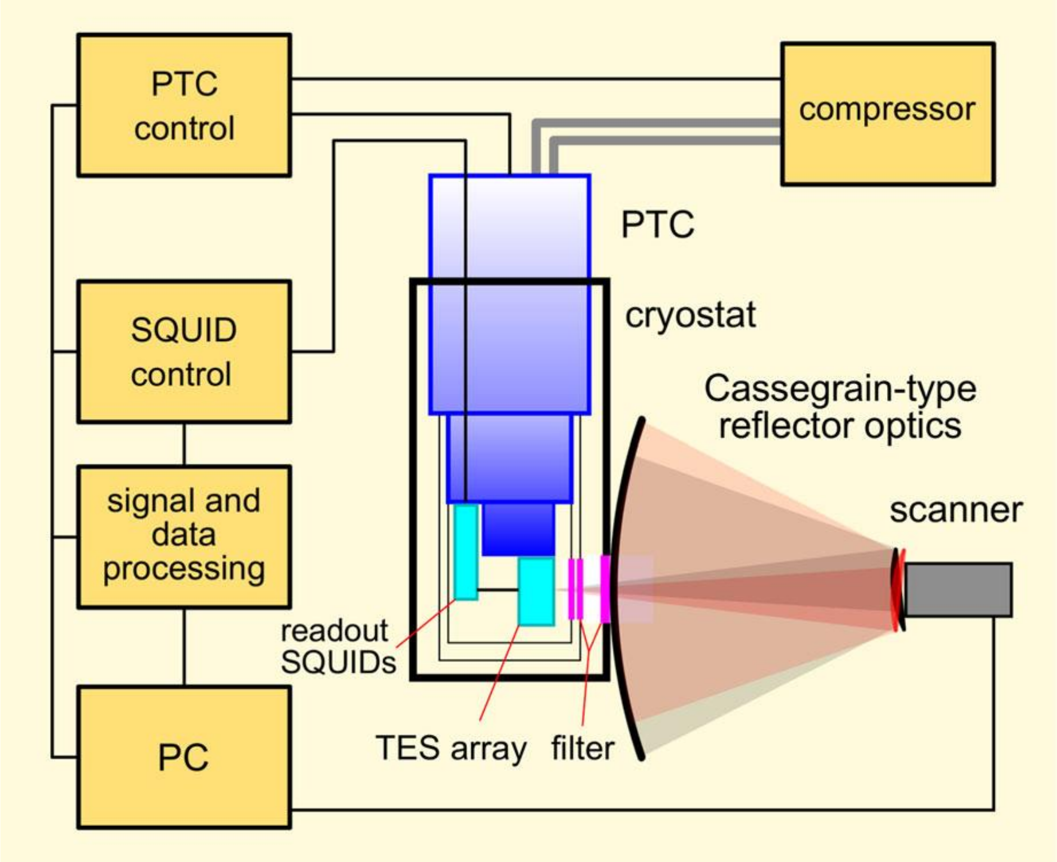

Figure 1- 4. Block diagram of 350 GHz passive video camera using TES array [11]

On the other hand, the relatively simple Kinetic Inductance Detectors (KID) camera is built in [9]. Lumped-element KIDs-as opposed to distributed KIDs-are designed so that the absorbing element of the detector is part of the resonator structure itself. In this configuration, it is possible to achieve a high filling factor in FPA without using additional coupling optics such as micro-lens or feed horn arrays. For example, Figure 1- 6 shows such an imaging system working at 350 GHz with 152 lumped-

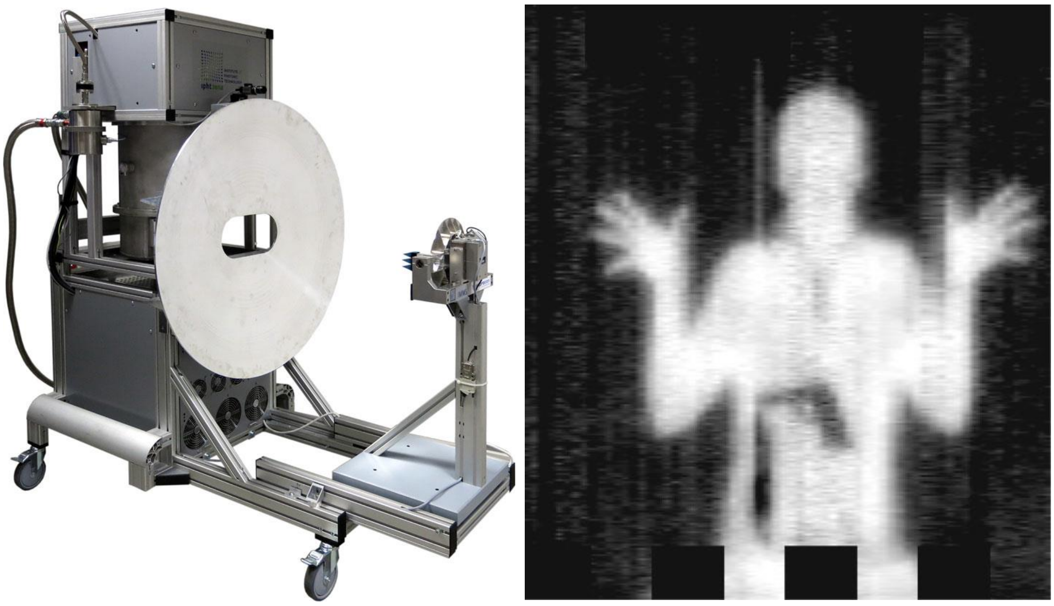

Figure 1- 5. Passive 350 GHz video imaging system with 64 detector linear scanner [11]

element KID (LEKID) and its performed image [9]. The camera uses a linear array of detectors housed in a cryostat retrofitted with a window of 250 mm diameter in the base. After going through a refractive optics system and a flat beam-folding mirror, incoming radiation is coupled to the detectors. A thin horizontal section of the object plane is observed in any one instant. This section is scanned continuously in the vertical direction by oscillation of the beam-folding mirror. A fast (*f*/0.9) triplet of high-density polyethylene (HDPE) lenses has been designed to keep the optics simple and compact, given limitations on where the focal plane array could be situated within the cryostat. The detector array in use is composed of 152 LEKIDs so that it is capable of achieving a 1 cm resolution at a target distance of 3 – 5 m. The constraint set by the scanning mechanism and the high noise have limited the frame rate to 2 Hz/s for an NEΔT of 0.1 K/frame with the camera in its current configuration [9]. As shown in Figure 1- 6, it not possible to reveal the shape of the concealed target well since this passive image system relies on the emissivity contrast to form the image. What is worse, this contrast will decrease around the concealed target when warmed up by the human body. Besides, it takes around 36 hours to cool down this demonstration system from room temperature with the Pulse Tube Cryocooler (PTC) cold head settling at 3.2 K. The optical baffles on the radiation shields settle at 4.2 K and 60 K, respectively, and the cold lens settle with a radial temperature gradient ranging between 100 and 150 K [9]. In the current configuration, the fridge runs for approximately 16 - 18 hours at a time at 250 mK and requires 3 – 4 hours for recycling [9]. Therefore, the continuous operation of this passive imaging system has been constrained.

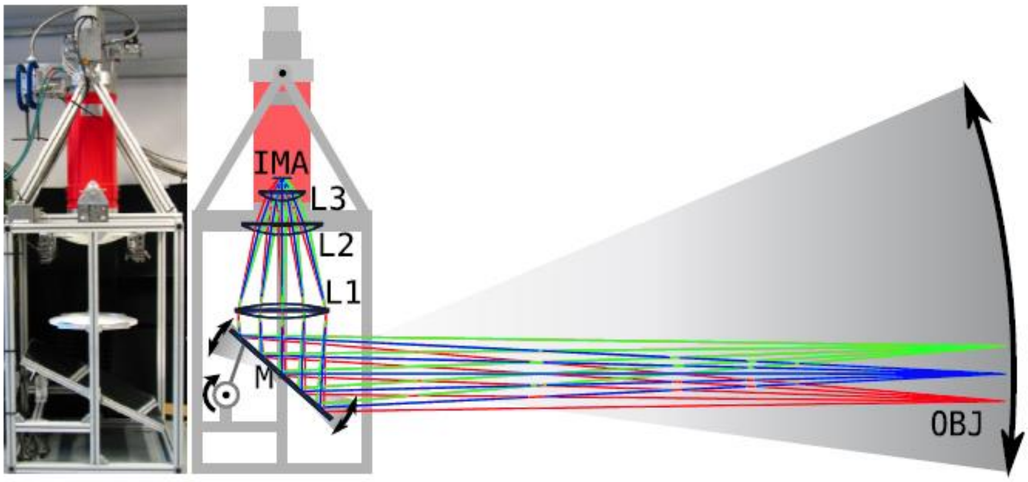

(a)

(b)

Figure 1- 6. (a) Passive 350 GHz imaging system using 152 LEKIDs and (b) a snap shot from a 2 Hz/s video in which the 350 GHz imaging system (left) were displayed simultaneously with frames from a standard web-cam (center) and a thermal NIR camera (right) [9]

More FPA passive imaging systems at millimeter frequency are proposed [5, 26-28]. An alternative principle and algorithm of imaging processing are described in [26]. However, FPA has also been applied in the active imaging system, which is rarely reported. For example, a possible schematic diagram of 64-element active FPA imaging system has been shown in Figure 1- 7. The optics consisting of plano-convex lenses with curved surfaces facing together has been designed to maximize the field of view. The array employs end-fire slot antennas. Each antenna is coupled to a detector diode. An appropriate synchronous detector circuit at the output of the slot antennas converts the reflected power into a DC voltage [25].

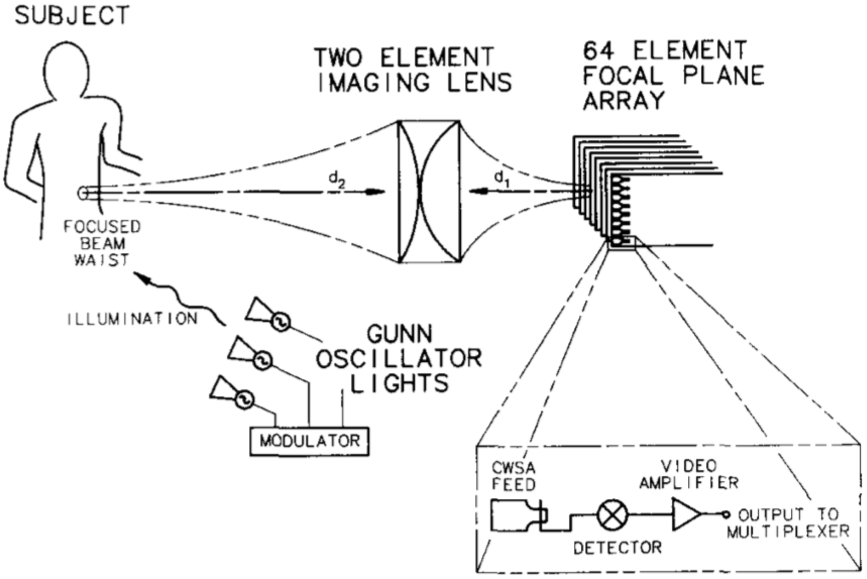

Figure 1- 7. Schematic diagram of active FPA imaging system [25]

1.2.2. Advanced Quasi-optical Imaging System

Another potential scheme to gain a 2-D aperture data for real time imaging is the advanced optical-mechanical imaging system that relies on rotating of one or more mirrors/reflectors to scan the target. In order to gain a high scanning speed, a mirror/reflector with a large aperture known as main aperture is often employed [30, 31, 33, 35-37, 41-43]. Unlike aforementioned FPA imaging systems that may use mirror or reflectors to achieve the scanning, forming the image only based on amplitude information. This kind of advanced quasi-optical system is an active imaging system that uses the heterodyne transceivers to capture both amplitude and phase information in forming the image. There are several comparatively mature active THz quasi-optical imaging systems for personnel screening developed by SynView, Pacific Northwest National Laboratory (PNNL), and NASA Jet Propulsion Laboratory (JPL). The schematic diagrams of the systems are shown in Figure 1- 8.

As shown in Figure 1- 8(a), a 645 GHz active quasi-optical system has been developed by SynView, consisting of two lenses, three mirrors and a beam splitter [43]. The beam emitted by the source is collimated by the collimator lens and then divided into two parts by the beam splitter. One is absorbed while the other one passes through the beam splitter [43]. The spherical mirror with a 102 mm diameter leads the beam to

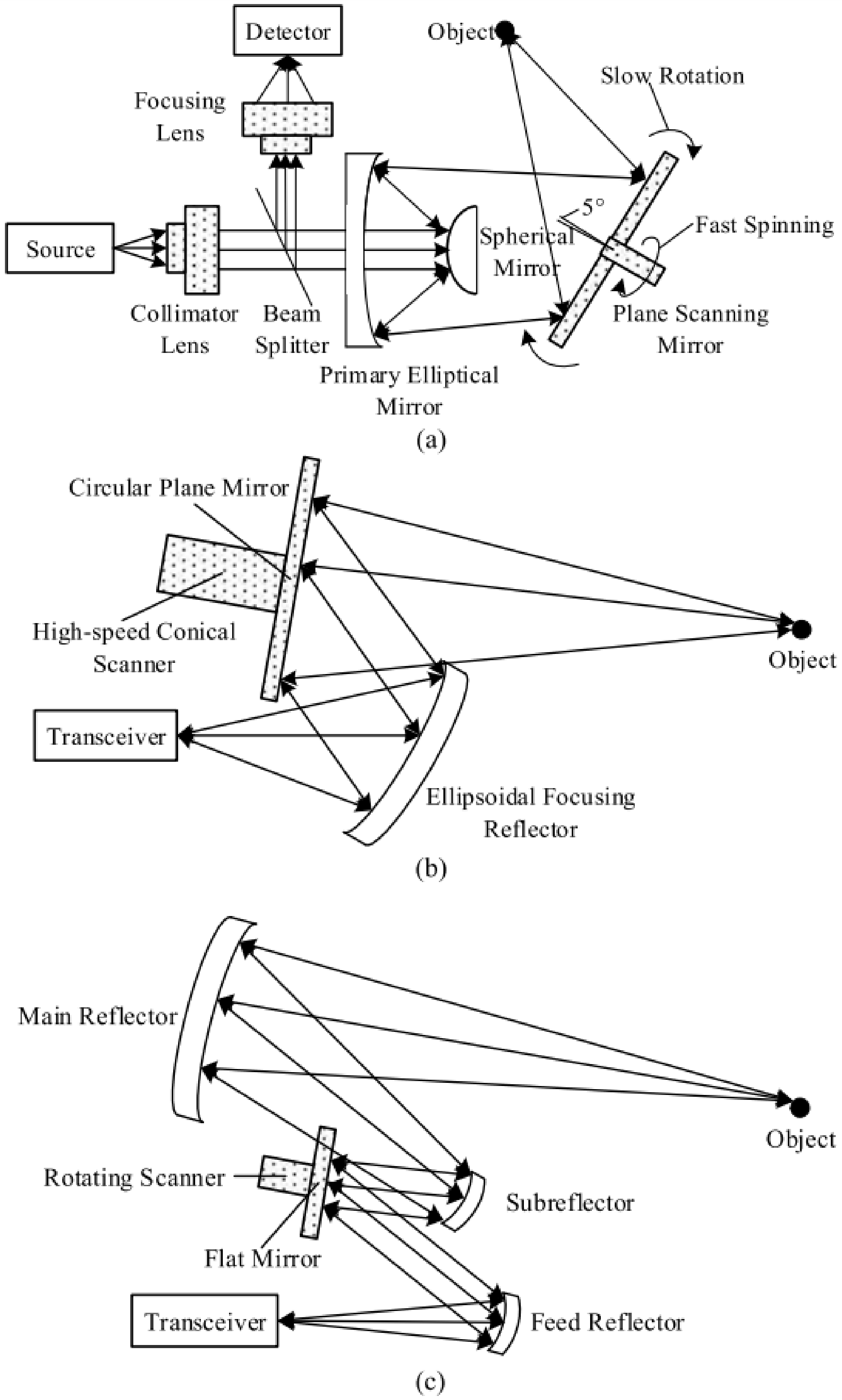

Figure 1- 8. Schematic diagrams of the advanced THz quasi-optical imaging systems developed by (a) SynView (b) PNNL and (c) JPL [3]

the primary elliptical mirror with a 230 mm diameter, and the large plane-scanning mirror with a 320 mm diameter that concentrates the beam onto one object point. The reflected beam from the beam splitter is focused onto the detector by the focusing lens.

The plane-scanning mirror has 5° angle of inclination with respect to its fast spinning axis, so an elliptical scanning pattern is achieved. The plane mirror is also rotated slowly along the vertical axis perpendicular to the fast one, and horizontal shift of the elliptical trail is realized. The resulting FOV looks like a cycloid region.

As shown in Figure 1- 8 (b), a 350 GHz active standoff imaging system has been presented by PNNL, employing a high-performance heterodyne transceiver coupled to a near diffraction limited quasi-optical focusing and scanning system [31, 32]. The transceiver illuminates an off-axis reflector with a fixed focus. The beam is subsequently reflected from a circular plane mirror mounted on a high-speed conical scanner, concentrating to an object point. The conical scanner steers the circular plane mirror, which is mounted with a slight wedge. The wedge offsets the deviation angle, and the object point traces out a circular pattern when the mirror is rotated [31, 32]. The circular pattern is then scanned vertically to fill out the imaging area, and the FOV is an oval region as shown in Figure 1- 9(a). Figure 1- 9 (b) shows the prototype of this advanced 350 GHz quasit-optical imaging system. The transceiver horns are mounted 1 meter from the focusing reflector that has one focus at the transceiver and the other focus placed at 5 m from the scanning reflector. Other focal length reflectors have also been fabricated which allow for operation at ranges of 2 m and 10 m. The scanning mirror is placed at 1 m from the focusing reflector. The scanning aperture is 1.25 m × 2.5 m and the lateral resolution limited by diffraction is approximately 1.0 cm at 5 m. The system can be operated at ranges of 2, 5, or 10 meters and obtains a full 3-D image

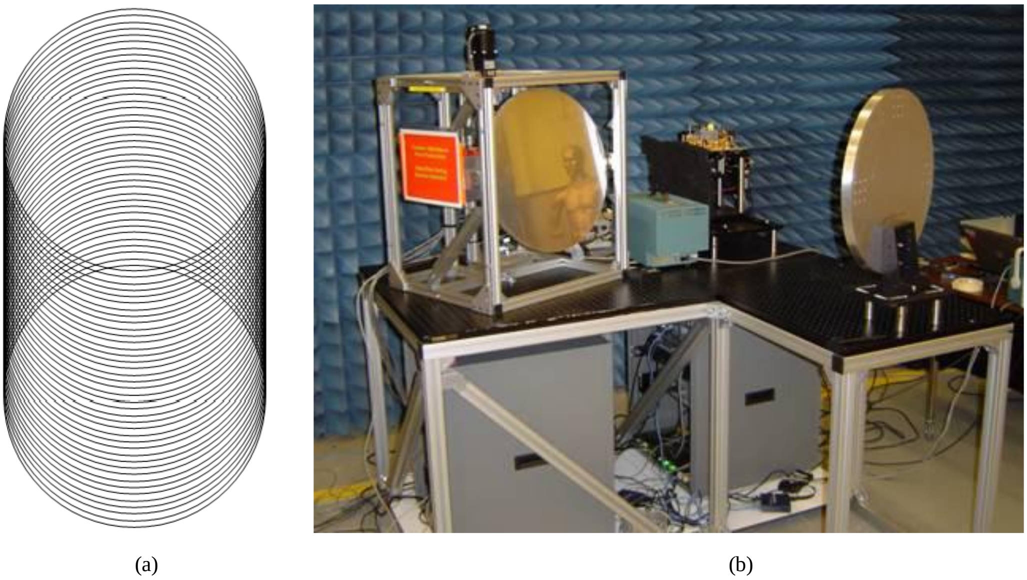

(a) (b)

Figure 1- 9. Active 350 GHz quasi-optical imaging system (a) Scanning pattern with 1.25 m (W) × 2.50 m (H) (b) Photograph of porotype [31]

of human body in 10 seconds. Figure 1- 10 shows one imaging result cited from [31]. Although it has demonstrated imaging capability, the quality and achieved resolution are not sufficient for accurate target identification [31].

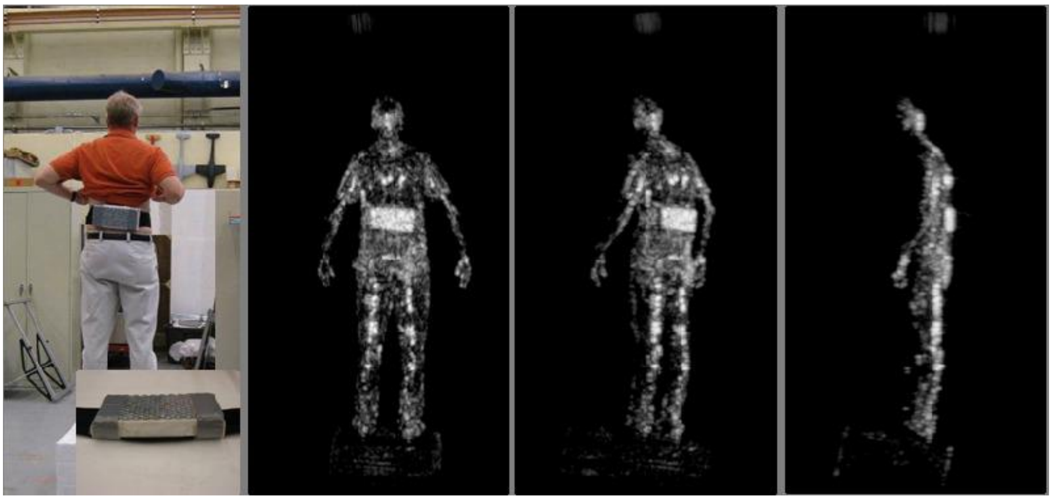

Figure 1- 10. Photograph (left) and the reconstructed 3-D images of a man with a concealed mock explosive (inset) with projections shown at normal, off-normal, and 90 degree from normal (left to right, respectively) [31]

The aforementioned two systems have a lot in common. Both have an electronic FMCW heterodyne transceiver coupled to a quasi-optical focusing system, utilizing a plane mirror with rotating and tilt scanning to achieve the 2D FOV. The quasi-optical focusing design could minimize aberrations and allow for significantly off-axis performance with minimal degradation. But this focusing design has a limited size, constraining the collection of all reflections. Compared to the above two systems, an improved 675 GHz imaging system has been developed by JPL that increases the imaging speed and the standoff distance. Both systems in SynView and PNNL will steer the beam after the main ellipsoidal focusing reflector. This makes them difficult to be used with large diameter apertures, resulting in a limited working distance for reasonable resolution. However, the system in the JPL, as shown in Figure 1- 8 (c), has achieved the beam scanning by the lightweight flat mirror placed in the feed optics of the main reflector, which has only a 130 mm diameter rotating about ±2.5° in elevation and azimuth. So the corresponding beam coverage is ±20 cm in the horizontal and vertical directions at 25 m standoff distance [36-38]. The use of a small lightweight flat mirror with 13-cm-diameter is beneficial to reduce the scanning time and increase the imaging speed. The scanning flat mirror is illuminated by a collimated beam rather than an expanding beam, and the design relaxes the tolerances on the position of the principal axes of scanning mirror, which otherwise will be difficult to align at 675

GHz. Besides fast scanning, the angular position of the flat mirror is controlled precisely by using a servomotor and a rotary encoder, so aberrations are suppressed dramatically. This 675 GHz quasi-optical imaging system works like a FMCW radar and it forms image based on power spectrum and peak finding algorithm [33, 37]. The FMCW radar is preferred over the more common pulse radar when the maximum power of the radiation source is too low to obtain a high signal-to-noise ratio (SNR) for short-duration pulses. So for the solid state Schottky diode based frequency-multiplier THz source that produces only about 0.7 mW at 675 GHz, the fast scanning quasi-optical imaging system using FMCW approach has been developed as shown in Figure 1- 11[37]. A 1-m-diameter main aperture focuses the beam to a (two-way) spot size of about 1 cm at 25-m standoff. The image can be obtained in 5 seconds. Figure 1- 12 shows the corresponding imaging results [37]. We can only roughly see the target shape and feel difficult to identify details if the target is smaller. Some improvements, such as an array set-up and time-delay multiplexing techniques are anticipated to increase the frame rates [35-38].

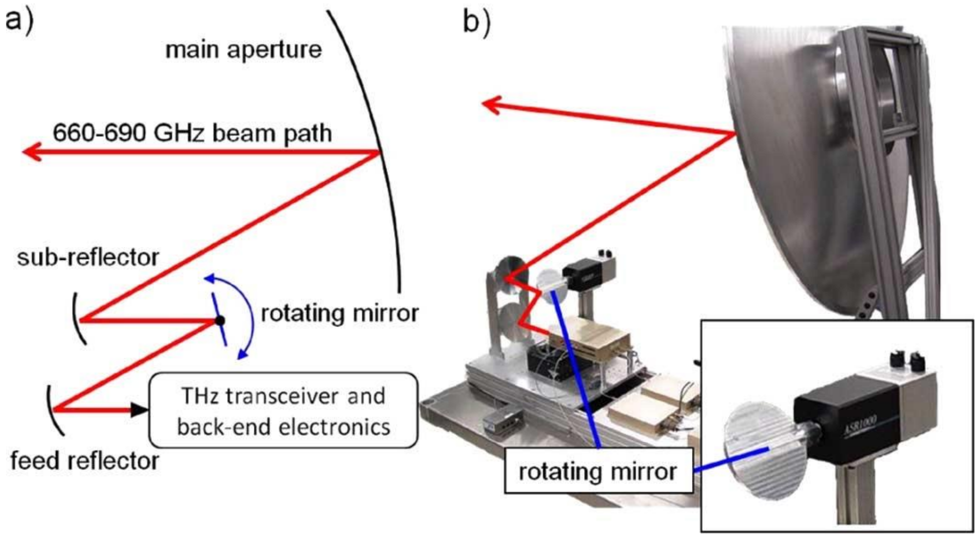

Figure 1- 11. 675-GHz THz radar. (a) Beam path (b) A photograph of the optics with an set showing the fast-scanning mirror mounted on an ASR-1000 rotary stage [37]

Furthermore, a bifocal ellipsoidal Gregorian reflector system (BEGRS) based on the confocal Gregorian subsystem used in the JPL system has been designed by García-Pino *et al.* [41]. The nominal reflector surfaces are substituted by shaped surfaces to reduce the beam aberrations, and the FOV of this imaging system could be increased. For example, the FOV-enhanced 300 GHz imaging system proposed by Grajal *et al.* has been illustrated in Figure 1- 13 [42]. Its prototype and block diagram have been shown in Figure 1- 14. This imaging system has a 27 GHz bandwidth, so

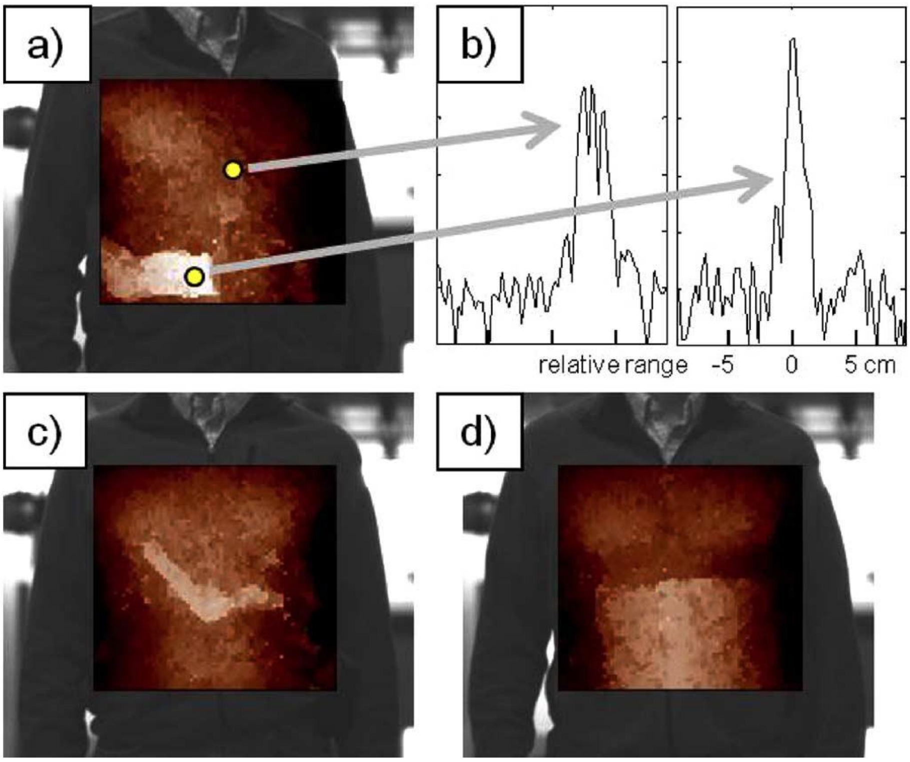

Figure 1- 12. (a) Radar image revealing Play-Doh container concealed under a jacket (b) Radar spectra corresponding to two selected points in the radar image. In left spectrum with multi-peaks, the farthest peak is included in the back surface reconstruction. Radar images revealing (c) a hidden mock handgun and (d) a bomb belt [37]

Table. 1- 1. Specifications of active quasi-optical imaging systems developed by SynView, PNNL, JPL, and Grajal et al [3]

Specifications	SynView	PNNL	JPL	Grajal et al.
Center Frequency	645 GHz	350 GHz	675 GHz	300 GHz
Bandwidth	10 GHz	9.6 GHz	28.8 GHz	27 GHz
Primary Aperture Diameter	23 cm	50 cm	100 cm	60 cm
Imaging Speed	9 s (Measurement time)	10 s	1 s	0.5 s
Standoff Distance	0.75 ~ 1.5 m	2 ~ 10 m	4 ~ 25 m	8 m
FOV	20 cm×30 cm (at 1 m)	1.25 m×2.5 m (at 5 m)	0.4 m×0.4 m (at 25 m)	0.5 m×0.9 m (at 8 m)
Lateral Resolution	4 mm at 1 m	10 mm at 5 m	5 mm at 4 m	16 mm at 8 m
Range Resolution	42 cm	Null	0.7 cm	1 cm

the range resolution is 0.55 cm. Besides, the spot size at 8 m is supposed to be 1.6 cm. It is capable of providing a spatial cross-range resolution of about 2 cm and the scanning area of 100 cm × 50 cm. Figure 1- 15 shows the target scenario under test where a mock explosive is hidden under a T-shirt worn on mannequin, and the reconstructed image based on most powerful detection [42]. It is noted that the image quality is not sufficient for target discrimination. The specifications of the four active standoff imaging systems are listed in Table. 1- 1.

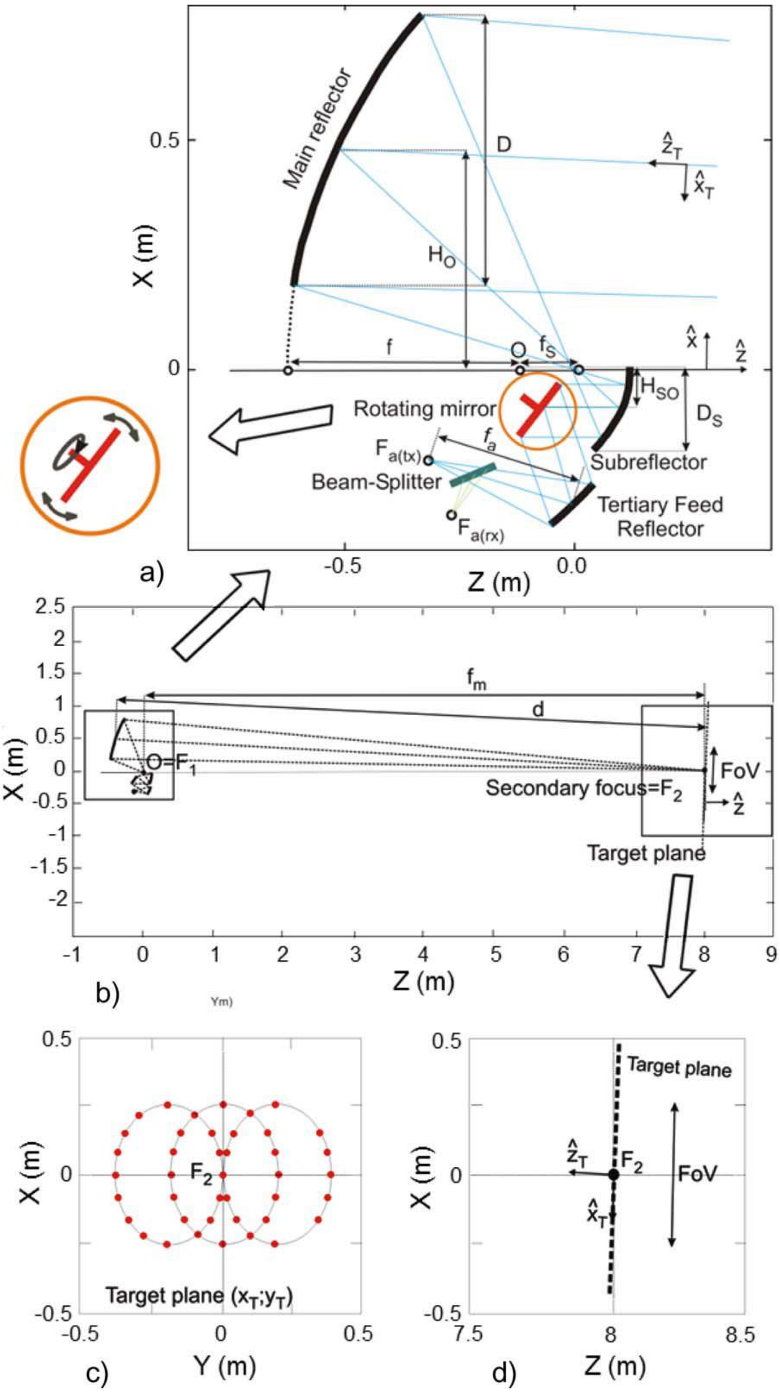

Figure 1- 13. (a) Profile of the baseline CEGRS antenna and main geometrical parameters (b) CEGRS antenna and target plane (c) Front view of the target plane and beam trajectory (d) Side view of the target plane [42]

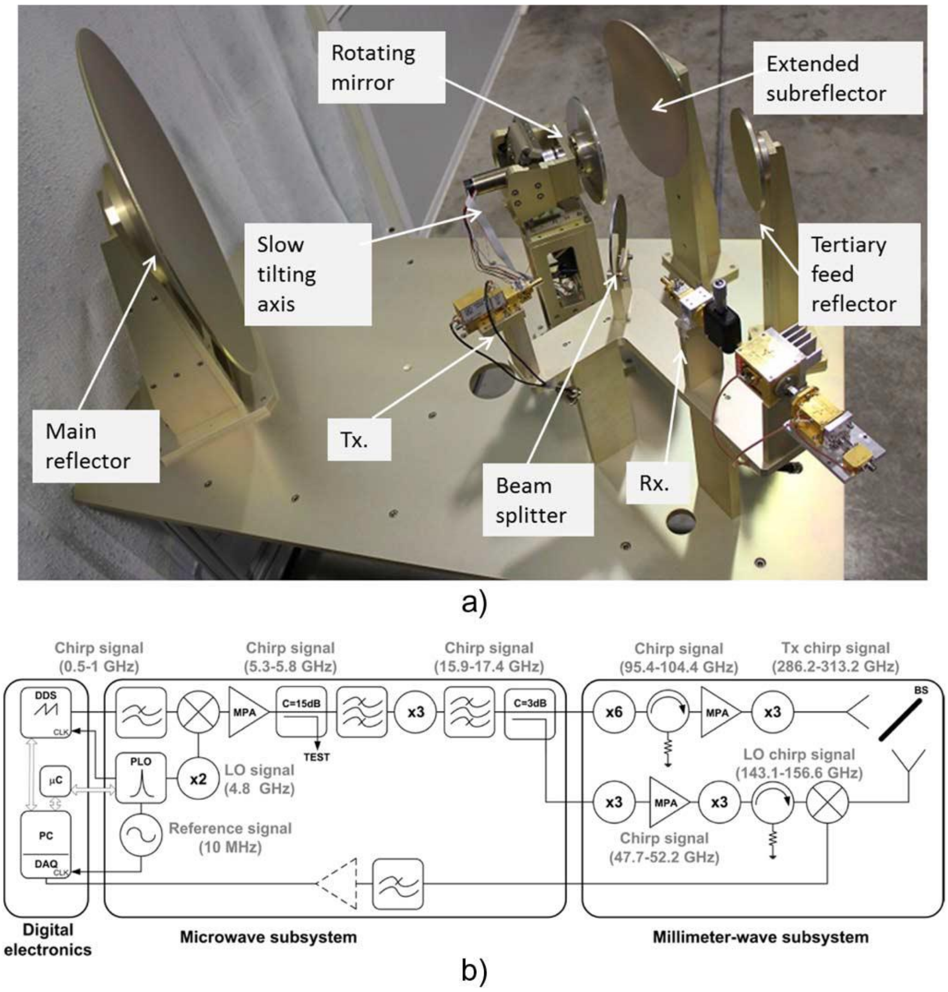

Figure 1- 14. (a) Photograph of prototype with labels introducing the electronics and antenna subsystems (b) Block diagram of the radar system at 300 GHz [42].

(a)

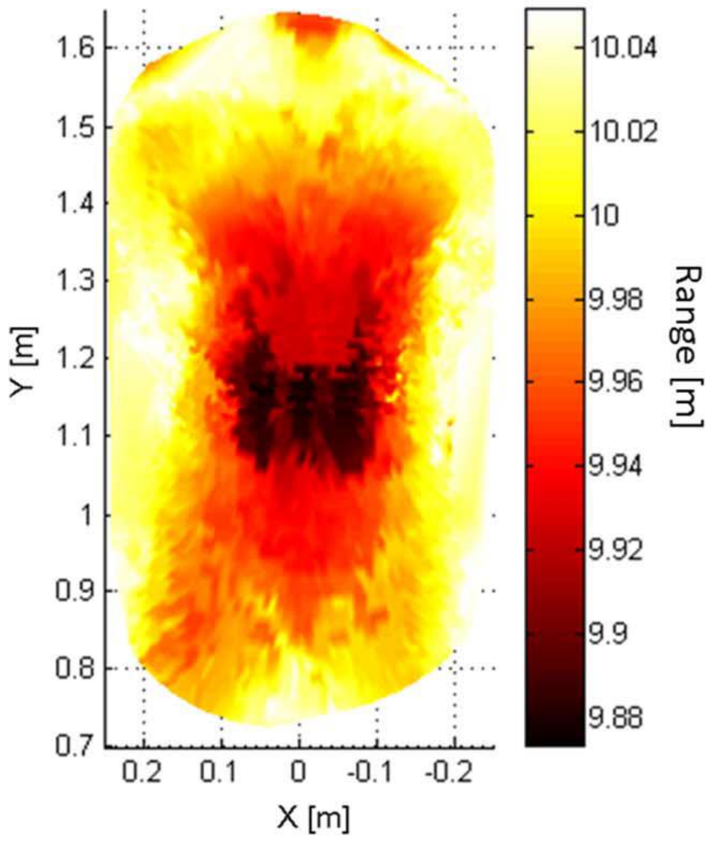

(b)

Figure 1- 15. (a) Target scenario with a mock explosive concealed underneath a T-shirt (b) Image reconstruction based on most powerful detection. An offset of 1.8 m is present in the measurements due to the extra length of the electrical path in the millimeter-wave and scanning antenna subsystems [42]

In addition, Figure 1- 16 shows the schematic diagram of an advanced optical-mechanical scanning THz imaging scheme at 0.2 THz that uses both heterodyne architecture and synthetic aperture imaging techniques [30]. The system uses a pillbox-like transceiver antenna to generate a fan-beam with its wide side lying along the vertical direction (**x**-direction) and narrow side lying along the horizontal direction (**y**-direction). Based on the fast rotation of the small sub-reflector, the fan-beam can quickly scan along the **y**-direction. Combining the linear scanning along the **x**-direction by the motorized stage, the phase and amplitude of reflected signal in a 2-D aperture can be collected to reconstruct a focusing image of target. In the above imaging scheme, the high resolution in the **y**-direction can be directly achieved by the focusing of the main reflector while the high resolution in the **x**-direction can be obtained by the synthetic aperture technique. The results have shown that the system has a d = 0.45 m focusing distance, 7 mm horizontal resolution and 4 mm vertical resolution with a 10 GHz bandwidth, and the entire reconstruction requires 3 seconds. Figure 1- 17 and Figure 1- 18 show the experimental resolution, we can see the theoretical resolutions can be basically achieved with the wideband operation. Besides, Figure 1- 19 compares the experimental imaging performance of wideband operation but with the target tilted. It can be seen from the Figure 1- 19 (b) that the image quality will deteriorate with the increase in tilted angles of target. Finally, Figure 1- 20 shows the experimental 3-D images of a man wearing a T-shirt and a concealed plastic cap gun with different views. Similarly, we can only gain the best image quality in Figure 1- 20 (c) in which the wideband operation is used and there is no tilted view angle.

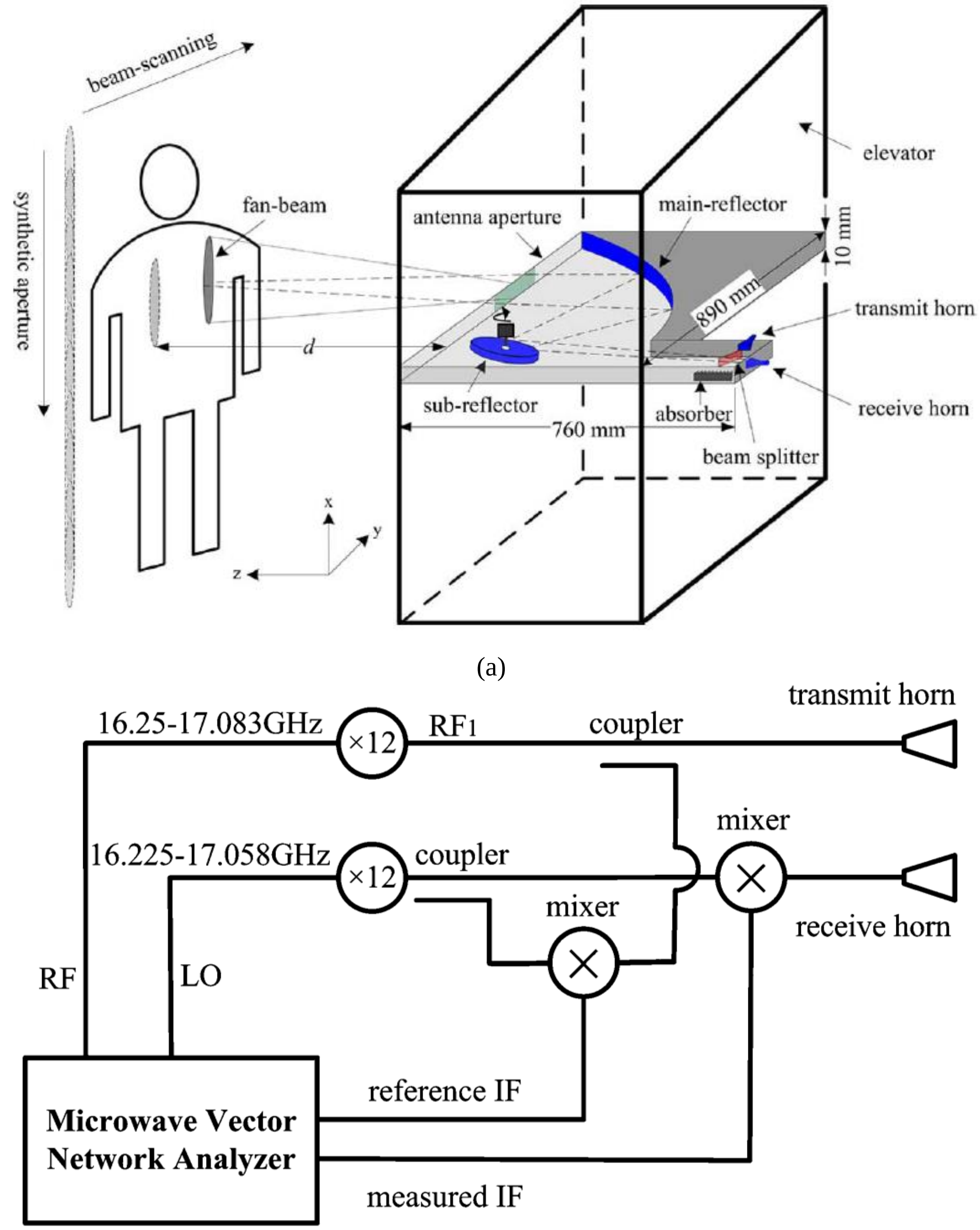

(a)

(b)

Figure 1- 16. 0.2 THz imaging scheme combining fan-beam scanning and synthetic aperture technique. (a) Schematic diagram and (b) Heterodyne transceiver [30]

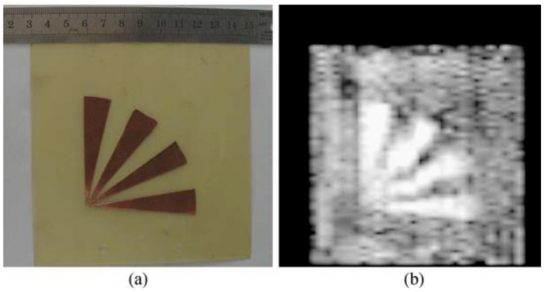

Figure 1- 17. (a) Photograph of target of four fan-shaped metallic strips and (b) corresponding 0.2 THz single-frequency reconstructed image [30]

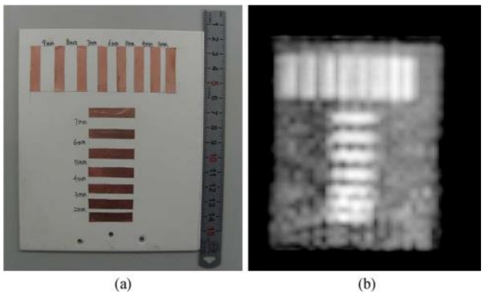

Figure 1- 18. (a) Photograph of target of metallic strips and (b) corresponding wideband 0.195 – 0.205 THz reconstructed image [30]

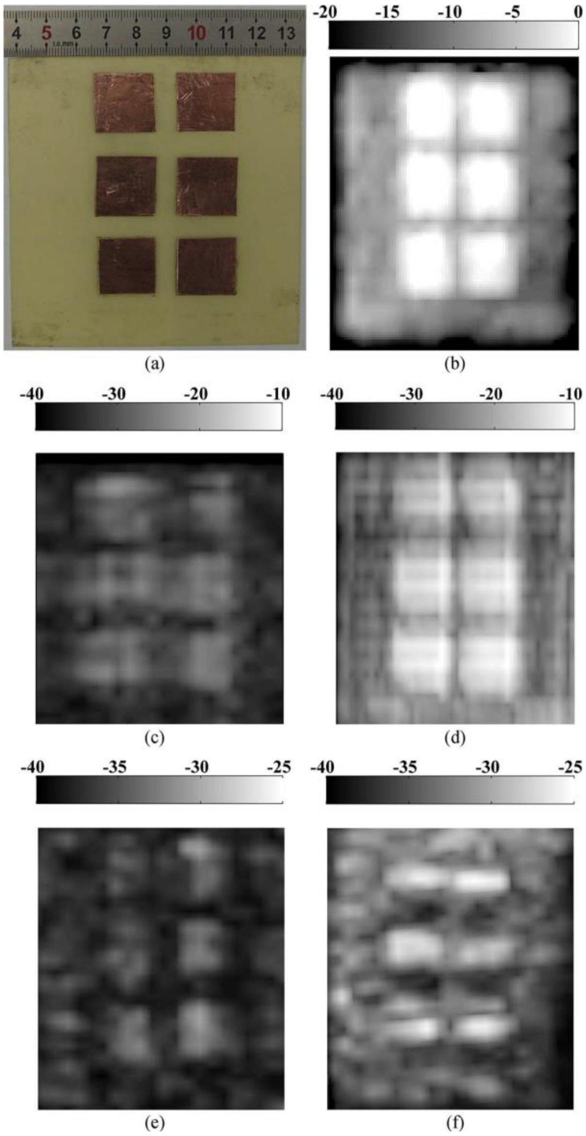

Figure 1- 19. (a) Photograph and 0.195 – 0.205 THz reconstructed images of six square metallic patches with (b) no tilted angle in either the horizontal or vertical direction (c) 10° tilted angle in the horizontal direction (d) 10° tilted angle in the vertical direction (e) 30° tilted angle in the horizontal direction and (f) 30° tilted angle in the vertical direction [30]

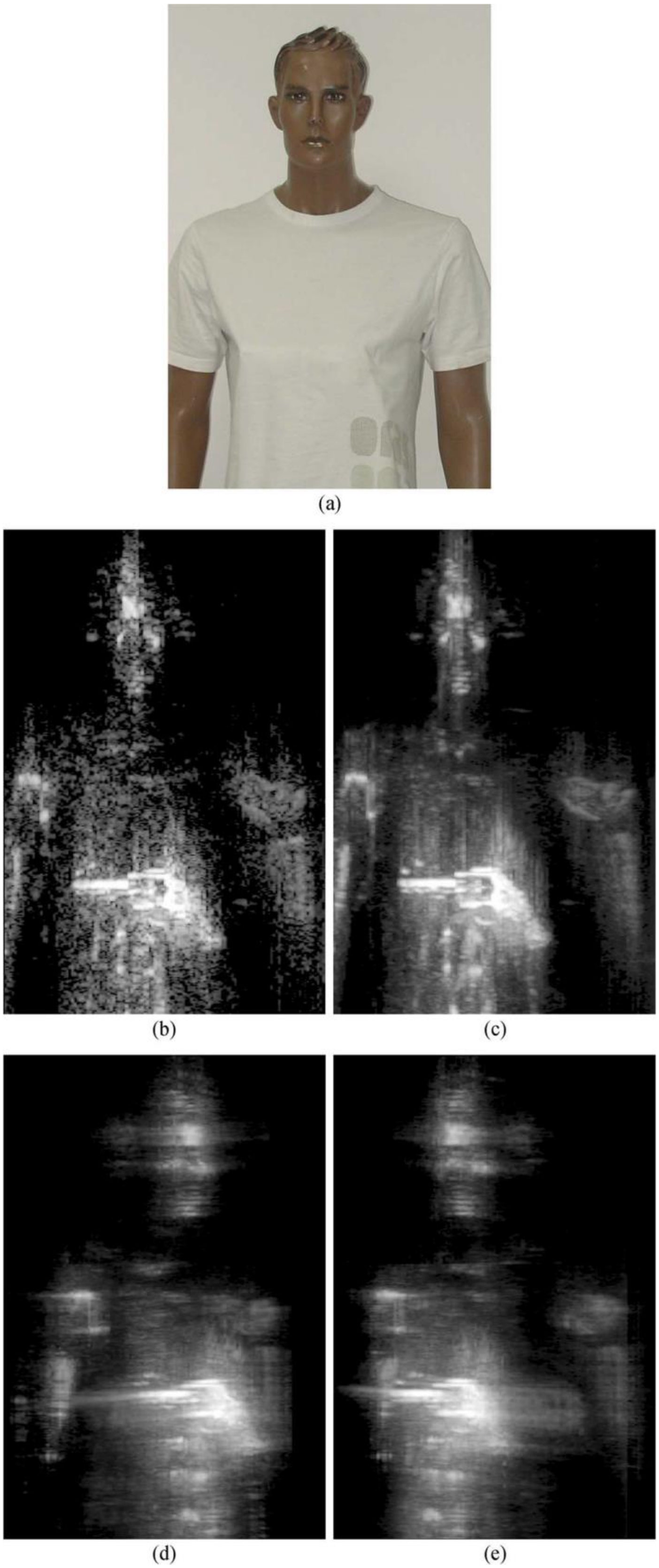

Figure 1- 20. (a) Photograph of mannequin target under test (b) corresponding 0.2 THz single-frequency reconstructed image, and wideband (0.195 – 0.205 THz) 3-D images of a mannequin wearing a T-shirt and a concealed plastic cap gun with (c) front view (d) 35° left-side view and (e) 35° right-side view, respectively [30]

In addition to the aforementioned quasi-optical imaging systems using a single transmitter-receiver(TR) pair, an TR array can also be integrated with such a kind of quasi-optical scheme, as shown in Figure 1- 21 [39]. The experimental set-up consists of 4 Tx and 16 Rx with 4 mm Tx element spacing, operating at 340 GHz with 16 GHz bandwidth. The scanning area is 1.8 m × 0.9 m at 4 m distance and the corresponding theoretical resolutions is 1.5 cm. The mechanical scanning time costs 2 s and extra 1 s is needed to reconstructed the 3 D image. In addition, Burg's method as an efficient and widely used power spectral density (PSD) estimation algorithm can achieve higher resolution and lower side-lobes than the FFT algorithm [39]. The corresponding experimental imaging results reconstructed by FFT and Burg-based method are shown in Figure 1- 22 and Figure 1- 23, respectively [39]. However, the images in Figure 1- 23 have not shown sufficient details to identify the concealed weapons due to the small aperture of array used and the intrinsic drawback of picking up echoes in this scanning scheme.

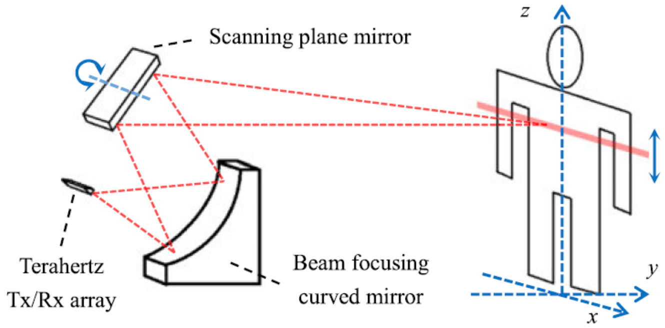

(a)

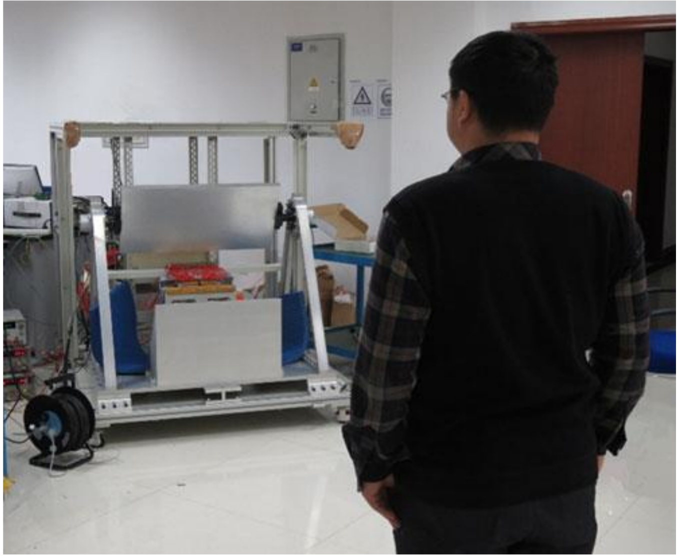

(b)

Figure 1- 21. (a) Schematic diagram of the 340 GHz quasi-optical imaging system (b) Experimental imaging scenario of a human carrying a concealed handgun model [39]

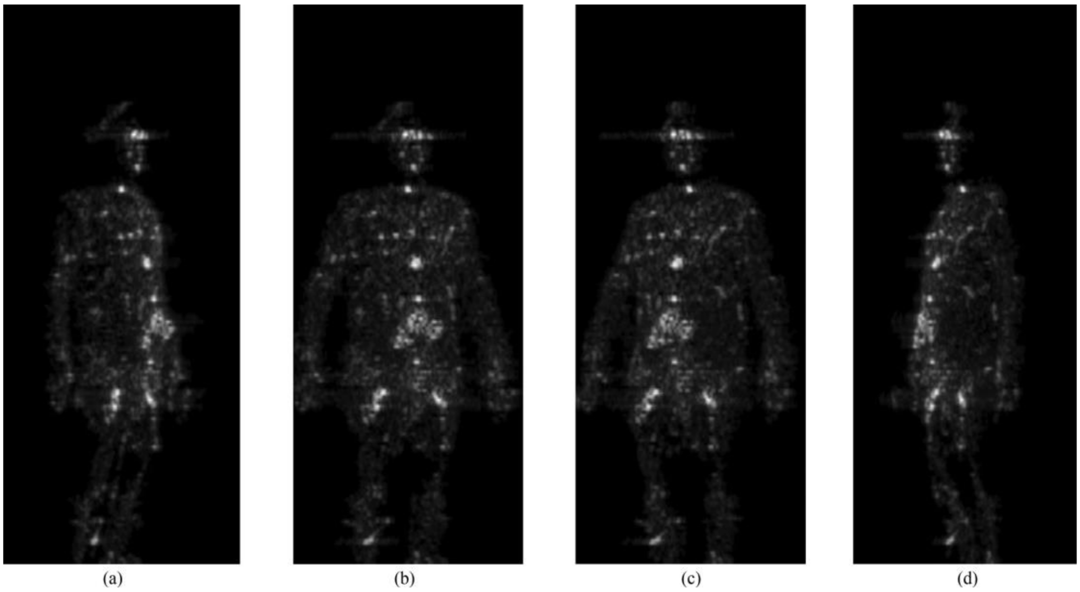

Figure 1- 22. 3-D images reconstructed by using FFT algorithm with different azimuth view angles. (a) −60° (b) −20° (c) 20° (d) 60° [39]

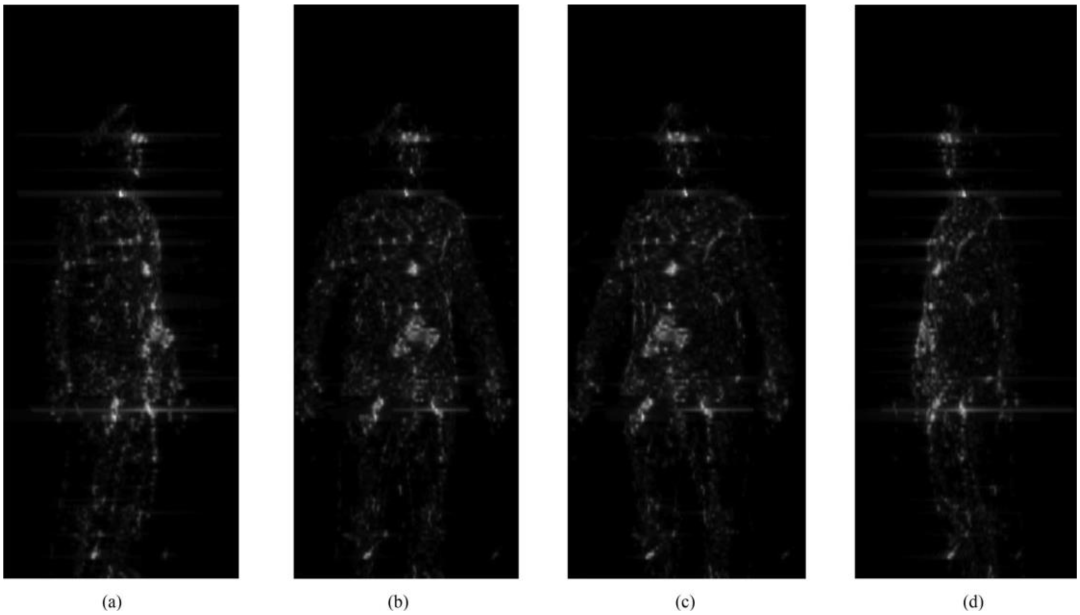

Figure 1- 23. 3-D images reconstructed by using Burg-based method with different azimuth view angles. (a) −60° (b) −20° (c) 20° (d) 60° [39]

In my opinion, in the above advanced quasi-optical imaging systems, no matter whether they use synthetic aperture technique or not, the imaging inherently rely on receiving the reflected signals from the target. Small focusing reflectors have advantage of compact size but cannot achieve a large scanning aperture or FOV. The beam has abbreviations at wide scanning angle. In contrast, large-scale reflector causes disadvantages in cost and size.

1.2.3. Interferometric Array Imaging System

In order to perform fast and high performance THz imaging, one promising solution is to employ the interferometry technique. Therefore, signals at two or more points in space with the proper delay are used to produce the brightness distribution [44]. This technique measures both amplitude and phase of the incoming signals. If a sufficient number of sampling points in the aperture plane are measured, the original brightness distribution can be synthesized (imaged) through standard Fourier inversion. The raw images after inversion can be improved through standard image reconstruction techniques to reduce ambiguities (called side-lobes) in the images [44]. In contrast to the aforementioned advanced quasi-optical imaging system, the interferometric array imaging system discussed in this section has eliminated the quasi-optics for beam focusing or scanning.

The interferometric/synthetic aperture imaging combines the THz signals collected from various pairs of detectors to reconstruct the image. It does not require the source to be phase coherent with the detector, so it has some flexibility in integrating a high power source with an independent detection array [44, 45, 50]. The interferometric array consists of individual detectors or sensors measuring the amplitude and phase of incoming THz radiation. As a wave front of THz radiation encounters the array, each pair of detectors as shown in Figure 1- 24(a) measures one spatial Fourier component of the incoming THz signal as determined, known as a baseline. Each spatial Fourier component is represented as a point in the Fourier transform plane (also known as the u-v plane). In order to image the source, additional measurements from other baselines must be carried out. For a given number of detectors N, there are N × (N-1)/2 possible baseline combinations, as shown in Figure 1- 24(b). An image is reconstructed from the spatial Fourier components of all the different pair combinations. The quality of an image depends on the coverage of the u-v plane, i.e. the number of different points generated in the u-v plane. This in turn depends on the arrangement of the detecting elements of the interferometric array. Efficient u-v plane coverage with a small number of detectors may be achieved by rotating the array about a fixed axis. If measurements are made 10 times during the rotation of an N element planar or spherical array, the equivalent number of baselines will be 10 times of N × (N-1)/2. This will improve image quality and equivalently lead to a reduction in the number of required detectors in the array for a given image quality.

This aperture synthesis technique is capable of achieving a larger effective collecting area hence spatial resolution is increased without fully populated antennas [60]. The primary disadvantage of this system/technique is that the close-range large-aperture operation causes the depth of focus to be very short. Therefore, the image of a target with significant depth, such as the human body, cannot be reconstructed in complete focus. However, wideband holographic imaging even allows to form a 3D image, which overcomes the short focus depth of single frequency holographic imaging [47].

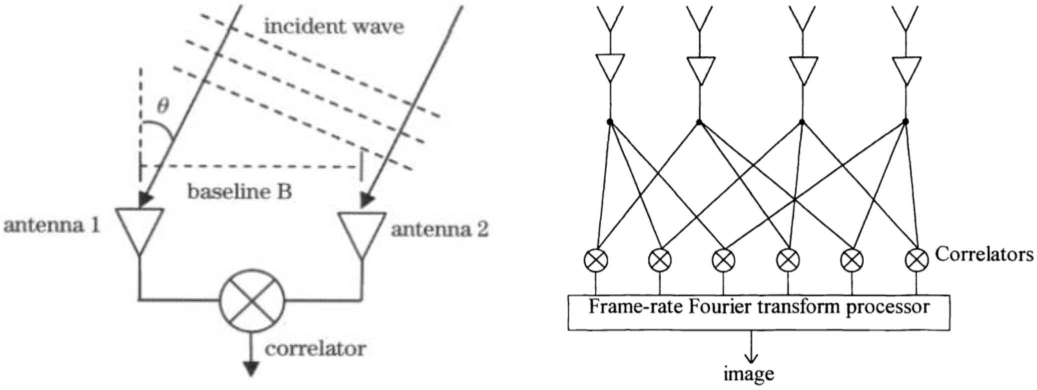

(a) (b)

Figure 1- 24. Interferometric set-up. (a) TR pair (b) Array imaging system [61]

I. Dense Array Imaging System: Quasi-monostatic Linear Array

For example, a single-frequency 35-GHz transceiver has been used to generate an image of a clothed mannequin with a large concealed metallic handgun, as shown in Figure 1- 25(a) and (b) [47]. The hologram image shows the raw data, which are input to the BP based FFT image reconstruction algorithm (see Appendix I). The reconstructed image shows the resolution of about 5 mm, and the handgun can be easily recognized in the image. The image of the mannequin body shows the artifacts due to complex interference from varying reflection points on the body at different ranges. This effect will be largely eliminated when the wide-band 3-D imaging technique is used. Moreover, a reconstructed 350-GHz image of a Glock-17 has been shown in Figure 1- 25(c). In the image, the aperture is 25 cm × 25 cm, and the depth to the target is 7.4 cm. The hologram consists of 512 × 512 data points, sampled with an interval of approximately 0.5-mm. The scanning takes approximately 10 min. This image has shown a resolution of less than 1 mm. Due to a very large number of samples required at a high frequency for achieving a high resolution image, a trade-off should be made in a practical weapon detection system.

(a) (b) (c)

Figure 1- 25. Target of a mannequin carrying a concealed handgun of (a) 35-GHz hologram (raw input data) and (b) corresponding reconstructed 35-GHz image and (c) reconstructed 350-GHz image of a Glock-17 9-mm handgun [47]

The 3-D imaging technique employing active, wideband, coherent RF transceivers has been proposed to optimize the quality of the images from data gathered from a 2-D aperture. These data are sampled at sub-wavelength (often 0.25 to 0.5 wavelengths) intervals. This increases the time of data acquisition dramatically for mechanically scanning method. However, a practical application demands a full-body scan in about 1–2 s (or less). In addition, a full-body scan requires sampling at less than one-wavelength spacing over an aperture of at least 0.70 m × 2.0 m [47]. In this case, switched antenna arrays may be used to eliminate mechanical scanning on one or both axes of the aperture. This is typically accomplished by creating a dense linear or planar antenna array and electronically sequencing across the array with use of electronically controlled microwave or millimeter-wave switches [47]. The simplest configuration of a sequentially switched linear array has two column arrays of transmitter antennas and receiver antennas, separately [47]. This combined array can simulate a single transceiver array. A transmitter and receiver pair effectively sample one spatial point. The array is sequentially sampled by switching on the first transmitter antenna and the first receiver antenna and collecting the first spatial sample. The second transmitter antenna can then be switched on and the second sample collected (with the first receiver antenna still switched on). The second receiver antenna is then switched on (with the second transmitter antenna still on while the first transmitter antenna switched off) to collect the third spatial sample [51]. This process is then continued across the array [51]. This technique still requires approximately one antenna per spatial sample, but allows the antennas to be separated by twice the distance and separates the T and R functions, which improves array performance [49, 51, 52, 62]. A block diagram of such an imaging system operating from 27 to 33 GHz has been shown in Figure 1- 26. There are 128 antenna elements organized as an upper row of 64 transmitter antennas, and a lower row of 64 receiver antennas. A logic circuitry sequences transmitter and receiver antennas to transmit from one antenna and receive the wide-band signal from each of the two neighboring antennas in the receiver row. This configuration places a virtual sampling point halfway in between each transmitter and receiver antenna. The transmitter row and receiver row are offset by half the antenna, thus, the effective sample spacing is one-half of the single-row antenna spacing [47].

The wide-band millimeter-wave imaging system has been tested extensively on personnel carrying concealed weapons [47]. Figure 1- 27 shows a significant improvement in image quality by improving the single-frequency millimeter-wave imaging system to wide-band imaging operation. The single-frequency images show obvious degradation due to lack of focus over many parts of the image. In addition, some degradation is apparent due to poor sensitivity in the single-frequency transceiver. In contrast, the wide-band images are fully focused due to the 3-D image reconstruction. Besides, an apparent higher dynamic range has been obtained in wide-band imaging operation due to better focus and the high-sensitivity transceiver [47].

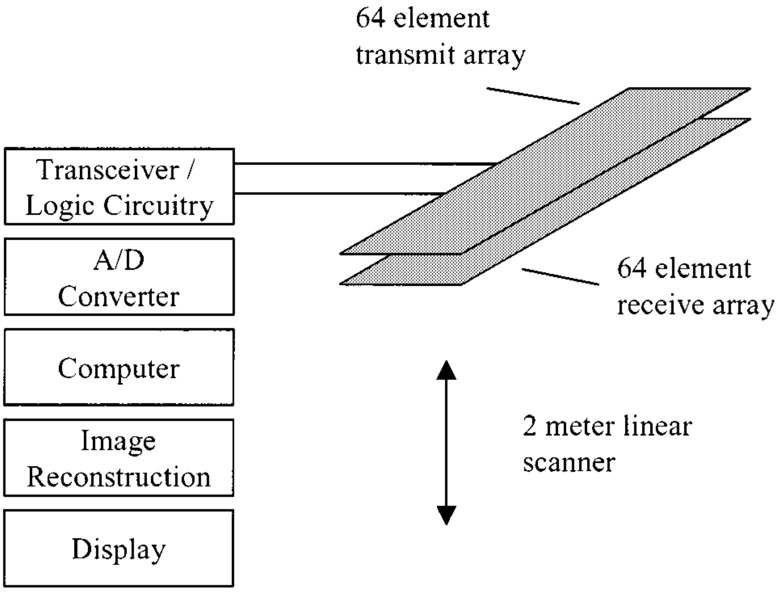

Figure 1- 26. Block diagram of 27 – 33 GHz quasi-monostatic linear array imaging system [47]

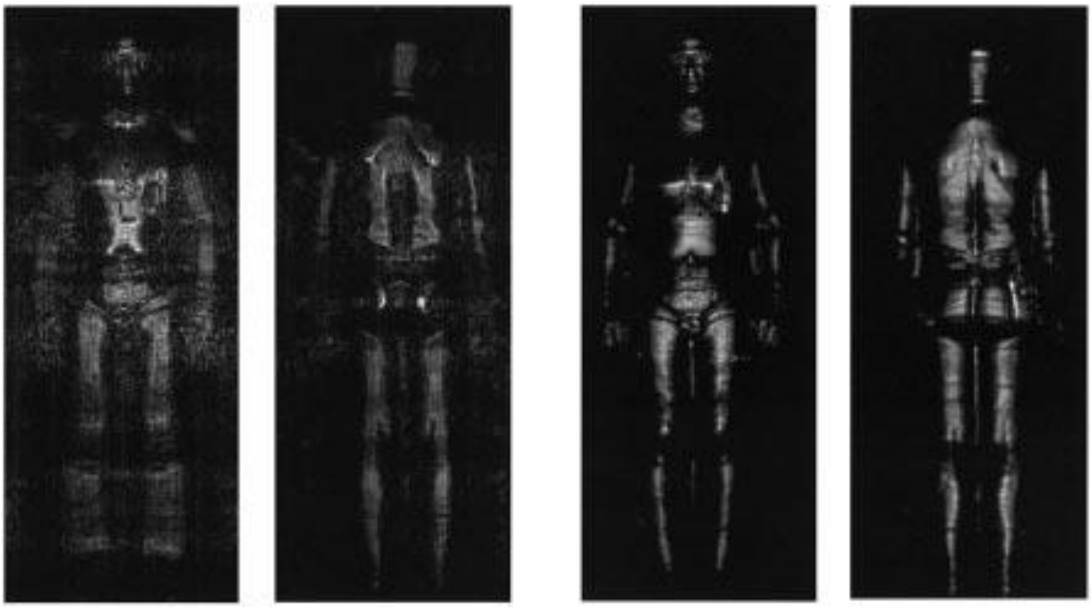

(a) (b)

Figure 1- 27. (a) Reconstructed single-frequency (35 GHz) images of a man (b) Reconstructed wide-band (27 – 33 GHz) images of the same man [47]

Figure 1- 28 shows six wide-band (27 – 33 GHz) images of a man carrying two concealed handguns and several innocuous items. The first image shows a Glock-17 handgun tucked at the beltline underneath the man's shirt. The second image shows a small handgun in the man's left-hand-side pants pocket. The third image shows a paper checkbook in the left-hand-side back pocket. The fifth image shows a leather wallet in the man's right-hand-side back pocket [47].

In addition to this planar imaging technique, a cylindrical imaging technique and an alternative polarimetric technique are also studied under such an imaging scheme [48, 49, 63]. The distinct advantage is that a single scan can be acquired and used to inspect the person from all angles. Figure 1- 29 shows such cylindrical scanning images of a mannequin taken in the range of 40 – 60 GHz [49]. These images were obtained by using the standard cylindrical image reconstruction algorithm. Various small and medium sized objects including a Glock handgun were placed on the mannequin. These objects have been readily revealed when viewing an animation of the reconstructed images over all angles. The single aspect image presented in Figure 1- 29 (center) emphasizes the concealed handgun on the lower left thigh. The 40 – 60 GHz frequency range allows extremely high lateral in the order of 3 mm and range resolution of approximately 7.5 mm [49]. In addition, the polarimetric technique can be used to enhance detection of many concealed objects. For linear polarization, a co-polarized configuration (transmitter and receiver use the same polarization) tends to receive strong reflections from smooth surfaces like human body. A cross-polarized configuration (transmitter and receiver use orthogonal polarization) tends to reject the reflection from smooth surfaces and accentuates raised edges, corners and dihedrals. This behavior is apparent by comparing the results from Figure 1- 29 (center, co-polarized) and Figure 1- 29 (right, cross polarized) [49].

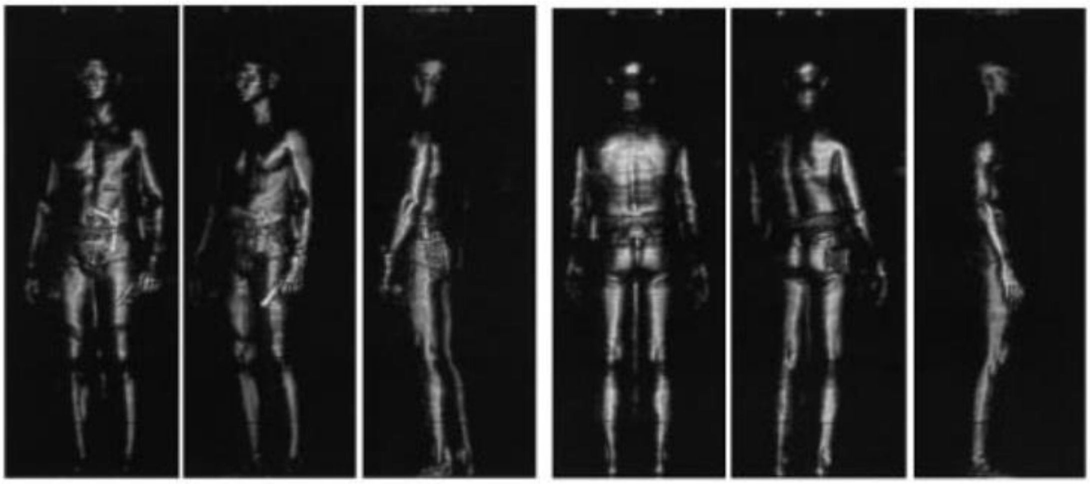

Figure 1- 28. Reconstructed wide-band (27 – 33 GHz) images of a man carrying concealed handguns and innocuous items [47]

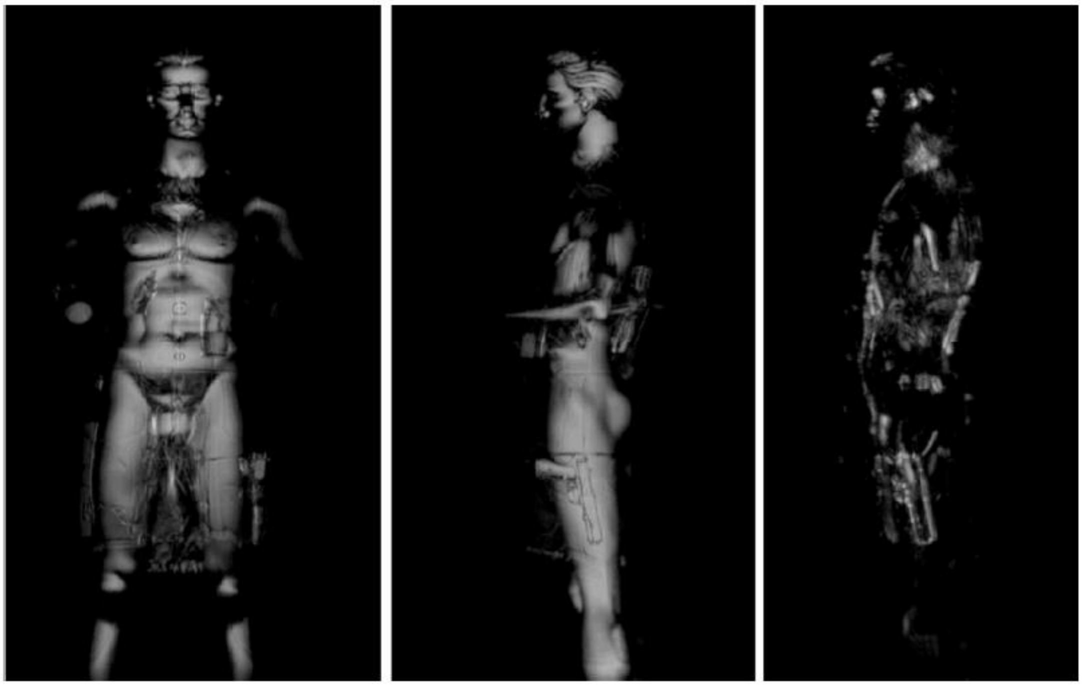

Figure 1- 29. Reconstructed wideband (40 – 60 GHz) images with cylindrical scanning of a clothed mannequin. Left image: cylindrical image reconstruction (linearly polarized, transmit vertical, receive vertical); Center image: another angle from left-image set emphasizing a concealed handgun; Right image: linear cross-polarized image (transmit vertical, receive horizontal) at the same angle as the center co-polarized image [49]

II. Two-Column Multi-static Sparse Array with Multiple TR Combinations

Implicit the two-column array sampling technique described above is the quasi-monostatic approximation. This approximation is that transmitter and receiver antennas separated near each other effectively operate as a single transmitter-receiver (TR) antenna placed at the midpoint of the line joining the phase centers of both antennas. This approximation introduces a path length or phase error that is not significant for closely spaced antennas, but will be more significant for the multi-static array configuration [51, 52]. Therefore, the two-column sparse array sampling technique has been proposed in order to save cost with the utilization of multi-static set-up [51, 52]. It essentially uses a multi-static approach in which each single transmitter is coupled to a number of receivers. Therefore, this multiple use of each transmitter and receiver produces a more finely sampled array without the cost and complexity of a fully populated array [51, 52].

This kind of array can be analyzed using an effective sampling concept [52]. As shown in Figure 1- 30, the left Tx array, Array 1, has N1 elements over a unit cell length D with a spacing of D/N1. The right Rx array, Array 2, has N2 elements over a unit cell length D with a spacing of D/N2. The total number of unit is Nc [52]. In order to meet the requirement close separation between transmitter and receiver, only separations of less than D are used. Therefore, each Tx element in Array 1 has 2N2 effective samples available. Larger separations could be used. However, these will result in redundant sampling. An elegant arrangement that meets the uniform dense sampling requirement is obtained when N1 and N2 are set to be unequal (N2 > N1 is typically assumed), and they are assumed to share no common factors. In general, the number of samples per unit cell is $N_{samples} = 2N1 \cdot N2$, and the effective sampling spacing is $\Delta y = D/(2N1 \cdot N2)$. A convenient figure of merit for the sparse multi-static array is the number of effective samples divided by the number of antennas required (per unit cell), or $N_{samples} / N_{antennas} = 2N1 \cdot N2 / (N1 + N2)$ [52].

A series of array configurations with increasing sparsity is shown in Figure 1- 31. The left blue circles represent locations of Tx antennas, and the right red circles represent locations of Rx antennas. Points in the connection lines between representative T and R locations indicate the effective sample locations. The 1:1 array shown in Figure 1- 31 (a) is equivalent to the currently deployed airport screeners and achieves approximately one sample per antenna ($N_{samples} / N_{antennas} = 2N1 \cdot N2 / (N1 +$

N2)). The 1:2 array achieves approximately 1.33 samples per antenna. The 2:3 configuration achieves approximately 2.4 samples per antenna, and the 3:4 configuration achieves approximately 3.43 samples per antenna [51].

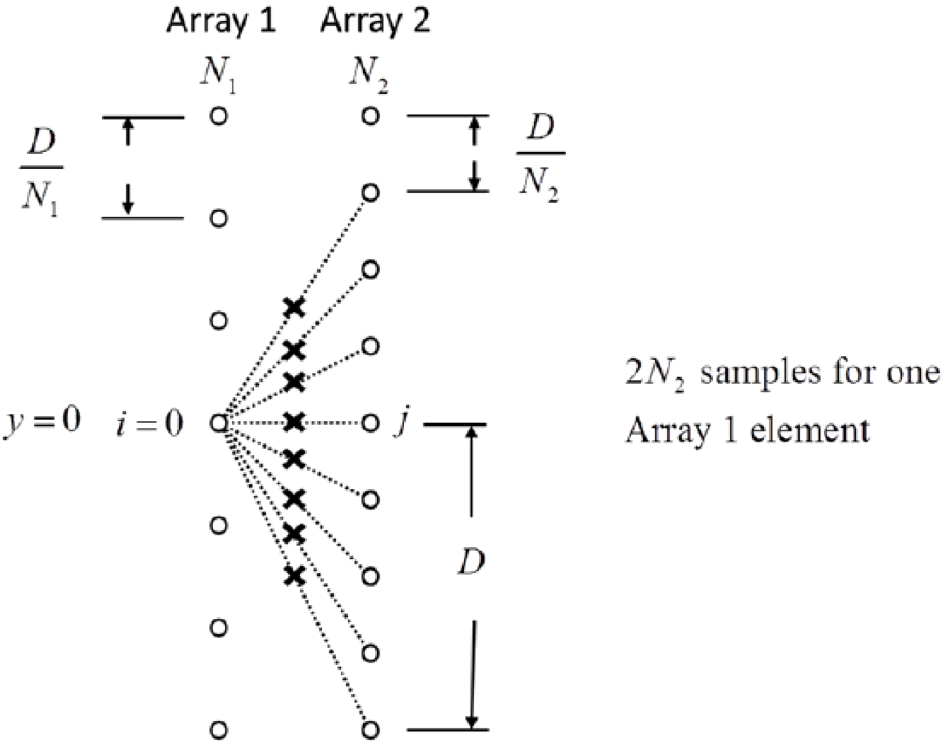

Figure 1- 30. Effective sampling analysis of two-column multi-static sparse array [52]

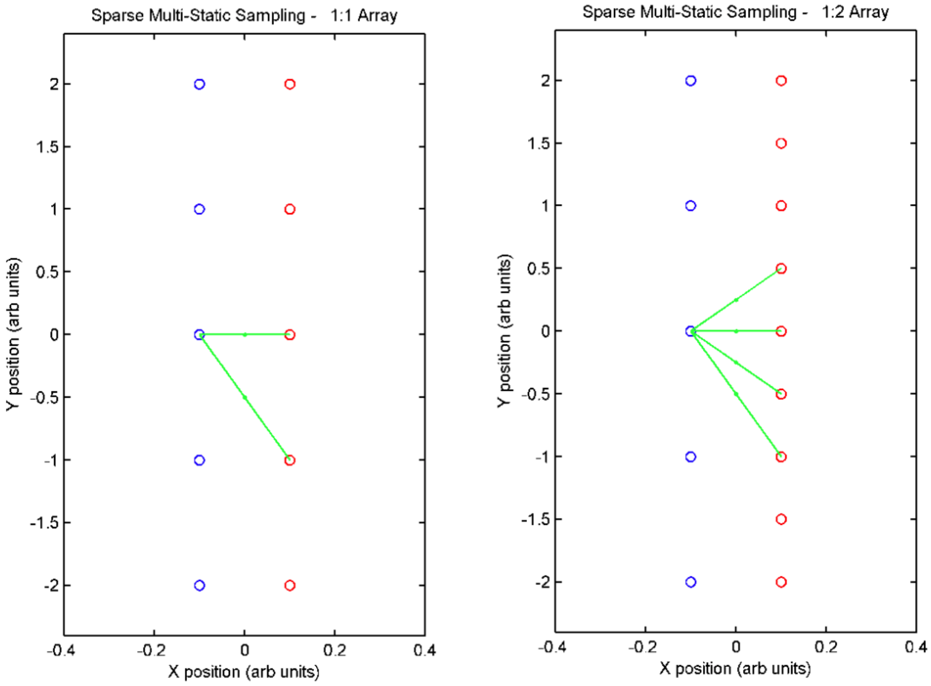

(a) (b)

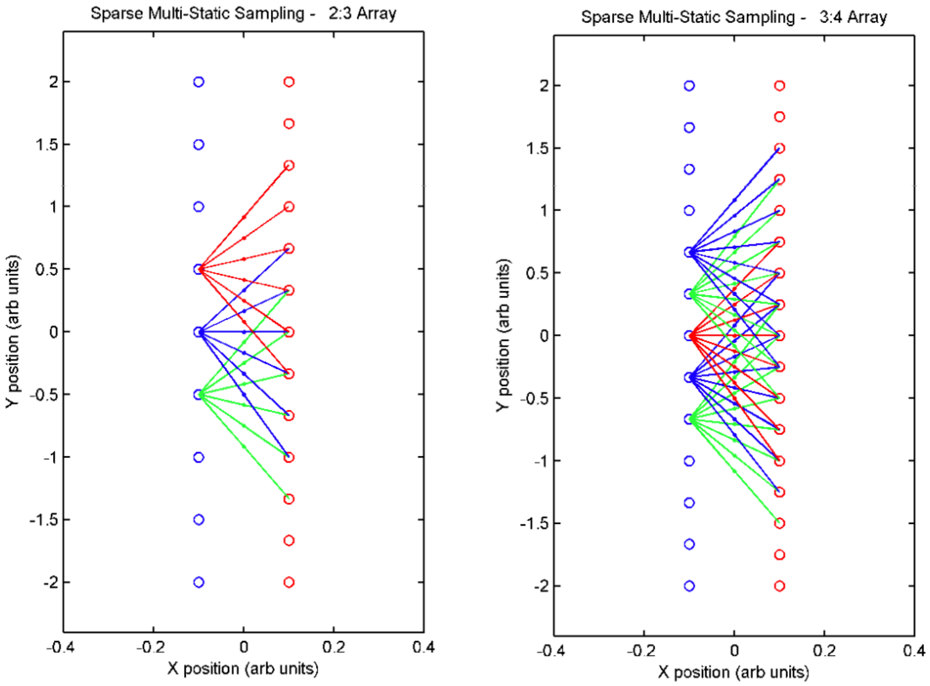

(c) (d)

Figure 1- 31. Effective sampling for (a) 1:1 (b) 1:2 (c) 2:3 (d) 3:4 arrays [51]

An important issue of implementing the multi-static sparse array in imaging application is that there are significant path length differences between effective transceiver samples due to the different baseline separations of the paired transmitter and receiver antennas [51]. The path length differences can be compensated using the array calibration techniques that essentially range or phase-shift the transceiver data to remove the error. The array calibration techniques are approximate because they assume a direction of wave travel in order to estimate the path error [51]. The GSAFT(Generalized Synthetic Aperture Focusing Technique) algorithm is capable of producing better results because it uses the exact Tx and Rx locations for each sample location while the FFT-SAR (Fast Fourier Transform-Synthetic Aperture Radar) algorithm assumes that the T and R antennas are effectively located at the midpoint sample position [51].

The effectiveness of the sparse array technique has been explored using the data simulated for a variety of sparse array configurations in [51]. For all configurations simulated, a 1 m linear array length and a frequency range of 20 – 40 GHz with 1024 samples are used. The target is defined as a collection of two letter-F test targets each is composed of 9-point scatters separated by 3.0 cm. And two F letters are centered with respect to the array and at ranges of 0.5 m and 1.0 m, respectively. The individual sparse arrays are denoted by N1:N2: Nc (number of transmitters per unit cell: number of receivers per unit cell: number of unit cells).

Figure 1- 32 shows the imaging results in a 2:3:24 array reconstructed by using both GSAFT and FFT-SAR methods. In this array configuration, both reconstruction techniques yield similar results since the separation between Tx and Rx locations is not wide in the low sparsity array. So the calibrated quasi-monostatic approximation is reasonably accurate. This array has a unit cell length of 4.17 cm, 48 Tx antennas, 72 Rx antennas, 287 samples, 0.35-wavelength (at 30 GHz) sampling spacing and 2.35 samples/antenna [51].

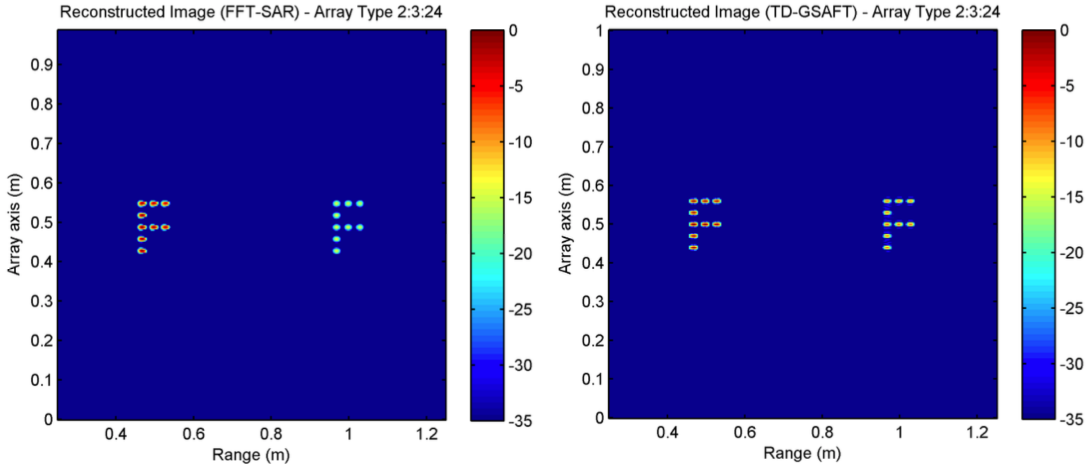

(a) (b)

Figure 1- 32. 35-dB dynamic range images reconstructed by using (a) the FFT-SAR technique and (b) the multi-static GSAFT technique with a 2:3:24 array configuration [51]

Figure 1- 33 shows the imaging results in a 3:4:12 array. In this array configuration, the FFT-SAR algorithm shows some artifacts of the F at 0.5m, which is probably due to the wide baseline between Tx and Rx antennas. The GSAFT reconstruction shows no artifacts for either F. This array has a unit cell length of 8.33 cm, 36 Tx antennas, 48 Rx antennas, 283 samples, 0.35-wavelength (at 30 GHz) sampling spacing and 3.29 samples/antenna [51].

Figure 1- 34 shows the imaging results in a 5:6:5 array. In this array configuration, the FFT-SAR algorithm shows significant artifacts for both F letters, which are likely due to the wider baseline between Tx and Rx antennas. The GSAFT reconstruction shows some moderate artifacts for the F at 0.5 m and no artifacts at 1.0 m. In addition, the GSAFT algorithm shows a sharper lateral focus than the FFT-SAR algorithm, possibly due to the more exact treatment of the T and R locations. This array has a unit

cell length of 20 cm, 25 Tx antennas, 30 Rx antennas, 281 samples, 0.33-wavelength (at 30 GHz) sampling spacing and 4.93 samples/antenna [51].

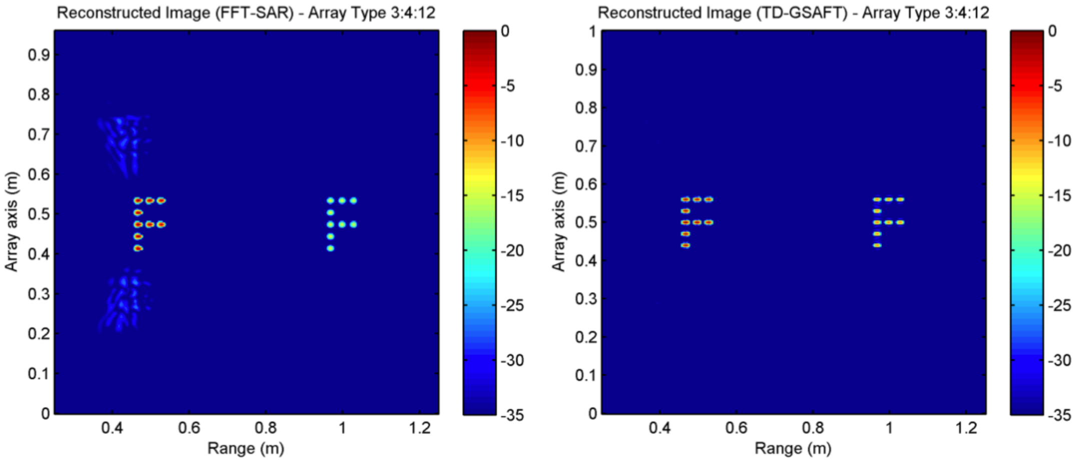

(a) (b)

Figure 1- 33. 35-dB dynamic range images reconstructed by using (a) the FFT-SAR technique and (b) the multi-static GSAFT technique with a 3:4:12 array configuration [51]

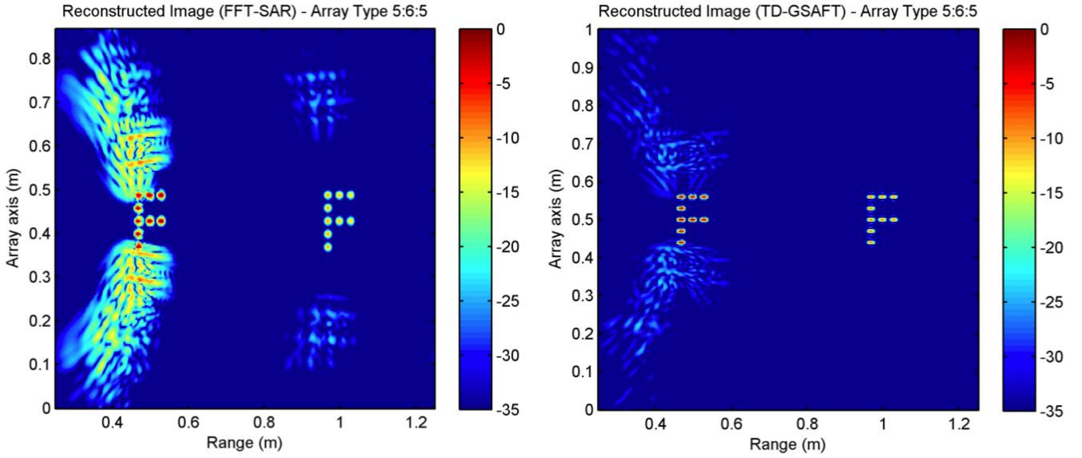

(a) (b)

Figure 1- 34. 35-dB dynamic range images reconstructed by using (a) the FFT-SAR technique and (b) the multi-static GSAFT technique with a 5:6:5 array configuration [51]

The two-column multi-static sparse array demonstrated here can be used to reduce the cost and complexity of a full array without significantly reducing system performance. Performance of a variety of imaging arrays has been demonstrated through numerical simulation. The quasi-monostatic approximation, upon which the two-column multi-static sparse array technique is based, holds well for targets at greater distances from the array, and for arrays with small maximum T/R baseline separations. The FFT-SAR algorithm also works well in these cases with the described array calibration techniques. The GSAFT algorithm accurately reconstructs images based on the exact Tx and Rx locations, and therefore does not require that the quasi-monostatic approximation is strictly valid. However, in highly sparse arrays, such as the 5:6:5 array, the baselines are very widely separated that thereby introduce some artifacts as observed in Figure 1- 34. It is important to note that the GSAFT technique is simple but computationally expensive. Therefore, the FFT-SAR technique is often preferred, especially for 3-D imaging configurations [51].

III. Multi-static Linear Sparse Periodic Array Imaging System

A multi-static linear sparse periodic array (SPA) places the transmitter elements at two ends of receiver elements and all the TR combinations are used to record the echo data for image reconstruction [64]. The feature of this array is that the radiation pattern of its effective aperture has a suppressed side lobe due to properly distributed Tx and Rx elements, which is helpful to gain a high quality image (see detailed introduction in 2.1). Based on this kind of sparse array, many imaging systems have been proposed and studied [53-55, 65-67]. For example, Figure 1- 35 shows a SPA consisting of 4 transmitter and 8 receiver elements working from 2.8 GHz to 19.5 GHz. The width of the transmitter array is 0.5 m ($18.6\lambda_c$) and the receiver array is 0.412 m ($15.3\lambda_c$), so it produces a uniformly distributed effective aperture with a spacing of $1.1\lambda_c$. Figure 1- 36 shows the experimentally imaging results at a range distance of 0.5 m using this SPA when scanning mechanically in the vertical direction compared to the one using the 2-D synthetic aperture radar (SAR) technique where a monostatic transceiver scans along two dimensions [53]. In both approaches, the shape of the mannequin and weapon have been basically reconstructed completely, and the weapon can be identified to some extent. In summary, the SPA-SAR configuration has generated comparable the results as the 2-D SAR. Instead of 51 antenna pairs required for the SAR data acquisition in the azimuth plane, only 12 antennas have been used in the SPA imaging system, thus demonstrating the advantage of such SPA imaging system [53].

Furthermore, another SPA has been proposed particularly optimised for near field imaging operating in the range of 75-90 GHz and at 0.6 m target distance [55]. Figure 1- 37(a) shows the first array (SPA_{FF}) that is the aforementioned conventional SPA design based on far-field assumptions. Figure 1- 37 (b) shows the optimized SPA for the near field (SPA_{NF}) scenario, which is based on the proposed design procedure [55]. Both sparse arrays consist of a receiver array with LR = 0.6 m length and Δz_R = 24 mm Rx element spacing; this leads to NR = 26 receiver channels. High lateral

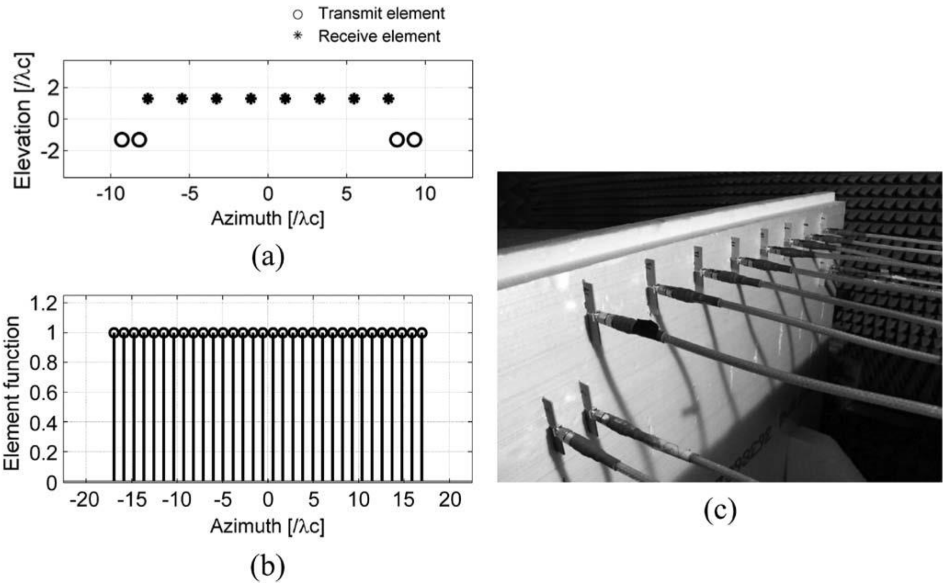

Figure 1- 35. SPA design. (a) Set-up configuration (b) Corresponding effective aperture and (c) Array constructed in the experiment [53]

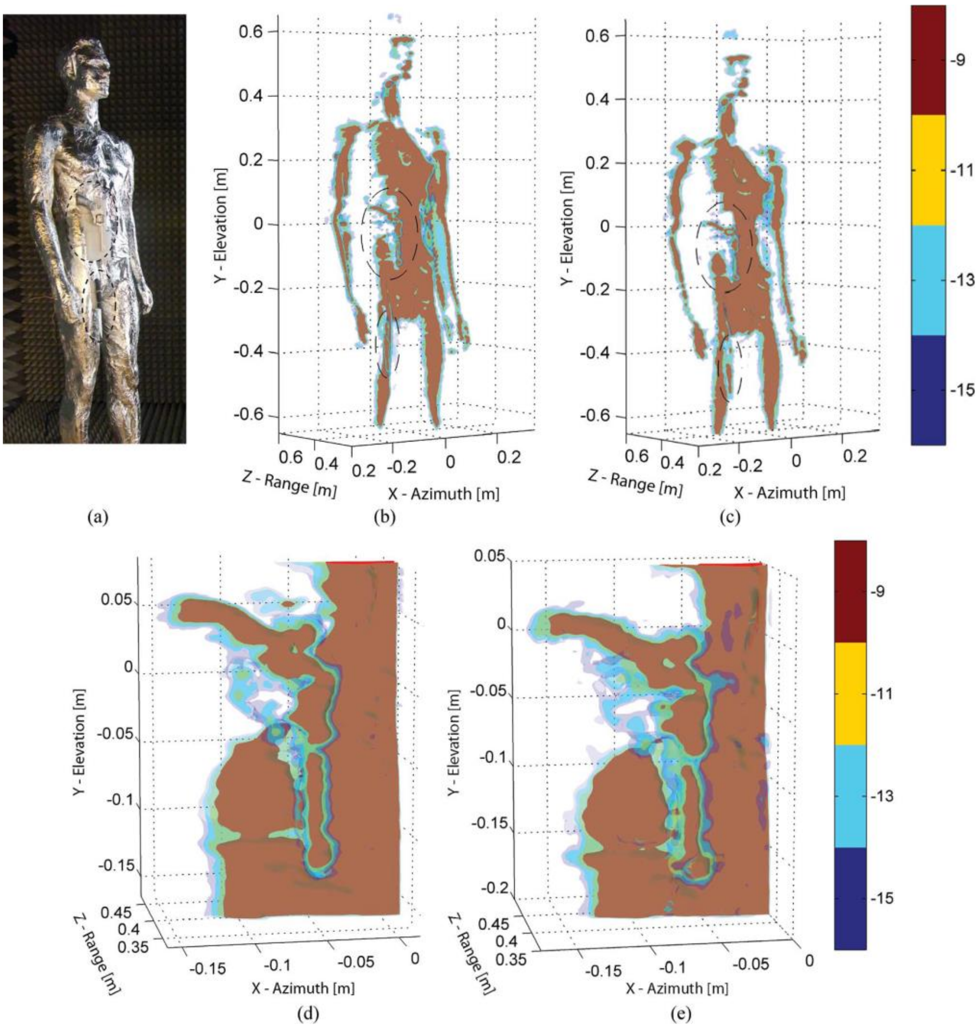

Figure 1- 36. Imaging using SAR and SPA-SAR system. (a) Mannequin under test carrying a handgun (b) Image reconstructed by using 2-D SAR (c) Image reconstructed by using SPA-SAR. Zoomed-in images of handgun of (d) 2-D SAR and (e) SPA-SAR [53]

resolution and optimal target illumination are achieved by two separated dense transmitter array sections with length $L_{T,B}$ and Δz_T = 2 mm Tx element spacing. The lengths of the transmitter array sections of SPA_{FF} are $L_{T,B}$ = 22 mm, which leads to the total number of NT = 24 transmitter elements. In order to keep a moderate number of transmitter channels, the length of each transmit array in SPA_{NF} is limited to $L_{T,B}$ = 30 mm, which leads to 36 transmitter elements.

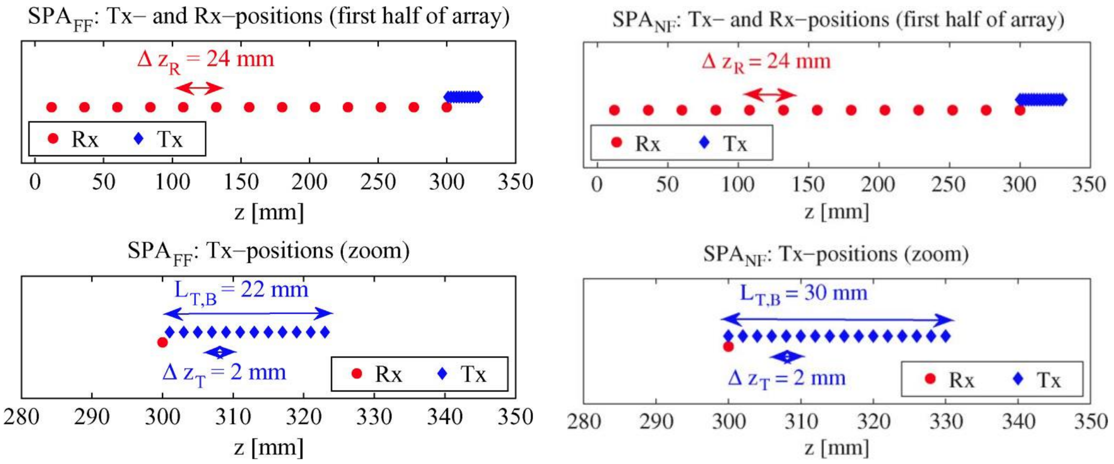

(a) (b)

Figure 1- 37. (a) Traditional SPA design (SPA_{FF}) based on far field assumption (b) optimized SPA design (SPA_{NF}) for near field imaging [55].

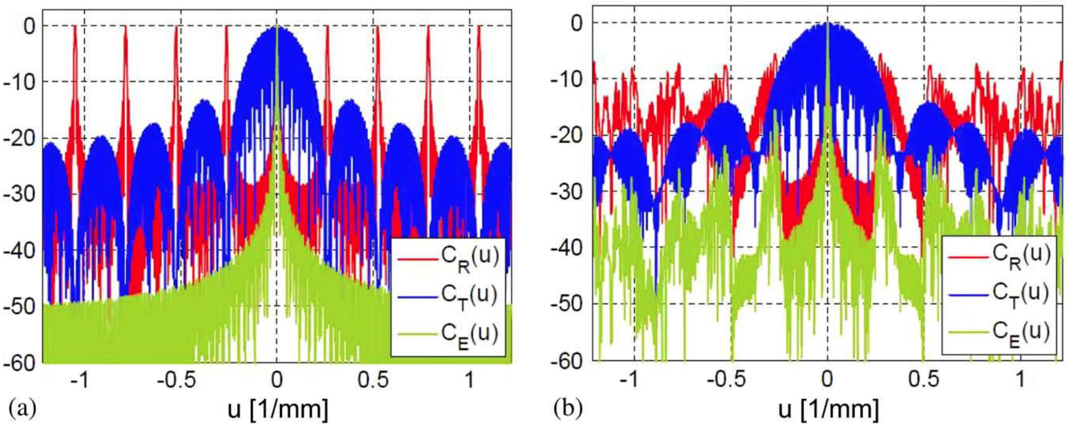

(a) (b)

Figure 1- 38. Characteristics $C_T(u)$, $C_R(u)$, and $C_E(u)$ of the transmitter, receiver, and multi-static SPA_{FF} arrays in the range of (a) array far field (Zt → ∞) and (b) array near field (Zt = 0.6 m) [55]

Figure 1- 38 shows the characteristics (PSF: Point Spread Function) of the traditional SPA design in Figure 1- 37(a) at a far field distance and at a near field distance Zt of 0.6 m. We can see the characteristics at near field distance differs from that at a far field assumption where the null of Tx pattern locates at the grating lobes of the Rx pattern. Since the grating lobes of Rx pattern slightly shift away from the null positons of Tx pattern, the characteristic of the effective array will have risen side lobe

as shown in Figure 1- 38 (b). However, this side lobe can be suppressed in the optimized $SPAF_{NF}$ array of Figure 1- 37 (b) since the null of Tx pattern will be optimized at the grating lobes of the Rx pattern again. As shown in Figure 1- 39, the side lobe level of SPA_{NF} for near field imaging has improved by 9 dB compared to SPA_{FF} for near field imaging. Figure 1- 40 shows the images obtained using SPA_{NF}. Figure 1- 41 have compared the imaging performance of both SPA_{FF} and SPA_{NF}. The SPA_{NF} has demonstrated a certain degree of superiority to the SPA_{FF} [55].

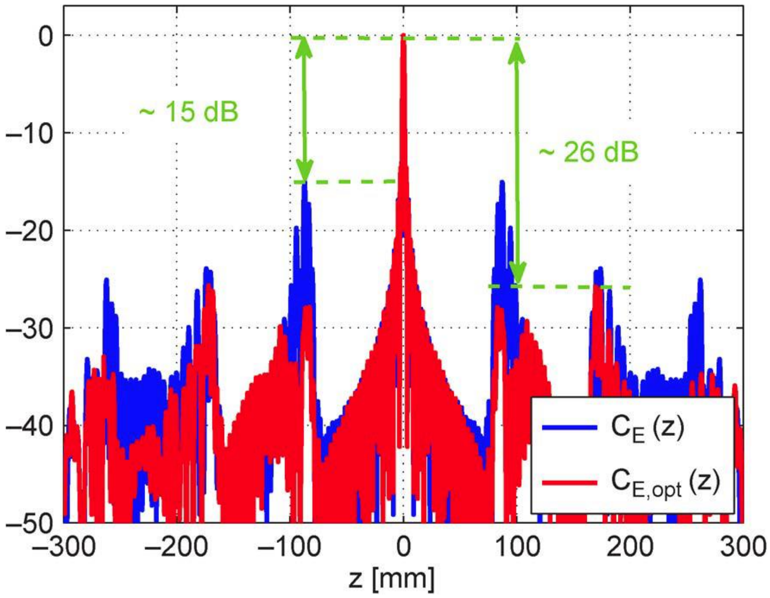

Figure 1- 39. Multi-static characteristics $C_{E(z)}$ of SPA_{FF} and $C_{E, opt(z)}$ of SPA_{NF} in the array near field range (Zt = 600 mm) [55].

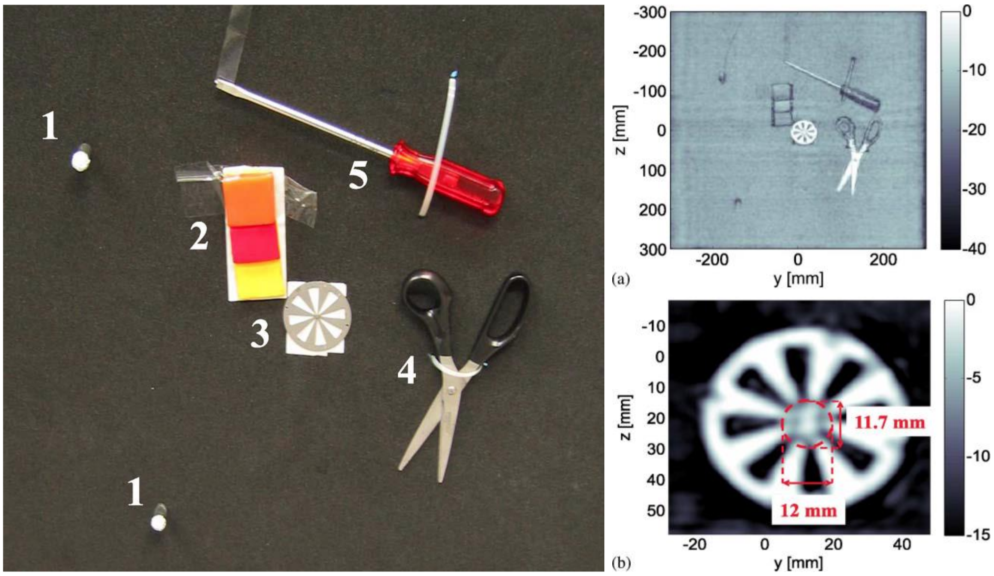

Figure 1- 40. Measured imaging scenario with two (1) point targets (2) a step wedge made of wax (3) a Siemens star test pattern (4) a pair of scissors (5) a screw wrench and images (magnitude in decibels) of broadband reconstruction with array SPA_{NF} (a) complete image (b) zoom of Siemens star test pattern [55]

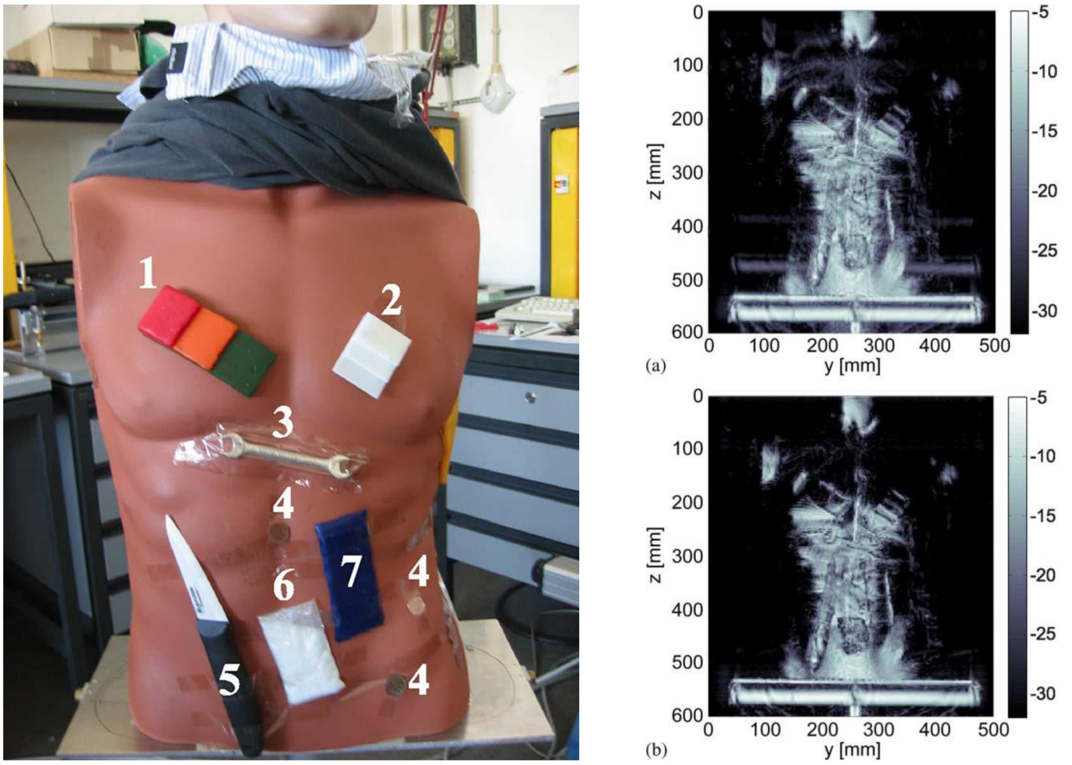

Figure 1- 41. Measured imaging scenario with male mannequin. The front is assembled with (1) a step wedge made of wax, (2) step wedge made of polyethylene, (3) wrench, (4) cent coins, (5) ceramic knife, (6) bag with sodium chloride, (7) wax stripe, and the images (magnitude in decibels) of broadband and coherently averaged reconstruction of male mannequin using (a) Array SPA_{FF} and (b) Array SPA_{NF} [55]

IV. Multi-Static Planar Array Imaging System

In order to further increase the imaging rate, the mechanical scanning along one dimension in the 1-D array scheme can also be replaced by the electronic scanning, so the 2-D array imaging system has been proposed and investigated [56, 57, 68, 69]. However, this scheme is not cost effective so it is not dominant in the industry and academia. Take a planar multi-static sparse array imaging system proposed by researchers in Rohde & Schwarz GmbH & Co. KG as an example [56], it operates in the band of 72 - 80 GHz and has demonstrated a lateral resolution of 2 mm at 0.5 m distance, as shown in the measured imaging results in Figure 1- 42 and Figure 1- 43. However, in order to achieve an array aperture of around 50 cm × 50 cm, 4 × 4 clusters resulting in a total of 736 Tx antennas and 736 Rx antennas are used, as shown in the Figure 1- 44. The imaging system is fully shown in Figure 1- 45. Besides, a stepped-frequency continuous-wave (SFCW) radar operating from 70 GHz to 80 GHz for personnel screening has been proposed, using nonuniform sampling approach to offer high resolution but simultaneously reduce the ambiguities and allow a moderate number of sampling points [57]. Figure 1- 46 shows this imaging system and its block

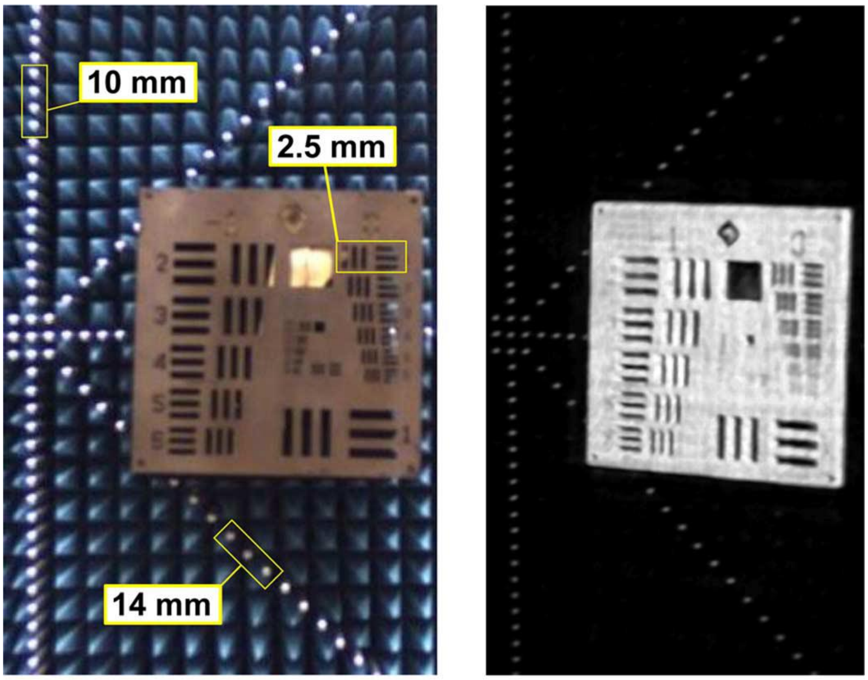

(a) (b)

Figure 1- 42. Measured target of the USAF resolution test pattern placed in front of a bed of nails test object prepared with pyramidal absorbers. (a) Photograph (b) Reconstructed image [56]

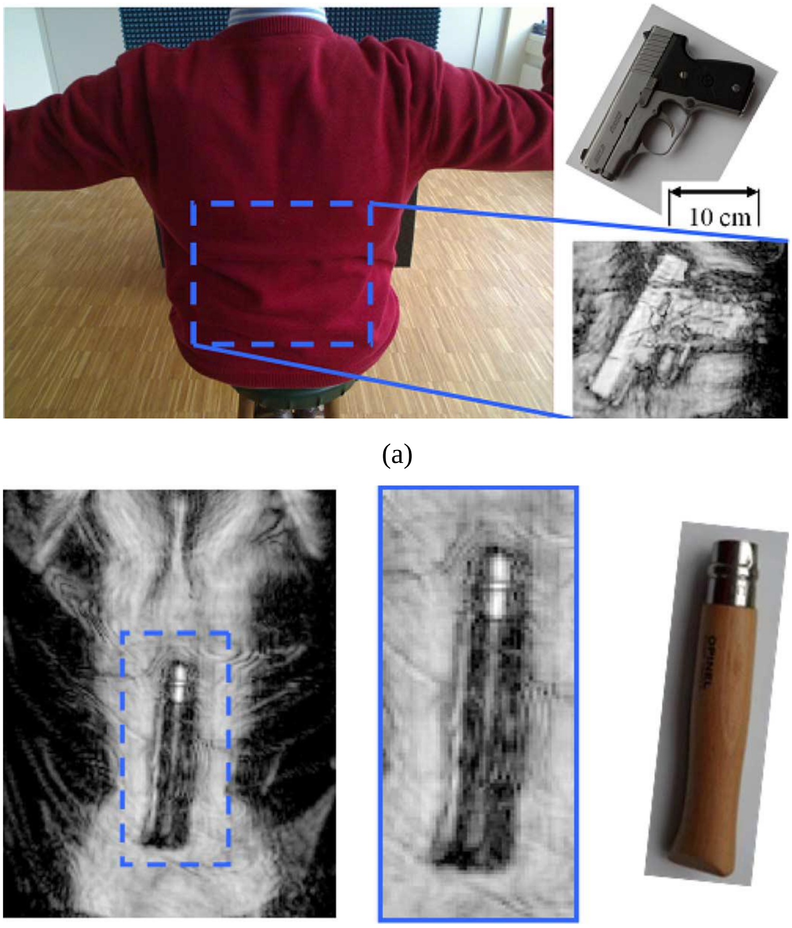

(a)

(b)

Figure 1- 43. Measurements of a person. (a) Carrying a small concealed handgun (b) Carrying a concealed clasp knife [56]

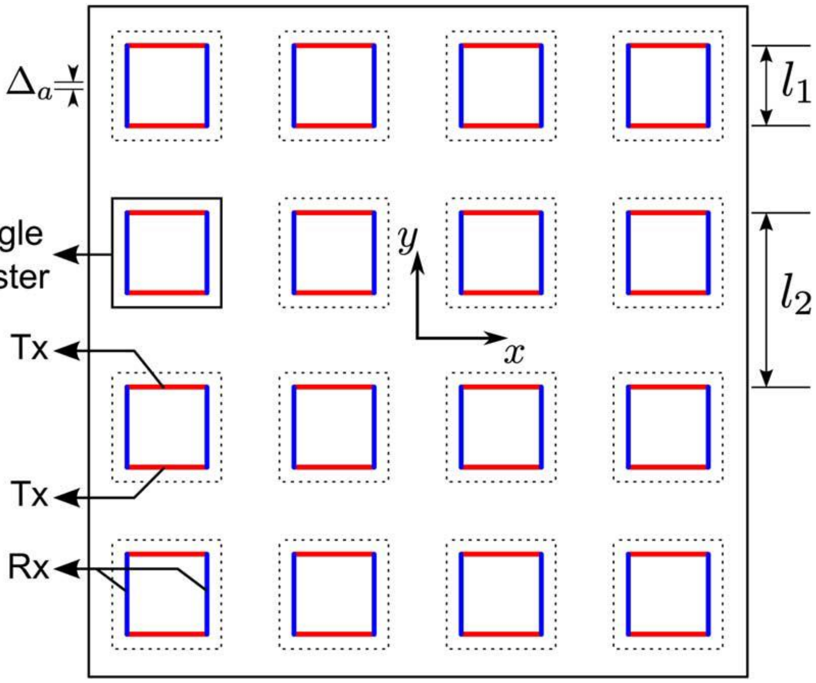

Figure 1- 44. Multi-static planar sparse array geometry with 4 × 4 clusters. Horizontal lines represent Tx arrays and vertical lines represent Rx arrays [56]

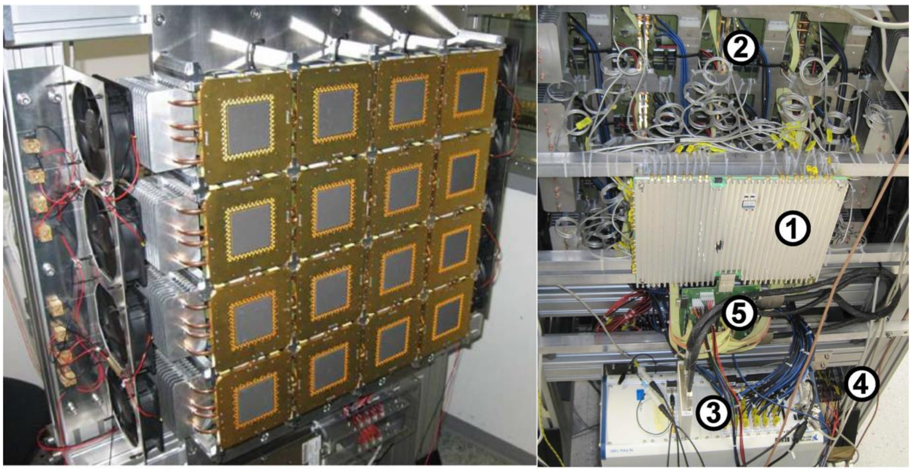

(a) (b)

Figure 1- 45. Photographs of full electronic imaging system with 736 Tx and 736 Rx antennas, showing the front and backside of the system. (a) 16 clusters Array (b) Signal generating and processing hardware [56]

diagram. It has an aperture of 1 m × 2 m to guarantee a 2 mm lateral resolution, consisting of 32 clusters with 94 Tx and 94 Rx antennas in each cluster, so it results in 3008 transmitter and 3008 receiver antenna in total. On the other hand, a densely sampled aperture, with the same size and 3 mm antenna spacing, would require about $334 \times 667 = 223112$ receiver or transmitter antennas to achieve the same resolution and illumination properties. Thus, the sparse array design requires only 3% of the sensors compared with the densely sampled aperture while keeping optimal image quality [57]. Figure 1- 47 and Figure 1- 48 show the maximum intensity projection

(MIP) of the reconstruction of a male person holding a test pattern. The person has been scanned by the 2-D imaging system using an equidistant frequency sweeping and nonuniform frequency sweeping, respectively. Both approaches are capable of generating high quality images. The proposed nonuniform frequency sweeping approach leads to reduction of the range ambiguities that are visible in Figure 1- 47(a), which has been further verified by the zoomed-in details shown in Figure 1- 48 [57].

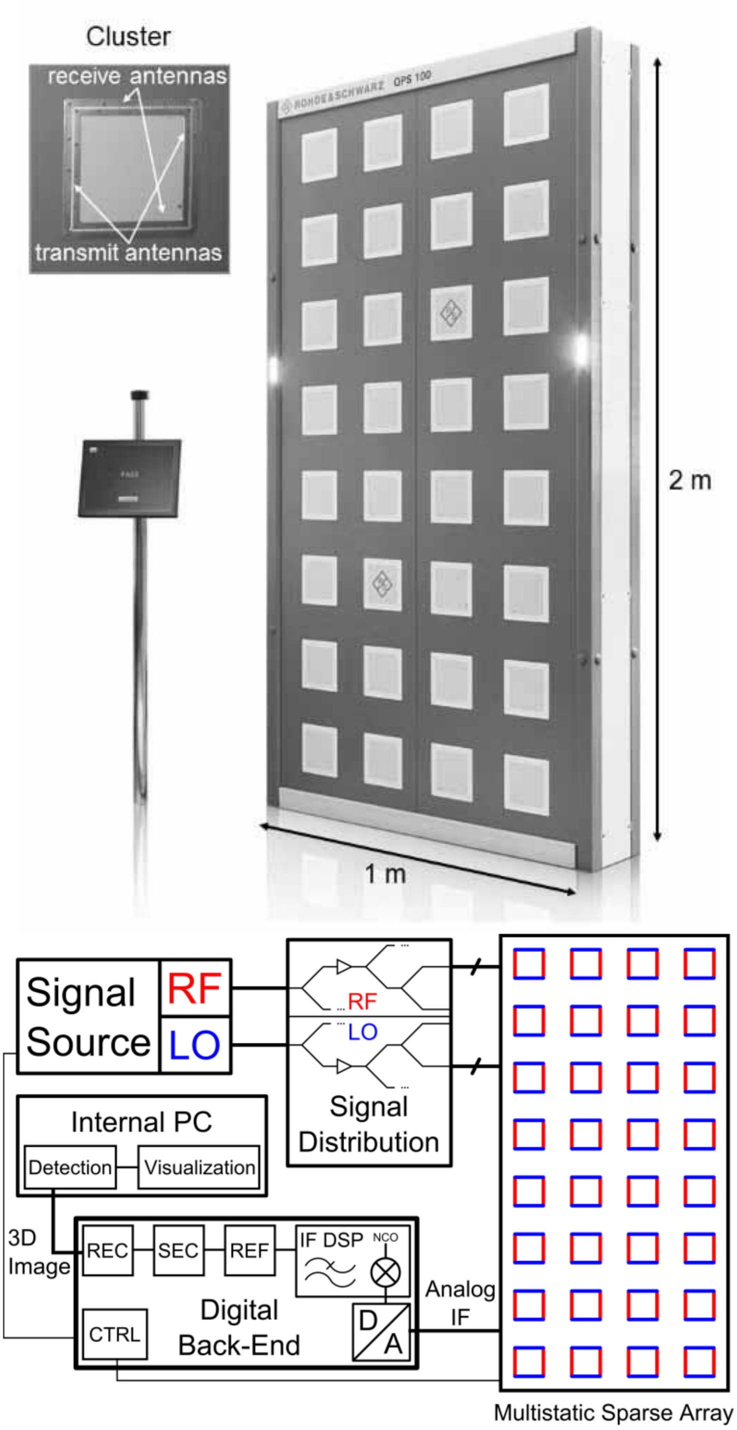

Figure 1- 46. 2-D SFCW imaging system and its block diagram [57]

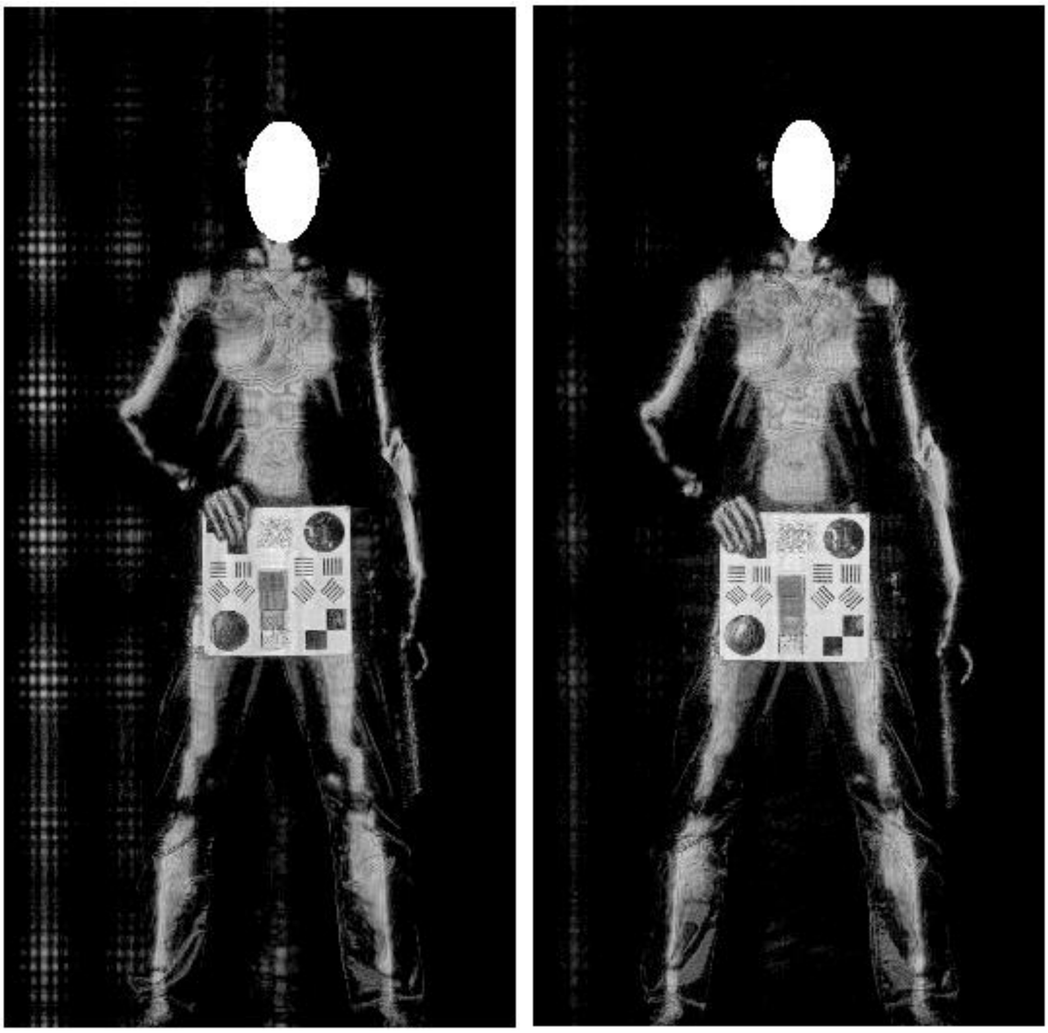

(a) (b)

Figure 1- 47. MIP of (a) Equidistant SFCW sweeping (b) Nonuniform SFCW sweeping [57]

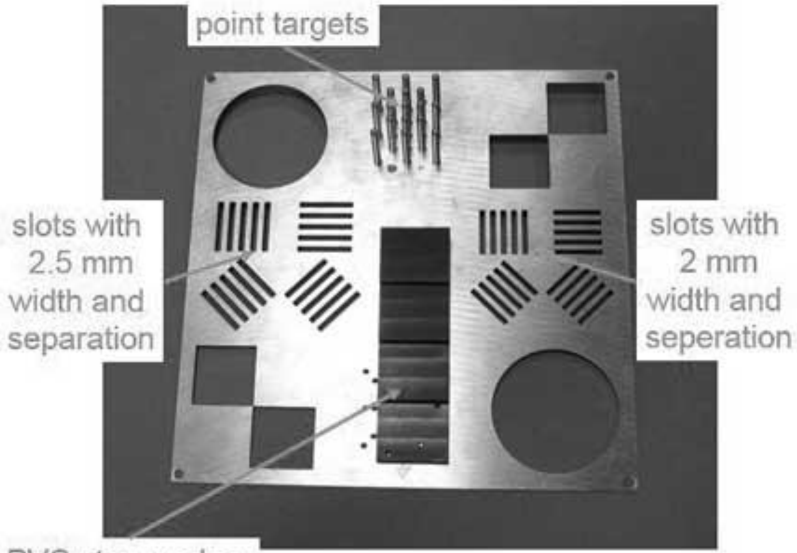

(a)

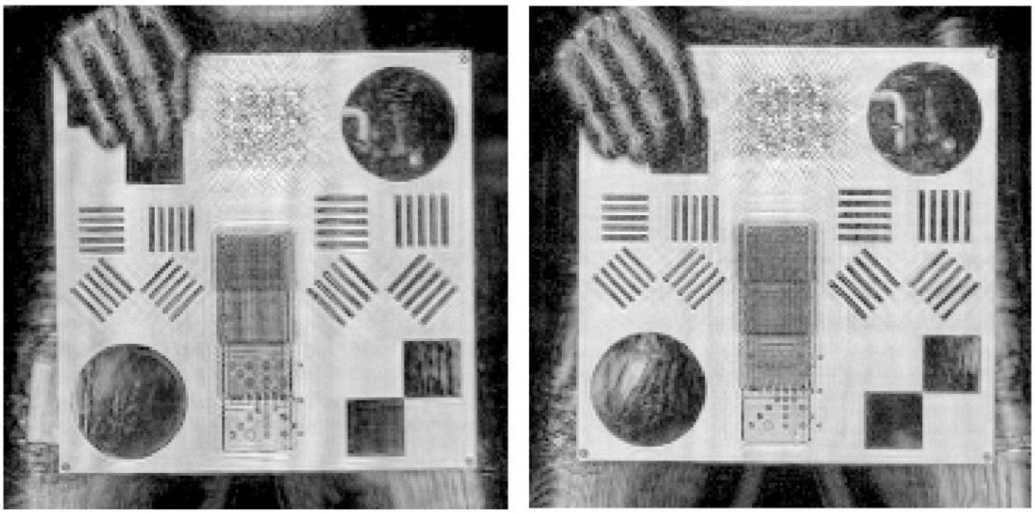

(b) (c)

Figure 1- 48. (a) Test pattern and zoomed-in reconstruction in Figure 1- 47 (b) Equidistant SFCW sweep (c) Nonuniform SFCW sweep [57]

1.3. Challenges and Motivations

As reviewed in previous sections, current imaging products mainly work at microwave or low millimeter wave band due to the maturity of the technology. However, they are suffering relatively poor image resolution due to long wavelength. Therefore, it is desirable to develop an imaging system operating in a high frequency band. But there are challenges in two aspects. The first challenge is how to achieve a fast imaging without compromising image quality. The second one is how to keep the cost low for the practical implementation while maintaining image quality. The researchers have shown that the passive imaging scheme has the advantage of fast frame rate, but it suffers from insufficient sensitivity to detect small radiometric temperature differences. The solutions of using a large number of detectors or high sensitive detectors such as TES and KIDs either increase the system cost or requires a long cooling time that blocks the continuous operation of the imaging system. The active imaging system has an intrinsic merit of better imaging quality and needs many more array elements/channels due to the requirement of Nyquist sampling criterion. Therefore, the key concern is to find a proper scheme and system design that can reduce the system cost while maintaining a good image quality and a fast frame rate. The FPA imaging system usually has drawbacks of low resolution because of fewer detectors used and a bulky size due to the use of lens. The advanced quasi-optic imaging system that relies on mechanical movement of mirrors/reflectors to accomplish a fast scanning is not only bulky and costly, but also needs almost normal incident of the wave on the object, which is difficult to be guaranteed in practice especially at wide scanning angle [30, 70].

In terms of interferometric array imaging system, heterodyne transceiver and synthetic aperture focusing technique can improve the image quality significantly. Accordingly, the quasi-monostatic sequentially switched antenna arrays have been developed successfully by PNNL in many near real-time systems including the commercial products currently deployed at airports worldwide. The primary cost of quasi-monostatic sequentially switched arrays comes from the number of antenna elements, which is under the restriction of sub-wavelength sampling, and this increases the complexity of the switching matrix behind the antenna array too. Therefore, its operation frequency only reaches up to 60 GHz [47-49]. Although multi-static array also known as MIMO array may offer a promising and practical way to solve these problems [53-55, 65, 66], especially the multi-static sparse linear array imaging system as introduced before with multiple TR combinations. However, it is only verified at a frequency range of 20 – 40 GHz in simulation. And the minimum TR elements utilized is 55 with a sampling spacing of 0.33 wavelength at 30 GHz [51]. Therefore, it is necessary to explore the multi-static sparse array imaging in THz band.

This project aims to investigate a THz imaging system for concealed threats detection based on the linear sparse periodic array. It requires a comprehensive study on the THz SPA imaging system, including the scheme set-up, simulation, theoretical analysis, assessment and experimental evaluation. In order to further reduce the cost of this imaging scheme, we have proposed an improved image reconstruction algorithm to increase the array element spacing. Therefore, we need to gain a full knowledge of this kind of THz imaging scheme after the study, deriving a complete design principle and procedures for practical implementation. In addition, in order to save data acquisition time, we have proposed to apply the compressive sensing technique to this imaging scheme, not only proposing the CS-SPA reconstruction model, but also demonstrating its feasibility using both the simulated and measured imaging data.

1.4. Organisation of the Thesis

The rest of the thesis is organized as follows:

Chapter 2 firstly gives a detailed introduction on the linear sparse periodic array (SPA) that is particularly suitable for the imaging application. After that, the potential

THz imaging schemes using this SPA have been proposed. Finally, some basic definitions and specifications used to assess the imaging system have been introduced, including the point spread function, reconstruction algorithm based on generalized synthetic aperture focusing technique.

Chapter 3 mainly shows the comprehensive imaging simulation of using SPA operating at 0.22 THz, including different configurations with different element spacing, ghost images generation and suppression, wideband 3D imaging and imaging on targets with curved surface. Finally, two larger SPA arrays working at 220 GHz and 94 GHz separately for two different scanning schemes have been proposed for more realistic target imaging, including the dielectric, curved surface and full body model.

Chapter 4 firstly introduces the compressive sensing (CS) theory and its advantage using two simple examples, which shows its potential to reduce the sampling points or channels when applied in the proposed SPA-THz imaging system. Afterwards, the corresponding discrete CS-SPA reconstruction model has been proposed and verified using the simulated data.

Chapter 5 mainly presents the experimental results and essential analysis of this proposed SPA-THz imaging system. At the beginning, the experimental set-up of this THz imaging system has been introduced. Afterwards, the measured imaging results have been analyzed in comparison with the simulated ones in the realistic scenario. Finally, the experimental images reconstructed by the Generalized Synthetic Aperture Focusing Technique (GSAFT), improved GSAFT and CS reconstruction approaches have been compared, demonstrating the feasibility of improved GSAFT for ghost images suppression and the capability of CS application in reducing the sampling points or elements/channels in the future practical implementation of proposed SPA-THz imaging system.

Chapter 6 summarizes the research work in this thesis and points out the future work.

1.5. References

[1] R. Appleby and H. B. Wallace, "Standoff Detection of Weapons and Contraband in the 100 GHz to 1 THz Region," *IEEE Transactions on Antennas and Propagation*, vol. 55, no. 11, pp. 2944-2956, 2007.

[2] J. F. Federici *et al.*, "THz imaging and sensing for security applications—explosives, weapons and drugs," *Semiconductor Science and Technology,* vol. 20, no. 7, p. S266, 2005.

[3] Z. Wang, T. Chang, and H. Cui, "Review of Active Millimeter Wave Imaging Techniques for Personnel Security Screening," *IEEE Access,* vol. 7, pp. 148336-148350, 2019.

[4] L. Yujiri, M. Shoucri, and P. Moffa, "Passive millimeter wave imaging," *IEEE Microwave Magazine,* vol. 4, no. 3, pp. 39-50, 2003.

[5] L. Yujiri, "Passive Millimeter Wave Imaging," in *2006 IEEE MTT-S International Microwave Symposium Digest*, 2006, pp. 98-101.

[6] J. Abril, E. Nova, A. Broquetas, F. Torres, J. Romeu, and L. Jofre, "Combined Passive and Active Millimeter-Wave Imaging System for Concealed Objects Detection," (in English), *35th International Conference on Infrared, Millimeter, and Terahertz Waves (Irmmw-Thz 2010),* 2010.

[7] M. Kowalski, M. Kastek, M. Walczakowski, N. Palka, and M. Szustakowski, "Passive imaging of concealed objects in terahertz and long-wavelength infrared," *Applied Optics,* vol. 54, no. 13, pp. 3826-3833, 2015.

[8] M. Kowalski and M. Kastek, "Comparative Studies of Passive Imaging in Terahertz and Mid-Wavelength Infrared Ranges for Object Detection," *IEEE Transactions on Information Forensics and Security,* vol. 11, no. 9, pp. 2028-2035, 2016.

[9] S. Rowe *et al.*, "A passive terahertz video camera based on lumped element kinetic inductance detectors," *Review of Scientific Instruments,* vol. 87, no. 3, p. 033105, 2016.

[10] J. Qiu, H. Liu, N. Wang, and S. Lan, "Research on Multi-Beam Focusing Antenna for Passive Millimeter Wave Imaging System," in *2018 IEEE Asia-Pacific Conference on Antennas and Propagation (APCAP)*, pp. 171-174, 2018.

[11] E. Heinz *et al.*, "Passive 350 GHz Video Imaging Systems for Security Applications," *Journal of Infrared, Millimeter, and Terahertz Waves,* vol. 36, no. 10, pp. 879-895, 2015.

[12] E. Heinz *et al.*, *Toward high-sensitivity and high-resolution submillimeter-wave video imaging*. SPIE, 2011.

[13] M. Kowalski, "Real-time concealed object detection and recognition in passive imaging at 250 GHz," *Applied optics,* vol. 58, no. 12, pp. 3134-3140, 2019.

[14] Y. Meng, A. Qing, C. Lin, J. Zang, Y. Zhao, and C. Zhang, "Passive Millimeter Wave Imaging System Based on Helical Scanning," *Scientific Reports,* vol. 8, no. 1, p. 7852, 2018.

[15] W. AlSaafin, S. Villena, M. Vega, R. Molina, and A. K. Katsaggelos, "Compressive sensing super resolution from multiple observations with application to passive millimeter wave images," *Digital Signal Processing,* vol. 50, pp. 180-190, 2016.

[16] R. Li, C. Li, H. Li, S. Wu, and G. Fang, "Study of Automatic Detection of Concealed Targets in Passive Terahertz Images for Intelligent Security Screening," *IEEE Transactions on Terahertz Science and Technology,* vol. 9, no. 2, pp. 165-176, 2019.

[17] S. López-Tapia, R. Molina, and N. P. d. l. Blanca, "Deep CNNs for Object Detection Using Passive Millimeter Sensors," *IEEE Transactions on Circuits and Systems for Video Technology,* vol. 29, no. 9, pp. 2580-2589, 2019.

[18] S. López-Tapia, R. Molina, and N. Pérez de la Blanca, "Using machine learning to detect and localize concealed objects in passive millimeter-wave images," *Engineering Applications of Artificial Intelligence,* vol. 67, pp. 81-90, 2018.

[19] H. Feng *et al.*, "A passive video-rate terahertz human body imager with real-time calibration for security applications," *Applied Physics B,* vol. 126, no. 8, p. 143, 2020.

[20] P. M. Blanchard, A. H. Greenaway, A. R. Harvey, and K. Webster, "Coherent optical beam forming with passive millimeter-wave arrays," *Journal of Lightwave Technology,* vol. 17, no. 3, pp. 418-425, 1999.

[21] V. Mackowiak, J. Peupelmann, Y. Ma, and A. Gorges, "NEP–noise equivalent power," in *Thorlabs, Inc.*, 2015.

[22] S. Yeom *et al.*, "Real-time outdoor concealed-object detection with passive millimeter wave imaging," *Optics Express,* vol. 19, no. 3, pp. 2530-2536, Jan 31 2011.

[23] Z. Y. Sun, C. Li, S. M. Gu, and G. Y. Fang, "Fast Three-Dimensional Image Reconstruction of Targets Under the Illumination of Terahertz Gaussian Beams With Enhanced Phase-Shift Migration to Improve Computation Efficiency," (in English), *Ieee Transactions on Terahertz Science and Technology,* vol. 4, no. 4, pp. 479-489, Jul 2014.

[24] S. Gu, C. Li, X. Gao, Z. Sun, and G. Fang, "Three-Dimensional Image Reconstruction of Targets Under the Illumination of Terahertz Gaussian Beam-Theory and Experiment," *IEEE Transactions on Geoscience and Remote Sensing,* vol. 51, no. 4, pp. 2241-2249, 2013.

[25] P. F. Goldsmith, C. T. Hsieh, G. R. Huguenin, J. Kapitzky, and E. L. Moore, "Focal plane imaging systems for millimeter wavelengths," *IEEE Transactions on Microwave Theory and Techniques,* vol. 41, no. 10, pp. 1664-1675, 1993.

[26] S. Yeom *et al.*, "Real-time outdoor concealed-object detection with passive millimeter wave imaging," *Opt Express,* vol. 19, no. 3, pp. 2530-6, Jan 31 2011.

[27] R. Appleby *et al.*, "Mechanically scanned real time passive millimetre wave imaging at 94GHz," (in English), *Passive Millimeter-Wave Imaging Technology Vi and Radar Sensor Technology Vii*, vol. 5077, pp. 1-6, 2003.

[28] J. Richter, D. Notel, F. Kloppel, J. Huck, H. Essen, and L. p. Schmidt, "A Multi-Channel Radiometer with Focal Plane Array Antenna for W-Band Passive Millimeterwave Imaging," in *2006 IEEE MTT-S International Microwave Symposium Digest*, pp. 1592-1595, 2006.

[29] G. C. Trichopoulos, H. L. Mosbacker, D. Burdette, and K. Sertel, "A Broadband Focal Plane Array Camera for Real-time THz Imaging Applications," *IEEE Transactions on Antennas and Propagation*, vol. 61, no. 4, pp. 1733-1740, 2013.

[30] S. M. Gu, C. Li, X. Gao, Z. Y. Sun, and G. Y. Fang, "Terahertz Aperture Synthesized Imaging With Fan-Beam Scanning for Personnel Screening," *IEEE Transactions on Microwave Theory and Techniques*, vol. 60, no. 12, pp. 3877-3885, Dec 2012.

[31] D. M. Sheen, T. E. Hall, R. H. Severtsen, D. L. McMakin, B. K. Hatchell, and P. L. J. Valdez, "*Active wideband 350GHz imaging system for concealed-weapon detection"* SPIE Defense, Security, and Sensing, pp. 73090I-73090I-10, 2009.

[32] D. M. Sheen, D. L. McMakin, T. E. Hall, and R. H. Severtsen, "Active millimeter-wave standoff and portal imaging techniques for personnel screening," in *2009 IEEE Conference on Technologies for Homeland Security*, pp. 440-447, 2009.

[33] K. B. Cooper *et al.*, "Penetrating 3-D Imaging at 4- and 25-m Range Using a Submillimeter-Wave Radar," *IEEE Transactions on Microwave Theory and Techniques*, vol. 56, no. 12, pp. 2771-2778, 2008.

[34] K. B. Cooper *et al.*, "An Approach for Sub-Second Imaging of Concealed Objects Using Terahertz (THz) Radar," *Journal of Infrared, Millimeter, and Terahertz Waves*, journal article vol. 30, no. 12, pp. 1297-1307, 2009.

[35] N. Llombart, R. J. Dengler, and K. B. Cooper, "Terahertz Antenna System for a Near-Video-Rate Radar Imager [Antenna Applications]," *IEEE Antennas and Propagation Magazine*, vol. 52, no. 5, pp. 251-259, 2010.

[36] N. Llombart, K. B. Cooper, R. J. Dengler, T. Bryllert, and P. H. Siegel, "Confocal Ellipsoidal Reflector System for a Mechanically Scanned Active Terahertz Imager," *IEEE Transactions on Antennas and Propagation*, vol. 58, no. 6, pp. 1834-1841, 2010.

[37] K. B. Cooper, R. J. Dengler, N. Llombart, B. Thomas, G. Chattopadhyay, and P. H. Siegel, "THz Imaging Radar for Standoff Personnel Screening," *IEEE Transactions on Terahertz Science and Technology*, vol. 1, no. 1, pp. 169-182, 2011.

[38] K. B. Cooper *et al.*, "Fast high-resolution terahertz radar imaging at 25 meters," Terahertz Physics, Devices, and Systems IV: Advanced Applications in Industry and Defense, vol. 7671, pp. 76710Y-76710Y-8, 2010.

[39] J. Gao *et al.*, "Fast Three-Dimensional Image Reconstruction of a Standoff Screening System in the Terahertz Regime," *IEEE Transactions on Terahertz Science and Technology,* vol. PP, no. 99, pp. 1-14, 2017.

[40] X. Gao, C. Li, S. Gu, and G. Fang, "Study of a New Millimeter-Wave Imaging Scheme Suitable for Fast Personal Screening," *IEEE Antennas and Wireless Propagation Letters,* vol. 11, pp. 787-790, 2012.

[41] A. Garcia-Pino, N. Llombart, B. Gonzalez-Valdes, and O. Rubinos-Lopez, "A Bifocal Ellipsoidal Gregorian Reflector System for THz Imaging Applications," *IEEE Transactions on Antennas and Propagation,* vol. 60, no. 9, pp. 4119-4129, 2012.

[42] A. Garcia-Pino *et al.*, "Bifocal Reflector Antenna for a Standoff Radar Imaging System With Enhanced Field of View," *IEEE Transactions on Antennas and Propagation,* vol. 62, no. 10, pp. 4997-5006, 2014.

[43] C. am Weg, W. von Spiegel, R. Henneberger, R. Zimmermann, T. Loeffler, and H. G. Roskos, "Fast Active THz Cameras with Ranging Capabilities," *Journal of Infrared, Millimeter, and Terahertz Waves,* journal article vol. 30, no. 12, pp. 1281-1296, December 01 2009.

[44] J. F. Federici *et al.*, "Terahertz imaging using an interferometric array," *Applied Physics Letters,* vol. 83, no. 12, pp. 2477-2479, 2003 2003.

[45] K. P. Walsh, B. Schulkin, D. Gary, J. F. Federici, R. Barat, and D. Zimdars, "Terahertz near-field interferometric and synthetic aperture imaging," in *Defense and Security,* pp. 9-17, 2004.

[46] Z. Liu, K. Su, D. E. Gary, J. F. Federici, R. B. Barat, and Z. H. Michalopoulou, "Video-rate terahertz interferometric and synthetic aperture imaging," *Appl Opt,* vol. 48, no. 19, pp. 3788-95, Jul 01 2009.

[47] D. M. Sheen, D. L. McMakin, and T. E. Hall, "Three-dimensional millimeter-wave imaging for concealed weapon detection," *IEEE Transactions on Microwave Theory and Techniques,* vol. 49, no. 9, pp. 1581-1592, Sep 2001.

[48] D. M. Sheen, D. L. McMakin, and T. E. Hall, "Cylindrical millimeter-wave imaging technique and applications," in *Defense and Security Symposium,* pp. 62110A-62110A-10, 2006.

[49] D. Sheen, D. McMakin, and T. Hall, "Near-field three-dimensional radar imaging techniques and applications," *Applied Optics,* vol. 49, no. 19, pp. E83-E93, 2010.

[50] K. Su, Z. Liu, R. B. Barat, D. E. Gary, Z.-H. Michalopoulou, and J. F. Federici, "Two-dimensional interferometric and synthetic aperture imaging with a hybrid

terahertz/millimeter wave system," *Applied optics,* vol. 49, no. 19, pp. E13-E19, 2010.

[51] D. M. Sheen and T. E. Hall, "Reconstruction techniques for sparse multistatic linear array microwave imaging," in *Proc. SPIE 9078, Passive and Active Millimeter-Wave Imaging XVII,* vol. 9078, pp. 90780I-90780I-12, 2014.

[52] D. M. Sheen, "Sparse multi-static arrays for near-field millimeter-wave imaging," in *2013 IEEE Global Conference on Signal and Information Processing*, pp. 699-702, 2013.

[53] X. Zhuge and A. G. Yarovoy, "A Sparse Aperture MIMO-SAR-Based UWB Imaging System for Concealed Weapon Detection," *IEEE Transactions on Geoscience and Remote Sensing,* vol. 49, no. 1, pp. 509-518, 2011.

[54] F. Gumbmann, P. Tran, J. Weinzierl, and L. P. Schmidt, "Multistatic Short Range Ka-Band Imaging System," in *2009 German Microwave Conference*, pp. 1-4, 2009.

[55] F. Gumbmann and L. P. Schmidt, "Millimeter-Wave Imaging With Optimized Sparse Periodic Array for Short-Range Applications," *IEEE Transactions on Geoscience and Remote Sensing,* vol. 49, no. 10, pp. 3629-3638, 2011.

[56] S. S. Ahmed, A. Schiessl, and L. P. Schmidt, "A Novel Fully Electronic Active Real-Time Imager Based on a Planar Multistatic Sparse Array," *IEEE Transactions on Microwave Theory and Techniques*, vol. 59, no. 12, pp. 3567-3576, 2011.

[57] F. Gumbmann and A. Schiessl, "Short-Range Imaging System With a Nonuniform SFCW Approach," *IEEE Transactions on Microwave Theory and Techniques*, vol. 65, no. 4, pp. 1345-1354, 2017.

[58] Y. Zhang and X. Li, "The study of characteristics of the beam scanning for millimeter-wave focal plane array imaging systems," in *Microwave and Millimeter Wave Technology Proceedings, 1998. ICMMT '98. 1998 International Conference on*, pp. 626-629, 1998.

[59] N. A. Salmon, S. Hayward, R. Walke, and R. Appleby, "Electronic scanning for passive millimetre wave imaging," (in English), *Passive Millimeter-Wave Imaging Technology Vi and Radar Sensor Technology Vii*, vol. 5077, pp. 71-76, 2003.

[60] D. M. Le Vine, "The sensitivity of synthetic aperture radiometers for remote sensing applications from space," *Radio Science,* vol. 25, no. 4, pp. 441-453, 1990.

[61] A. R. Harvey, R. Appleby, P. M. Blanchard, and A. H. Greenaway, "Beam - steering technologies for real time passive millimetre wave imaging," (in English), *Passive Millimeter-Wave Imaging Technology Ii,* vol. 3378, pp. 63-72, 1998.

[62] D. M. Sheen and T. E. Hall, "Reconstruction techniques for sparse multistatic linear array microwave imaging," Passive and Active Millimeter-Wave Imaging XVII, vol. 9078, pp. 90780I-90780I-12, 2014.

[63] A. Cenanovic, F. Gumbmann, and L. P. Schmidt, "Automated threat detection and characterization with a polarimetric multistatic imaging system," in *9th European Conference on Synthetic Aperture Radar*, pp. 195-198, 2012.

[64] G. R. Lockwood, L. Pai-Chi, M. O. Donnell, and F. S. Foster, "Optimizing the radiation pattern of sparse periodic linear arrays," *IEEE Transactions on Ultrasonics, Ferroelectrics, and Frequency Control*, vol. 43, no. 1, pp. 7-14, 1996.

[65] F. Gumbmann, P. Tran, and L. P. Schmidt, "Sparse linear array design for a short range imaging radar," in *2009 European Radar Conference (EuRAD)*, pp. 176-179, 2009.

[66] F. Gumbmann and L. P. Schmidt, "Design of sparse MIMO arrays for short range imaging applications," in *2010 Asia-Pacific Microwave Conference*, pp. 1653-1656, 2010.

[67] F. Gumbmann and L. P. Schmidt, "Short Range Imaging with Optimized Sparse Array," in *8th European Conference on Synthetic Aperture Radar*, pp. 1-4, 2010.

[68] X. Zhuge and A. Yarovoy, "Near-field ultra-wideband imaging with two-dimensional sparse MIMO array," in *Proceedings of the Fourth European Conference on Antennas and Propagation*, pp. 1-4, 2010.

[69] X. Zhuge and A. G. Yarovoy, "Study on Two-Dimensional Sparse MIMO UWB Arrays for High Resolution Near-Field Imaging," *IEEE Transactions on Antennas and Propagation*, vol. 60, no. 9, pp. 4173-4182, 2012.

[70] B. Gonzalez-Valdes, Y. Alvarez, S. Mantzavinos, C. M. Rappaport, F. Las-Heras, and J. A. Martinez-Lorenzo, "Improving Security Screening: A Comparison of Multistatic Radar Configurations for Human Body Imaging," *IEEE Antennas and Propagation Magazine*, vol. 58, no. 4, pp. 35-47, 2016.

Chapter 2 THz Imaging Theory and the Proposed THz Imaging System Using SPA

2.1. Introduction to Linear Sparse Periodic Array (SPA)

The interferometric array imaging system uses amplitude and phase information to construct an image through a mathematical focusing algorithm, integrated with synthetic aperture technique that allows using fewer antennas to gain a large effective collecting area hence further increasing the imaging resolution. However, the quasi-monostatic sequentially switched antenna arrays developed by PNNL in commercial systems in use at airports have high cost and complexity, this limits its operation frequency up to 60 GHz by 2014 [1-3]. For example, the currently deployed L-3 Safeview system in use at airports operates in the band of 24.25 – 30 GHz; it consists of 384 antennas in each of transmitting and receiving arrays [4]. To the best of my knowledge, there are commercial products working around 100 GHz but they are not prevalent, yet. The THz security screening system still stays in the lab, facing challenges in practice.

The primary cost and complexity of quasi-monostatic sequentially switched arrays come from a large number of array elements used. The sparse array also known as MIMO array that is categorized as multi-static scenario offers a promising and practical way to ease these problems [5-9]. However, the design of randomly distributed elements in a sparse array is a difficult task. Without a simple mathematical solution to this problem, it is very challenging to design an optimal sparse array. In addition to the two-column multi-static sparse array that uses repeatable Tx and Rx units with different spacing, another multi-static sparse array named linear sparse periodic array (SPA) uses “effective aperture” concept as a design guideline [10], in which two-way radiation pattern of this effective aperture has the low side lobe level that is ideal for imaging. SPA makes full use of TR combinations so it can further reduce the number of elements. The effective aperture of an array is simply the receiver aperture that would produce an identical two-way radiation pattern if the transmitter aperture were a point source (It is noted that the definition is different from the effective sampling aperture, which is the length from the phase centre of first sampling points to the last one). In the far field range or the focal region of a phased array, the continuous wave 1-D (dimensional) radiation pattern $P_{\mathrm{T,1\text{-}D}}(s)$ is given by the Fourier transform of the transmitter aperture function $a_{\mathrm{T,1\text{-}D}}(x/\lambda)$ as equation (2- 1) [10].

$$P_{\mathrm{T,1\text{-}D}}(s) = \int_{-\infty}^{+\infty} a_{\mathrm{T,1\text{-}D}}(\frac{x}{\lambda}) e^{i2\pi(x/\lambda)s} d(\frac{x}{\lambda}) \tag{2- 1}$$

where the transmitter aperture function describes the transmitter element weighting as a function of the element position, $s = \cos(\varphi)$, φ is the azimuth angle measured from the array (axis), and x/λ is the element location in wavelengths (see Figure 2- 1). Similarly, the radiation pattern $P_{\mathrm{R,1\text{-}D}}(s)$ is given by the Fourier transform of the receiver aperture function $a_{\mathrm{R,1\text{-}D}}(x/\lambda)$ [10].

It is worth noting that this equation (2- 1) is same to the array factor (AF) for an M-element linear array, as shown in equation (2- 2).

$$AF_{(1-\mathrm{D})} = \sum_{m=1}^{M} e^{j(kx_m \cos\varphi)} \tag{2- 2}$$

where x_m is the position of m-th element.

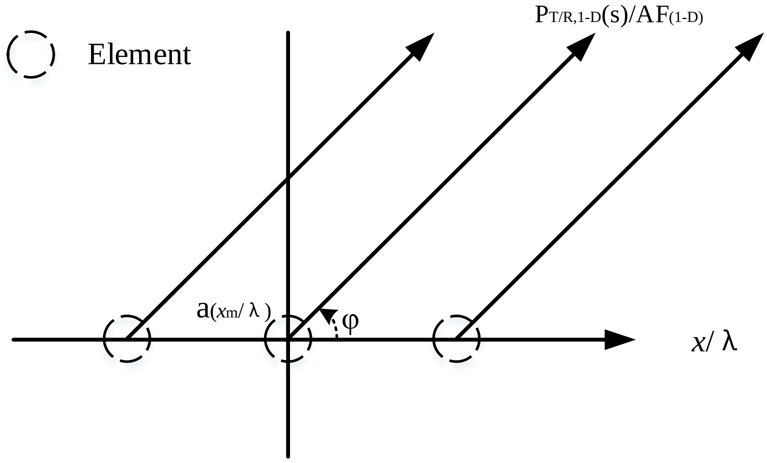

Figure 2- 1. Coordinate system for relating the aperture function $a(x/\lambda)$ to the 1-D radiation pattern $P_{\mathrm{T/R,1\text{-}D}}(s)$ [10]

The two-way or pulse-echo 1-D radiation pattern $P_{\mathrm{TR,1\text{-}D}}(s)$ can be derived from equations (2- 3) by the product of the transmitter 1-D radiation pattern $P_{\mathrm{T,1\text{-}D}}(s)$ and the receiver 1-D radiation pattern $P_{\mathrm{R,1\text{-}D}}(s)$ [10].

$$P_{\mathrm{TR,1\text{-}D}}(s) = P_{\mathrm{T,1\text{-}D}}(s) \cdot P_{\mathrm{R,1\text{-}D}}(s) \tag{2- 3}$$

This is equivalent to the Fourier transform of convolution of the transmitter aperture function $a_{\mathrm{T,1\text{-}D}}(x/\lambda)$ and the receiver aperture function $a_{\mathrm{R,1\text{-}D}}(x/\lambda)$, as shown in equation (2- 4) [10].

$$P_{\mathrm{TR,1\text{-}D}}(s) = F\{a_{\mathrm{T,1\text{-}D}}(x/\lambda) * a_{\mathrm{R,1\text{-}D}}(x/\lambda)\} \qquad (2\text{- }4)$$

From the definition of an effective aperture, it follows that the 1-D effective aperture $E_{\mathrm{TR,1\text{-}D}}(x/\lambda)$ of the system can be derived by the convolution of the 1-D transmitter aperture function and 1-D receiver aperture function as equation (2- 5) [10].

$$E_{\mathrm{TR,1\text{-}D}}(x/\lambda) = a_{\mathrm{T,1\text{-}D}}(x/\lambda) * a_{\mathrm{R,1\text{-}D}}(x/\lambda) \qquad (2\text{- }5)$$

Since the two-way radiation pattern of the TR array is given by the Fourier transform of the effective aperture, we can design the TR array by selecting the transmitter and receiver aperture functions such that a desired effective aperture is obtained. A desired effective aperture usually has approximately λ/2 element spacing (which ideally assures Nyquist sampling criterion satisfied so that phase shift between 2 sampling points is less than π), a smooth aperture shape, so the grating lobes in the two-way radiation pattern that affect the imaging performance can be suppressed [10]. Therefore, the design principle of linear sparse periodic array (SPA) can be concluded as follow. The array consists of **Nt** transmitter elements with a spacing of **dt**, half placed at two ends of the **Nr**-elements receiver array with a spacing of **dr** that equals to 0.5 · Nt · dt (Positions of transmitter and receiver elements are exchangeable). As a result, the corresponding effective array will have Nt · Nr elements with an identical spacing of dt except for the central one with an element spacing of 2·dt [10]. The aperture length of this effective array is Nt · Nr · dt that is equal to Lt+Lr.

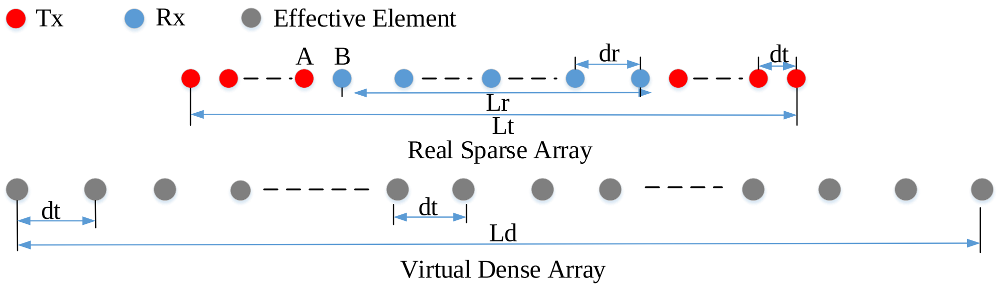

Figure 2- 2. Illustration of element distributions of TR linear sparse array and corresponding effective array [10]

As one example of 8 transmitter antennas located at the two ends of 8 receiver antennas with the spacing of half wavelength whose aperture functions are shown in Figure 2- 3, it is seen that the side lobes of one-way radiation pattern of Rx exactly locates the null of the Tx beam. Thus, the effective aperture with 64 elements with half wavelength spacing can be gained as shown in Figure 2- 4, whose side lobes can be minimized well for imaging and this is verified by the two-way radiation pattern shown in Figure 2- 4. However, there is a far-field imaging assumption in radiation pattern. When target is closer to the aperture than the far-field distance, radiation patters directly gained by the Fourier transform of aperture functions would have a few distortions. They cannot predict the imaging performance accurately, thus point spread functions (PSFs) should be utilized to slightly modify above TR distribution to further improve the imaging performance [7, 11].

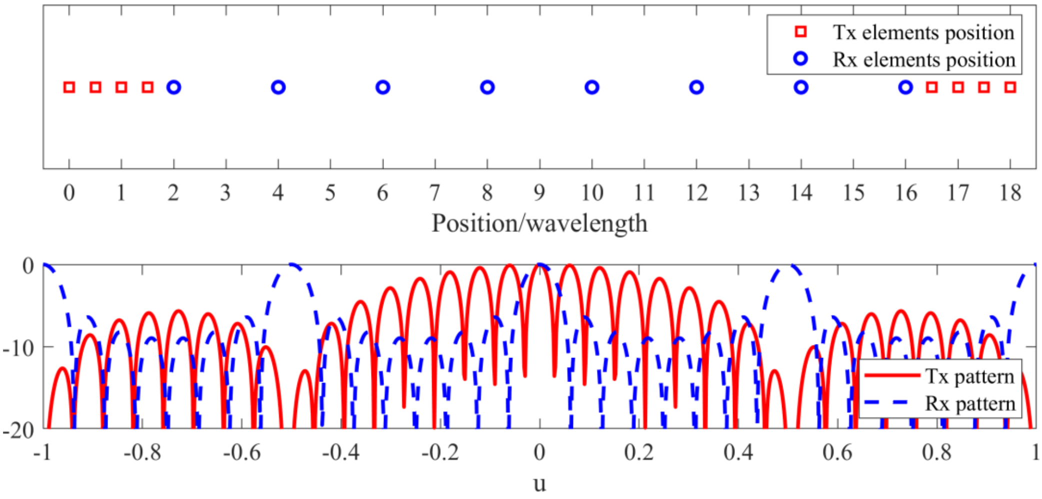

Figure 2- 3. Aperture functions of receiver and transmitter arrays and their one-way radiation patterns (in dB)

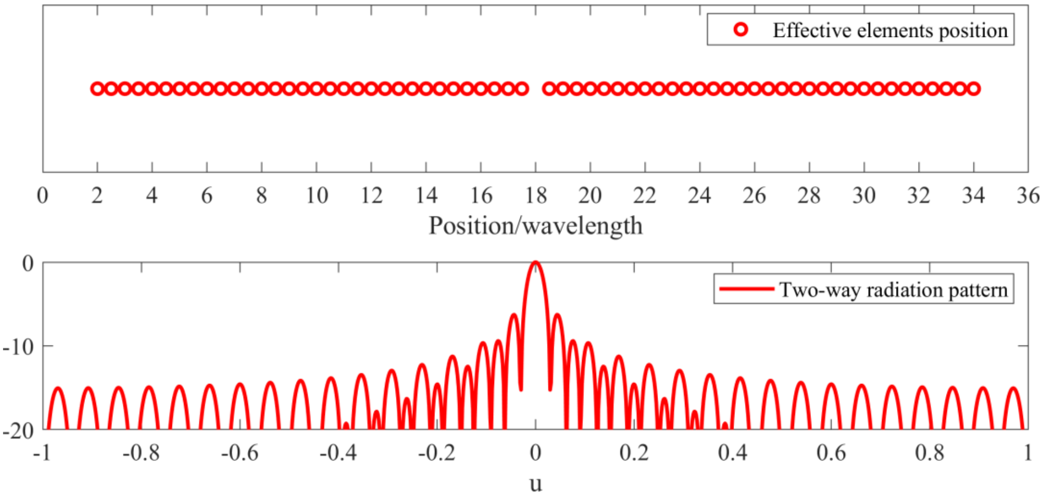

Figure 2- 4. Effective aperture function of the sparse array and its two-way radiation pattern (in dB)

2.2. Proposed THz Imaging System with SPA

This kind of imaging system utilizing electronic scanning and mechanical scanning methods probably have two kinds of set-ups that are shown in Figure 2- 5 and Figure 2- 6. The difference in two set-ups lies in mechanical scanning approach along one direction. A linear sparse periodic array with switches is used to electronically scan along one (like horizontal) direction. In the application, Tx antennas are turned on and off sequentially. While one Tx antennas is on, all Rx antennas record the received data for each combination of Tx-Rx elements. When all combinations are recorded, the output beam moves to illuminate the next spot along the other direction by either mechanical rotation of the optic reflector like shown in Figure 2- 5 or array movement as shown in Figure 2- 6 and then the above procedure is repeated until the full 2D aperture data are gained to reconstruct the image. The proposed THz SPA imaging system uses synthetic aperture technique to achieve a high-quality image. Theoretically, a higher-quality image due to multi-pass interferometric synthetic aperture imaging can be carried out by a single radar/system scanning in different passes [12]. Besides the mechanical scanning, the SPA in the proposed imaging system can also move positions along the electronic scanning direction to gain several phase-correlated datasets that correspond to each single-pass synthetic aperture image. Therefore, an improved multi-pass interferometric synthetic aperture image can be synthesized when necessary. Furthermore, images at different frequencies can be utilized to reduce the ambiguity and form 3D image.

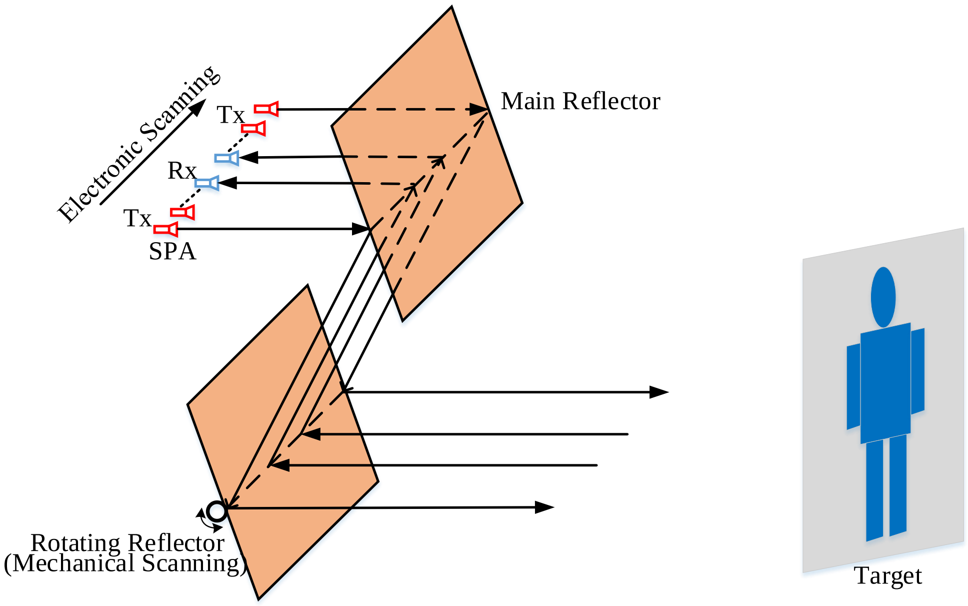

Figure 2- 5. Schematic illustration of the THz-SPA imaging system with rotating reflector

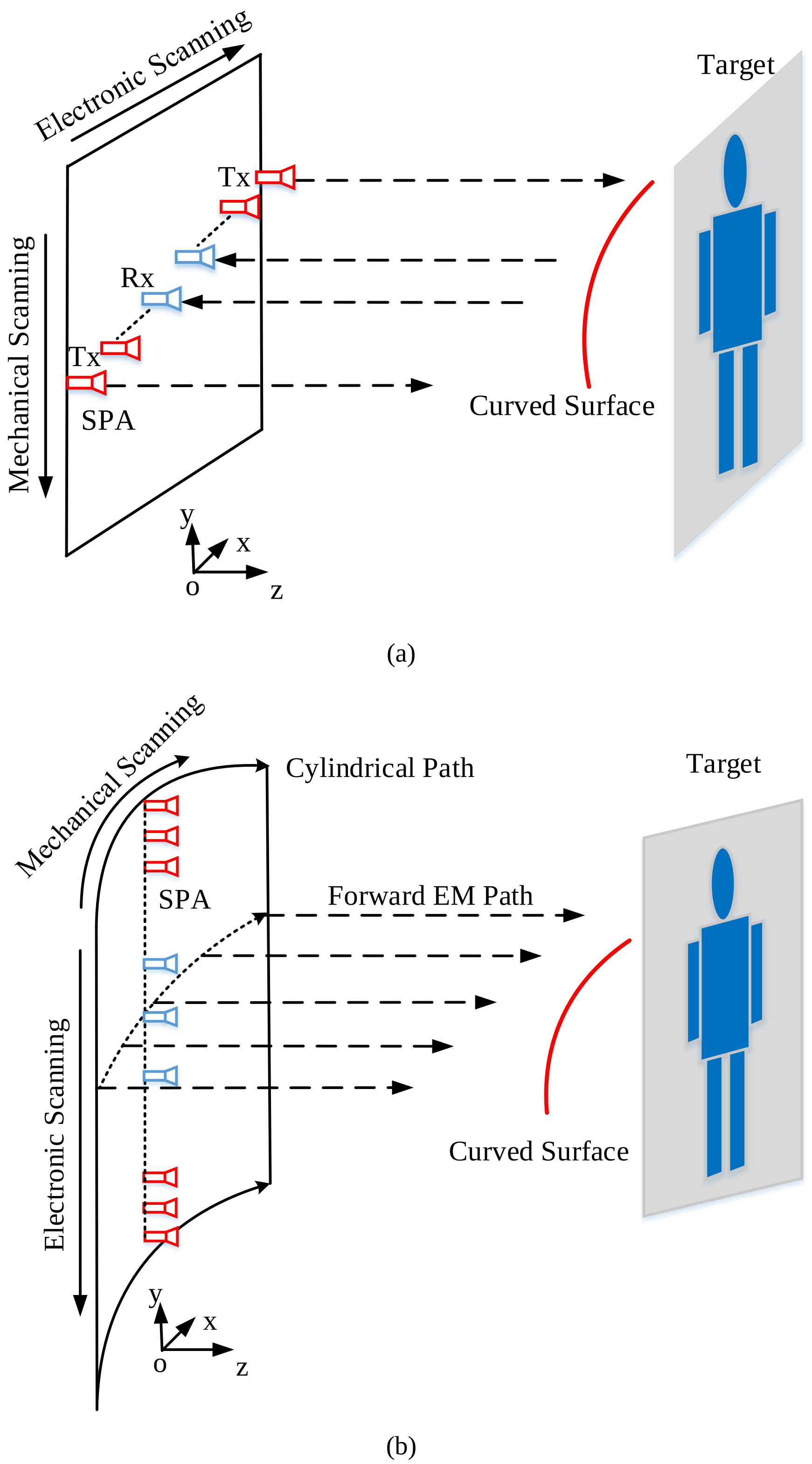

Figure 2- 6. Schematic illustration of THz imaging system with SPA (a) vertical and (b) horizontal scanning

2.3. Theoretical Analysis on the Proposed THz Imaging System

2.3.1. Point Spread Function

In addition, the one-way radiation pattern of equation (2- 2) can be generalized into a form for 2-D (planar) array as shown in equation (2- 6), which has randomly distributed elements as shown in Figure 2- 7.

$$AF_{(2-\mathrm{D})} = \sum_{m=1}^{M}\sum_{n=1}^{N} e^{j(kx_m \sin\theta\cos\varphi + ky_n \sin\theta\sin\varphi)} \tag{2- 6}$$

where (x_{m},y_{n}) is the position of element with indexes (m, n) along x and y axes, φ and θ are the azimuth and elevations angles in spherical coordinate system.

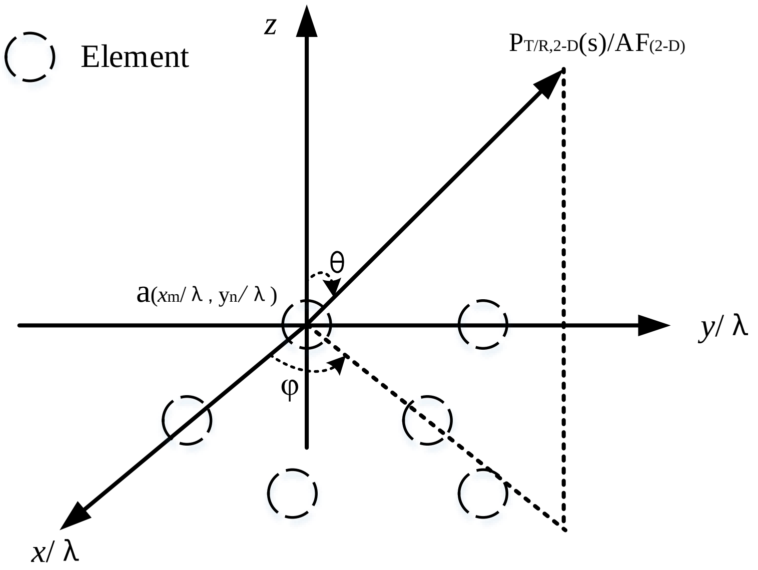

Figure 2- 7. Coordinate system for relating the planar aperture function to 2-D radiation pattern

Equation (2- 6) is based on the far field assumption, similarly in equation (2- 2). Accordingly, we can gain a more general calculating equation taking account of the target distance particularly for this SPA imaging system, as shown in equation (2- 7) and equation (2- 8), which are also the point spread functions (PSFs) of the transmitter and receiver arrays, respectively.

$$PSF_{2D,Tx}(o) = \sum_{w=1}^{W}\sum_{p=1}^{Nt} e^{jk\left|\overrightarrow{R_{to}^{p,w}}\right|} \tag{2- 7}$$

or

$$PSF_{2D,Rx}(o)=\sum_{w=1}^{W}\sum_{q=1}^{Nr}e^{jk\left|\overrightarrow{R_{ro}^{q,w}}\right|} \tag{2- 8}$$

wherein $\overrightarrow{R_{to}^{p,w}}$ and $\overrightarrow{R_{ro}^{q,w}}$ as shown in Figure 2- 8 and calculated as equation (2- 9) are the vectors between the position $(x_t^{p,w},y_t^{p,w})$ of ***p***th transmitter element at ***w***th mechanical scanning position and the position $(x_r^{q,w},y_r^{q,w})$ of ***q***th receiver element at ***w***th mechanical scanning position to the target point **o**, respectively.

$$\begin{aligned}\left|\overrightarrow{R_{to}^{p,w}}\right|&=\sqrt{(x_t^{p,w}-x_o)^2+(y_t^{p,w}-y_o)^2+z_o{}^2}\\ \left|\overrightarrow{R_{ro}^{q,w}}\right|&=\sqrt{(x_r^{q,w}-x_o)^2+(y_r^{q,w}-y_o)^2+z_o{}^2}\end{aligned} \tag{2- 9}$$

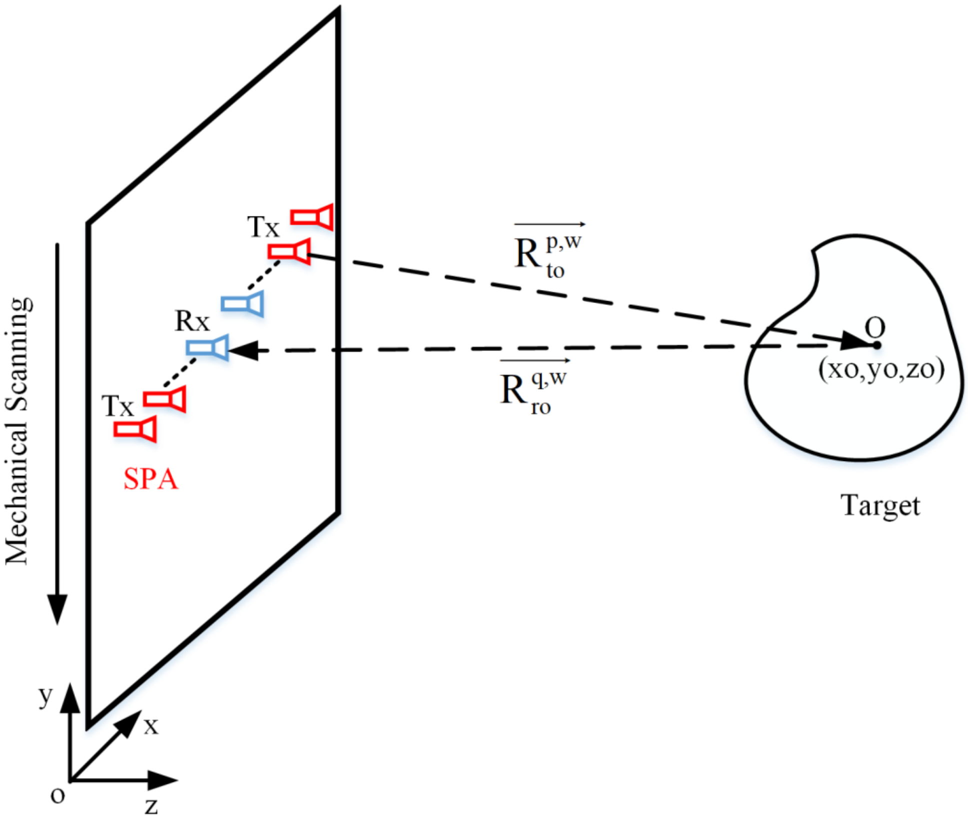

Figure 2- 8. Imaging schematic with a multi-static array (SPA)

Therefore, the planar two-way radiation pattern/PSF of this array (imaging system)-the product of planar one-way radiation pattern/PSF of transmitter and receiver arrays can be derived in equation (2- 10).

$$PSF_{2D,SPA}(o) = \sum_{w=1}^{W}\sum_{p=1}^{Nt}\sum_{q=1}^{Nr} e^{jk\left(\left|\overrightarrow{R_{to}^{p,w}}\right| + \left|\overrightarrow{R_{ro}^{q,w}}\right|\right)} \tag{2- 10}$$

It is worth noting that equations (2- 7) ~ (2- 10) can be used to assess the performance for both near and far range imaging scenarios. In addition, the 1-D radiation patter/PSF is the slice of 2-D radiation patter/PSF. For example, Figure 2- 9 shows the 2-D PSFs of Tx, Rx and SPA in simulation. The simulation details are concluded in Table. 2- 1. Figure 2- 10 shows the corresponding 1-D PSFs, we can see that 1-D PSFs of Tx and Rx in Figure 2- 10 (a) are the (Y = 0) slices of 2-D PSFs in Figure 2- 9 (a) and (b). Similarly to the Figure 2- 10 (b) and Figure 2- 9 (c). Besides, the X-horizontal and Y-vertical resolutions are 3.906 mm and 2.50 mm, verified by the first nulls of PSFs in Figure 2- 10 (d).

Table. 2- 1. Details of imaging system in MATLAB simulation on PSF

Frequency	220 GHz
SPA	8 Tx + 8 Rx
Tx element spacing dt & mechanical scanning interval (total scanning length)	6 mm & 4 mm (0.3 m)
Mechanical scanning length	0.3 m
Target distance	1.1 m
Resolutions (Horizontal & Vertical directions)	3.91 mm & 2.50 mm

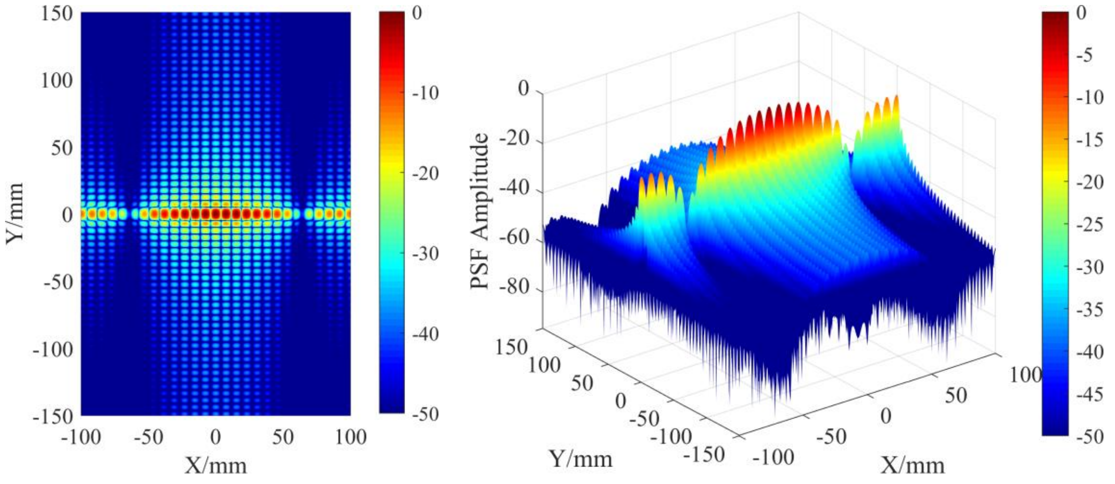

(a)

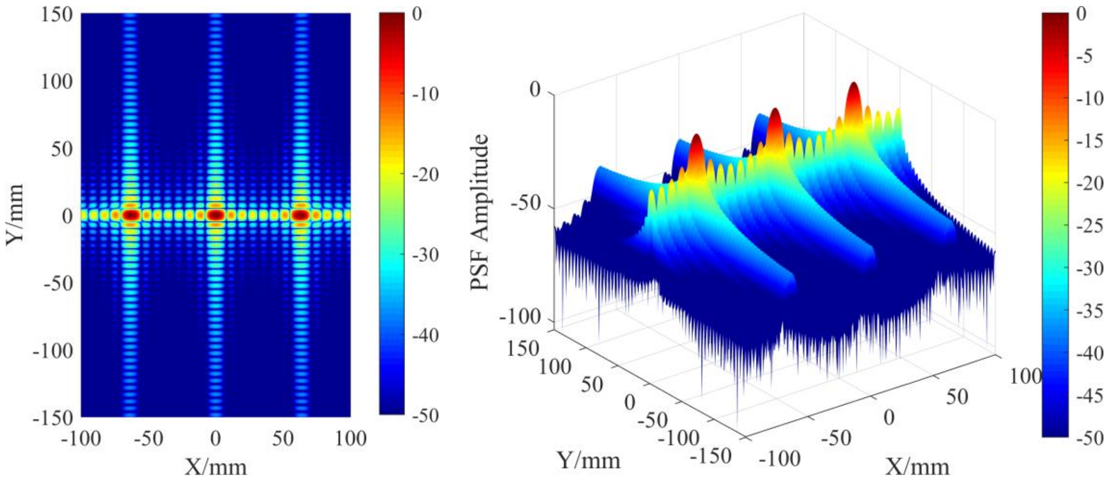

(b)

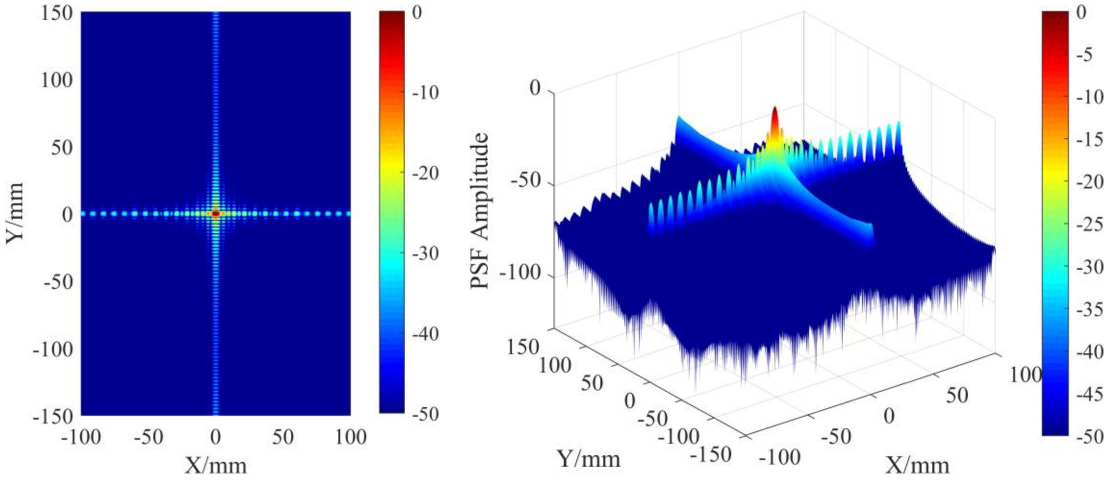

(c)

Figure 2- 9. 2-D (a) $\mathrm{PSF}_{\mathrm{Tx}}$ (b) $\mathrm{PSF}_{\mathrm{Rx}}$ and (c) $\mathrm{PSF}_{\mathrm{SPA}}$

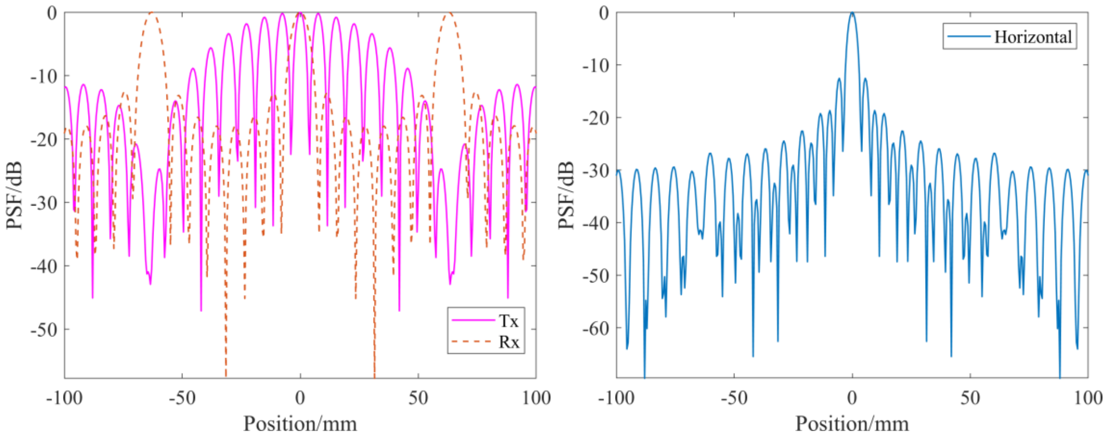

(a)

(b)

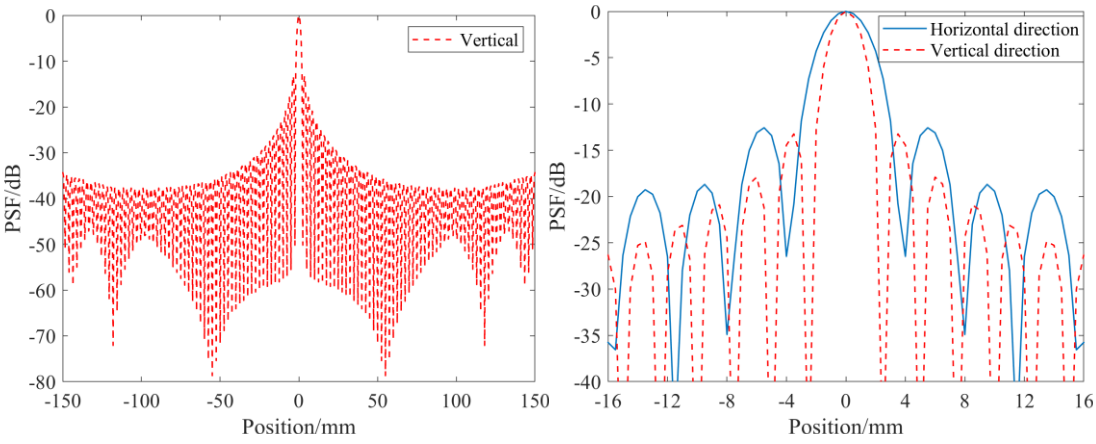

(c) (d)

Figure 2- 10. 1-D PSFs of (A) Tx and Rx (b) SPA (c) vertical scanning and (d) zoomed-in PSFs along two dimensions

2.3.2. Spatial and Frequency Sampling

Data sampling and image reconstruction will require that the data and the subsequent image be discretized. Traditional theory requires this sampling or discretization to meet the Nyquist sampling criterion. The satisfied sampling along an aperture is determined by a number of factors including the wavelength, size of the aperture, size and distance of the target [1, 5]. The Nyquist criterion will be satisfied if the phase shift from one sample point to the next is less than π rad [1, 5]. The worst case will occur for a target very near to the aperture and the sample points near the edge of the aperture, as shown in Figure 2- 11 [1, 5].

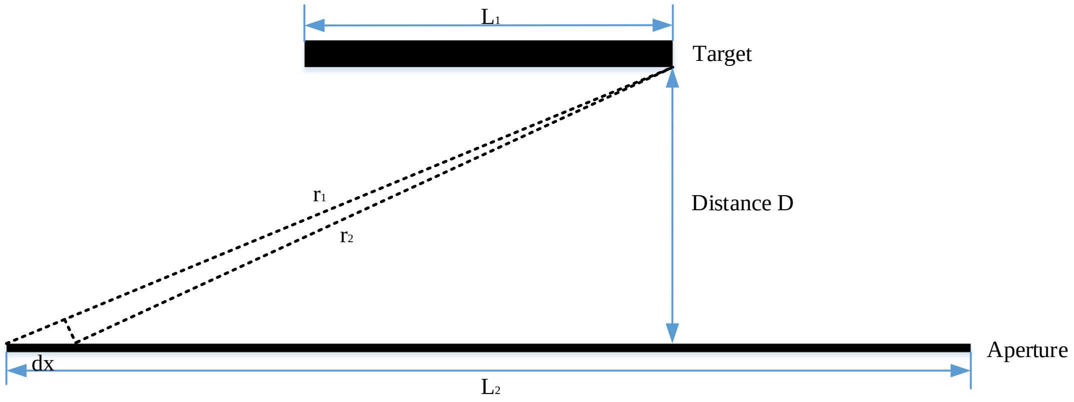

Figure 2- 11. Illustration of Nyquist sampling criterion for aperture spatial sampling

Therefore, the worst case will have a phase shift of $2k|r_1\text{-}r_2|$ where 2 is for round trip and $k = 2\pi/\lambda$ is the wavenumber [1, 5]. It is not more than $2k\mathrm{d}x$ since dx is the hypotenuse. Therefore, the sampling interval can be derived as

$$dx < \frac{\lambda}{4} \tag{2- 11}$$

This result is more restrictive than it is usually required since the target is often at a moderate distance from the aperture. Consequently, practical imaging systems can often employ sampling intervals in the order of $\lambda/2$ [1].

The required frequency sampling is determined in a similar way. The phase shift resulting from a change in wavenumber Δk is $2\Delta k\mathrm{D}_{\max}$, where $\mathrm{D}_{\max}$ is the maximum target range [1].

Requiring that this phase shift be less than π rad yields $\Delta k < \pi/(2\mathrm{D}_{\max})$ or

$$\Delta f < \frac{c}{4D_{\max}} \tag{2- 12}$$

where Δf is the required frequency sampling interval [1].

Alternatively, the number of frequency samples in a bandwidth of B must be

$$N_f > \frac{2D_{\max}}{(c/2B)} \tag{2- 13}$$

This is an interesting result since it indicates that per range resolution cell needs two frequency samples where the range resolution is defined by c/2B [1].

2.3.3. Imaging Algorithms

I. Generalized Synthetic Aperture Focusing Technique

For the monostatic imaging system using raster scanning scheme or mono-static array shown in Figure 2- 12, the Fast Fourier Transform (FFT) based on the back propagation (BP) algorithm can be used to reconstruct the image [1], see details in Appendix I. It is an interferometric imaging using both incoming amplitudes and phase of each TR pair to form the image on the target plane. And the TR separation is small compared to the target distance, so the phase error caused by approximation of using the central positon rather than the exact Tx and Rx positions to calculate the phases to target is neglectable. However, regarding the SPA configuration being a multi-static scenario, aforementioned approximation and reconstruction algorithm are not applicable. Therefore, Generalized Synthetic Aperture Focusing Technique (GSAFT) using exact Tx and Rx positions to calculate the phase difference is required, as shown in equation (2- 14).

$$g(\overrightarrow{r_o}) = \sum_{w=1}^{W}\sum_{p=1}^{Nt}\sum_{q=1}^{Nr} S(\overrightarrow{R_{to}^{p,w}}, \overrightarrow{R_{ro}^{q,w}}) \cdot e^{jk(|\overrightarrow{R_{to}^{p,w}}|+|\overrightarrow{R_{ro}^{q,w}}|)} \tag{2- 14}$$

wherein **g** is the reflectivity function that is used to depict the target, forming the image, **S** is the S-parameters, $\overrightarrow{\mathrm{R}_{\mathrm{to}}^{\mathrm{p,w}}}$ and $\overrightarrow{\mathrm{R}_{\mathrm{ro}}^{\mathrm{q,w}}}$ are the vectors between the position $(\mathrm{x}_{\mathrm{t}}^{\mathrm{p,w}}, \mathrm{y}_{\mathrm{t}}^{\mathrm{p,w}})$ of ***p***th transmitting antenna at ***w***th mechanical scanning position and the position $(\mathrm{x}_{\mathrm{r}}^{\mathrm{q,w}}, \mathrm{y}_{\mathrm{r}}^{\mathrm{q,w}})$ of ***q***th receiving antenna at ***w***th mechanical scanning position to the target point **o**, as calculated in equation (2- 9). We can see equation (2- 14) equals to S-parameters multiplied by PSF depicted in equation (2- 10), which is also named as imaging system response.

Like the multi-pass interferometric synthetic aperture radar (inSAR) achieving imaging with the exact same radar systems on the same aircraft (or spacecraft) flying by in different passes [12-15], the proposed SPA imaging system can also use multi-pass phase-correlated datasets to improve the image quality. Therefore, the SPA can simply move positions along the electronic scanning direction with a number of ***N***, collecting ***N*** phase-correlated data. The corresponding reconstruction is shown in equation (2- 15).

$$g(\overrightarrow{r_o}) = \sum_{n=1}^{N}\sum_{w=1}^{W}\sum_{p=1}^{Nt}\sum_{q=1}^{Nr} S(\overrightarrow{R_{to,n}^{p,w}}, \overrightarrow{R_{ro,n}^{q,w}}) \cdot e^{jk(|\overrightarrow{R_{to,n}^{p,w}}|+|\overrightarrow{R_{ro,n}^{q,w}}|)} \tag{2- 15}$$

where $\overrightarrow{\mathrm{R}_{\mathrm{to,n}}^{\mathrm{p,w}}}$ and $\overrightarrow{\mathrm{R}_{\mathrm{ro,n}}^{\mathrm{p,w}}}$ are the vectors in the ***n***th path between the position $(\mathrm{x}_{\mathrm{t,n}}^{\mathrm{p,w}}, \mathrm{y}_{\mathrm{t,n}}^{\mathrm{q,w}})$ of ***p***th transmitting antenna at ***w***th mechanical scanning position and the position $(\mathrm{x}_{\mathrm{r,n}}^{\mathrm{p,w}}, \mathrm{y}_{\mathrm{r,n}}^{\mathrm{p,w}})$ of ***q***th receiving antenna at ***w***th mechanical scanning position to the target point **o**, as calculated in equation (2- 16).

$$\begin{aligned}\left|\overrightarrow{R_{to,n}^{p,w}}\right| &= \sqrt{(x_{t,n}^{p,w}-x_o)^2+(y_{t,n}^{p,w}-y_o)^2+{z_o}^2}\\ \left|\overrightarrow{R_{ro,n}^{q,w}}\right| &= \sqrt{(x_{r,n}^{q,w}-x_o)^2+(y_{r,n}^{q,w}-y_o)^2+{z_o}^2}\end{aligned} \tag{2- 16}$$

Regarding the reconstruction algorithm of 3D image using wideband operation, based on the GASFT in equation (2- 14), the average of amplitudes of different frequencies at each specific (x, y, z) position are calculated to represent each pixel at this position, as depicted in equation (2- 17) in which ***Nf*** is the number of frequency samples.

$$\overline{g(\overrightarrow{r_o})} = \frac{1}{Nf}\sum_{f}^{Nf}\sum_{w=1}^{W}\sum_{p=1}^{Nt}\sum_{q=1}^{Nr} S(\overrightarrow{R_{to}^{p,w}},\overrightarrow{R_{ro}^{q,w}})\cdot e^{jk\left(\left|\overrightarrow{R_{to}^{p,w}}\right|+\left|\overrightarrow{R_{ro}^{q,w}}\right|\right)} \tag{2- 17}$$

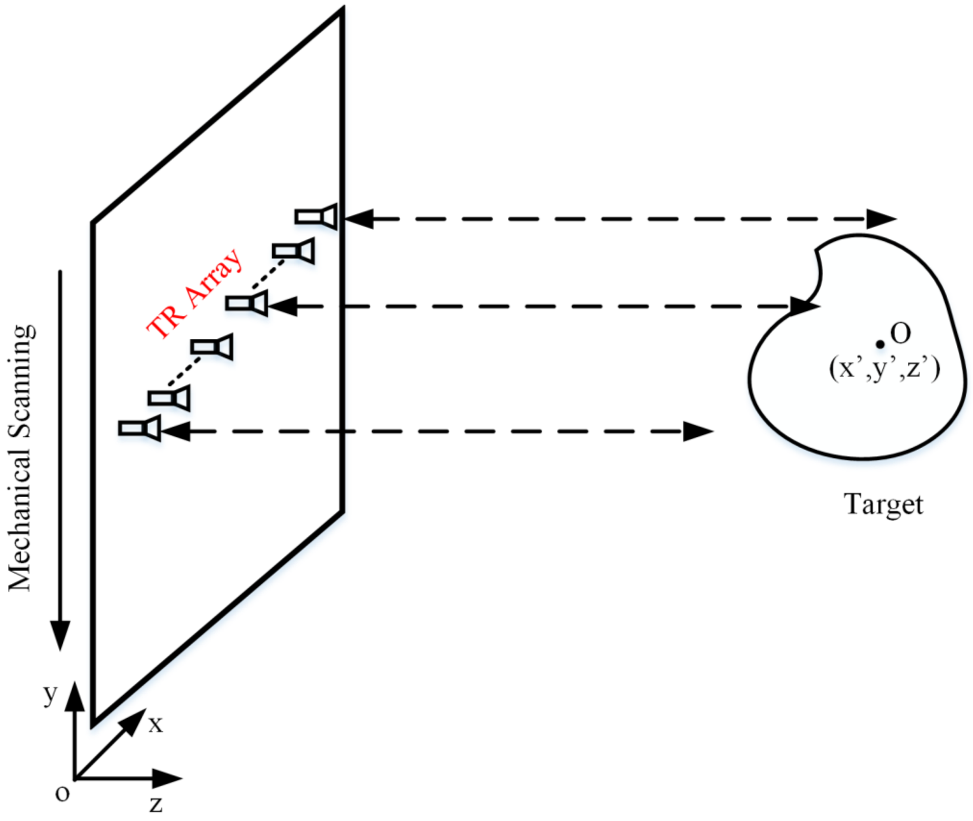

Figure 2- 12. Imaging schematic with a monostatic array

II. Improved GSAFT Proposed for Ghost Images Suppression

As depicted in equation (2- 14) based on GSAFT, each pixel (point) in the desired image space is evaluated by all the recorded data of each TR combination. However, this kind of reconstruction method will cause ghost images when the sampling spacing is large. Therefore, we introduce a weighting function f_{g} into the traditional GSAFT imaging algorithm in order to filter the echoes data for each point reconstruction [16]. The working concept of the proposed imaging algorithm is illustrated in Figure 2- 13 and equation (2- 18). Due to the weighting function f_{g}, each imaging target point is synthesized by the specific recorded data within coverage area instead of all the recorded data in traditional imaging algorithm. Thus, the weighting function is defined by equations (2- 19) ~ (2- 21) [16].

$$g(\overrightarrow{r_o}) = \sum_{w=1}^{W}\sum_{p=1}^{Nt}\sum_{q=1}^{Nr} f_{\mathrm{g}} \cdot S(\overrightarrow{R_{to}^{p,w}}, \overrightarrow{R_{ro}^{q,w}}) \cdot e^{jk\left(\left|\overrightarrow{R_{to}^{p,w}}\right| + \left|\overrightarrow{R_{ro}^{q,w}}\right|\right)} \tag{2- 18}$$

If

$$\begin{aligned} &\left|(x_t^{p,w} + x_r^{q,w})/2 - x_o\right| < Rx \\ &\left|(y_t^{p,w} + y_r^{q,w})/2 - y_o\right| < Ry \end{aligned} \tag{2- 19}$$

then

$$f_{\mathrm{g}} = 1 \tag{2- 20}$$

else

$$f_{\mathrm{g}} = 0 \tag{2- 21}$$

wherein $\overrightarrow{\mathrm{R}_{\mathrm{to}}^{\mathrm{p,w}}}$ and $\overrightarrow{\mathrm{R}_{\mathrm{ro}}^{\mathrm{q,w}}}$ are the vectors same as shown in equation (2- 9). In addition, **Rx** and **Ry** are two independent thresholds/radiuses around half of ΔS_x and ΔS_y, which would be introduced in section 3.2.2.

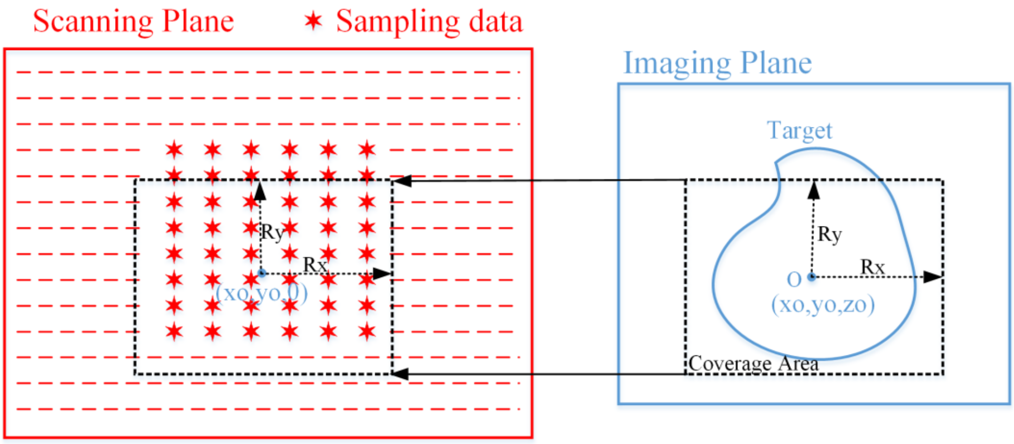

Figure 2- 13. Illustration on working concept of the improved GSAFT imaging algorithm proposed for suppressing ghost images

2.3.4. Specifications of Imaging System

Field of view (FOV) of an imaging system depicts the area that can be seen by this imaging system, so it is crucial to an imaging system. It is related to the scanning aperture and the surface curvature of the target that affects the path of the reflection.

The resolution of an imaging system is the minimum separation that can be identified. There are two categories of range resolution and cross-range resolution. The resolution obtained in the image can be determined by examining the extent or width of the coverage in the spatial frequency domain [1]. In one dimension, uniform frequency coverage (rectangular function) width of Δk results in a spatial pulse width of $2\pi/\Delta k$. For a 3-D image reconstruction, the spatial frequency coverage is a polar region as shown in Figure 2- 14 [1]. If this region is approximated as rectangular, then the width in the k_x-direction is approximately $4k_c\sin(\theta_b/2)$ where k_c is the wavenumber at the center frequency and θ is the minimum of the full beam width of the antenna or the angle subtended by the aperture[1]. This results in a cross-range resolution along x-direction of

$$\delta_x \approx \left. \frac{\lambda_c}{4\cdot\sin(\theta/2)} \right|_{\theta=\min(\theta_{HPBW},2\arctan(\frac{L_x}{2D}))} \tag{2- 22}$$

where L_x is the scanning aperture along x-direction. Cross-range resolution along the y-direction will be same except that the beam-width may be different. The cross-range resolution can also be predicted by the point spread function, which has been demonstrated in Figure 2- 10 (b). For an aperture-limited imaging system in which target distance D is much larger than scanning aperture length or the receiver antenna has about 180° beam width, θ_{min} is equal to $2\cdot\arctan(L_x/(2D))$ so $\delta_x = \lambda_c/(2L_x)\cdot D$. This prediction agrees well with the equation (2- 23) proposed to estimate the resolution of a SPA that does not take account of the beam-width due to omnidirectional radiation pattern of point source assumption [10],

$$\delta_c = \lambda_c / L \cdot D \tag{2- 23}$$

where L is the aperture length of effective array, illustrated as Ld in Figure 2- 2 or the two times of mechanical scanning length in order to estimate the resolution along mechanical scanning direction.

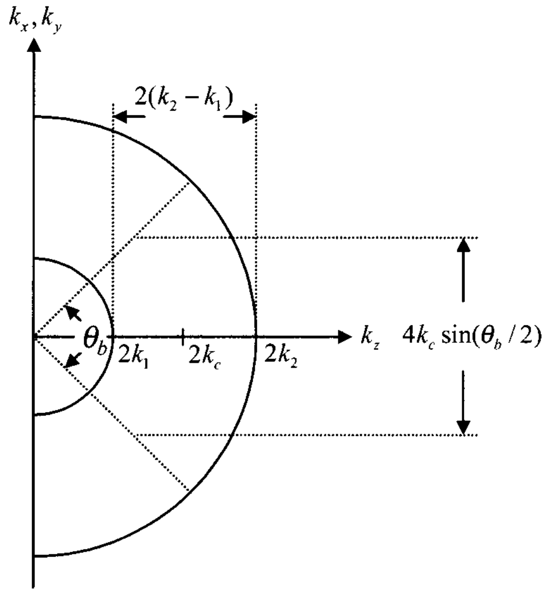

Figure 2- 14. Spatial frequency coverage in the range and cross-range directions [1]

The range resolution of an imaging system can be gained by the wideband imaging operation, derived by equation (2- 24) where the B is the frequency bandwidth of the system [1].

$$\delta_R \approx \frac{2}{2(k_2 - k_1)} = \frac{c}{2B} \tag{2- 24}$$

The SNR of the image, unlike the SNR of the imaging system, is a concept used to quantitatively assess the image quality, defined as the ratio of difference in brightness between bright and dark areas to the standard deviation of the dark area in equation (2- 25) [17].

$$SNR_I = \frac{\overline{B_{bright}} - \overline{B_{dark}}}{\sigma(B_{dark})} \tag{2- 25}$$

where $\overline{B_{bright}}$ and $\overline{B_{dark}}$ are the mean brightness of the target area and non-target area. $\sigma(B_{dark})$ is the standard deviation of the dark area brightness [17].

2.4. Summary

This chapter has introduced the fundamental design guideline and working principle of the linear sparse periodic array that provides a high imaging quality with fewer array elements. This kind of array is anticipated to be applied in several potential THz imaging schemes, which will be assessed in the following work. Besides, the multi-pass interferometric synthetic aperture imaging technique and the improved GSAFT reconstruction algorithm have been proposed to apply in the system. Finally, the point spread function, imaging algorithms and several specifications used to assess the imaging performance have been introduced.

2.5. References

[1] D. M. Sheen, D. L. McMakin, and T. E. Hall, "Three-dimensional millimeter-wave imaging for concealed weapon detection," *IEEE Transactions on Microwave Theory and Techniques*, vol. 49, no. 9, pp. 1581-1592, Sep 2001.

[2] D. M. Sheen, D. L. McMakin, and T. E. Hall, "Cylindrical millimeter-wave imaging technique and applications," in *Defense and Security Symposium*, pp. 62110A-62110A-10: 2006.

[3] D. Sheen, D. McMakin, and T. Hall, "Near-field three-dimensional radar imaging techniques and applications," *Applied Optics*, vol. 49, no. 19, pp. E83-E93, 2010.

[4] D. M. Sheen and T. E. Hall, "Reconstruction techniques for sparse multistatic linear array microwave imaging," in *Proc. SPIE 9078, Passive and Active Millimeter-Wave Imaging XVII,*vol. 9078, pp. 90780I-90780I-12, 2014.

[5] X. Zhuge and A. G. Yarovoy, "A Sparse Aperture MIMO-SAR-Based UWB Imaging System for Concealed Weapon Detection," *IEEE Transactions on Geoscience and Remote Sensing*, vol. 49, no. 1, pp. 509-518, 2011.

[6] F. Gumbmann and L. P. Schmidt, "Design of sparse MIMO arrays for short range imaging applications," in *2010 Asia-Pacific Microwave Conference*, pp. 1653-1656, 2010.

[7] F. Gumbmann and L. P. Schmidt, "Millimeter-Wave Imaging With Optimized Sparse Periodic Array for Short-Range Applications," *IEEE Transactions on Geoscience and Remote Sensing*, vol. 49, no. 10, pp. 3629-3638, 2011.

[8] F. Gumbmann, P. Tran, J. Weinzierl, and L. P. Schmidt, "Multistatic Short Range Ka-Band Imaging System," in *2009 German Microwave Conference*, pp. 1-4, 2009.

[9] F. Gumbmann, P. Tran, and L. P. Schmidt, "Sparse linear array design for a short range imaging radar," in *2009 European Radar Conference (EuRAD)*, pp. 176-179, 2009.

[10] G. R. Lockwood, L. Pai-Chi, M. O. Donnell, and F. S. Foster, "Optimizing the radiation pattern of sparse periodic linear arrays," *IEEE Transactions on Ultrasonics, Ferroelectrics, and Frequency Control*, vol. 43, no. 1, pp. 7-14, 1996.

[11] F. Gumbmann and L. P. Schmidt, "Short Range Imaging with Optimized Sparse Array," in *8th European Conference on Synthetic Aperture Radar*, pp. 1-4, 2010.

[12] M.-H. Ka, E. P. Shimkin, I. A. Baskakov, and I. M. Babokin, "A New Single-Pass SAR Interferometry Technique with a Single-Antenna for Terrain Height Measurements," *Remote Sensing*, vol. 11, no. 9, 2019.

[13] G. Fornaro, F. Lombardini, and F. Serafino, "Three-dimensional multipass SAR focusing: experiments with long-term spaceborne data," *IEEE Transactions on Geoscience and Remote Sensing*, vol. 43, no. 4, pp. 702-714, 2005.

[14] J. Homer, I. D. Longstaff, Z. She, and D. Gray, "High resolution 3-D imaging via multi-pass SAR," *IEE Proceedings - Radar, Sonar and Navigation*, vol. 149, no. 1, pp. 45-50, 2002.

[15] M. Schmitt and U. Stilla, "Adaptive Multilooking of Airborne Single-Pass Multi-Baseline InSAR Stacks," *IEEE Transactions on Geoscience and Remote Sensing*, vol. 52, no. 1, pp. 305-312, 2014.

[16] S. Hu, M. Zhou, X. Chen, and Y. Alfadhl, "Suppressing Ghost Images for Synthetic Aperture THz Imaging With Large Sampling Spacing," in *12th European Conference on Antennas and Propogation*, London, 2018.

[17] A. Tamminen, J. Ala-Laurinaho, and A. V. Räisänen, "Indirect holographic imaging: evaluation of image quality at 310 GHz," in *SPIE Defense, Security, and Sensing*, vol. 7670, p. 11: SPIE, 2010.

Chapter 3 Simulation Study and Assessment of the Proposed THz Imaging Scheme

3.1. Introduction to Simulation Methods

Computational electromagnetics (CEM) is applied to model the interaction between electromagnetic fields with the objects such as antenna, aircraft and their environment [1-3]. This simulation as an effective method to assure the practical performance is essential to the design of device or system. The methods in CEM can be categorized into three types because of solver type used [2, 3]. The integral equation solver based methods include popular Method of Moments (MOM), Finite Integration Technique (FIT) and Fast Multipole Method (FMM). Differential equation solvers based methods include Finite Element Method (FEM) and Finite Difference Time Domain (FDTD) Method. The other methods include electric current based Physical Optics (PO) and electric field based Geometric Optics (GO) [2].

Most widely used CEM simulation tools are CST Studio Suite based on Finite Integration Technique (FIT) [4, 5], Ansys HFSS based on FEM [6] and Altair FEKO^{TM} based on MOM and FEM [1, 7]. However, all these methods have their own limitations. MOM has difficulties in modeling inhomogeneous, interior of conducting enclosures and dielectrics with non-linearity. FEM is not suitable for efficient modeling of thin wires, large radiation problems and Eigen value problem due to its unstructured mesh. FDTD is difficult in modeling structure with sharp edges. Therefore, each method has its specialized application as shown in Figure 3- 1, and these commercial computational tools now incorporate several solvers with different methods for various scenarios [7]. FEKO^{TM} is originally effective in handling large structures like large-scale phase array. Besides, as MOM based software, the Multilevel Fast Multipole Method (MLFMM) in FEKO^{TM} is more efficient, which reduces the memory complexity and solving complexity [8]. The FEKO^{TM} is suitable not only for large-scale and complicated 3D objects such as reflect-array and aircraft, but also for the far field imaging that involves a long target distance of free space up to meters. Therefore, we have chosen the FEKO^{TM} as our imaging simulation tool. In addition, the hybrid method of MOM and PO in FEKO^{TM} enables the imaging simulation with various targets on a limited Random-access Memory (RAM) resource and within an acceptable time [9]. For example, the MOM/PO or MLFMM/PO hybrid method can be employed for a large pure metallic target with smooth surface in which the MOM or MLFMM are used as the global solver while the PO is used as the local solver for the target [9]. PO is based on finding the current density induced on a surface, so it is applicable in large scatters. For extremely large metallic target, the Large Element PO (LE-PO) can be used instead of PO, which allows much larger mesh sizes that lead to dramatic computational cost savings compared to standard PO [9]. However, if the target includes the dielectric, the PO method is not applicable. So the Ray-Launching Geometrical Optics (RL-GO) method that is also sometimes referred as Shooting and Bouncing Rays (SBR) should be adopted [1, 9]. This is a field-based method in which the equivalent currents on geometric plane are set up using ray tracing. GO meshing elements are much larger than those in the MOM and PO. Therefore, the mesh storage is reduced remarkably, so it is very suitable for electrically large PEC and dielectric objects with multiple reflections [9]. It is worth mentioning that the RL-GO in hybrid simulation approach can be coupled with the MOM rather than MLFMM. Beside, since the elements in the SPA are uniform, we can also use the equivalent source of its far field instead of the real element model to further save the computational time and RAM resource, especially for a large array and target. In summary, the full workflow of this simulation study has been concluded in a flow chart of Figure 3- 2. Based on the desired imaging specifications, the configurations of SPA and mechanical scanning are firstly designed according to the design guideline we proposed. Then, the full wave simulation is conducted in FEKO^{TM}.

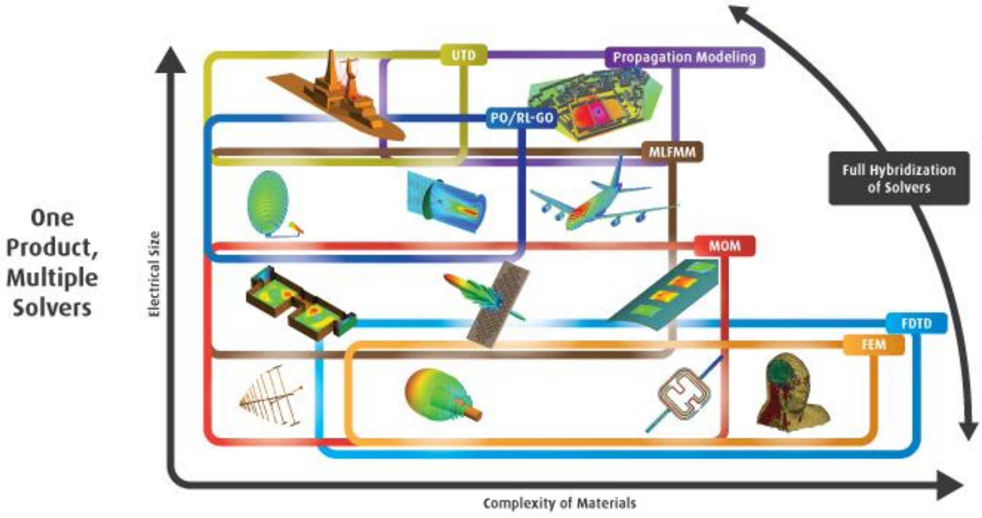

Figure 3- 1. Applications of various computational methods [7]

Thereafter, the simulated data are input to imaging program in MATLAB thus the target image is reconstructed.

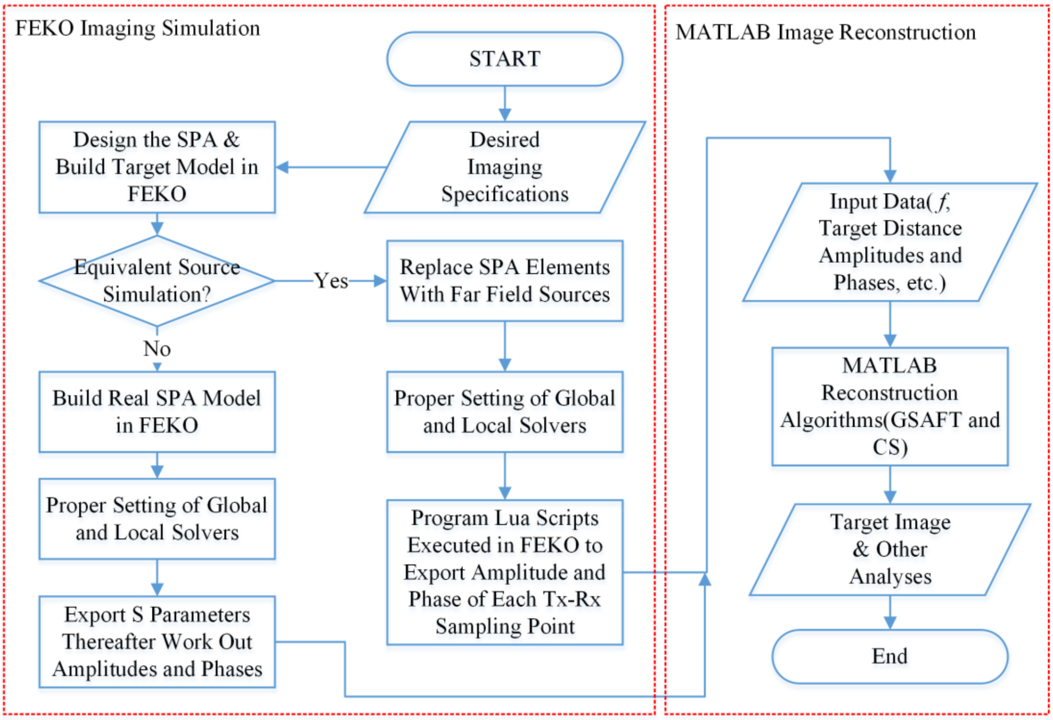

Figure 3- 2. Flow chart of imaging simulation study including the imaging simulation in FEKO^{TM} and the image reconstruction in MATLAB

3.2. Comprehensive Simulation Study and Results Analysis

3.2.1. Imaging Performance of Different SPA Configurations

In the first stage of simulation study, a pyramidal horn has been chosen as the element to form the SPA working for 0.22 THz imaging. The geometry of the pyramidal horn is illustrated in Figure 3- 3 and the radiation pattern at 0.22 THz (shown in Figure 3- 3) demonstrates that it has a 3 dB beam width of about 42° and a peak gain of 12.95 dB. Due to this wide beam-width in simulation study, the spatial resolution is normally predicted by equation (2- 23) for an aperture-limited imaging system.

In this simulation study, the SPA consists of 8 transmitting and 8 receiving elements as configured in Figure 2- 2. Therefore, the real array aperture **Lt** equals **36·dt**, and the virtually effective array aperture **Ld** equals **64·dt**. The target in the simulation drawn in Figure 3- 4 (a) is placed at a distance of **D = 1 m** from the scanning plane of TR sparse array. So the spatial resolution along the direction of array orientation can be predicted by the equation (2- 23). Different schemes consisting of different element spacing of **dt** and beam mechanical scanning spacing **dv**, shown in Table. 3- 1, are studied to assess the corresponding imaging performance. And the reconstructed images are compared in Figure 3- 4 (b), Figure 3- 4 (c) and Figure 3- 4 (d), respectively.

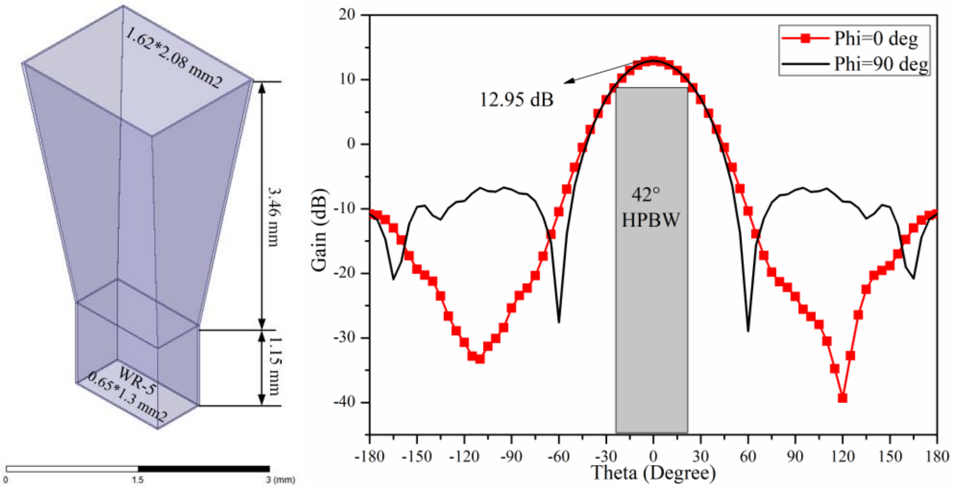

Figure 3- 3. Geometry and radiation pattern at 0.22 THz of the pyramidal horn

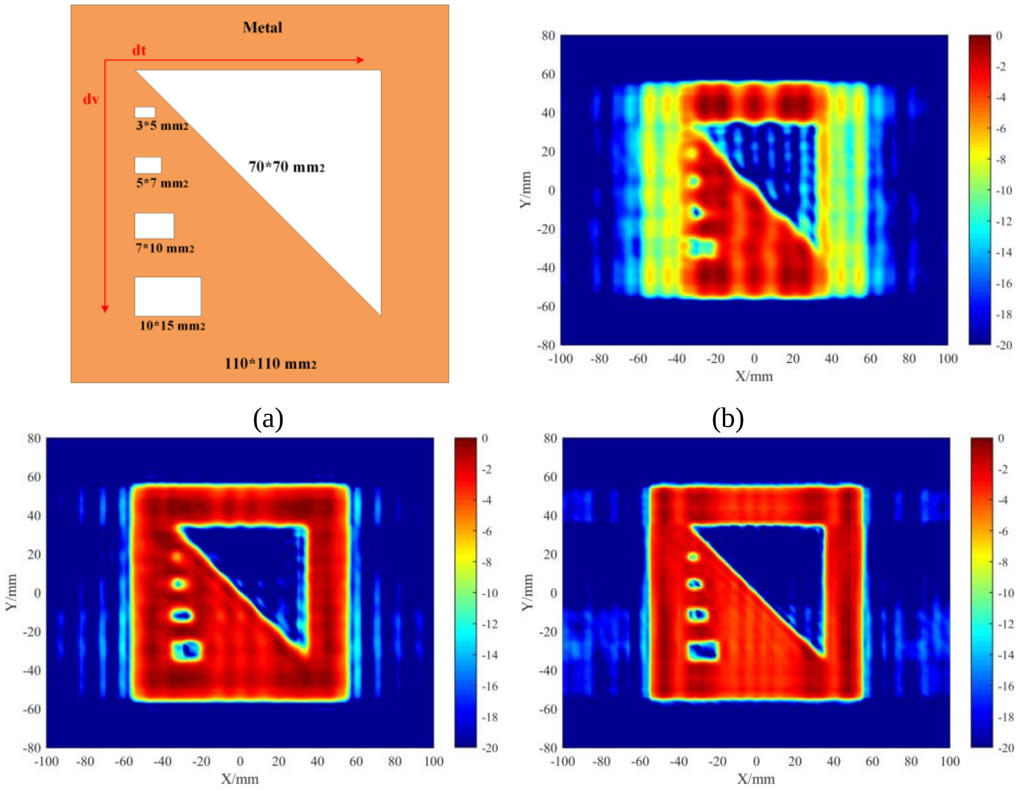

(a) (b)

(c) (d)

Figure 3- 4. Target (a) drawing and reconstructed images with 20-dB dynamic range of (b) Scheme I (c) Scheme II and (d) Scheme III

As shown in Figure 3- 4 (b), when the real array aperture is narrower than the target width (like scheme I), the target cannot be reconstructed completely. That is because the FOV of such a THz SPA imaging system for detecting a flat target

Table. 3- 1. Schemes (8 Tx & 8 Rx) with different Tx element spacing and same 41 mechanical scanning spots (dv = 4 mm, total scanning length: 160 mm)

Parameters(mm) **Schemes**	**dt**	**FOV**	**Lt**	**Ld**	**Theoretical resolution**
Scheme I	2.5 (1.83λ)	80	90	160	$\frac{1.364}{160}\cdot 1000 = 8.525$
Scheme II	4 (2.93λ)	128	144	256	$\frac{1.364}{256}\cdot 1000 = 5.328$
Scheme III	6 (4.40λ)	192	216	384	$\frac{1.364}{384}\cdot 1000 = 3.552$

detection is 0.5 · dt · Nt · Nr as shown in equation (3- 1), which is the length between the first and last sampling points as illustrated in Figure 3- 5 and derived on the basis of SPA configuration (introduced in Chapter 2.1). This FOV principle of equalling to the sampling aperture also applies to the mechanical scanning approach or electronic scanning of other kinds of arrays.

$$dr\cdot(Nr-1)+0.5\cdot dt\cdot Nt=0.5\cdot dt\cdot Nt\cdot Nr \qquad (3\text{- }1)$$

So the FOV of scheme I is 80 mm, consequently the area beyond ±40 mm cannot be reconstructed in Figure 3- 4 (b) while the target image can be reconstructed completely in Figure 3- 4 (c) of scheme II and in Figure 3- 4 (d) of scheme III. Moreover, it is found that Figure 3- 4 (d) shows a superior resolution compared to Figure 3- 4 (c) because the array in scheme III has a longer real and virtual effective array aperture.

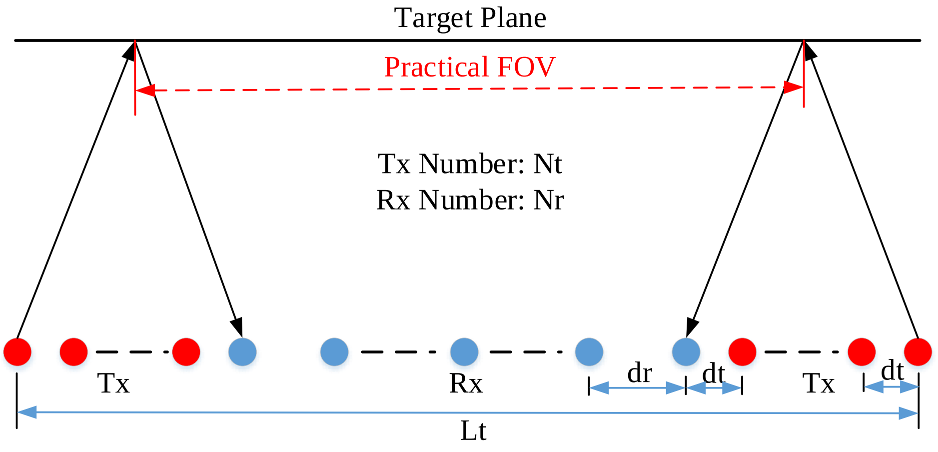

Figure 3- 5. Field of view of the SPA imaging system

3.2.2. *Large Sampling Spacing and Ghost Images Period*

Although the scheme II and scheme III can be adopted for the THz imaging system to detect and reconstruct images successfully, a wider (>4.40λ) element spacing is still desired to further reduce elements and sampling points. Moreover, the knowledge on the relationship between element spacing of **dt** as well as mechanical scanning spacing **dv** and corresponding imaging performance is needed for a design guideline. Therefore, parametric study has been conducted and the results are presented as follows.

Firstly, we have studied the effect of mechanical scanning interval, keeping the array element spacing same with scheme III of dt = 6 mm (4.40λ) and increasing the mechanical scanning interval from 4 mm to 6 mm. The reconstructed image as shown in Figure 3- 6 (a) indicates that the ghost images will emerge periodically along the mechanical scanning direction when directly using traditional GSAFT reconstruction algorithm if this mechanical sampling interval is too large. Besides, we found that the large array element spacing **dt** will also cause ghost images along the electronic scanning direction, as shown in Figure 3- 6 (b) with **dt** = 12 mm and **dv** = 6 mm. Although we can crop the image to eliminate the pseudo targets, we do not know where and what area we should crop when we conduct a practical personnel screening. Thus, we need to study the cause of this issue and fundamentally suppress it.

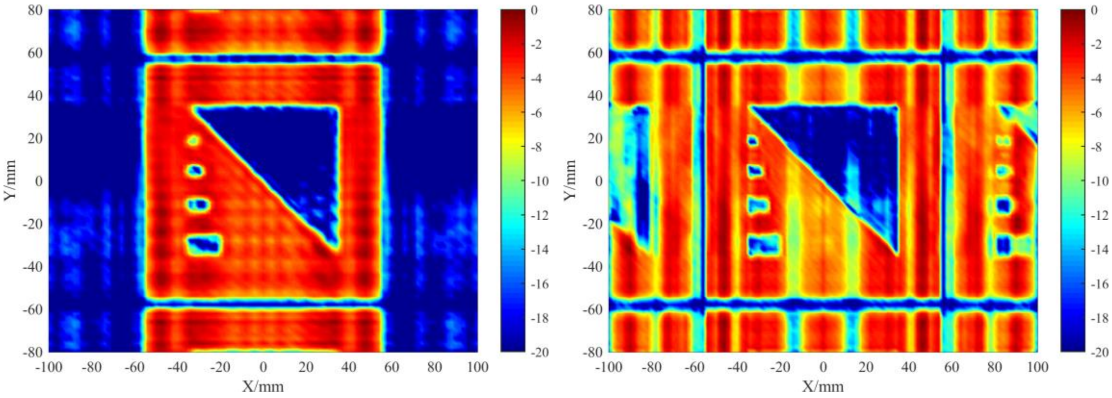

(a) (b)

Figure 3- 6. The reconstructed images with 20-dB dynamic range of (a) dt = 6 mm, dv = 6 mm and (b) dt = 12 mm, dv = 6 mm

In the simulation, we have discovered that the ghost images along two dimensions become dense with the increase of the array element spacing and mechanical scanning interval, respectively. As is known to us all, the grating lobes emerge in a broadside array when the uniform element spacing becomes larger than one wavelength.

Similarly, the grating lobes in a radiation pattern of a uniform array become dense with the increase of array element spacing.

The grating lobes in a broadside array periodically appear at the angle of θ_B (angle measured from perpendicular to the array as shown in Figure 3- 7) that can be calculated from equation (3- 3) derived from equation (3- 2), which depicts the forming condition of the grating lobes in a uniform array,

$$k \cdot ds \cdot \sin\theta_B = N \cdot 2\pi \tag{3- 2}$$

$$\Delta \sin\theta_B = \lambda / ds \tag{3- 3}$$

wherein *k* is wave number. λ is wavelength, N is the number of element. *ds* is Tx element spacing along electronic scanning direction by the SPA. As one example, one radiation pattern of SPA with dt = 6 mm is shown in Figure 3- 8.

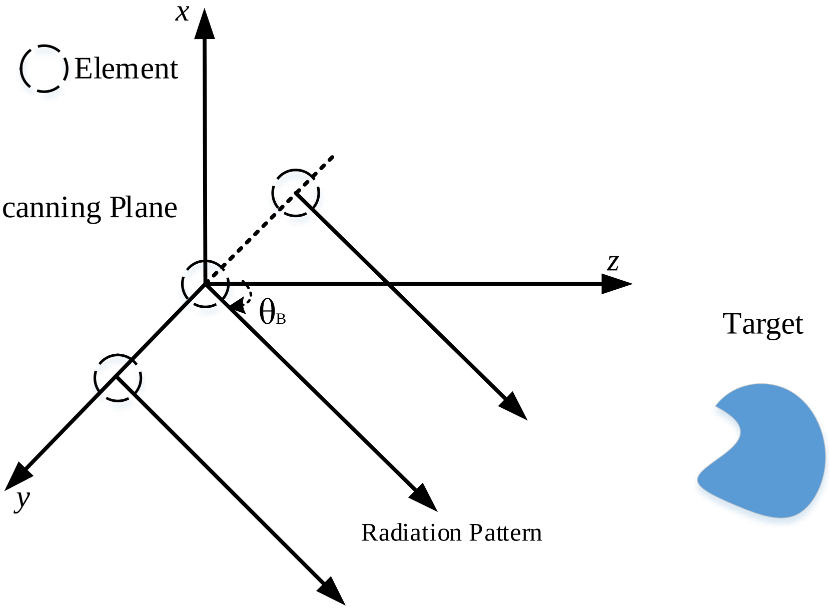

Figure 3- 7. Radiation of a broadside array

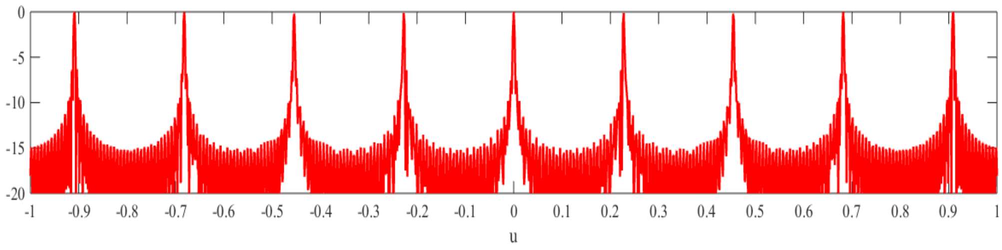

Figure 3- 8. The estimated equivalent radiation pattern of a SPA with dt = 6 mm

Therefore, we speculate the period of ghost images calculated by equation (3- 4) after we obtain the θ_B,

$$\Delta S = D \cdot \Delta \tan \theta_B \tag{3- 4}$$

wherein D is the target distance, ΔS is predicted period of ghost images. Regarding the mechanical scanning direction, the ds in equation (3- 3) is equal to $2 \cdot \mathrm{dv}$. That is because the $2 \cdot \mathrm{dv}$ element spacing will be required for a uniform TR array to electronically sample these data with an interval of dv, as illustrated in Figure 3- 9. That is also why the image of Figure 3- 6 (b) with dt = 12 mm and dv = 6 mm has same periods of ghost images along both directions.

In order to verify the proposed cause of ghost images, the ghost image periods ΔS for different element spacing of linear sparse periodic arrays are calculated that agree quite well with those obtained in reconstructed images in simulation, as shown in Table 3-2. Therefore, we have confirmed that these ghost images are really caused by the grating lobes. The quantitative relationship between sampling spacing (array element spacing and mechanical moving spacing) and the period of target images is depicted in equations (3- 2) ~ (3- 4).

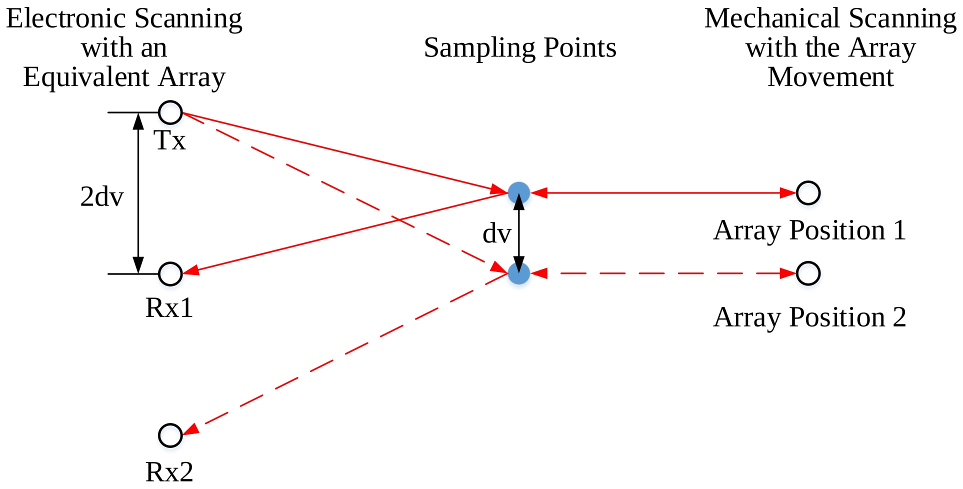

Figure 3- 9. Illustration of the mechanical scanning by an equivalent array

Based on scheme III in Table. 3- 1, we have kept configuration of **dt** = 6 mm unchanged, increasing mechanical scanning spacing **dv** to 6 mm (27 sample spots, scanning length 156 mm) and 8 mm (21 sample spots, scanning length 160 mm), respectively. The reconstructed images by traditional and improved GSAFT approaches are compared in Figure 3- 10. It is seen that the two-dimensional spatial resolutions in Figure 3- 10 are same with that in Figure 3- 4 (d) since their schemes have the same array aperture and near vertical scanning length, but artifacts are enhanced as mechanical scanning spacing increases. However, as shown in Figure 3- 10 (a) and Figure 3- 10 (c), images directly reconstructed by traditional GSAFT have the ghost image along the mechanical scanning direction, which can be successfully suppressed by the improved GSAFT in Figure 3- 10 (b) and Figure 3- 10 (d). In addition, the contrast and resolutions in Figure 3- 10 (b) have no noticeable

Table. 3- 2. Period calculations of ghost images in different array element spacing at 1 m target distance (Units: mm)

dt	λ/dt	Calculated ΔS	Simulated ΔS
6	0.2273	233.38	234
8	0.1705	172.99	174
10	0.1364	137.65	140
12	0.1136	114.38	116
16	0.0852	85.54	86

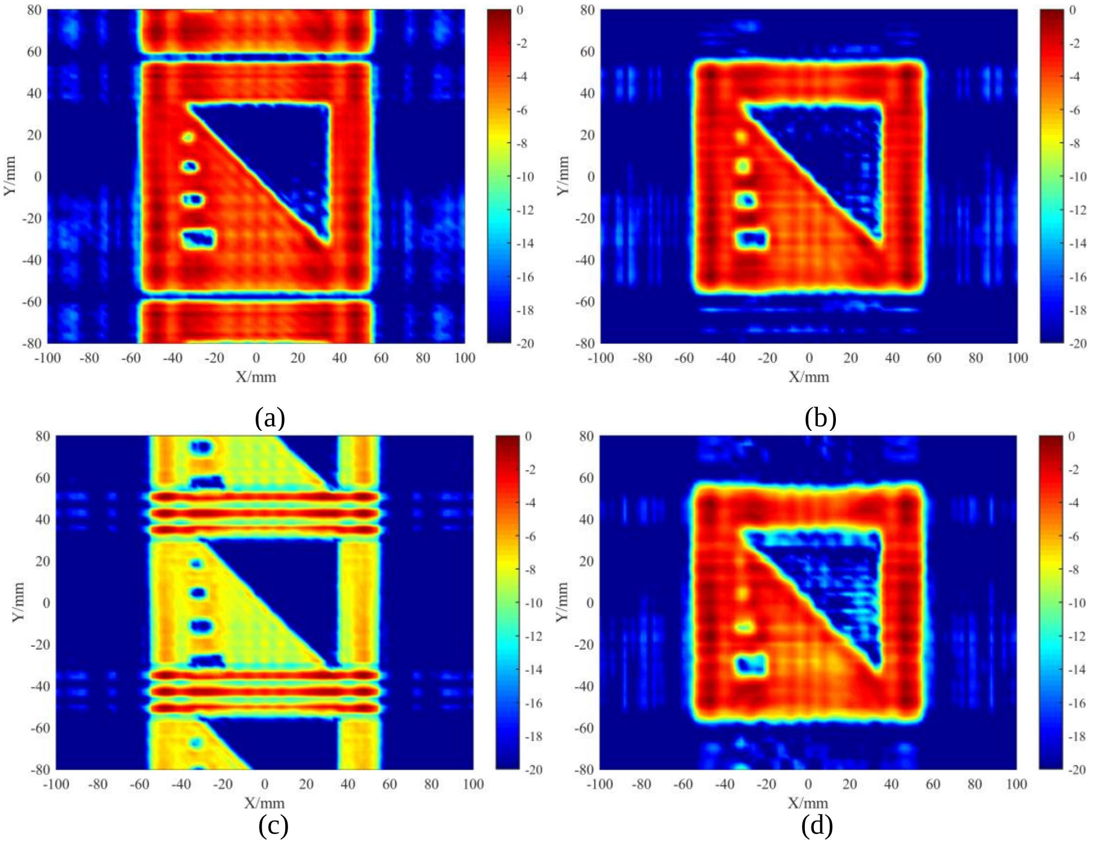

(a) (b)

(c) (d)

Figure 3- 10. Reconstructed images with 20-dB dynamic range of dt = 6 mm, dv = 6 mm (a) with traditional GSAFT (b) with the improved GSAFT and of dt = 6 mm, dv = 8 mm (c) with traditional GSAFT (d) with the improved GSAFT

deterioration but the number of mechanical scanning spots is reduced from 41 of scheme III in Table. 3- 1 to 27. If the number is reduced further to 21, real and pseudo target images will overlap a little (dt = 6 mm, dv = 8 mm), causing image to degrade too much as shown in Figure 3- 10 (c), but the improved GSAFT approach can still help to reconstruct the target image successfully as shown in Figure 3- 10 (d).

Secondly, we have kept mechanical scanning spacing of *dv* = *6* mm unchanged and studied the effect of array element spacing **dt** by increasing it to 8 mm (5.87λ), 10 mm (7.33λ) and 12 mm (8.80λ), respectively. The reconstructed images with both algorithms have been compared in Figure 3- 11. Similarly, the ghost images arise and can be suppressed well with the improved GSAFT algorithm [10, 11]. Comparing Figure 3- 11 (b) and Figure 3- 11 (d) with Figure 3- 10 (b), it is seen that the horizontal spatial resolution increases with the increase of element spacing since both the real and effective array aperture are lengthened, but the artifacts(strips) are enhanced as well. In addition, it is demonstrated from Figure 3- 11 (f) with the array element spacing of 12 mm (8.80λ) that the real target can still be recognized in the extreme situation where the real target image is tightly surrounded by the pseudo target images having the comparable quality .

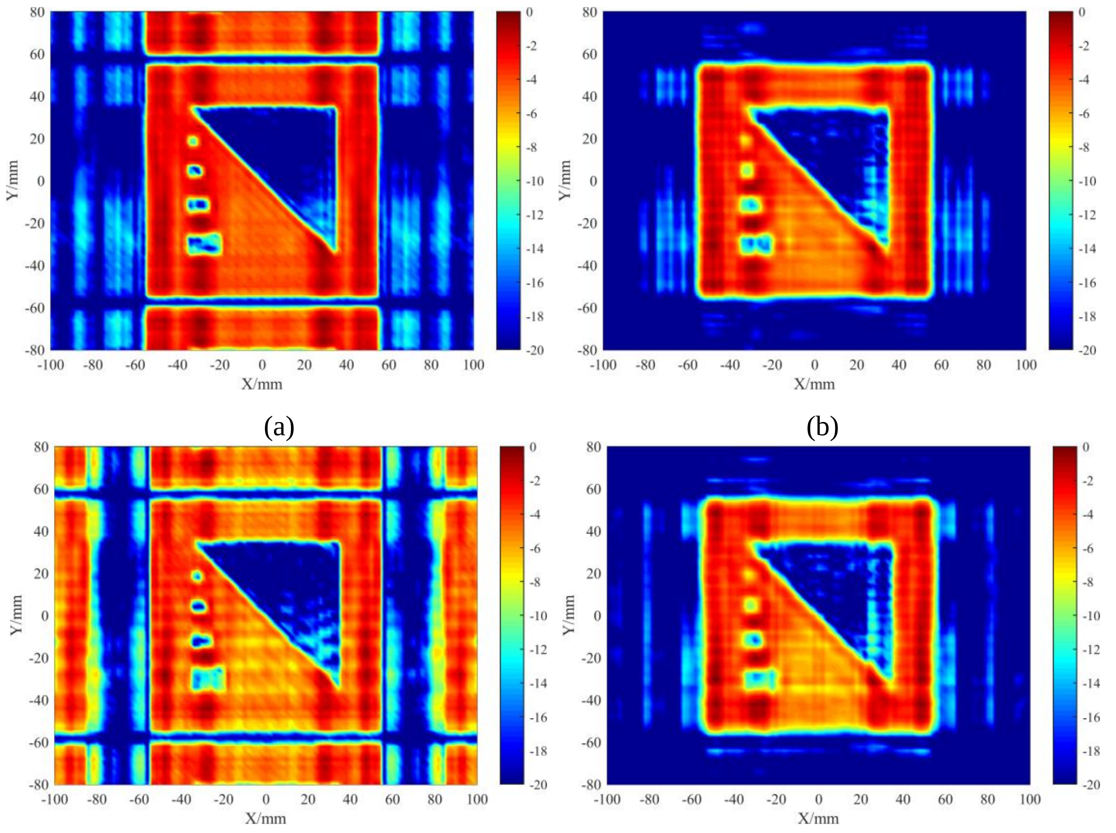

(a)

(b)

(c)

(d)

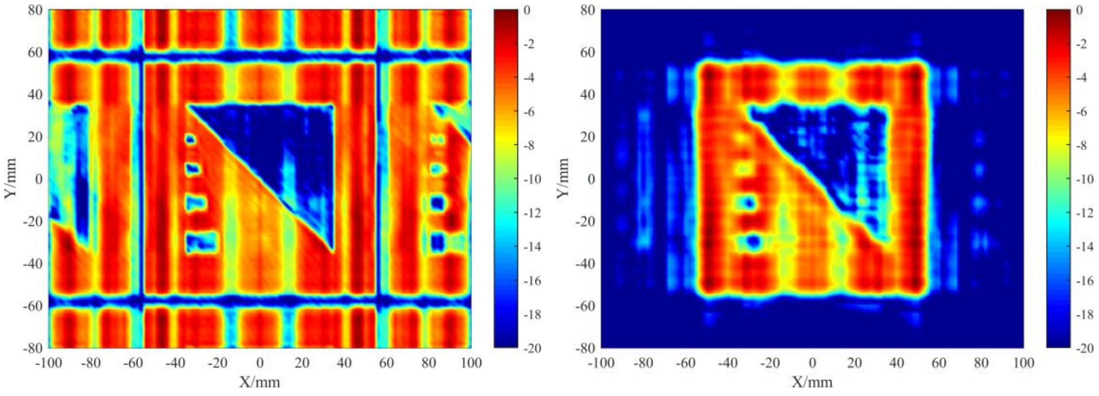

(e) (f)

Figure 3- 11. Reconstructed images with 20-dB dynamic range of dt = 8 mm, dv = 6 mm (a) with traditional GSAFT (b) with the improved GSAFT, of dt = 10 mm, dv = 6 mm (c) with traditional GSAFT (d) with the improved GSAFT and of dt = 12 mm, dv = 6 mm (e) with traditional GSAFT (f) with the improved GSAFT

In the aforementioned simulation studies, it is shown that the ghost images caused by employing large spacing of mechanical scanning steps can be effectively suppressed. Then, we have conducted advanced simulations of wideband imaging of more realistic targets, further assessing such a THz imaging system.

3.2.3. Wideband 3D Imaging Test

In practical application, we prefer to three dimensional (3D) image rather than 2D flat image that helps to identify the target/weapons. Therefore, we have roughly studied how to achieve a 3D image with the wideband operation in simulation. The target in this simulation has the same shape as Figure 3- 4 (a) but with a thickness of 20 mm, placed 1 m far away from the scanning plane. In addition, it requires a 15 GHz bandwidth in order to achieve a 10 mm range-resolution according to $c/2B$ in equation (2- 13). Therefore, the operating frequencies in the simulation are in the band of 210 – 230 GHz with an interval of 1.25 GHz, which is much larger than the interval of 75 MHz required by the frequency sampling criterion of equation (2- 12) to save computational time. The SPA consists of 6 Tx and 10 Rx with the Tx element spacing **dt** of 6 mm and the mechanical scanning spacing **dv** is 6 mm same with the scanning scheme in Figure 3- 10 (a). Besides, 27 vertical sampling points are recorded at each operating frequency, so theoretical resolutions derived from equation (2- 23) are 3.79 mm and 4.37 mm along horizontal and vertical directions, respectively. According to 3D imaging algorithm in equation (2- 17), thickness of target can be obtained and three views of target image are shown in Figure 3- 12. In Figure 3- 12 (a), we found that 20 mm thickness of the target has been clearly indicated. Figure 3- 12 (b) has shown a higher resolution compared to previous single frequency imaging consequently the smallest hole can be clearly identified. However, the surfaces and edges in the reconstructed image are not smooth. That is because the sampling frequency points in this simulation are much less than required by the criterion. Besides, Figure 3- 12 (c) implies that the image along the mechanical scanning Y- direction has shown a better image quality than the electronic scanning X- direction of the array.

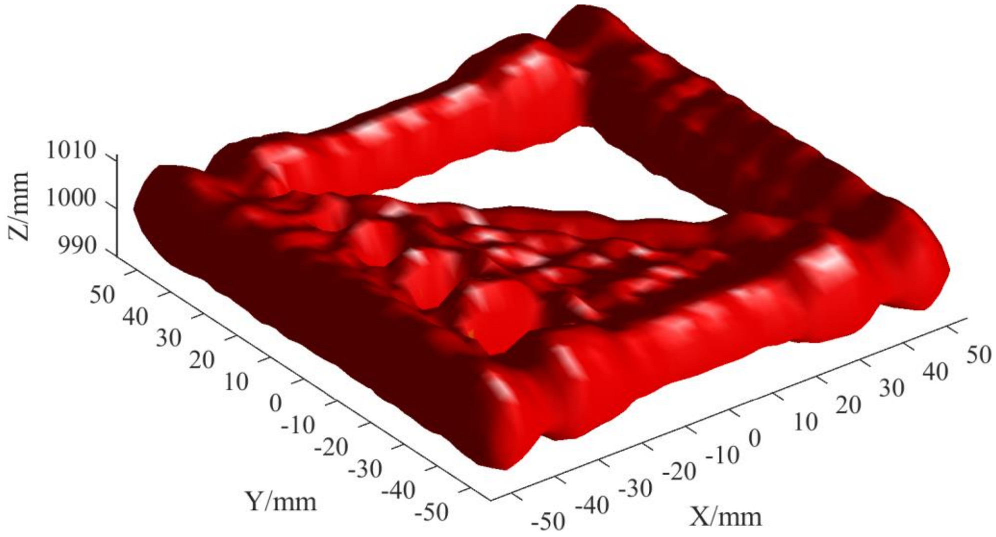

(a)

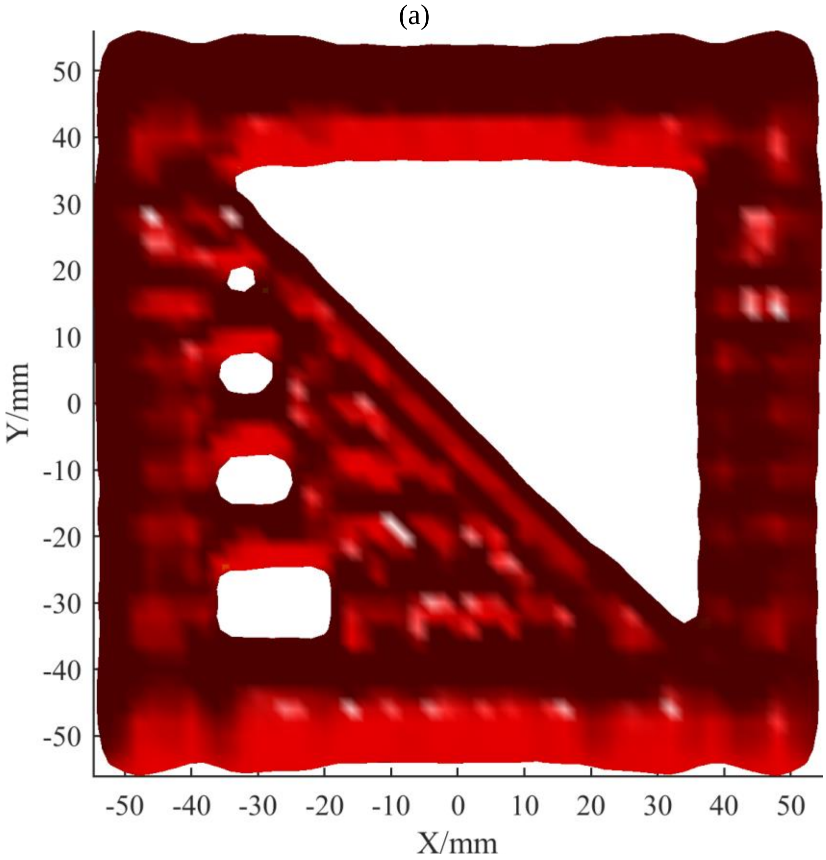

(b)

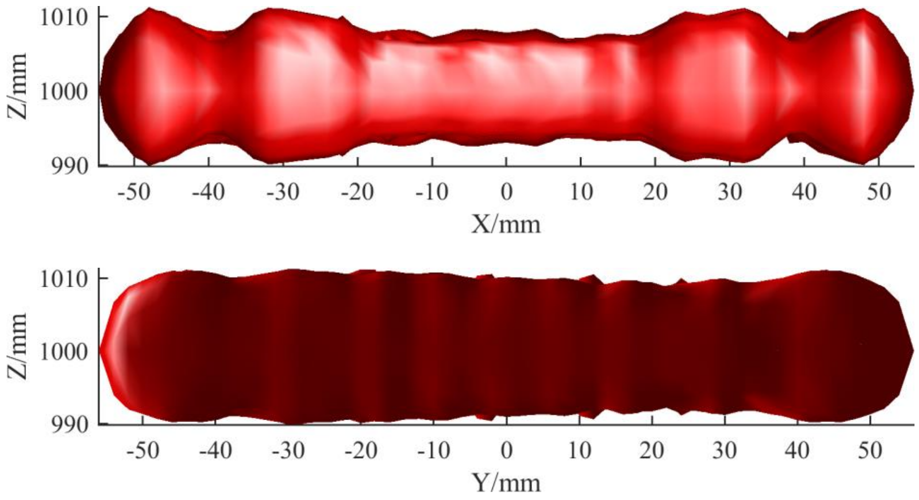

(c)

Figure 3- 12. Three views of the reconstructed 3D Image. (a) Perspective view (b) Top view and (c) Side view

3.2.4. Targets with Wide Width and Curved Surface

In addition to the aforementioned small and flat targets, we have investigated the imaging on a wide target as wide as a human body and target having a curved surface that is more like a human body. Besides the default MLFMM solution dealing with long free space, local solutions of physical optics (PO) or large element physical optics (LE-PO) are adopted on the targets to save computational time.

Firstly, pure metallic target with a 0.8 m width has been tested in the imaging simulation. The SPA consisting of 14 Tx and 16 Rx with a spacing dt = 7 mm is utilized and horizontally placed as schematic Figure 2- 6 (a), so real array length Lt is 833 mm, and its effective sampling length (FOV on a flat target) is 784 mm. The vertical mechanical scanning spacing is as large as 6 mm and only 81 scanning points are recorded. Therefore, theoretical horizontal and vertical resolutions are 3.48 mm and 5.68 mm at a target distance of 4 m, respectively, calculated by using equation (2-23). The targets, the reconstructed images in linear and decibel units are compared in Figure 3- 13. As we can see, the reconstructed image in the central area has the best quality so the smallest slots with dimensions of 3 mm × 5 mm is clearer. It degrades at two edges since the phase shift increases, as implied in Figure 2- 11, but the slots with dimensions of 5 mm × 7 mm have been still resolved very well. In addition, the reconstructed image beyond the FOV (784 mm) is deteriorated obviously, agreeing with our previous observation. In summary, the results are consistent with the anticipation, demonstrating that the SPA can be built into a large array for imaging a large-scale target.

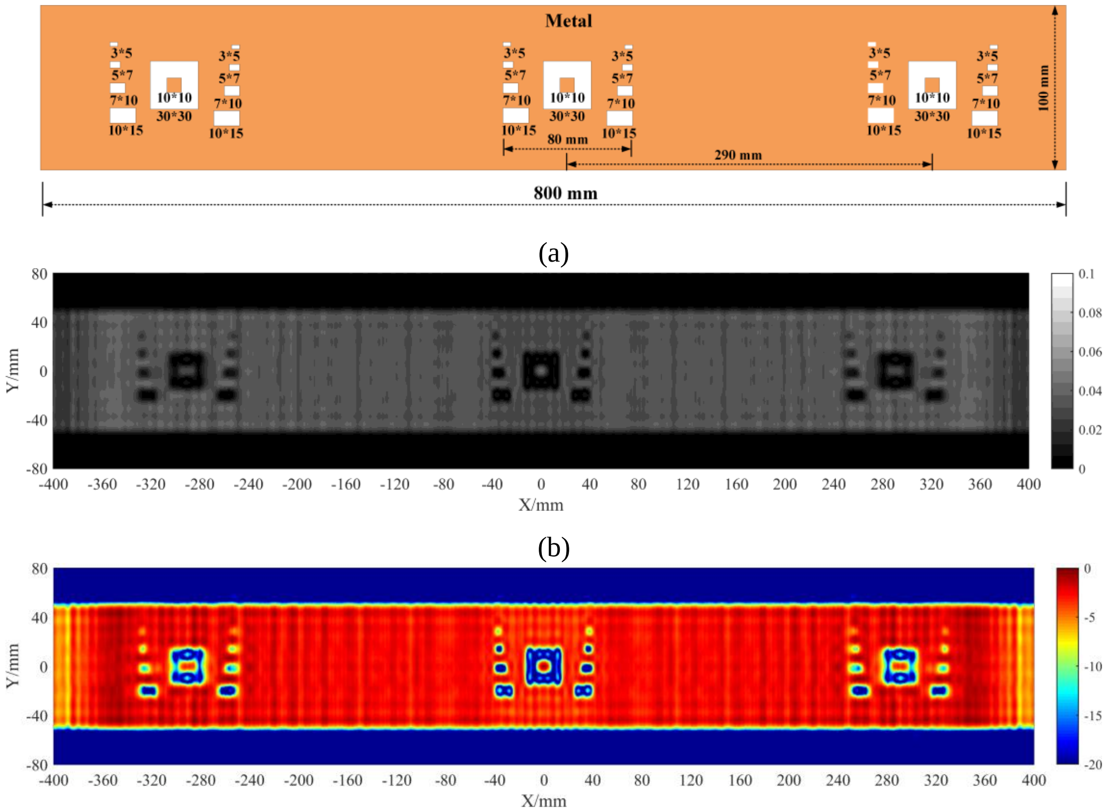

(a)

(b)

(c)

Figure 3- 13. Wide metallic flat target. (a) Drawing and reconstructed images in (b) linear (c) decibel units

Secondly, the surface of human body is not as flat as a mirror. The curved surface of human body will reflect the incident beams to different directions from the incident path according to the angle of arrival and the curvature. Therefore, it is necessary to study this effect before we build the real imaging system. However, the linear sparse periodic array can have two possible placements to the curved target. One is as shown in Figure 2- 6 (a) that the array is placed horizontally so it is parallel to the curved surface. But the other one is shown in Figure 2- 6 (b) that the array is placed vertically so it is perpendicular to the curved surface. Therefore, we have conducted simulation of both schemes, showing the results as follows.

One linear sparse periodic array consisting of 14 Tx and 16 Rx elements is placed on a plane as shown in Figure 2- 6 (a) to illuminate a target at a distance of 4 m. The SPA has a length of 595 mm with a 560 mm effective sampling length (practical FOV), and the mechanical scanning length is 564 mm. Two different configurations of forwarded Tx orientation and 4° inward tilted Tx orientation have been simulated. The

4° is the half of angle subtended by the target width, equalling to $\tan^{-1}(L/(2D))$ in which L is the width of the target and D is the target distance, as illustrated in Figure 3- 14 (a). Therefore, the main beams of titled Tx elements have been directed to the target centre. The details of the target and its reconstructed images with two different configurations have been shown in Figure 3- 14 (b), (c) and (d).

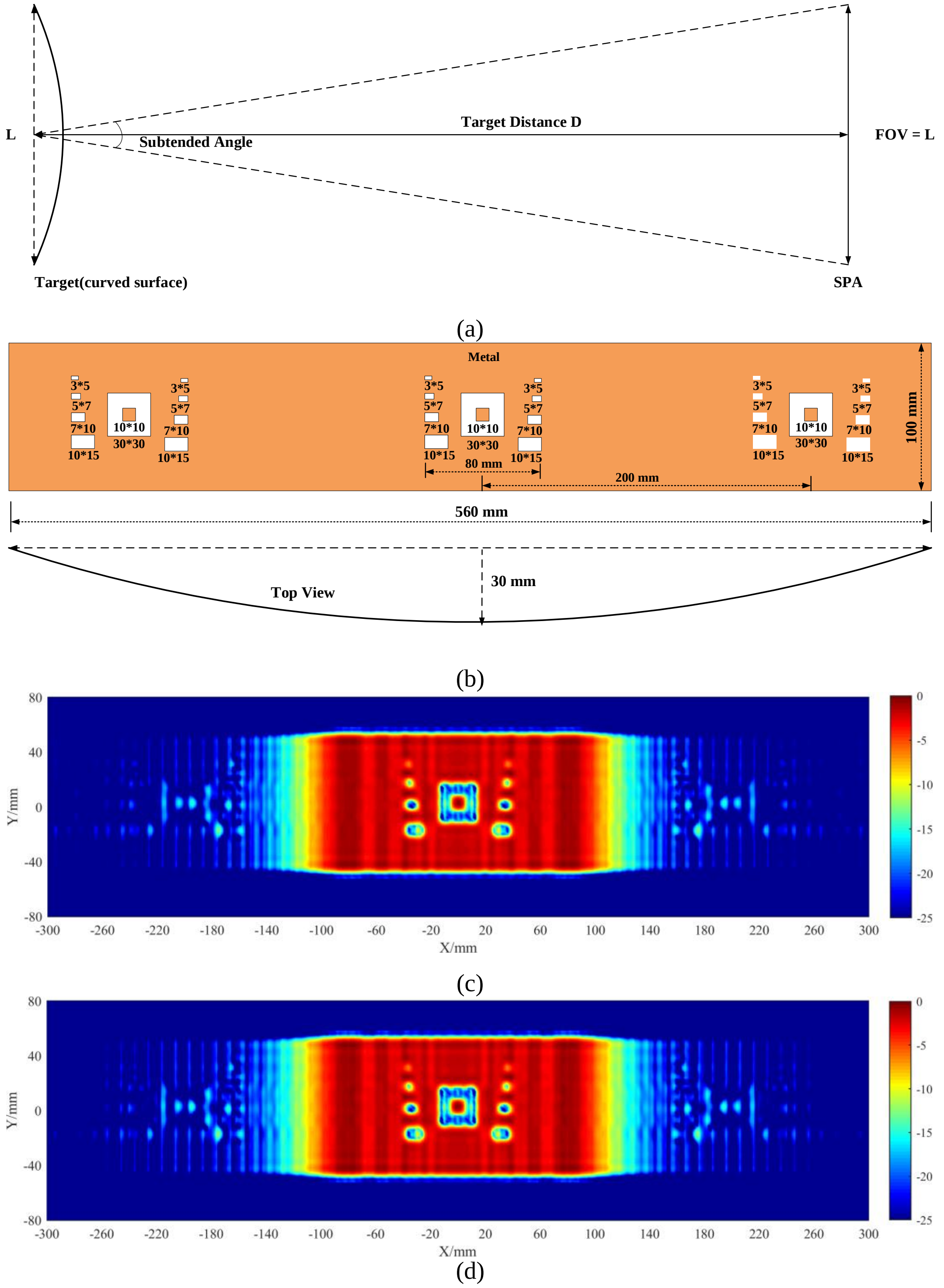

(a)

(b)

(c)

(d)

Figure 3- 14. (a) Imaging diagram (b) wide metallic target with curved surface, and its reconstructed images with 25-dB dynamic range having (c) forwarded Tx orientation and (d) 4° inward tilted Tx orientation

It can be found from the results in Figure 3- 14 that two edges of the target cannot be imaged. This can be explained by the method of ray tracing as illustrated in Figure 3- 15. In order to simplify the explanation, Tx and Rx positions are represented by one, but the principle based on ray tracing applies to the separated Tx and Rx positions too. Since the target has a curved surface, the receiver placed at the point **A** can only pick up the echo data from left side of target point **B2** instead of left side of target **B1** that is the edge of effective sampling length (FOV on a flat target). Therefore, the SPA that has a 560 mm FOV on a flat target can only record data within the aperture shorter than 560 mm. Besides, since the practical field of view (FOV) depends on the target distance, surface curvature of the target and the characteristics of receivers including positions, beam-width and orientations, only 4° inward tilted angle Tx cannot help to broaden the FOV, as compared in Figure 3- 14 (b) and Figure 3- 14 (c).

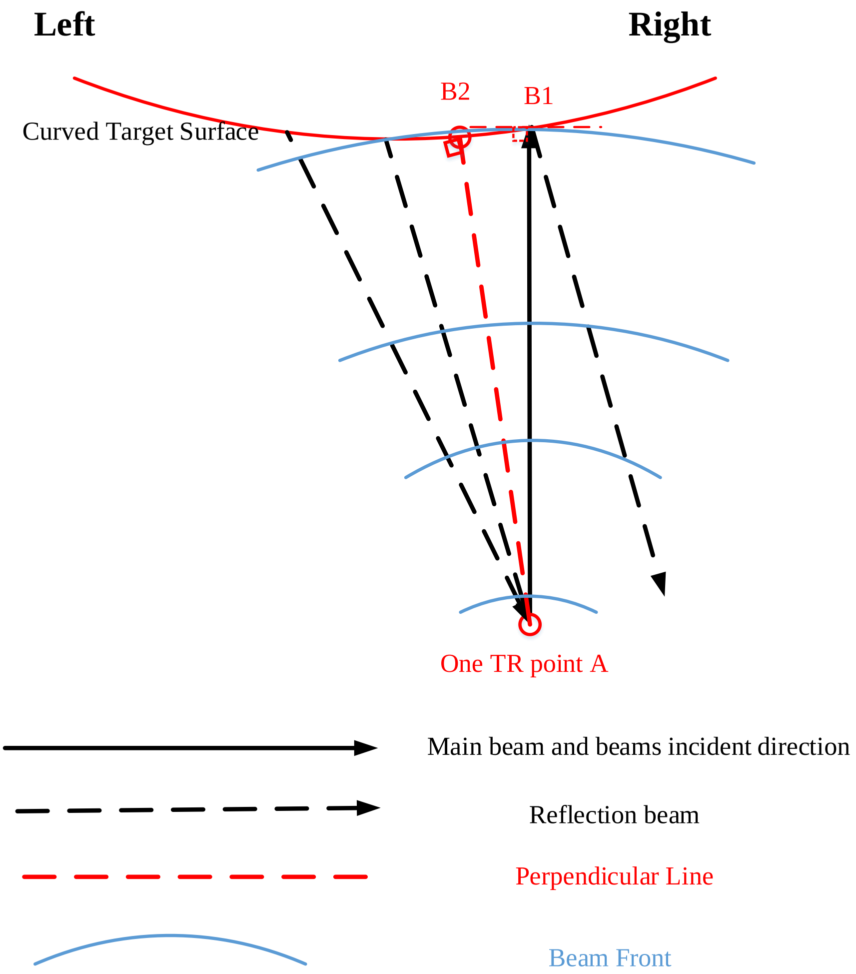

Figure 3- 15. Ray tracing of the illumination and reflections of the target with curved surface

In comparison, the same SPA placed as scheme in Figure 2- 6 (b) has also been simulated. The angle interval along mechanical scanning direction in simulation is 0.07 degree that corresponds to about 4.89 mm at a target distance of 4 m, the same scanning aperture about 560 mm × 560 mm has been undertaken for comparison. Besides, the difference of directly forwarded beams named scheme 1 in Figure 3- 16 (a) and output beams with tilted incident angels named scheme 2 in Figure 3- 16 (b) has been investigated. The SPA scanning path of both schemes in simulation is a circle arc with radius of 4 m. The curved surface of both schemes in simulation is an elliptical arc with minor axis of 60 mm and major axis of 560 mm as shown in Figure 3- 14 (b).

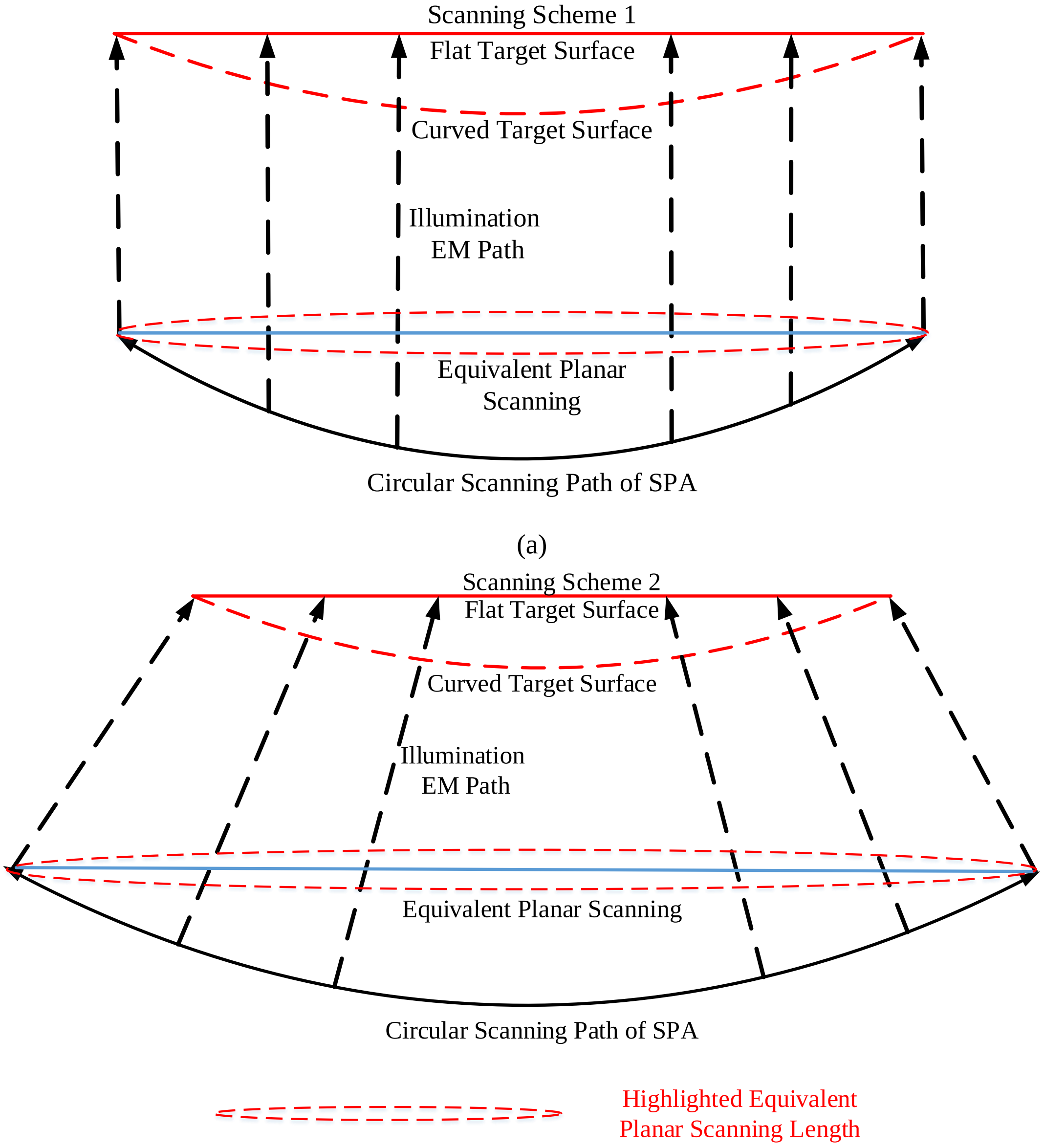

(b)

Figure 3- 16. Illustrations of cylindrical scanning system of (a) scheme 1 (b) scheme 2

Specifically, the central axes of elements are perpendicular to the flat surface in scheme 1 while they are perpendicular to the circle-scanning path rather than the curved surface (the curvatures of target surface and circle-scanning path are different) pointing to the circle center in scheme 2. Therefore, it is seen that this circular scanning path cannot help to broaden the FOV in this simulation due to the limited scanning aperture, as shown in Figure 3- 17 of reconstructed images for these two configurations. Similar to previous study on scheme of Figure 2- 6 (a), only part of target can be imagined due to the curved surface although the mechanical scanning aperture is 560 mm. In addition, there is no obvious improvements of titled illumination in scheme 2 due to single frequency imaging operation and different curvatures between target surface and scanning path.

Therefore, the imaging system as shown in Figure 2- 5 or any quasi-optic imaging systems achieving the scanning by rotating the reflectors will face a problem of missing reflection from the target when the rotating reflector is rotated so that the incident and reflected beams are tilted. This limits its imaging performance like image quality or field of view (FOV), which has been demonstrated in the references [12-14].

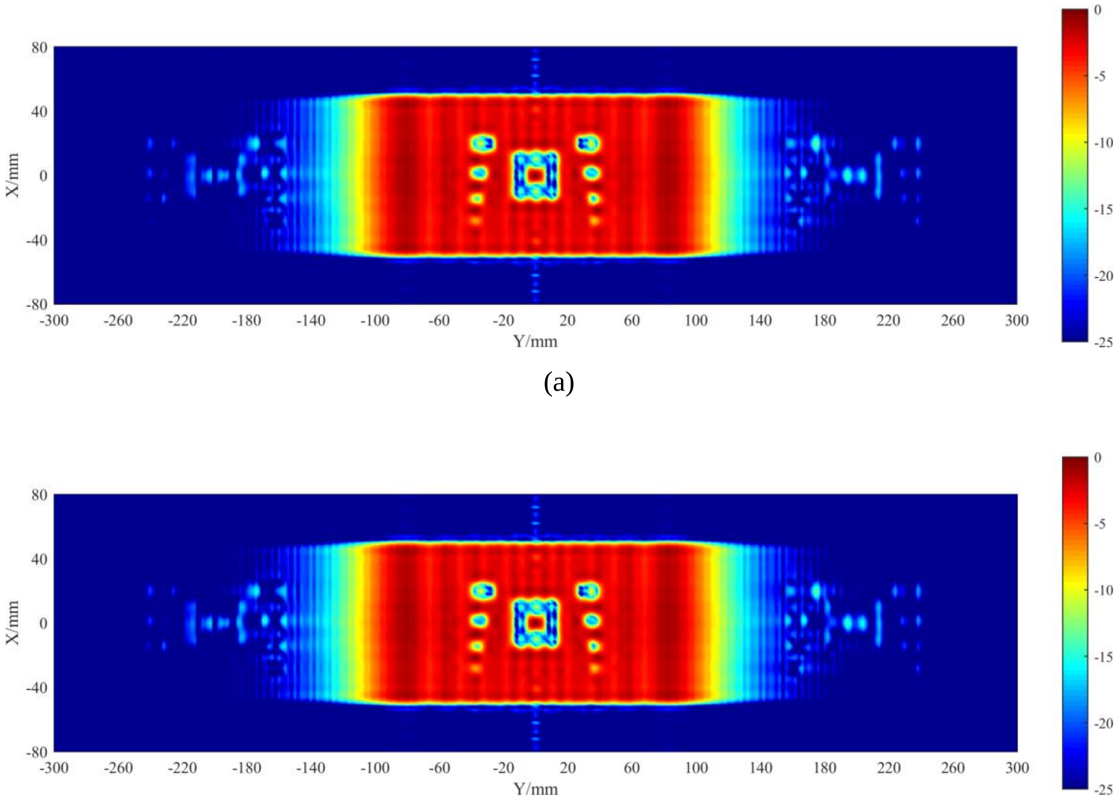

(a)

(b)

Figure 3- 17. Reconstructed images with 25-dB dynamic range of (a) scheme 1 and (b) scheme 2

3.3. Assessment of the Proposed Imaging Scheme on Body Model

3.3.1. 220 GHz Imaging of Body Chunk

The imaging performance of the proposed multi-static SPA-THz imaging system has been widely studied in above comprehensive simulations. Finally, we desire to take account of human body effects using more realistic target model in the simulation. Since now targets become more complicated and PO algorithm is not supported for dielectric, hybrid simulation method in the FEKO^{TM} of method of moments (MOM) and ray launching geometrical optics (RLGO) on the target is chosen to save PC resource. To save computational time, we have firstly simulated some metallic patches on a chunk of human body phantom (800 mm × 100 mm × 5 mm) as shown in Figure 3- 18 with a relative permittivity of 5.3 and a loss tangent of 0.75 at 220 GHz which are provided by GRASP (General Reflector Antenna Software Package) technical support at TICRA Provider. It is worth mentioning that these values should vary on operating frequency if wideband imaging is adopted.

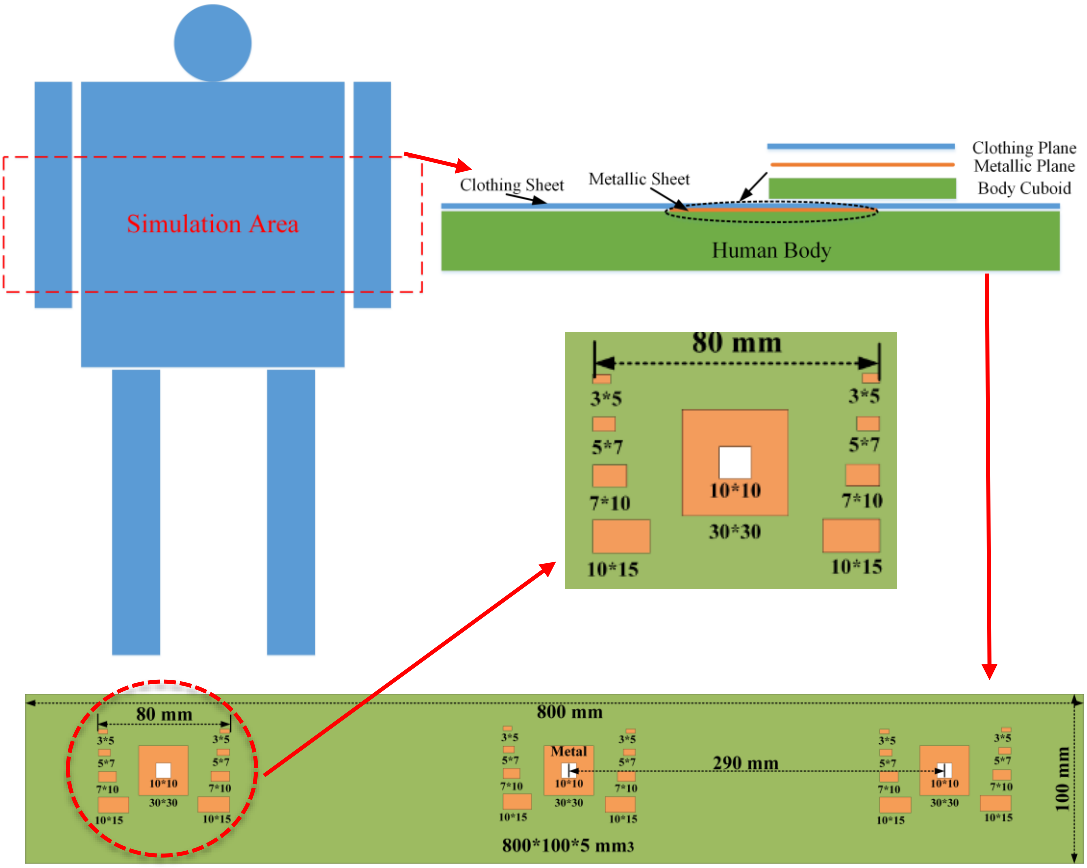

Figure 3- 18. Metal targets in front of a chunk of human body phantom (800 mm × 100 mm × 5 mm)

The SPA utilized in this simulation consists of 14 transmitters and 16 receivers with a transmitter element spacing of 7 mm (5.13λ). So it has a real aperture length of 0.833 m and a 0.784 m wide FOV on a flat target, which is supposed to achieve a theoretical resolution of 3.5 mm at 4 m. Moreover, the simulation set-up is same as Figure 2- 6 (a) where the planar scanning has been used and the SPA is placed horizontally. The vertically mechanical scanning interval is set as 12 mm (8.80λ), and 41 scans are recorded, which thus can provide a 5.68 mm vertical resolution. Both resolutions have also been verified by the simulated point spread function (PSF) in Figure 3- 19. It is worth mentioning that more dense scans are required in the practical application for imaging a taller target. Besides, we have also simulated the imaging of the target concealed under a thin (Nylon-610) clothing of 0.5 mm with a relative permittivity of 2.84 and a loss tangent of 0.012 based on the FEKO^{TM} material library.

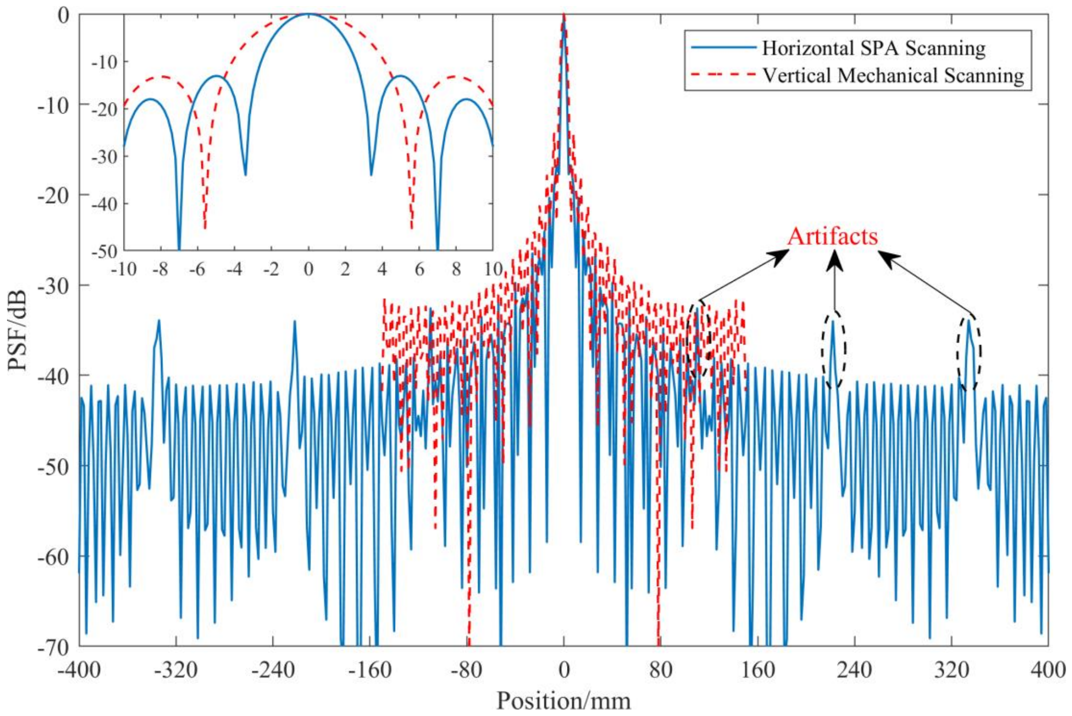

Figure 3- 19. Simulated PSF along two directions of the scheme configuration

The image of the exposed metallic patches on the human body chunk is reconstructed by the improved GSAFT reconstruction method, as shown in Figure 3-20. It has demonstrated that the smallest patches can be distinguished in the central part of image, indicating a horizontal resolution of 3.5 ^{mm} achieved. However, the resolution is getting poorer towards the two edges of the image because phase shift rises [15]and the FOV (0.784 m) is narrower than the width of body chunk. Regarding the concealed target underneath a thin clothing, the reconstructed image has been shown in Figure 3- 21. We can see the image contrast being improved when comparing it to the Figure 3- 20, because the relative permittivity and loss tangent of the thin (Nylon-610) clothing are lower.

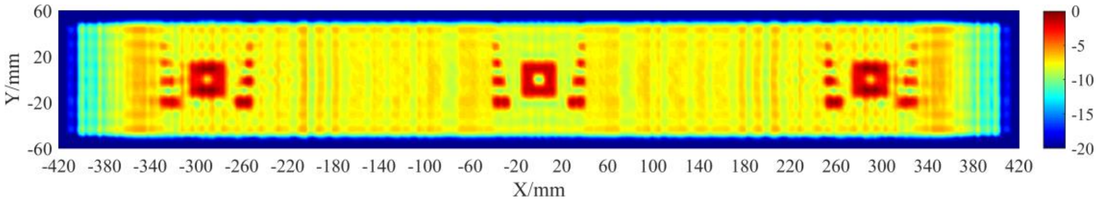

Figure 3- 20. The image of metallic targets and human body surface reconstructed by the improved GSAFT reconstruction method (20-dB dynamic range)

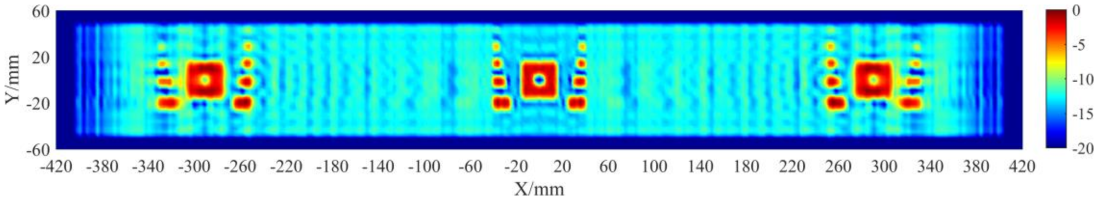

Figure 3- 21. The image of metallic targets and human body surface concealed underneath a thin (Nylon-610) clothing (800 mm × 100 mm × 0.5 mm) reconstructed by the improved GSAFT reconstruction method with full data (20-dB dynamic range)

3.3.2. 94 GHz Imaging of Body Chunk and Full Body Model

The imaging simulation operating at 94 GHz has been carried out in comparison. Since wavelength increases, the larger spacing subject to wavelength allows reduction in array elements as well as mechanical scanning points. For example, in order to achieve 0.825 m width of FOV, there are only 10 transmitting (Tx) antennas and 11 receiving(Rx) antennas placed horizontally as Figure 2- 6(a) with Tx element spacing of 15 mm (4.70λ). The array element in simulation has a 3 dB HPWB of 42° with a peak gain of 12.78 dB as shown in Figure 3- 22 so the theoretical resolution is 7.75 mm at 4 m target distance predicted by array effective aperture of (2- 23). The target in the simulation is the same one in 220 GHz imaging simulation shown in Figure 3- 18 except for a relative permittivity of 5.79 and a loss tangent of 1.29 at 94 GHz for chunk model derived from online database [16]. The images of targets exposed to the air or concealed underneath a 0.5 mm thick clothing (Nylon-610) have been shown in Figure 3- 23. From the results, it is seen that the theoretical resolution has been achieved because the second smallest patches with dimensions of 5 mm × 7 mm can be identified. The image quality including resolution and contrast degrades a little due to low operating frequency but the number of array elements/channels is also reduced.

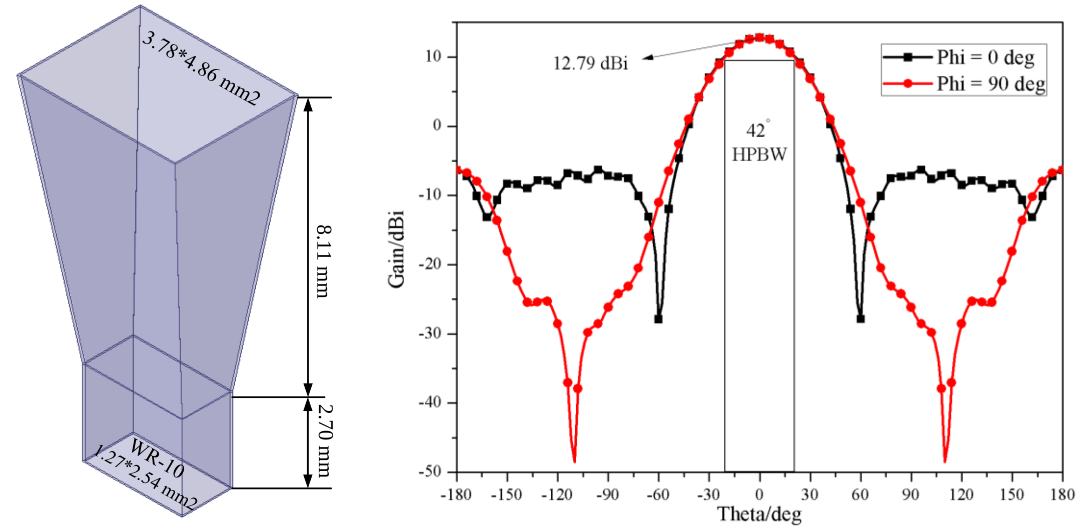

Figure 3- 22. Geometry and radiation pattern at 94 GHz of the pyramidal horn

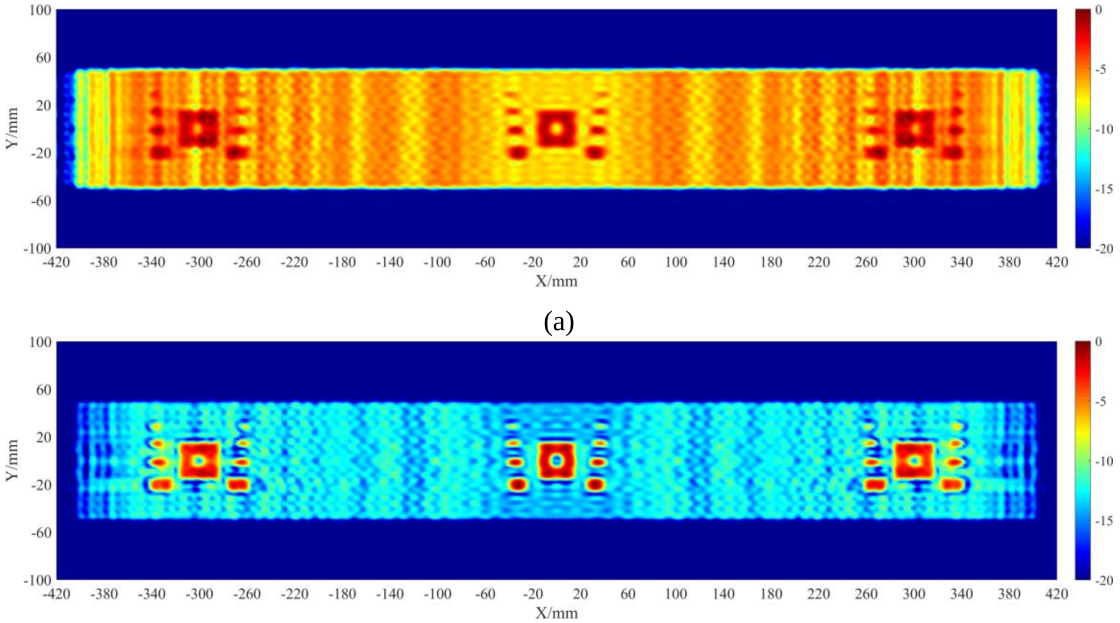

(a)

(b)

Figure 3- 23. Results of 94 GHz imaging simulation with 10 Tx and 11 Rx placed horizontally that are reconstructed by the improved GSAFT reconstruction method (20-dB dynamic range). The images of metallic targets and human body surface (a) directly exposed to the air or (b) concealed underneath a 0.5 mm thick (Nylon-610) clothing (800 mm × 100 mm × 0.5 mm)

Furthermore, the larger arrays with 14 Tx and 16 Rx elements have been investigated. The first large array has Tx element spacing of 7.366 mm so that it is capable of providing a resolution of 7.75 mm at 4 m target distance same as last small array. The corresponding reconstructed image based on simulated data is shown in Figure 3- 24 (a), which do not show an improvement compared with Figure 3- 23 (a). The Tx element spacing in the second large array increases to 15 mm so the FOV width is 1.68 m and the theoretical resolution is 3.81 mm at 4 m target distance predicted by array effective aperture of equation (2- 23). The corresponding reconstructed image is shown in Figure 3- 24 (b). The contrast and resolution have been improved in this configuration but non-uniform ripples are obvious.

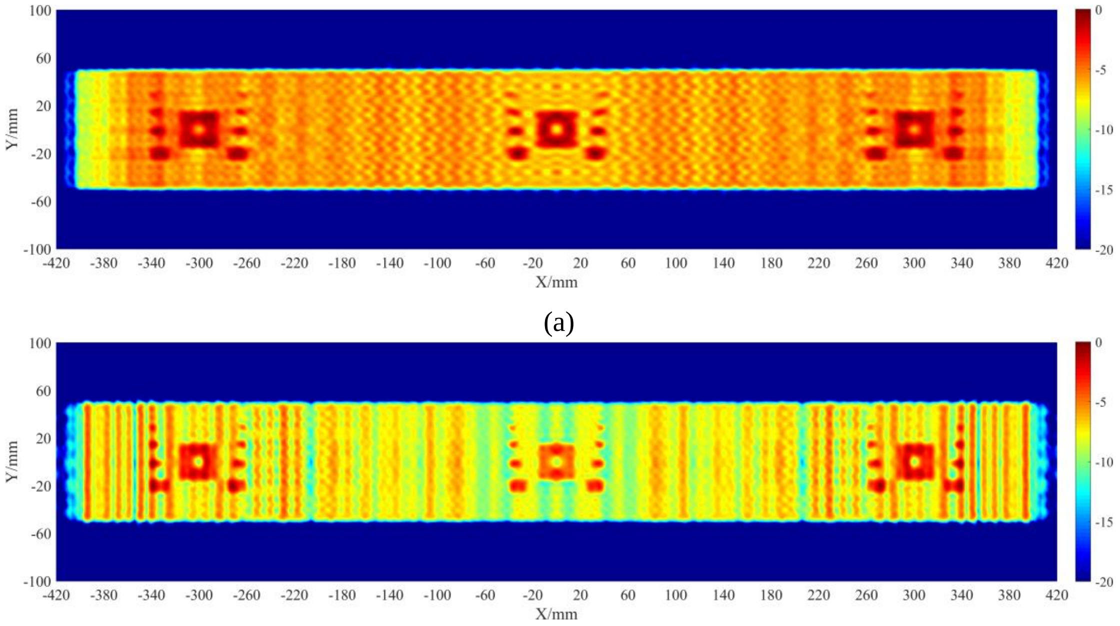

(a)

(b)

Figure 3- 24. Results of 94 GHz imaging simulation with 14 Tx and 16 Rx placed horizontally that are reconstructed by the improved GSAFT reconstruction method (20-dB dynamic range). Tx Element Spacing of (a) 7.366 mm and (b) 15 mm

In contrast, the imaging scenario using the set-up of Figure 2- 6 (b) has also been studied in which the last second larger SPA in Figure 3- 24 (b) is placed vertically. The physical array length is 1.785 m with a 1.68 m FOV (on a flat target). The target in the simulation, as shown in Figure 3- 25 (a), is 5 sets of metallic patches on a column of human body phantom (1600 mm × 100 mm × 5 mm) that has a relative permittivity of 5.79 and a loss tangent of 1.29 at 94 GHz obtained from online database [16]. The 15 mm transmitter element spacing leads to a 0.873 m period of ghost images, which is smaller than the target height of 1.6 m so the reconstructed images will overlap. Thus, reconstructions of using the traditional and improved GSAFT reconstruction algorithms have been compared in Figure 3- 25 (b) and Figure 3- 25 (c). The results have shown that the target image, as expected, deteriorates since ghost images have overlapped, but this issue can be significantly alleviated by using the improved GSAFT algorithm we proposed [17]. Besides, the sampling interval of circular scanning is 0.3°, and data at 41 horizontal positions corresponding to about 0.838 m width at 4 m are recorded for the image reconstruction. Thus, theoretical 3.80 mm and 7.64 mm resolutions along vertical and horizontal directions can be derived by equation (2- 23), which have been also implied by the point-spread functions (PSFs) in

Figure 3- 26. The slot of 5 mm × 7 mm in Figure 3- 25 (c) can be identified at a 4 m target distance, which verifies the theoretical resolutions.

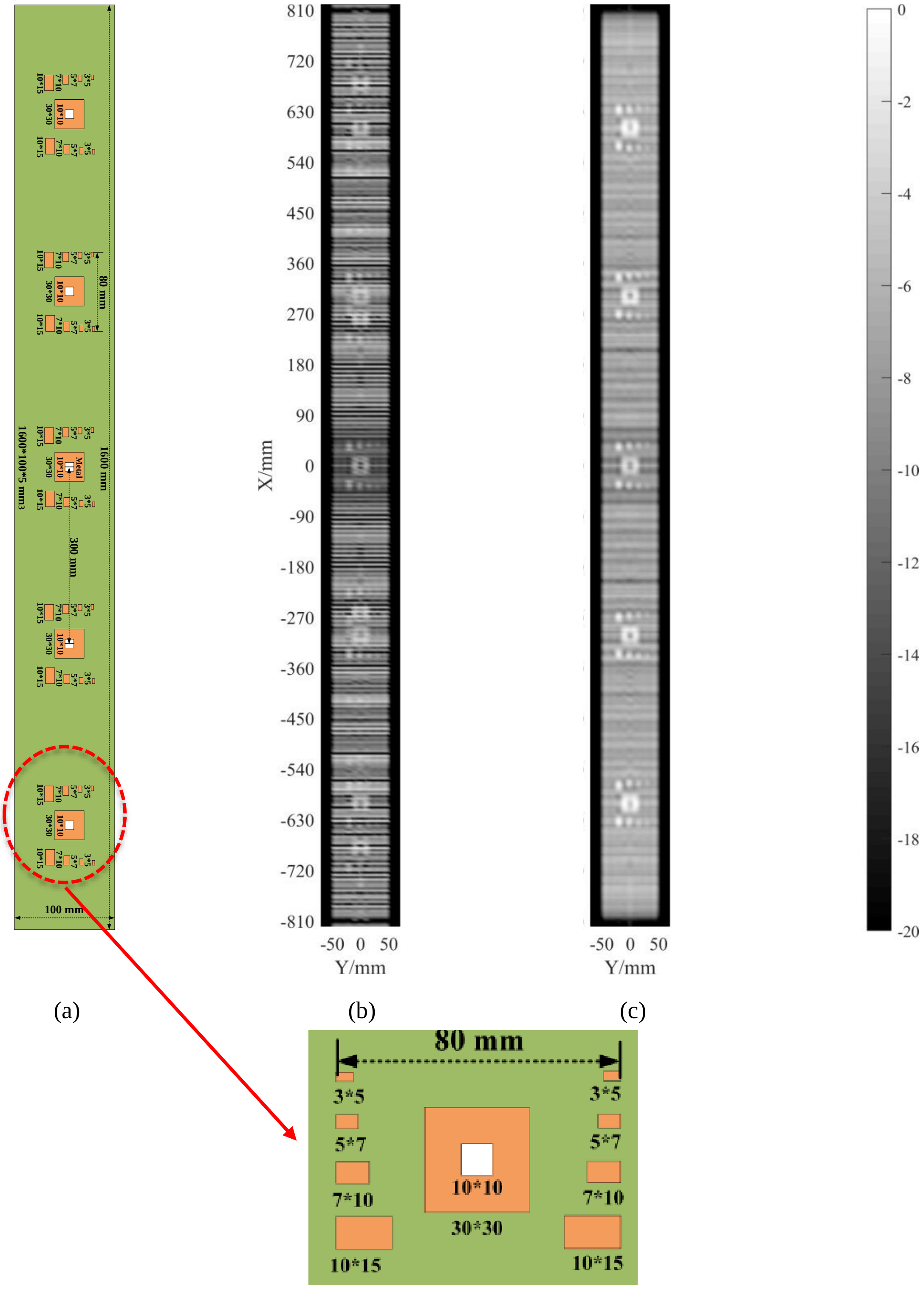

Figure 3- 25. Target (a) drawing and images with 20-dB dynamic range reconstructed by (b) traditional and (c) improved GSAFT reconstruction algorithms

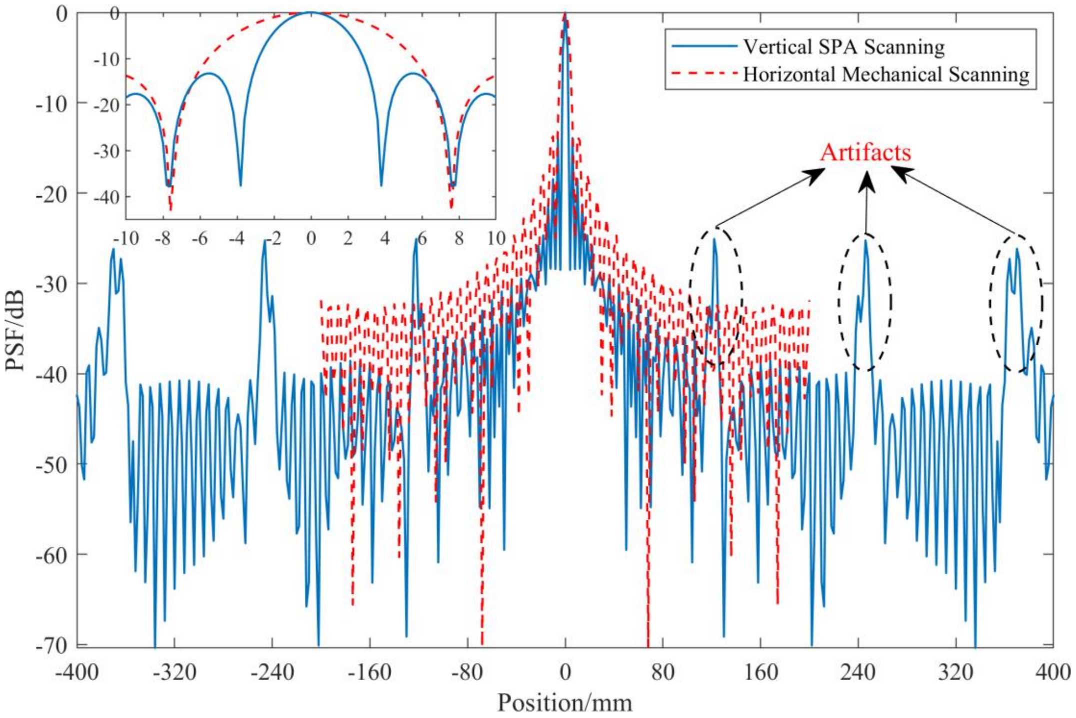

Figure 3- 26. PSFs of vertical SPA scanning and horizontal mechanical scanning

In addition, we have also conducted the simulation on a full body model with a flat surface. The model is 4 m far away from the scanning plane, having a total dimension of 0.8 m × 1.7 m × 0.005 m. The full body models having metallic patches placed in the central and left side have been shown in Figure 3- 27. The number of mechanical scanning in simulation is 237 and the angle interval is 0.05625° corresponding to 3.925 mm at 4 m distance. Therefore, theoretical resolutions along horizontal and vertical directions in this scenario should be 6.89 mm and 3.80 mm derived by equation (2- 23), respectively. The corresponding images reconstructed with the traditional and improved GSAFT reconstruction algorithms have been compared in Figure 3- 28. From the results, we can clearly identify the metallic patches on the body surface, which verifies the theoretical resolutions achieved. In addition, we can find that the improved GSAFT reconstruction method suppresses ghost images successfully as expected, this allows us to use larger array element spacing to reduce the array elements and related channels, saving the system cost.

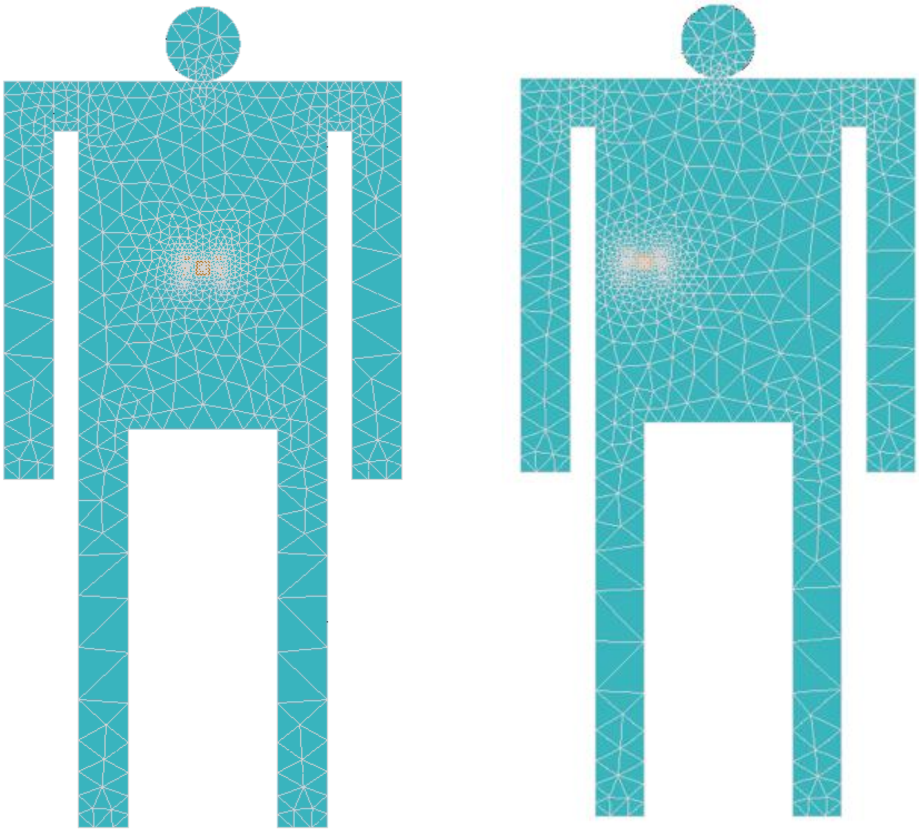

(a) (b)

Figure 3- 27. Models of full body with flat skin surface and metallic targets on the (a) center (b) left-side

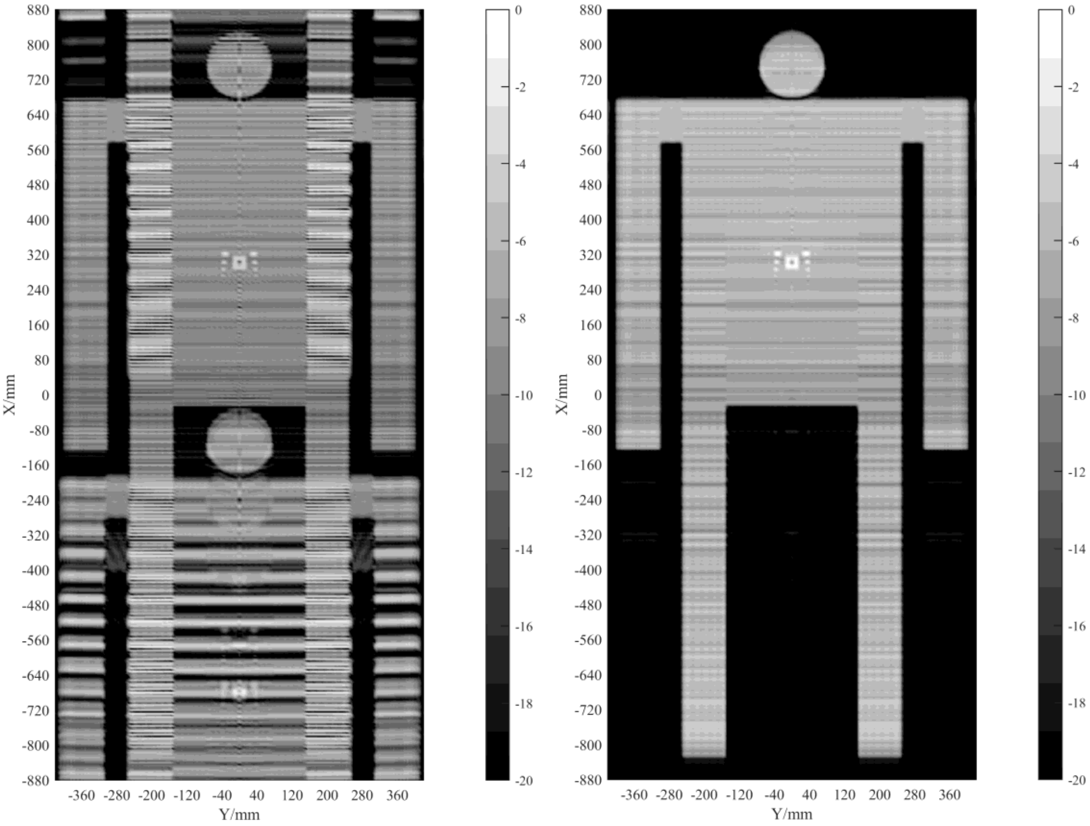

(a) (b)

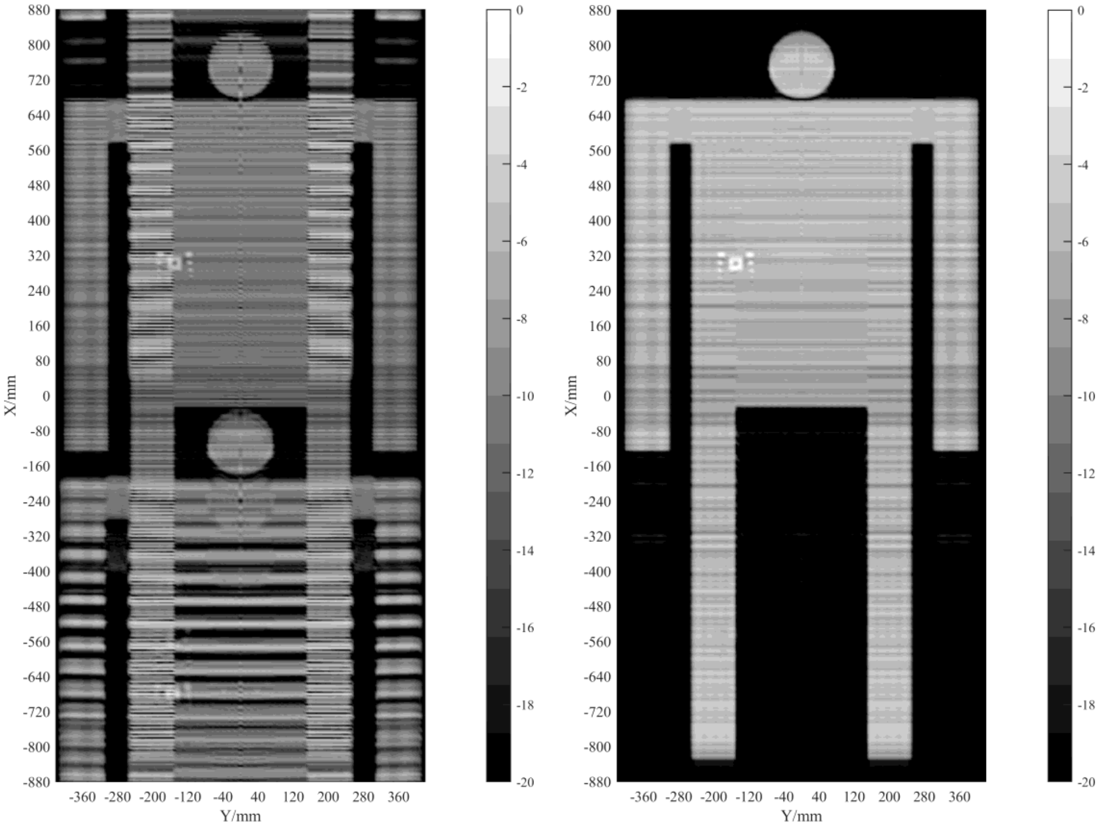

(c) (d)

Figure 3- 28. Reconstructed images with 20-dB dynamic range of flat surface body models having the metallic target in the center with (a) traditional and (b) improved GSAFT reconstruction algorithms or in the left side with (c) traditional and (d) improved GSAFT reconstruction algorithms

Finally, in our study in 3.2.4 and references [12, 14], we have already known that the curved surface or tilted incident angle deflect incident beams and the target cannot be fully reconstructed. Therefore, we have tested this effect again on a full human body model that partially has a curved surface, as shown in Figure 3- 29 (a). The angle interval of mechanical scanning is 0.05625° corresponding to 3.925 mm at target plane of 4 m distance. The body model and its reconstructed image have been compared in Figure 3- 29. We can see that the curved shin surface has not been fully reconstructed while two arms are reconstructed successfully. This result is same with our speculation based on the previous study in 3.2.4. It perfectly demonstrates that the curvature at two edges of curved surface deflects the incident beams away from the receivers while two arms in this model have a flat surface so they do not have this issue. There are solutions possibly to solve this problem: one is to rotate the T/R array over 180 degree as most commercial imaging products do, the other one is to place extra transmitters at sides of the array to make reflections from the curved surface propagate into the receivers [14].

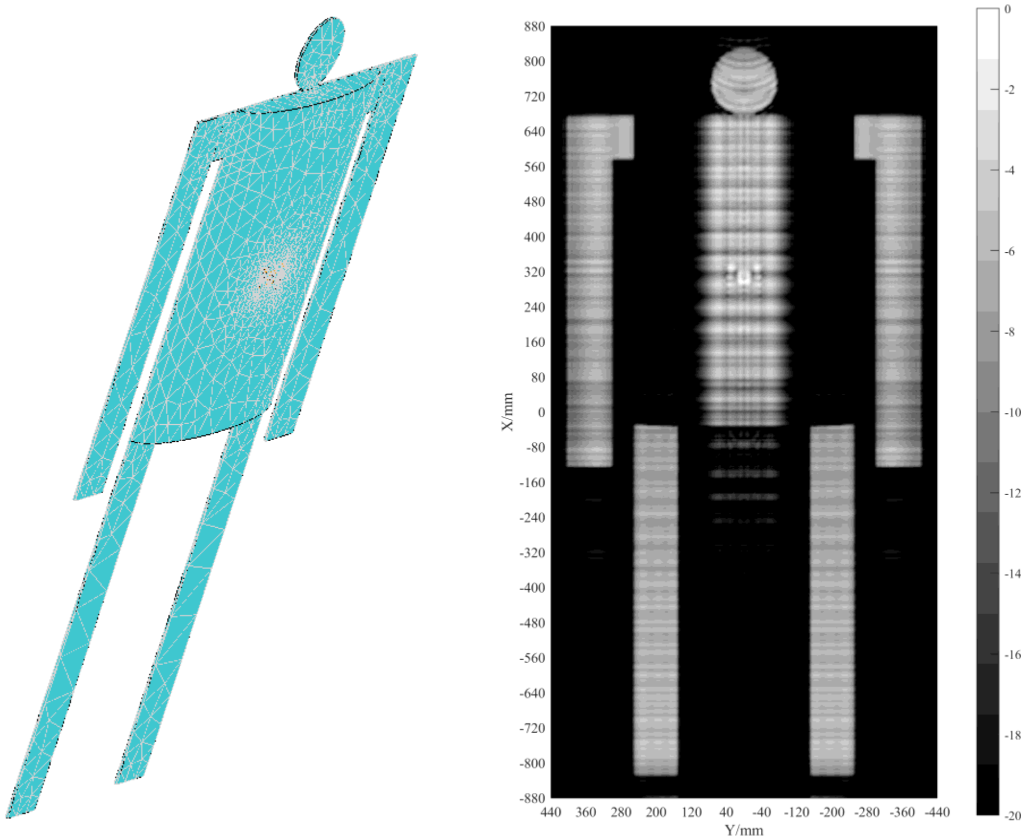

(a) (b)

Figure 3- 29. Full body of curved skin surface. (a) Model and (b) its image with 20-dB dynamic range reconstructed by using improved GSAFT algorithm

Therefore, based on the comprehensive simulation study above, the guidelines on designing this THz imaging system with a linear sparse periodic array can be summarized as follows.

Determine the scanning aperture according to the interested FOV, target distance and desired resolution with equation (2- 22) and (2- 23).

Derive the Tx element spacing and mechanical scanning interval with equation (3- 3) and (3- 4) to assure the ghost images not appear into the interested FOV, or this spacing can be increased if using the suppressing reconstruction algorithm we have proposed [11].

Calculate the number of array elements and mechanical sampling points according to the sampling spacing, interested FOV and desired resolution.

3.4. Summary

This chapter has firstly introduced the widely used solvers in electromagnetic simulation and the various simulation methods we used to deal with different imaging circumstances. Afterwards, the comprehensive simulation studies have been conducted to investigate the array configuration with different number, spacing of array elements, and different scanning paths, wideband 3D imaging and performance of imaging of more realistic targets. It has revealed the issue of the ghost images and effects of the targets on curved surface. We thus verified that the proposed improved GSAFT reconstruction algorithm is effective to suppress the ghost images. Besides, the complete imaging on the targets with a curvature can be achieved by using a sufficient scanning aperture or the extra transmitters.

Finally, we have conducted the simulations of imaging on a small body chunk and a full body model to verify the prosed imaging system thus derived the design guideline, demonstrating the superior imaging performance when using the proposed SPA imaging configuration.

3.5. References

[1] P. Sumithra and D. Thiripurasundari, "Review on computational electromagnetics," *Advanced Electromagnetics,* vol. 6, no. 1, pp. 42-55, 2017.

[2] Wikipedia. *Computational Electromagnetics*. Available: https://en.wikipedia.org/wiki/Computational_electromagnetics

[3] K. Sankaran, "Are you using the right tools in computational electromagnetics," *Engineering Reports,* vol. 1, no. 3, p. e12041, 2019.

[4] *CST Studio Suite*. Available: https://www.CST.com

[5] *FIT*. Available: https://www.microwaves101.com/encyclopedias/finite-integration-technique

[6] *Ansys HFSS*. Available: http://www.ansys.com/Products/Electronics/ANSYS-HFSS

[7] *Altair FEKO^{TM}*. Available: https://altairhyperworks.com/product/FEKO

[8] *MLFMM*. Available: https://en.wikipedia.org/wiki/Multilevel_fast_multipole_method

[9] A. G. Aguilar, J. v. Tonder, U. Jakobus, and F. Illenseer, "Overview of recent advances in the electromagnetic field solver FEKO," in *2015 9th European Conference on Antennas and Propagation (EuCAP)*, 2015.

[10] S. Hu, M. Zhou, X. Chen, and Y. Alfadhl, "Study on a sparse antenna array for terahertz imaging," in *2017 10th UK-Europe-China Workshop on Millimetre Waves and Terahertz Technologies (UCMMT)*, 2017.

[11] S. Hu, M. Zhou, X. Chen, and Y. Alfadhl, "Suppressing Ghost Images for Synthetic Aperture THz Imaging With Large Sampling Spacing," in *12th European Conference on Antennas and Propogation*, London, 2018.

[12] S. M. Gu, C. Li, X. Gao, Z. Y. Sun, and G. Y. Fang, "Terahertz Aperture Synthesized Imaging With Fan-Beam Scanning for Personnel Screening," (in English), *IEEE Transactions on Microwave Theory and Techniques,* vol. 60, no. 12, pp. 3877-3885, Dec 2012.

[13] J. Gao *et al.*, "Fast Three-Dimensional Image Reconstruction of a Standoff Screening System in the Terahertz Regime," *IEEE Transactions on Terahertz Science and Technology,* vol. PP, no. 99, pp. 1-14, 2017.

[14] B. Gonzalez-Valdes, Y. Alvarez, S. Mantzavinos, C. M. Rappaport, F. Las-Heras, and J. A. Martinez-Lorenzo, "Improving Security Screening: A Comparison of Multistatic Radar Configurations for Human Body Imaging," *IEEE Antennas and Propagation Magazine*, vol. 58, no. 4, pp. 35-47, 2016.

[15] X. Zhuge and A. G. Yarovoy, "A Sparse Aperture MIMO-SAR-Based UWB Imaging System for Concealed Weapon Detection," *IEEE Transactions on Geoscience and Remote Sensing,* vol. 49, no. 1, pp. 509-518, 2011.

[16] ITIS FOUNDATIOIN-VIRTUAL POPULATIOIN & VIZOO-TISSUE PROPERTIES-DATABASE-DIELECTRINIC PROOPERTIES [Online]. Available: https://www.itis.ethz.ch/virtual-population/tissue-properties/database/dielectric-properties/

[17] S. Hu, M. Zhou, X. Chen, and Y. Alfadhl, "Suppressing Ghost Images for Synthetic Aperture THz Imaging with Large Sampling Spacing," presented at the 12th European Conference on Antennas and Propogation, London, UK, 9-13, April, 2018.

Chapter 4 Compressive Sensing and Its Application in Proposed Imaging Scheme

4.1. Introduction to Compressive Sensing (CS) Method

The Nyquist Sampling Theorem states that a band-limited continuous-time signal can be sampled and perfectly reconstructed from its samples if the sampling frequency is greater than twice of the highest frequency component of the signal. This requires a large amount of sampling data. As a breakthrough, the compressive sensing has been proposed [1-3]. It demonstrates a signal or image, unknown but supposed to be compressible by a known transform, (e.g. wavelet or Fourier), can be accurately reconstructed with fewer measurements than the nominal number of data points. The samples are nonadaptive and measure 'random' linear combinations of the transform coefficients. Approximate reconstruction is obtained by solving the transform coefficients consistent with measured data for having the smallest possible l_1 norm, which is the sum of the absolute vector values as seen in Appendix II [1, 3, 4]. A full introduction to compressive sensing including signal models, sensing matrices, recovery theory, reconstruction algorithms and applications has been given in [5]. A systematic review on compressive sensing concepts, implementations and applications has been presented in [6]. Classical algorithms for compressive sensing of images have been compared, focusing on total variation algorithms in comparison with l_1 norm minimization algorithms in [7]. Reconstruction algorithms, transform domain formulations and applications have been reviewed in [8, 9]. Besides, compressive sensing in electromagnetics by 2015, including the state-of-the-art advances of CS formulations, methods and applications in electromagnetics has been fully reviewed in [10].

CS technique has been widely used in array synthesis, communications, and various imaging applications [8-10] including biomedical applications such as computed tomography (CT), magnetic resonance imaging (MRI) and radar imaging such as stepped-frequency continuous-wave ground penetrating radars [11], through-the-wall radar imaging[12] and SAR/ISAR imaging [13-17]. This technique is useful to save sampling time with fewer data but without noticeable loss in quality of target image, which is promising to improve the imaging rate for efficient security detection.

However, the researches for security detection are either on low frequency bands below 100 GHz [18-20] or simulation studies due to the technical difficulties and high cost in implementing a THz imaging system with a large scale of array [21]. The imaging performance of CS integrated into SAR imaging has been studied utilizing a stepped-frequency radar at Ka band (26.5 - 40 GHz), but experimental targets under test are only three simple corner reflectors [16]. A novel centralized sparse representation based on SAR (Synthetic Aperture Radar) imaging approach has been proposed to improve the image quality and reduce the reconstruction time, but it operates at C band (RADARSAT-1) [17]. Near-field 3-D MMW imaging using a fast CS method based on an interpolation-free holographic algorithm has been proposed in comparison with the Fourier-based imaging, which operates at 72 – 76 GHz in simulation and 92 – 94 GHz in experiment [18]. CS imaging performance on human profile (curved object) has been compared with SAR imaging approach with a multi-static portal system working in the range of 60 – 66 GHz, but there is no information on resolution or target identification [19]. CS application in a raster scanning scheme utilizing a mono-static TR pair at 100 GHz has been experimentally studied, compared with Fourier-transform-based CS (FT-CS) method and Definition-based CS method [20]. Therefore, we decide to study the CS application in THz imaging system operating at 220 GHz with a multi-static linear sparse periodic array, proposing the corresponding SPA CS reconstruction model to further reduce the sampling data but maintain the high image quality. In addition, we investigate the CS imaging operation at 94 GHz as a reference.

Firstly, we introduce the traditional CS measurement and recovery. Its measurement process can be described as a matrix form as shown in equation (4- 1), which is illustrated in form of diagram in Figure 4- 1. An unknown signal $X_{N\times1}$, if it is not sparse, generally can be transformed into a sparse form $S_{N\times1}$ in the another domain by a known sparse basis matrix $\Psi_{M\times N}$ that corresponds to the transform such as Fast Fourier Transform (FFT), Discrete Cosine Transform (DCT), Discrete Wavelet Transform (DWT). Then it can be projected onto a low dimension measurement domain by a known observation matrix $\Phi_{M\times N}$ wherein M is much less than N.

$$Y_{M\times1} = \Phi_{M\times N} X_{N\times1} = \Phi_{M\times N} \Psi_{N\times N} S_{N\times1} = \Theta_{M\times N} S_{N\times1} \tag{4- 1}$$

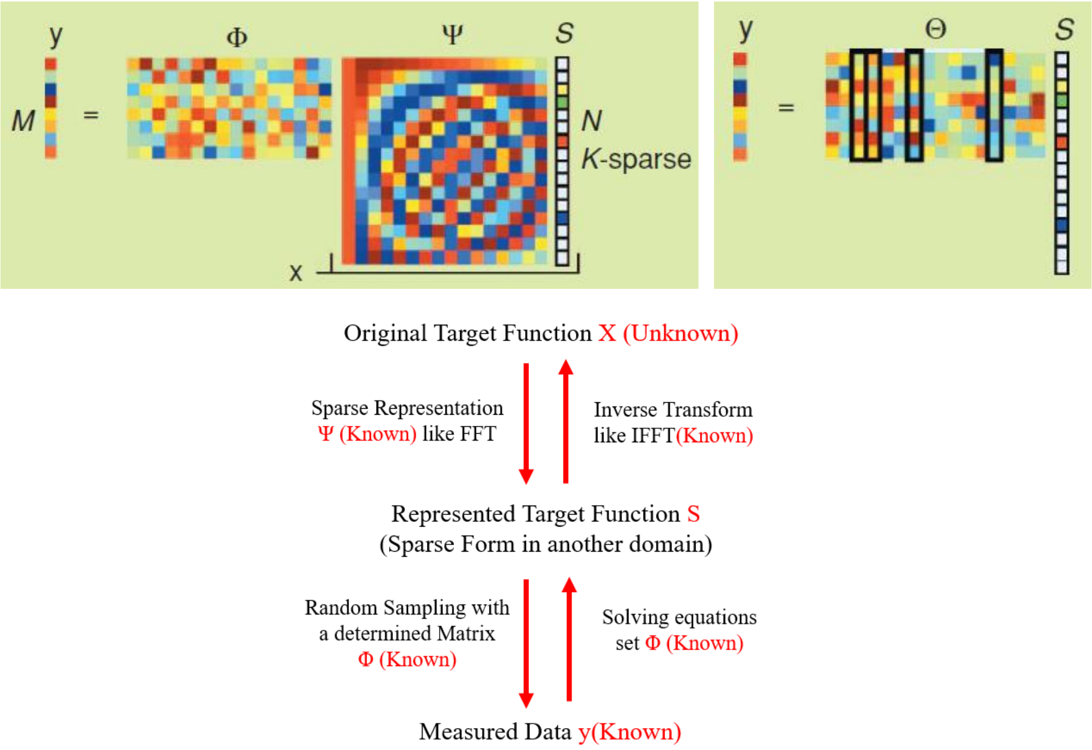

Figure 4- 1. Illustration of CS measurement process with a measurement matrix Φ and a transform matrix Ψ

The measurement matrix $\Phi_{M\times N}$ must allow the reconstruction of the length-N signal **X** from $M < N$ measurements. Since $M < N$, this problem appears ill-conditioned. A necessary and sufficient condition for this simplified problem to be well conditioned is the isometry constant $\delta_{2K} < 1$ or even $\delta_{3K} < 1$ with a more strict condition [2, 4, 22, 23]. The isometry constant δ_K is defined as the smallest quantity for any $c \in R^{|T|}$ such that Θ_T obeys

$$(1-\delta_K)\|c\|_2^2 \le \|\Theta_T c\|_2^2 \le (1+\delta_K)\|c\|_2^2 \tag{4- 2}$$

for all subsets $T \subset \{1,\cdots,N\}$, $|T| \le K$, Θ_T with the dimension of $K \times |T|$ is the submatrix consisting of the columns indexed by T from Θ. This condition is referred to as the Restricted Isometry Property (RIP) [2, 4, 22, 23]. If the $\Theta_{M\times N}$ satisfies RIP, the unknown $S_{N\times 1}$ can be approximately recovered from fewer measurements $Y_{M\times 1}$ by solving equation (4- 1). After that, the unknown signal $X_{N\times 1}$ can be reconstructed by multiplying $S_{N\times 1}$ with $\Psi^{-1}_{MN\times MN}$. The RIP depicted in equation (4- 2) can also be simply interpreted as measurement matrix $\Phi_{M\times N}$ is incoherent to sparse basis function $\Psi_{M\times N}$ [23]. However, both the RIP and incoherence can be achieved with high probability simply by selecting Φ as a random matrix. And the Gaussian measurement matrix is proved to be universal such that Θ meets the RIP [23].

The CS reconstruction aims to find the *K*-th sparse coefficient vector in N × M translated null space by solving [1, 4, 23]

$$\min_{S} \|S\|_0 \text{ subject to } \Theta S = y \tag{4- 3}$$

where $\|S\|_0 = \sum_{i=1}^{N} |S_i|^0$ is called l_0 –'norm' as seen in Appendix II. However, solving (4- 3) is unstable and difficult. The theory has proven that the l_0 problem can be approximated by l_1 problem obeys [1, 4, 23]

$$\min_{S} \|S\|_1 \text{ subject to } \Theta S = y \tag{4- 4}$$

where $\|S\|_1 = \sum_{i=1}^{N} |S_i|^1$. The proper reconstruction algorithms have two categories of convex optimization methods and greedy methods. Commonly used convex optimization methods include Basis Pursuit (BP), Basis Pursuit De-Noise (BPDN), Least Absolute Shrinkage and Selection Operator (LASSO) and adaptive gradient-based algorithm[8, 9]. The greedy methods have two groups: greedy pursuit methods and thresholding based methods. Greedy pursuit methods involve the orthogonal matching pursuit (OMP) and compressive sampling matching pursuit (CoSaMP) that are widely used in practical applications [8, 9]. Thresholding based methods include Iterative Shrinkage Thresholding (IST) Algorithm and the improved version: Two-step Iterative Shrinkage-Thresholding (TwIST) Algorithms for fast convergence [8, 9, 13].

OMP is an iterative greedy algorithm that selects at each step the column of Θ which is most correlated with the current residuals. This column is then added into the set of selected columns. The algorithm updates the residuals by projecting the observation *y* onto the linear subspace spanned by the columns that have already been selected and the algorithm then iterates. Compared with other alternative methods, a major advantage of the OMP is its simplicity and easy implementation, but iterations cost much time for 2D data like image processing [24]. SPGL1 (Spectral Projected-gradient for L1 minimization) solves the basis-pursuit problem by solving a sequence of Lasso problems with different values of maximum allowable l_1 norm of signal. Its high efficiency in memory and computational time makes it suitable for large-scale problems [7, 25, 26]. Thus, it has been adopted widely for image reconstruction in this thesis.

Secondly, taking a simple signal x(t) depicted by equation (4- 5) as an example, we illustrate the CS sampling and reconstruction as follow:

$$x(t) = 2\cdot\cos(2\pi\cdot f_1\cdot t) + 3\cdot\cos(2\pi\cdot f_2\cdot t) + 4\cdot\cos(2\pi\cdot f_3\cdot t) \qquad \text{(4- 5)}$$

wherein f_1 = 15 Hz, f_2 = 8 Hz, f_3 = 2 Hz. The x(t) in time domain and frequency domain have been shown in Figure 4- 2 in which the x(t) in time domain, as shown in Figure 4- 2(a), is depicted with a sampling frequency of 200 Hz (10 times of the lowest frequency) and 200 sampling points in one time-period. Besides, we can see three frequency components in the Fast Fourier Transform (FFT) of x(t) shown in Figure 4- 2(b), which corresponds to f_1 = 15 Hz, f_2 = 8 Hz and f_3 = 2 Hz correctly with correct amplitudes. Since there are only three nonzero entries in the frequency domain of x(t), it is a 3-sparse signal. Although x(t) does not show a sparse characteristic in the time domain, it has a sparse characteristic in the frequency domain so its sparse form can be firstly reconstructed by CS reconstructing method and then transformed back into the time domain to get the approximated x(t).

Figure 4- 3(a) shows the randomly sampled data from x(t) with a number of 40, which comprises the measured y(t) in equation (4- 1). The observation matrix Φ or called as measurement matrix used here consists of random uniform integers that works as the index to select 40 samples from x(t). The FFT of under-sampled y(t) has also been shown in Figure 4- 3 (b) in comparison with the FFT of original x(t) in Figure 4- 2 (b), we can see it has an obvious loss compared with the original signal. Finally, regarding the reconstruction process, the orthogonal matching pursuit (OMP) algorithm has been used with online-shared program codes [3, 24, 27]. Therefore, the reconstructed signal by CS method has been compared with the original one as well as the one with a uniform sampling number of 40 in Figure 4- 4. We can see that the reconstruction using CS method is in better agreement with the original signal x(t) than that using the uniform sampling. The difference between them is too tiny to discriminate, but the sampling ratio can reduce by 80% (from 200 Hz to 40 Hz) when using CS technique. However, the difference between the original signal and

uniformly under-sampled one is not too much, that is because the original signal *x*(t) is a simple one with 3 non-zeros entries.

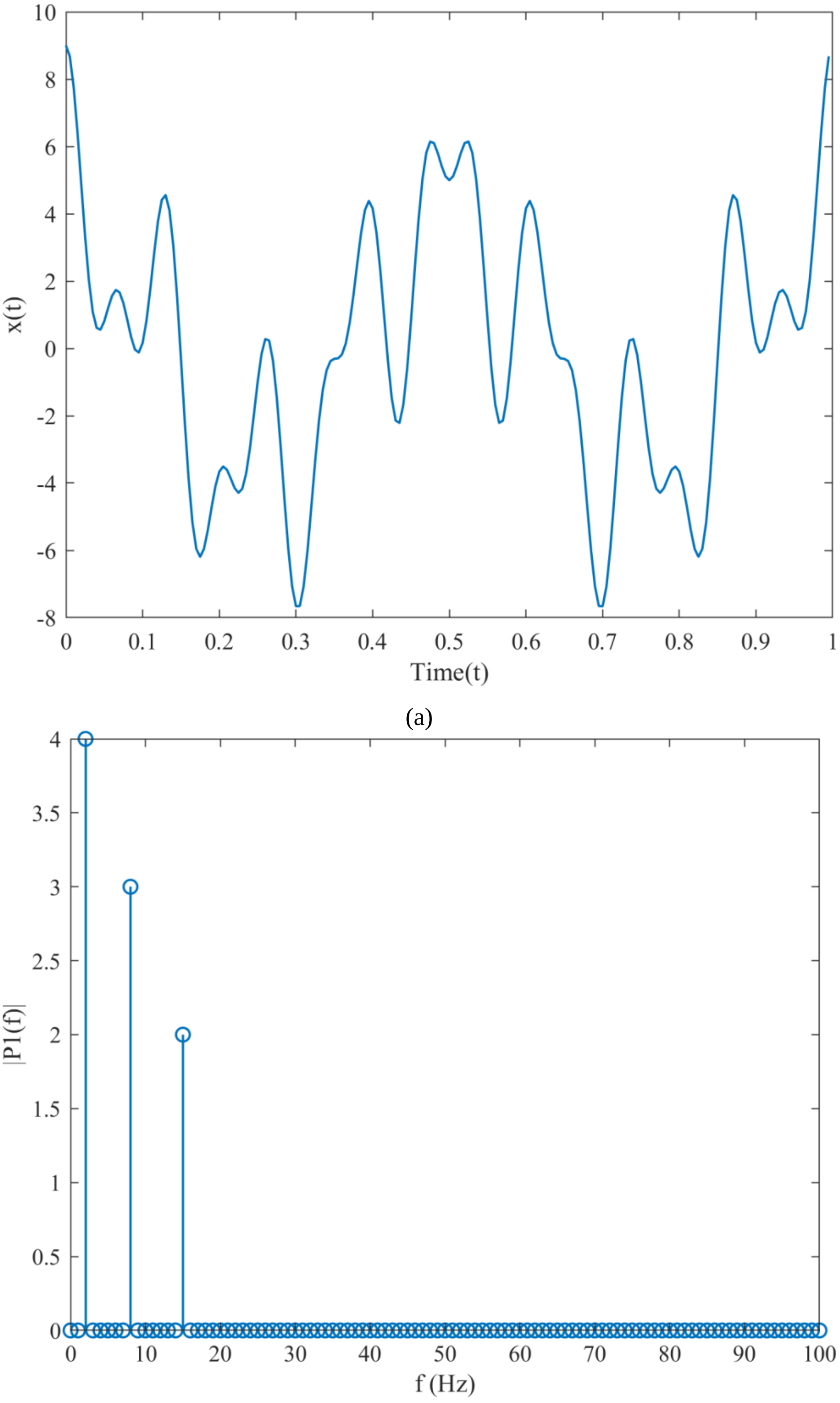

(a)

(b)

Figure 4- 2. Original *x*(t) (sampling rate 200 Hz) in (a) time domain and (b) frequency domain

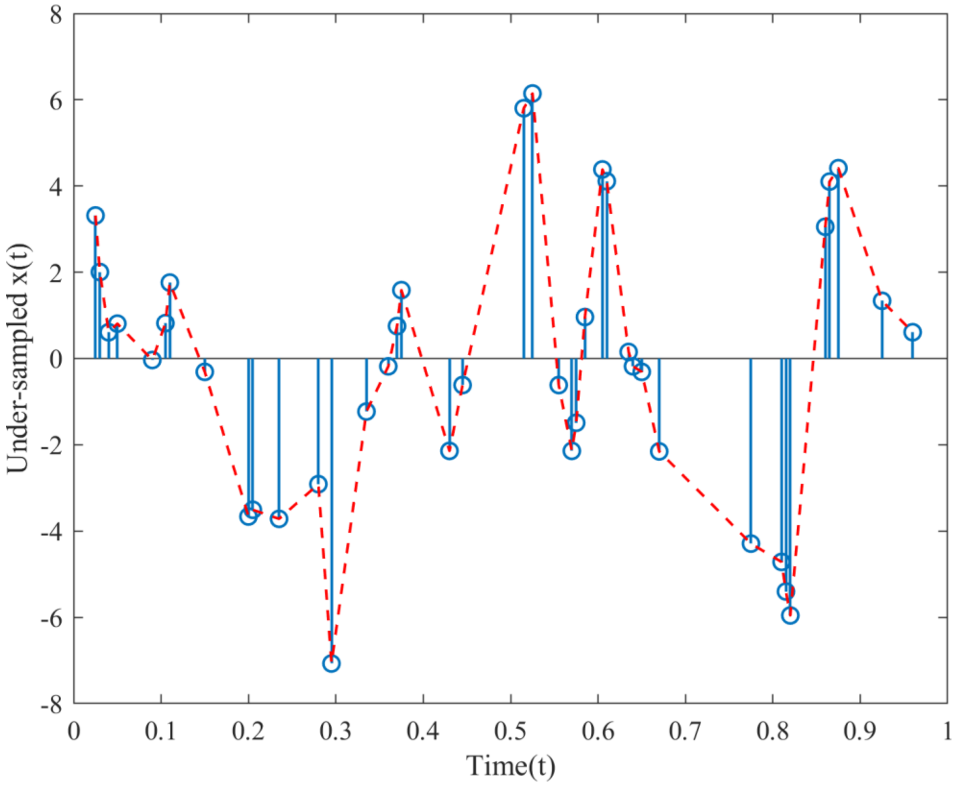

(a)

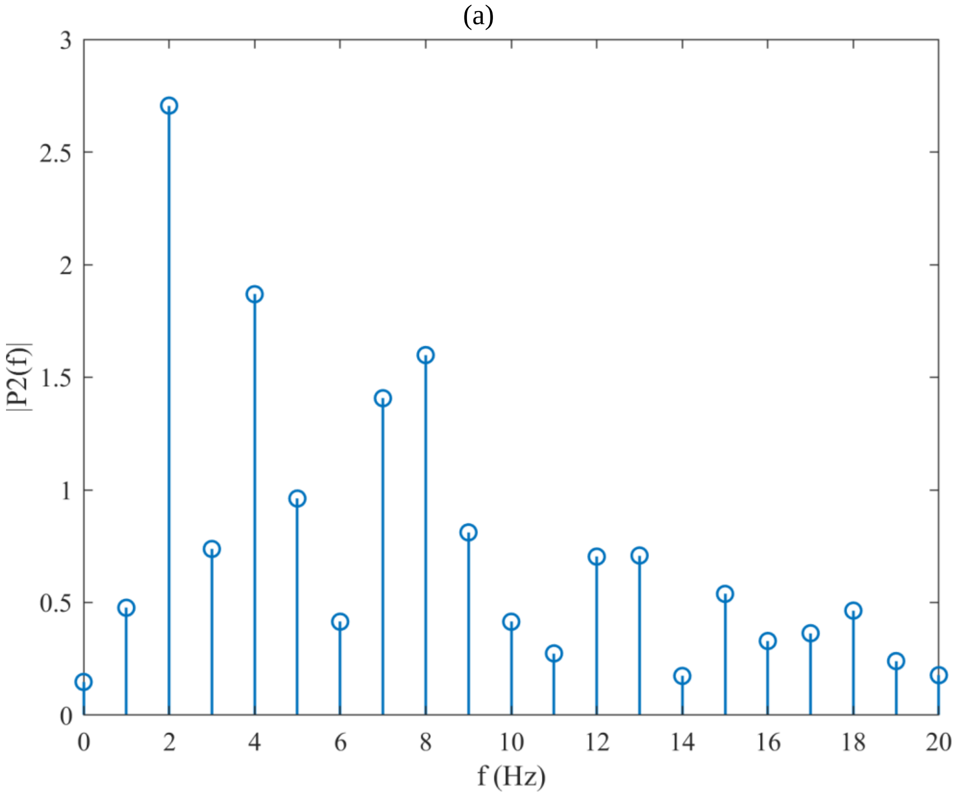

(b)

Figure 4- 3. Under-sampled signal of *x*(t) in (a) time domain and (b) frequency domain

Finally, in order to further demonstrate the merits of CS technique, we take a standard photo image, Lena shown in Figure 4- 5 (a), as an example. The testing image originally has 512 × 512 pixels. The reconstructed images by using 50% data and

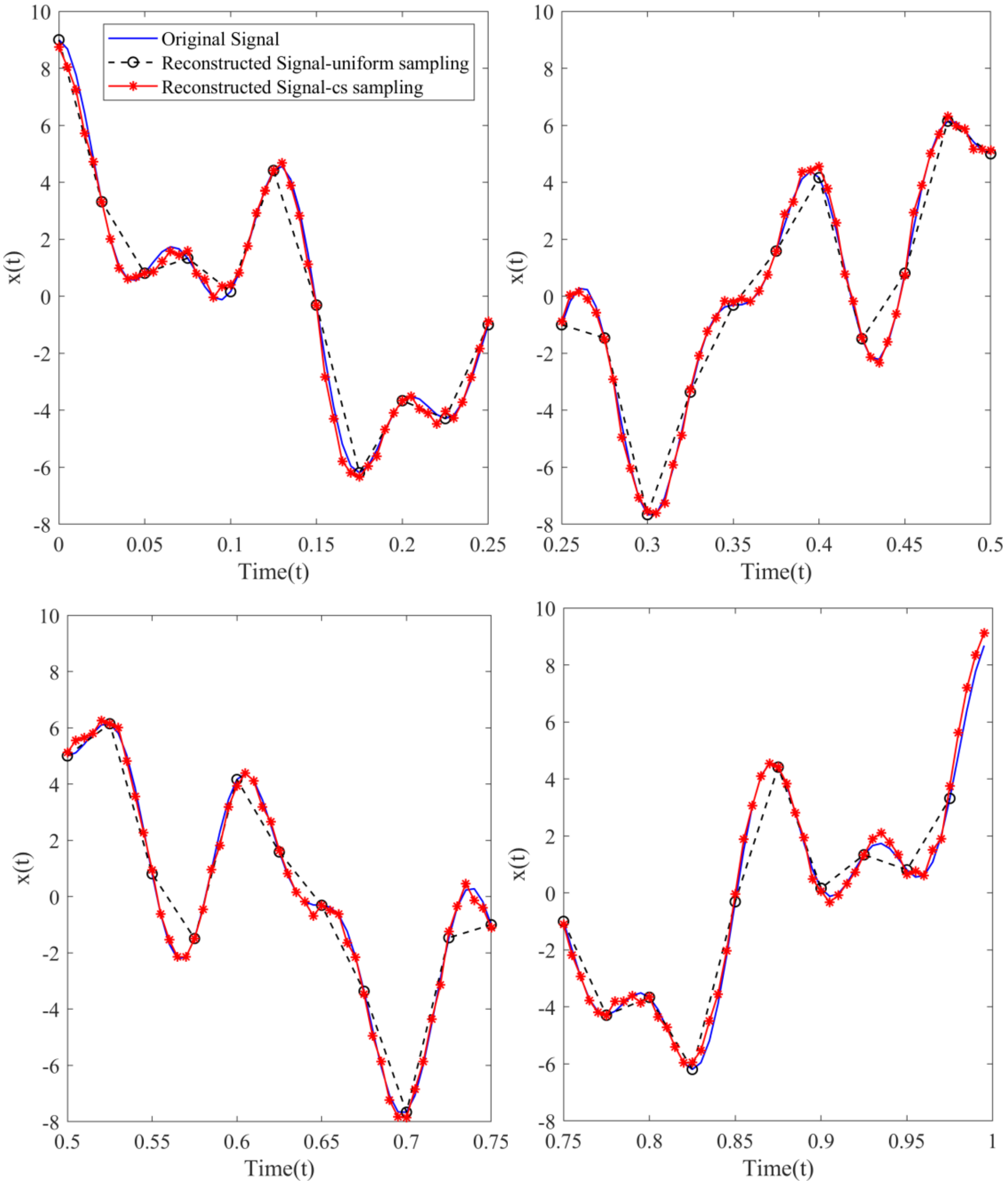

Figure 4- 4. The comparison between the reconstructed signal *x*(t) with less uniform sampling points (Number = 40), CS-OMP approach (Number = 40) and the original signal *x*(t)

the CS reconstruction approach of SPGL1 solver with Discrete Cosine Transform (DCT) sparse basis, Fast Fourier Transform (FFT) sparse basis and Haar-type Discrete Wavelet Transform (Haar-DWT) sparse basis have been compared in Figure 4- 5 (b), (c) and (d). We can see that the FFT and Haar-DWT sparse basis can provide better image quality than the DCT sparse basis in this example. The image reconstructed by using the CS approach with FFT is uniform while the image by using the CS approach with Haar-DWT is clean.

(a) (b)

(c) (d)

Figure 4- 5. (a) Standard photo image-Lena (512 × 512 pixels) and images reconstructed by using 50% data and CS-SPGL1 approach with (b) DCT sparse basis (c) FFT sparse basis and (d) Haar-DWT sparse basis

In addition, we have investigated the reconstruction using OMP and SPGL1 solvers in Figure 4- 6 and Figure 4- 7, respectively. Figure 4- 6 (a) and (b) are reconstructed by using OMP and FFT sparse basis with 40% and 70% data while Figure 4- 6 (c) and (d) are reconstructed by using OMP and Harr-DWT sparse basis using 40% and 70% data. We can see that only 40% data used is already sufficient to reconstruct the image with an obvious loss of the quality. When the data used is up to 70%, the loss decreases significantly. Besides, the CS reconstruction of using SPGL1 solver has improved the image quality a little in this example. We can see the difference when using two different sparse representation approaches and two different solvers.

(a) (b)

(c) (d)

Figure 4- 6. Lena images reconstructed by using the CS-OMP approach with FFT sparse basis. (a) 40% data (b) 70% data and Haar-DWT sparse basis (c) 40% data (d) 70% data

(a) (b)

(c) (d)

Figure 4- 7. Lena images reconstructed by using the CS-SPGL1 approach with FFT sparse basis. (a) 40% data (b) 70% data and Haar-DWT sparse basis (c) 40% data (d) 70% data

It is shown in the above example that the CS technique has a particular advantage of reconstructing a signal with fewer measurements. Nevertheless, different sparse representation bases or solvers have their own suitable applications or advantages, so most researches in past years have mainly focused on the fields like sparse representation, observation matrix and reconstruction algorithms. Regarding its application in THz imaging, it is different from the aforementioned photo example in which the original signal x(t) or image Lena are known in advance so the measurement Y are directly sampled parameters from the desired X or S in equation (4- 1). However, what we are able to measure in the THz imaging application are usually some parameters such as amplitude and phase of reflections rather than the sampled pixels from the target image. So these parameters should be transformed into the unknown target image by the specific correlation that corresponds to the imaging system response. Therefore, an applicable CS reconstruction model integrated with system response should be firstly developed.

4.2. Proposed Discrete Multi-static CS Reconstruction Model for the THz SPA Imaging Scheme

In this active SPA-THz imaging system, the echo data/S-parameters $\boldsymbol{s_g}$ between ***p***th transmitter and ***q***th receiver at ***w***th mechanical scanning position is the superposition of the target reflectivity function ***g***(x, y, z) multiplied by the roundtrip phases of $\overrightarrow{R_{p,w}^{tg}}$ and $\overrightarrow{R_{q,w}^{rg}}$, calculated as equation（4- 6）.

$$s_g(Tx_{p,w}, Rx_{q,w}) = \iint g(x,y,z) e^{-jk(|\overrightarrow{R^{tg}_{p,w}}| + |\overrightarrow{R^{rg}_{q,w}}|)} dxdy \tag{4- 6}$$

wherein $\overrightarrow{R^{tg}_{p,w}}$ and $\overrightarrow{R^{rg}_{q,w}}$ are calculated as equation (4- 7) with the simplification that the array has the position at z axis of zero.

$$\begin{aligned} |\overrightarrow{R^{tg}_{p,w}}| &= \sqrt{(x^t_{p,w} - x)^2 + (y^t_{p,w} - y)^2 + z^2} \\ |\overrightarrow{R^{rg}_{q,w}}| &= \sqrt{(x^r_{q,w} - x)^2 + (y^r_{q,w} - y)^2 + z^2} \end{aligned} \tag{4- 7}$$

Accordingly, a discrete version of $\boldsymbol{s_g}(\mathrm{Tx}_{p,w}, \mathrm{Rx}_{q,w})$ can be derived as equation (4-8), which supposes the target reflectivity function $\boldsymbol{g}$(x, y, z) is discretized as U × V grids while the fully sampled S-parameters $\boldsymbol{s_g}$ has Nt·Nr × W sampling positions in which W is the total number of SPA mechanical moving positions.

$$s_g(Tx_{p,w}, Rx_{q,w}) = \sum_{u=1}^{U} \sum_{v=1}^{V} g(u,v) \cdot e^{-jk(|\overrightarrow{R^{u,v}_{p,w}}| + |\overrightarrow{R^{u,v}_{q,w}}|)} \tag{4- 8}$$

wherein $\overrightarrow{R^{u,v}_{p,w}}$ and $\overrightarrow{R^{u,v}_{q,w}}$, the discrete version of $\overrightarrow{R^{tg}_{p,w}}$ and $\overrightarrow{R^{rg}_{q,w}}$, are calculated as equation (4- 9).

$$\begin{aligned} |\overrightarrow{R^{u,v}_{p,w}}| &= \sqrt{(x^t_{p,w} - x^g_{u,v})^2 + (y^t_{p,w} - y^g_{u,v})^2 + (z^g_{u,v})^2} \\ |\overrightarrow{R^{u,v}_{q,w}}| &= \sqrt{(x^r_{q,w} - x^g_{u,v})^2 + (y^r_{q,w} - y^g_{u,v})^2 + (z^g_{u,v})^2} \end{aligned} \tag{4- 9}$$

Inversely, the target image at point **o** reconstructed by the traditional Generalized Synthetic Aperture Focusing Technique (GSAFT) can be derived by equation (4- 10) [28],

$$g(\overrightarrow{r_o}) = \sum_{w=1}^{W} \sum_{p=1}^{Nt} \sum_{q=1}^{Nr} s_g(Tx_{p,w}, Rx_{q,w}) \cdot e^{jk(|\overrightarrow{R^{u,v}_{p,w}}| + |\overrightarrow{R^{u,v}_{q,w}}|)} \tag{4- 10}$$

It is worth mentioning that it is already an under-sampled imaging system because the Nt·Nr·W is much less than U·V that usually has the spacing meeting the Nyquist sampling criterion.

In order to utilize standard 1-D CS reconstruction algorithm, the discrete SPA imaging model $\boldsymbol{s_g}$ in equation (4- 8) should be reshaped into a 1-D column vector of $\boldsymbol{S_g}$ as shown in equation (4- 11) in which $\boldsymbol{s_g}(p\cdot q,w)$ is the simplified form of $\boldsymbol{s_g}(\mathrm{Tx}_{p,w}, \mathrm{Rx}_{q,w})$, similarly in $\mathrm{H}(p\cdot q,w)$ [29].

$$Sg_{Nt\cdot Nr\cdot W\times 1}=\begin{bmatrix} \mathrm{s}_g(1\cdot 1,1) \\ \vdots \\ s_g(Nt\cdot Nr,1) \\ \vdots \\ s_g(1\cdot 1,W) \\ \vdots \\ s_g(Nt\cdot Nr,W) \end{bmatrix} = \begin{bmatrix} H(1\cdot 1,1) \\ \vdots \\ H(Nt\cdot Nr,1) \\ \vdots \\ H(1\cdot 1,W) \\ \vdots \\ H(Nt\cdot Nr,W) \end{bmatrix} \begin{bmatrix} g(1,1) \\ \vdots \\ g(U,1) \\ \vdots \\ g(1,V) \\ \vdots \\ g(U,V) \end{bmatrix} \tag{4- 11}$$

wherein

$$\begin{aligned} H(p\cdot q,w)=\Bigg[& e^{-jk\left(\left|\overrightarrow{R_{p,w}^{1,1}}\right|+\left|\overrightarrow{R_{q,w}^{1,1}}\right|\right)}, \quad \cdots \quad e^{-jk\left(\left|\overrightarrow{R_{p,w}^{U,1}}\right|+\left|\overrightarrow{R_{q,w}^{U,1}}\right|\right)}, \\ & \cdots \quad , \; e^{-jk\left(\left|\overrightarrow{R_{p,w}^{1,V}}\right|+\left|\overrightarrow{R_{q,w}^{1,V}}\right|\right)}, \quad \cdots \quad , \; e^{-jk\left(\left|\overrightarrow{R_{p,w}^{U,V}}\right|+\left|\overrightarrow{R_{q,w}^{U,V}}\right|\right)} \Bigg] \end{aligned} \tag{4- 12}$$

Afterwards, in order to apply CS reconstruction, the equation set of discrete SPA-CS imaging model complying with equation (4- 1) can be gained as equation (4- 13),

$$\begin{aligned} Sy_{M\times 1} &= A.*Sg_{NtNrW\times 1} \\ &= A.*(H_{NtNrW\times UV}\, g_{UV\times 1}) \\ &= [\underline{A.*(H_{NtNrW\times UV}}\,\Psi^{-1}_{UV\times UV})]_{M\times UV}\,\underline{(\Psi_{UV\times UV}\, g_{UV\times 1})} \\ &= \underline{\Phi_{M\times UV}\,\Psi^{-1}_{UV\times UV}}\,\underline{\Psi_{UV\times UV}\, g_{UV\times 1}} \\ &= \Theta_{M\times UV}\, Xg_{UV\times 1} \end{aligned} \tag{4- 13}$$

where $\cdot *$ represents element-wise multiplication, $\Psi^{-1}_{MN\times MN}\Psi_{MN} = I$. Binary mask **A** is a randomly distributed sampling matrix that only contains 1 (sampled) and 0 (ignored), which makes each row of matrix **H** active or inactive, so **Sy** is a M-length vector sampling from the original S-parameters matrix **Sg** recorded by this THz SPA imaging system. When A is full of 1 (M = Nt·Nr·W), the full data collected by this SPA-THz imaging system can be used to reconstruct the target image, while M is less than Nt·Nr·W, the sampling data has been further reduced. In addition, the target images reconstructed with the traditional GSAFT approach are set as reference in comparison.

Since the large matrixes used in this paper (we use 32 Gigabytes of RAM to execute the CS processing on matrix with 18144 × 18144 elements smoothly in Microsoft Windows MATLAB platform) demand a large amount of computer resource, we have utilized the SPGL1 solver that is particularly suitable for the large-scale sparse reconstruction to obtain the CS result [25, 26]. What we have solved is to minimize the l_1 norm of the sparse form **Xg** of target reflectivity function **g** subjected to the condition shown in equation (4- 14) where the **σ** is the tolerance between the solution and measured data. Target reflectivity function **g** can be gained after the roots **Xg** are gained. The root-mean-square deviation (RMSD) also known as root-mean-square error (RMSE) defined in equation (4- 15) is used to quantitatively measure the difference between reconstructed target reflectivity function $\hat{g}_{u,v}$ and reference of true target reflectivity function $g_{u,v}$.

$$\min_{Sg}\|Xg\|_1 \quad \text{subject to} \quad \|\Theta Xg - Sy\|_2 < \sigma \tag{4- 14}$$

$$\text{RMSD}=\sqrt{\frac{\sum_{u=1,v=1}^{UV}(\hat{g}_{u,v}-g_{u,v})^2}{U\cdot V}} \tag{4- 15}$$

4.3. Simulation Assessment of the Image Reconstruction Using the Proposed Discrete Multi-static CS Model

4.3.1. *The Metal Target in Free Space*

We have conducted the CS reconstruction using the simulated data of Figure 3- 4 (d) - scheme III in Table. 3- 1. The Tx element spacing is 6 mm and the mechanical scanning step is 6 mm, respectively. When 30% randomly chosen simulated data of S-

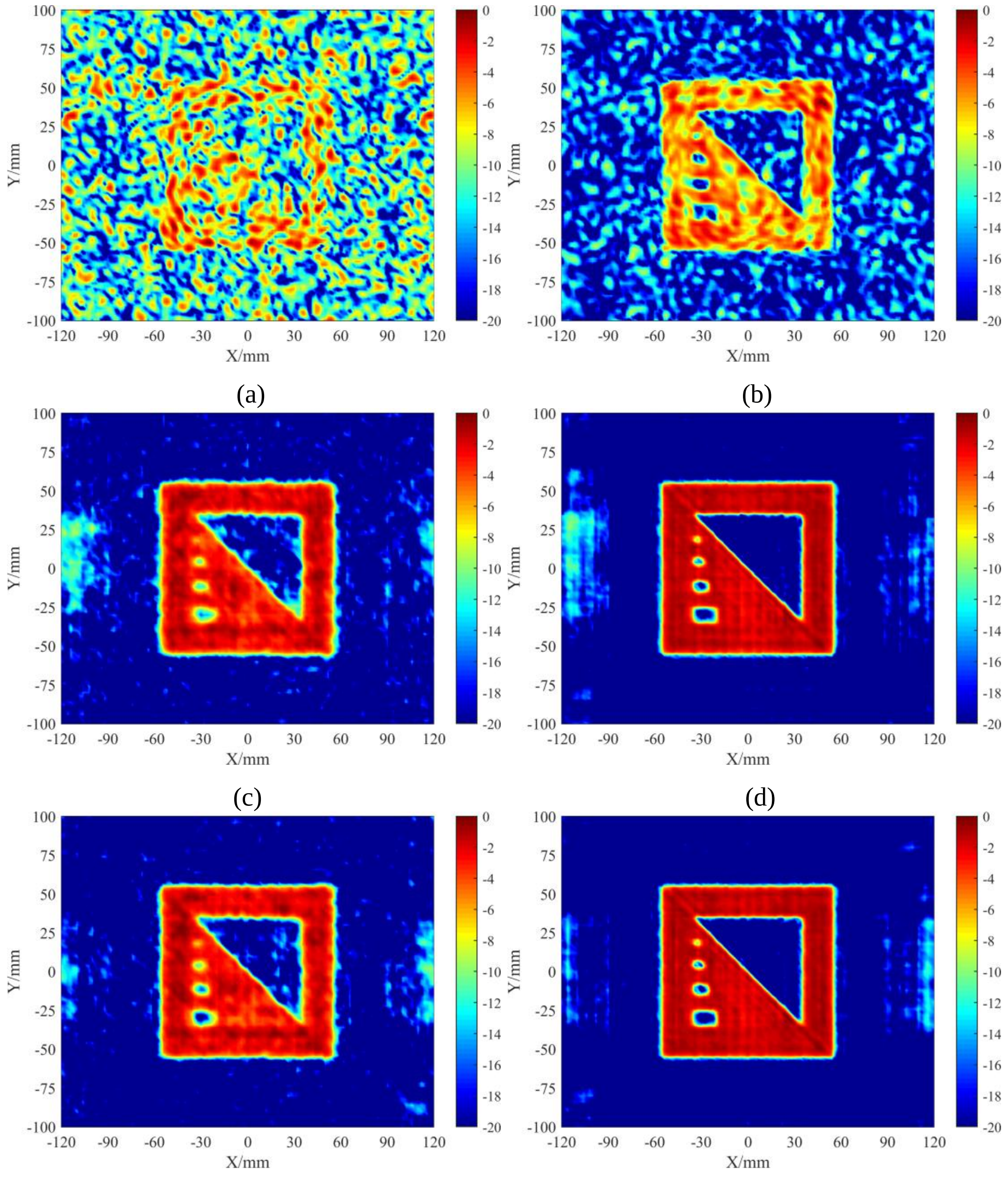

(a) (b)

(c) (d)

(e) (f)

Figure 4- 8. Images with 20-dB dynamic range reconstructed by using GSAFT approach with (a) 30% simulated data (b) 70% simulated data, by using CS approach of SPGL1 solver with FFT sparse basis (c) 30% simulated data (d) 70% simulated data, with Discrete Cosine Transform (DCT) sparse basis (e) 30% simulated data (f) 70% simulated data

parameters are used, the reconstructed images by using the traditional GSAFT approach, CS approaches of SGPL1 solver with Fast Fourier Transform (FFT) sparse basis and SPGL1 solver with discrete cosine transform (DCT) sparse basis have been compared in Figure 4- 8 (a), (c) and (e). The results of using 70% simulated data of S-parameters have been compared in Figure 4- 8 (b), (d) and (f). The corresponding root-mean-square deviations (RMSDs) with a reference of GSAFT reconstruction of 100% sampling data are calculated and shown in Figure 4- 9. It is shown that the traditional GSAFT approach does not reconstruct the target image successfully when the data used is not full. Thus, the RMSD has the highest value with GSAFT reconstruction. However, the CS reconstruction approach reconstructs the target image successfully even though 30% measured S-parameters data are used, so RMSD drops significantly and it becomes lower when 70% date are used. In addition, comparing the CS image using FFT sparse basis to the CS image using DCT sparse basis, we can see that the sparse representation with DCT sparse basis has shown a better image quality. This has also been verified by a lower RMSD of using CS-DCT reconstruction in Figure 4- 9. Therefore, the CS reconstruction with DCT sparse basis has been used in all the following studies in this thesis.

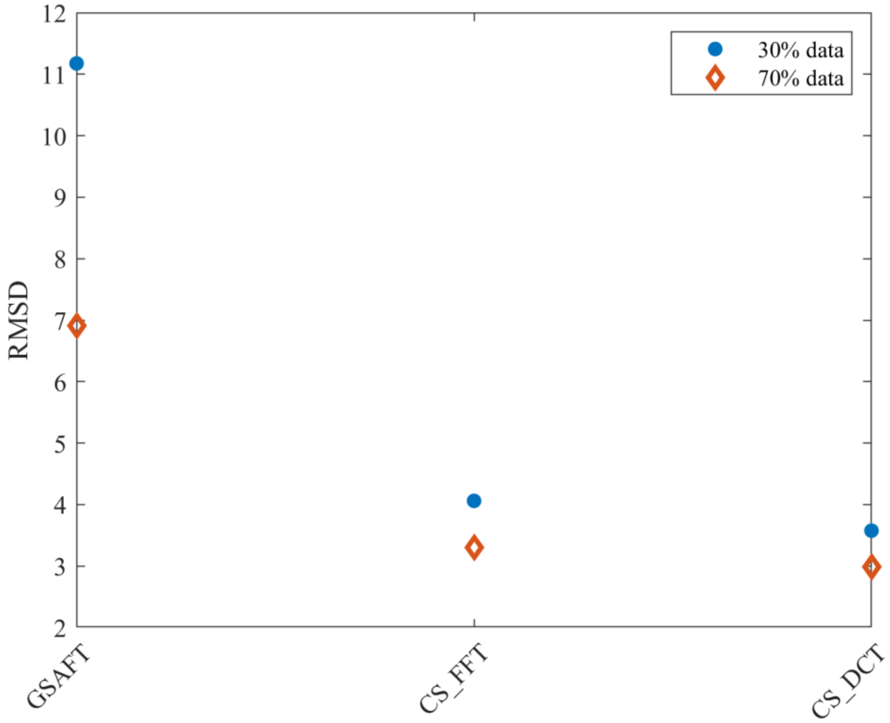

Figure 4- 9. Root-mean-square deviations (RMSDs) of Figure 4- 8 (a) ~ (f) in which different methods and data are used

4.3.2. The Target on Human Body

The simulation on the small chunk of human body phantom (800 mm × 100 mm × 5 mm) shown in Figure 3- 18 has been used to assess the CS image reconstruction. The body phantom model has a relative permittivity of 5.3 and a loss tangent of 0.75, the image reconstructed by the proposed CS reconstruction approach using only 50% data in comparison with the improved GSAFT using 100% data, as shown in Figure 4- 10. Similarly, we have also reconstructed the target concealed under a thin (Nylon-610) clothing of 0.5 mm with a relative permittivity of 2.84 and a loss tangent of 0.012 by the proposed CS reconstruction approach using 50% data compared with the reconstruction with the improved GSAFT using 100% data in Figure 4- 11. Both results have demonstrated that the proposed discrete SPA CS model for image

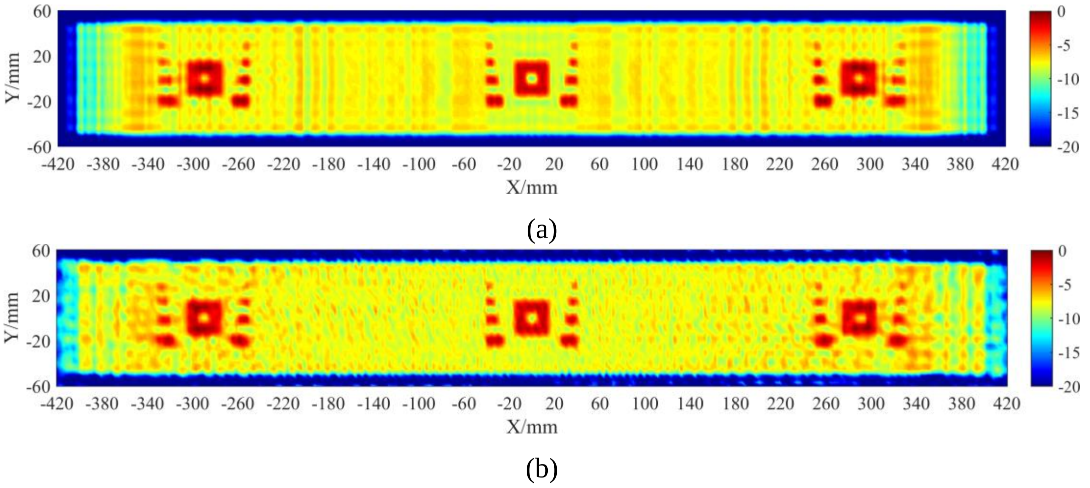

(a)

(b)

Figure 4- 10. The images of metal targets and human body (800 mm × 100 mm × 5 mm) surface reconstructed by (a) the improved GSAFT reconstruction approach with full data (b) CS reconstruction approach with 50% data (20-dB dynamic range)

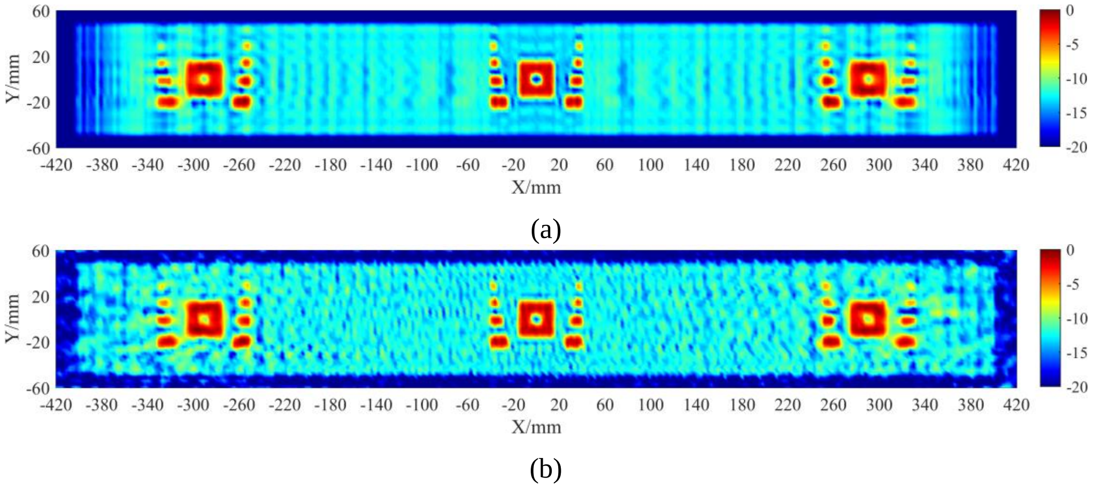

(a)

(b)

Figure 4- 11. The images of metal targets and human body surface concealed under a thin (Nylon-610) clothing (800 mm × 100 mm × 0.5 mm) reconstructed by (a) the improved GSAFT reconstruction approach with full data (b) CS reconstruction approach with 50% data (20-dB dynamic range)

reconstruction can provide a comparable image quality to the traditional reconstruction approach with an obvious reduction of data.

In addition, the simulated data of the small chunk of human body phantom (1600 mm × 100 mm × 5 mm) in chapter 3.3.2 has also been used to perform the CS image reconstruction. It has been demonstrated that the improved GSAFT reconstruction proposed by us enables to suppress ghost images caused by the large element spacing, as presented in Figure 4- 12 (b) and (c). The reconstructed images by the CS reconstruction approach with 100% (14 × 16 × 41 = 9184 sampling points), 50% and 30% of data collected by above SPA are compared in Figure 4- 12 (d), (e) and (f). The corresponding root-mean-square deviations (RMSDs) with a reference of Figure 4- 12 (c) are calculated and shown in Figure 4- 13.

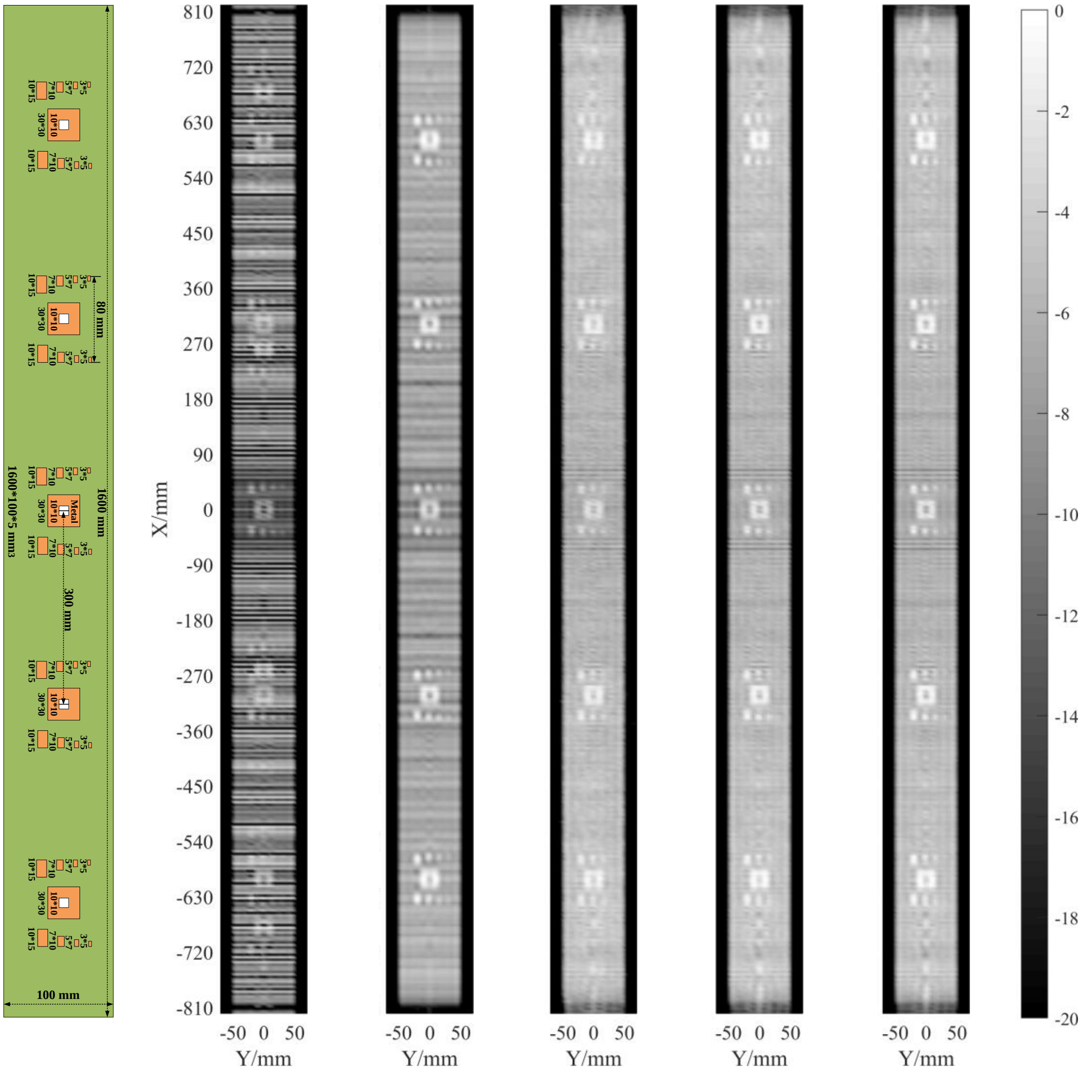

(a) (b) (c) (d) (e) (f)

Figure 4- 12. Target (a) drawing and images with 20-dB dynamic range reconstructed by (b) traditional and (c) improved GSAFT imaging algorithms as well as by the proposed CS approach with (d) 100 % (e) 50% (f) 30% of data collected by SPA

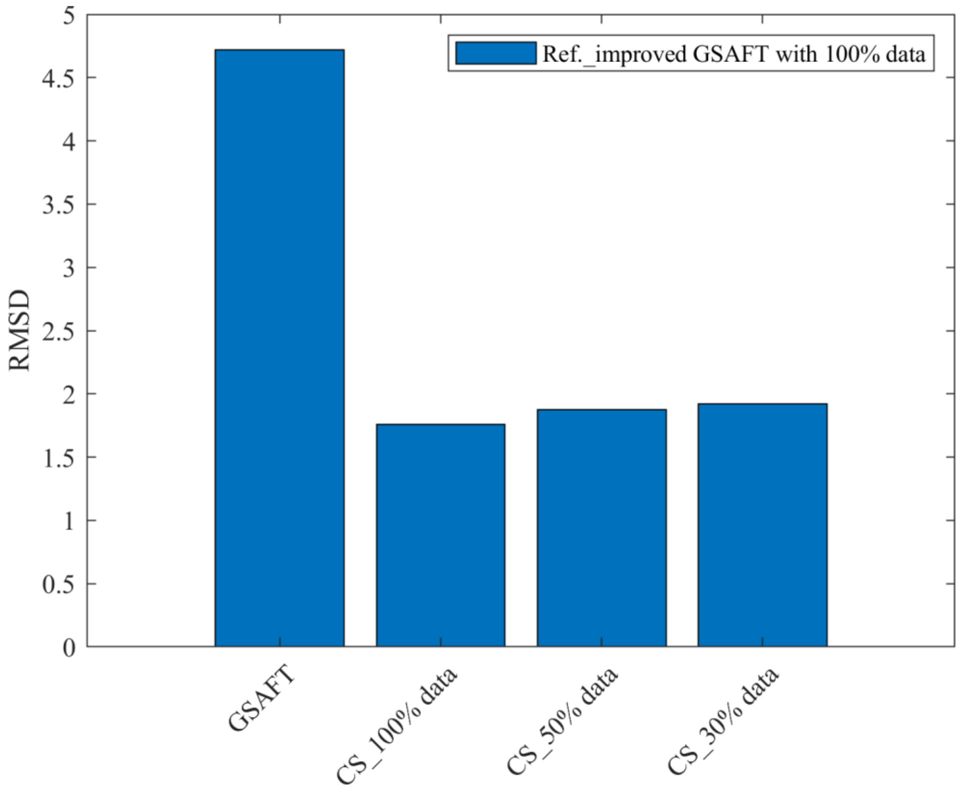

Figure 4- 13. Root-mean-square deviations (RMSDs) of Figure 4- 12 (b), (d), (e) and (f) with a reference of Figure 4- 12 (c)

It indicates from results that aliasing/artifacts in Figure 4- 12 (c) caused by too sparse receiver elements can be alleviated obviously with help of the CS reconstruction approach, so the RMSDs improve significantly by reducing from 4.72 to 2 below. In addition, 50% randomly chosen data is already enough to reconstruct an image as good as the image reconstructed by the improved GSAFT approach with full data. Furthermore, the image reconstructed with the CS approach using 30% data only deteriorates little, which only causes 0.042 drop in RMSD. Therefore, the image reconstruction approach based on the CS technique is not only capable of reducing the sampling points/data acquisition time without obvious loss in image quality, but also suppressing the appearance of ghost images since the data is randomly sampled.

4.4. Summary

This chapter has firstly introduced the compressive sensing theory including concept, recovery and state-of-the-art researches, giving two examples to show its working principle of sampling and reconstruction that demonstrates its advantage in approximating the original signal with few measurements. Consequently, the discrete multi-static CS reconstruction model for the proposed SPA imaging system has been proposed based on the CS technique integrated with the imaging system response. Finally, this proposed CS model has been assessed based on the simulated data in comparison with the reconstructed image using the improved GSAFT. The results have demonstrated that this CS imaging approach is capable of not only reconstructing the high image quality with few sampling data, but also suppressing the ghost images successfully.

4.5. References

[1] D. L. Donoho, "Compressed sensing," *IEEE Transactions on Information Theory,* vol. 52, no. 4, pp. 1289-1306, 2006.

[2] E. J. Candes, J. Romberg, and T. Tao, "Robust uncertainty principles: exact signal reconstruction from highly incomplete frequency information," *IEEE Transactions on Information Theory,* vol. 52, no. 2, pp. 489-509, 2006.

[3] Y. Tsaig and D. L. Donoho, "Extensions of compressed sensing," *Signal Processing,* vol. 86, no. 3, pp. 549-571, 2006.

[4] E. J. Candès, "The restricted isometry property and its implications for compressed sensing," *Comptes Rendus Mathematique,* vol. 346, no. 9, pp. 589-592, 2008.

[5] R. Baraniuk, M. A. Davenport, M. F. Duarte, and C. Hegde, "An introduction to compressive sensing," *Connexions e-textbook,* pp. 24-76, 2011.

[6] M. Rani, S. B. Dhok, and R. B. Deshmukh, "A Systematic Review of Compressive Sensing: Concepts, Implementations and Applications," *IEEE Access,* vol. 6, pp. 4875-4894, 2018.

[7] Y. Sher, "Review of Algorithms for Compressive Sensing of Images," *arXiv preprint arXiv:1908.01642,* 2019.

[8] A. Draganic, I. Orovic, and S. Stankovic, "On some common compressive sensing recovery algorithms and applications-Review paper," *arXiv preprint arXiv:1705.05216,* 2017.

[9] I. Orović, V. Papić, C. Ioana, X. Li, and S. Stanković, "Compressive Sensing in Signal Processing: Algorithms and Transform Domain Formulations," *Mathematical Problems in Engineering,* vol. 2016, p. 7616393, 2016.

[10] A. Massa, P. Rocca, and G. Oliveri, "Compressive Sensing in Electromagnetics - A Review," *IEEE Antennas and Propagation Magazine,* vol. 57, no. 1, pp. 224-238, 2015.

[11] A. B. Suksmono, E. Bharata, A. A. Lestari, A. G. Yarovoy, and L. P. Ligthart, "Compressive Stepped-Frequency Continuous-Wave Ground-Penetrating

Radar," *IEEE Geoscience and Remote Sensing Letters,* vol. 7, no. 4, pp. 665-669, 2010.

[12] W. Zhang, M. G. Amin, F. Ahmad, A. Hoorfar, and G. E. Smith, "Ultrawideband Impulse Radar Through-the-Wall Imaging with Compressive Sensing," *International Journal of Antennas and Propagation,* vol. 2012, p. 11, 2012.

[13] L. Qiao, Y. Wang, Z. Shen, Z. Zhao, and Z. Chen, "Compressive sensing for direct millimeter-wave holographic imaging," *Applied Optics,* vol. 54, no. 11, pp. 3280-3289, 2015.

[14] Y. Yuanyuan, C. Wei, and X. Tao, "An improved Compressed Sensing algorithm and its application in SAR imaging," in *2015 IEEE 16th International Conference on Communication Technology (ICCT),* pp. 196-201, 2015.

[15] H. Kajbaf, J. T. Case, Z. Yang, and Y. R. Zheng, "Compressed sensing for SAR-based wideband three-dimensional microwave imaging system using non-uniform fast fourier transform," *IET Radar, Sonar & Navigation,* vol. 7, no. 6, pp. 658-670, 2013.

[16] J. Yang, J. Thompson, X. Huang, T. Jin, and Z. Zhou, "Random-Frequency SAR Imaging Based on Compressed Sensing," *IEEE Transactions on Geoscience and Remote Sensing,* vol. 51, no. 2, pp. 983-994, 2013.

[17] J. C. Ni, Q. Zhang, Y. Luo, and L. Sun, "Compressed Sensing SAR Imaging Based on Centralized Sparse Representation," *IEEE Sensors Journal,* vol. 18, no. 12, pp. 4920-4932, 2018.

[18] S. Li, G. Zhao, H. Sun, and M. Amin, "Compressive Sensing Imaging of 3-D Object by a Holographic Algorithm," *IEEE Transactions on Antennas and Propagation,* vol. 66, no. 12, pp. 7295-7304, 2018.

[19] Y. Rodríguez-Vaqueiro, Y. Á. López, B. González-Valdes, J. Á. Martínez, F. Las-Heras, and C. M. Rappaport, "On the Use of Compressed Sensing Techniques for Improving Multistatic Millimeter-Wave Portal-Based Personnel Screening," *IEEE Transactions on Antennas and Propagation,* vol. 62, no. 1, pp. 494-499, 2014.

[20] Q. Cheng, A. Alomainy, and Y. Hao, "On the performance of compressed sensing-based methods for millimeter-wave holographic imaging," *Applied Optics,* vol. 55, no. 4, pp. 728-738, 2016.

[21] Q. Cheng, A. Alomainy, and Y. Hao, "Compressive Millimeter-Wave Phased Array Imaging," *IEEE Access,* vol. 4, pp. 9580-9588, 2016.

[22] E. J. Candes and T. Tao, "Decoding by linear programming," *IEEE Transactions on Information Theory,* vol. 51, no. 12, pp. 4203-4215, 2005.

[23] R. G. Baraniuk, "Compressive Sensing [Lecture Notes]," *IEEE Signal Processing Magazine,* vol. 24, no. 4, pp. 118-121, 2007.

[24] T. T. Cai and L. Wang, "Orthogonal Matching Pursuit for Sparse Signal Recovery With Noise," *IEEE Transactions on Information Theory,* vol. 57, no. 7, pp. 4680-4688, 2011.

[25] E. v. d. Berg and M. P. Friedlander. (2019). *SPGL1: a solver for large-scale sparse reconstruction*. Available: https://friedlander.io/spgl1

[26] E. v. d. Berg and M. P. Friedlander, "Probing the Pareto Frontier for Basis Pursuit Solutions," *SIAM Journal on Scientific Computing,* vol. 31, no. 2, pp. 890-912, 2009.

[27] J. A. Tropp and A. C. Gilbert, "Signal Recovery From Random Measurements Via Orthogonal Matching Pursuit," *IEEE Transactions on Information Theory,* vol. 53, no. 12, pp. 4655-4666, 2007.

[28] S. Hu, C. Shu, Y. Alfadhl, and X. Chen, "A THz Imaging System Using Linear Sparse Periodic Array," *IEEE Sensors Journal,* vol. 20, no. 6, pp. 3285-3292, 2020.

[29] S. Q. Hu, C. Shu, Y. Alfadhl, and X. D. Chen, "W Band Imaging System Using Linear Sparse Periodic Antenna Array and Compressive Sensing for Personnel Screening," *IEEE Access,* vol. 7, pp. 173603-173611, 2019.

Chapter 5 Evaluation on Proposed Experimental THz-SPA Imaging System

5.1. Introduction to the Experimental THz-SPA Imaging System

After the comprehensive simulation study, we need to have the proof-of-concept tests in the lab. Thus, we built an experimental system to verify the proposed imaging system and reconstruction approaches. However, the implementation of this SPA needs to employ a large number of Tx and Rx channels, which are expensive and for which it is difficult to achieve identical channels. Alternatively, we can use one Tx and one Rx element to fast scan the required positions in the proof-of-concept experiment. Besides, the Tx positions in Figure 5- 1 (a) are on the both sides of the Rx array, it is not possible to scan Tx positions in one go. Therefore, it is more convenient to let Tx and Rx elements scan on two different tracks separated by a distance S_{TR} as shown in Figure 5- 1 (b).

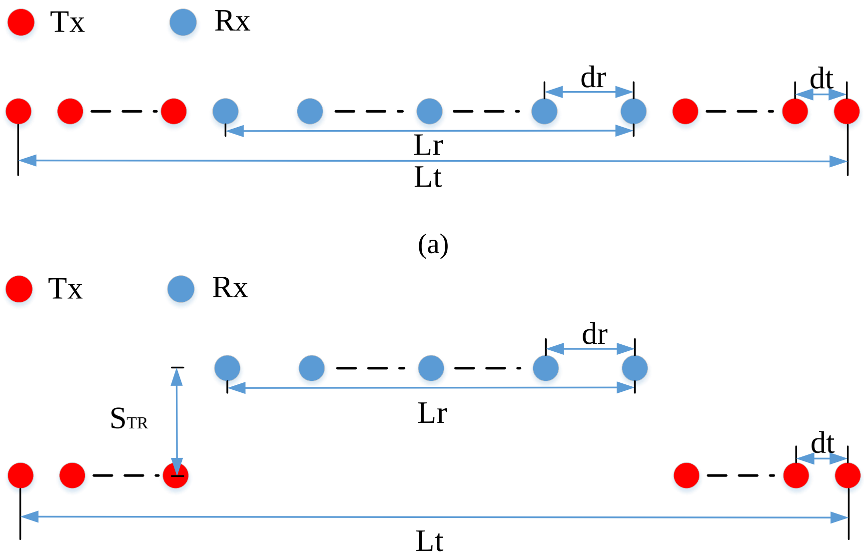

(a)

(b)

Figure 5- 1. Configuration of SPA in which Tx and Rx are (a) lined up (b) located on the different scanning tracks separated by as distance S_{TR}

Accordingly, the experimental system is set up as shown in Figure 5- 2. For achieving the vertical scanning, the target is mounted on the NSI 2000 scanner [1] to move vertically, which inversely imitates a relatively mechanical scanning of the array to a fixed target. For realizing the electronic scanning of SPA, two THz modules for transmitting and receiving THz wave highlighted in blue in Figure 5- 2 move to each

Tx and Rx element positions in the SPA, which are mounted on two linear horizontal scanning stages separated by a gap S_{TR} as shown in Figure 5- 1 (b). This experimental set-up only uses one Tx channel and one Rx channel to imitate the Tx and Rx arrays, respectively. This experimental approach not only avoids using a large number of real elements/channels with high cost, but also eliminates the phase calibration issue in the experiment. In addition, this set-up can also provide a possible solution to low-cost practical implementation of THz SPA imaging system.

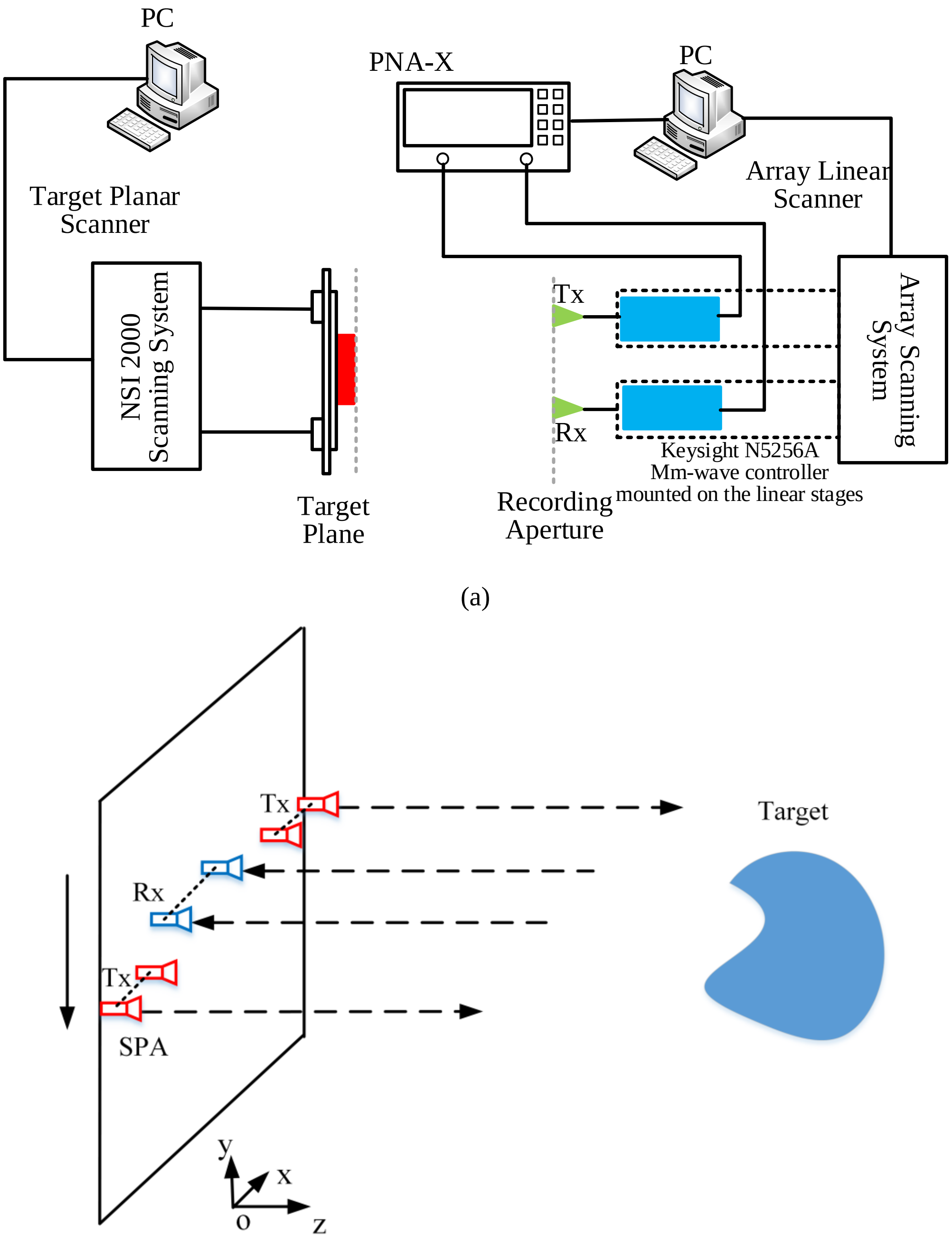

(a)

(b)

Figure 5- 2. (a) Schematic (b) Array configuration of practical THz-SPA experimental imaging system

5.2. Analysis on Realistic Simulation and Measured Imaging Results

5.2.1. 220 GHz Imaging Performance

I. Analysis on Effect of TR Separation

Because exact positions of each Tx and Rx elements are used to calculate phases for imaging of GSAFT as depicted in equation (2- 14) [2], we can theoretically investigate the point spread function (PSF) defined by equation (2- 10) in MATLAB to study the effect of separation between Tx and Rx arrays, which does not take account of scattering and multi-reflections. Besides, it is assumed that all reflections do not have any attenuation during one return or any amplitude scaling for different paths to simplify the case. The mechanical scanning length in simulation is 0.3 m with an interval of 4 mm. Accordingly, the PSFs at 220 GHz with a 1.1 m target distance of three schemes separated by a Tx/Rx track gap (S_{TR}) of 121 mm, 181 mm and 241 mm have been simulated respectively, as shown in Figure 5- 3. In Figure 5- 3 (a), we can see that all configurations nearly have same PSFs along the electronic scanning direction except for a little shift of null in both sides. However, the PSF along the vertical direction of lined-up SPA has the deepest null. The null is getting shallower and shifts with the increase of the track separation. Therefore, it should be better to keep this separation as small as possible in implementation. Finally, we have chosen 181 mm as the separation distance since this is the minimum gap for the smooth scanning movement of Tx and Rx mixers heads.

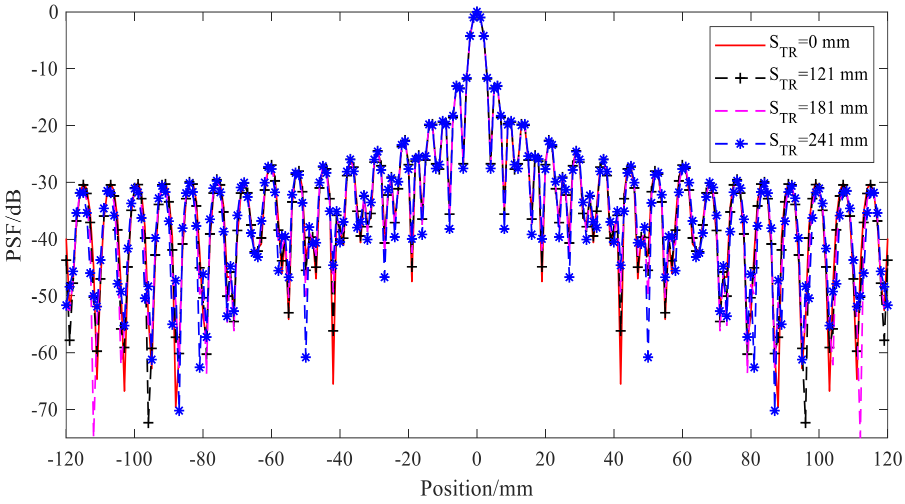

(a)

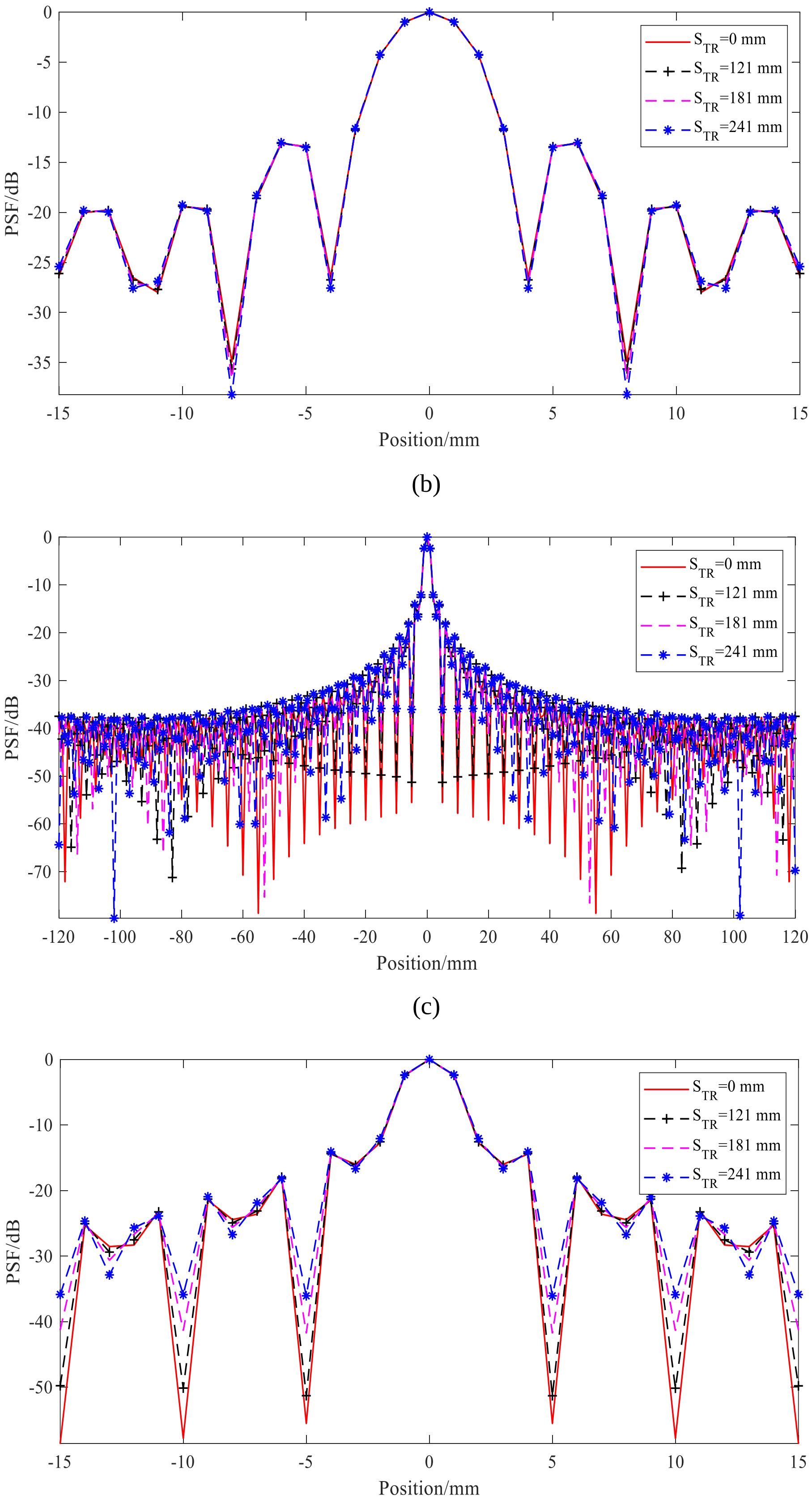

(b)

(c)

(d)

Figure 5- 3. 220 GHz PSFs of different SPA at 1.1 m. (a) Full view (b) Main beam zoomed along the horizontal direction and (c) Full view (d) Main beam zoomed along the vertical direction

We firstly conducted simulations of schemes in Table. 5- 1 (same as Table. 3- 1 in chapter 3.2.1) where the SPA is configured in a line as Figure 5- 1 (a), the mechanical scanning length is 0.2 m. The SPA consists of 8 Tx and 8 Rx with the element having a 3 dB beam width of about 42° and a peak gain of 12.95 dB as shown in Figure 3- 3. The target replaced by a model of realistic rectangular metallic plate (145 mm × 120 mm × 5 mm). There are a number of holes (diameters of 6 cylinder holes are 6 mm and 7 mm; top and bottom diameters of 4 screw holes are 5 mm and 8 mm) on the target

Table. 5- 1. Schemes (8 Tx & 8 Rx) with different Tx element spacing and same 41 mechanical scanning spots (dv = 4 mm, total scanning length: 160 mm)

Parameters(mm) / **Schemes**	**dt**	**FOV**	**Lt**	**Ld**	**Theoretical resolution**
Scheme I	2.5 (1.83λ)	80	90	160	$\frac{1.364}{160} \cdot 1000 = 8.525$
Scheme II	4 (2.93λ)	128	144	256	$\frac{1.364}{256} \cdot 1000 = 5.328$
Scheme III	6 (4.40λ)	192	216	384	$\frac{1.364}{384} \cdot 1000 = 3.552$

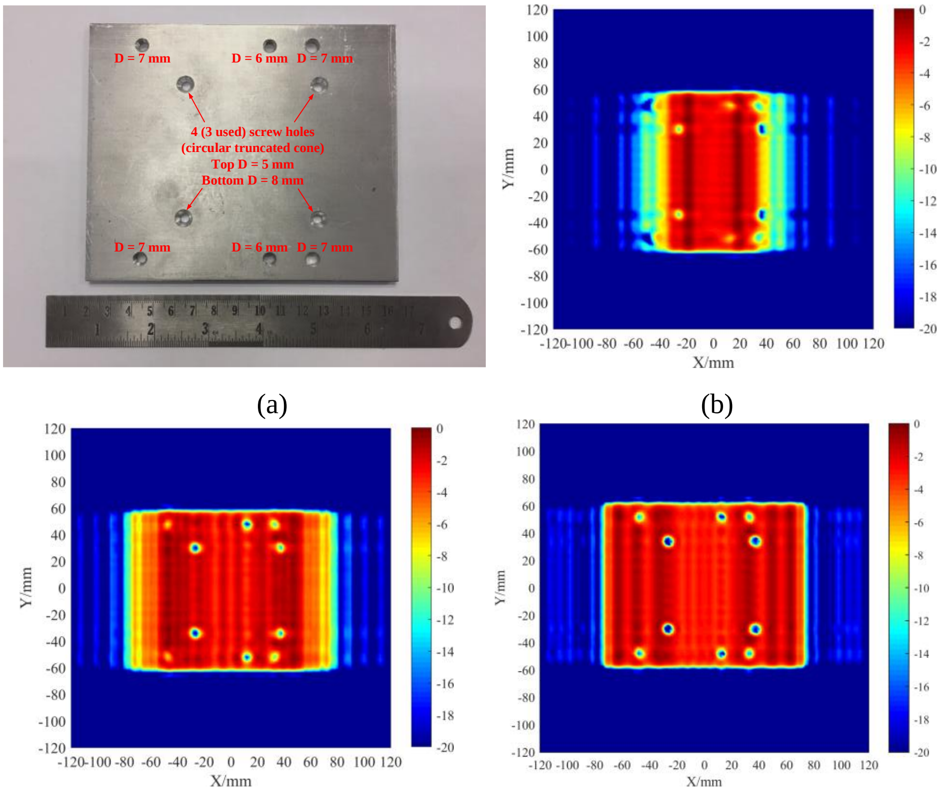

(a) (b)

(c) (d)

Figure 5- 4. (a) Target photo and reconstructed images with 20-dB dynamic range of (b) Scheme I and (c) Scheme II and (d) Scheme III in Table. 3- 1 in Chapter 3.2.1

that can be used as resolution identification. Moreover, the distance D to the target is set to be 1.1 m. The photograph of the realistic target and the images reconstructed with simulated data in different configurations have been shown in Figure 5- 4. As shown in Figure 5- 4 (b), when the real array aperture is narrower than the target width (like scheme I, 90 mm), the target cannot be imaged completely. Therefore, in scheme II with a FOV slightly smaller than the target width, the target can be imaged with blurred edges as shown in Figure 5- 4 (c). In scheme III, the target can be imaged completely as shown in Figure 5- 4 (d). Moreover, scheme III shows a superior resolution in Figure 5- 4 (d) compared to that in Figure 5- 4 (c).

In order to study the effect caused by the separation S_{TR} of Tx and Rx, we use configurations of Figure 5- 4 (d) but replace the mechanical scanning length with 0.3 m to conduct further simulation [3]. The reconstructed images of the testing target locating in the centre (0, 0) of the scanning area illuminated by the SPA, configured as in Figure 5- 1 (a) and (b), are compared in Figure 5- 5 (a) and (b), respectively.

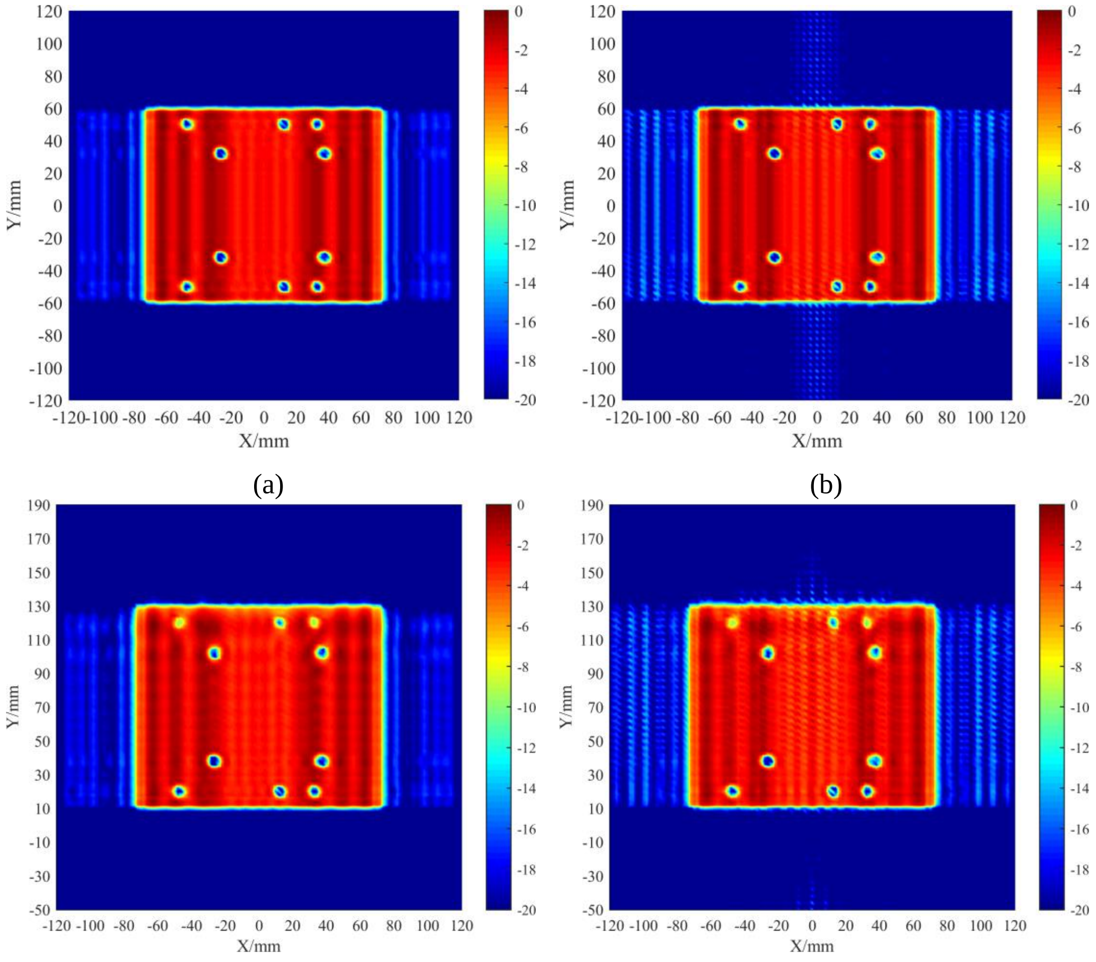

(a) (b)

(c) (d)

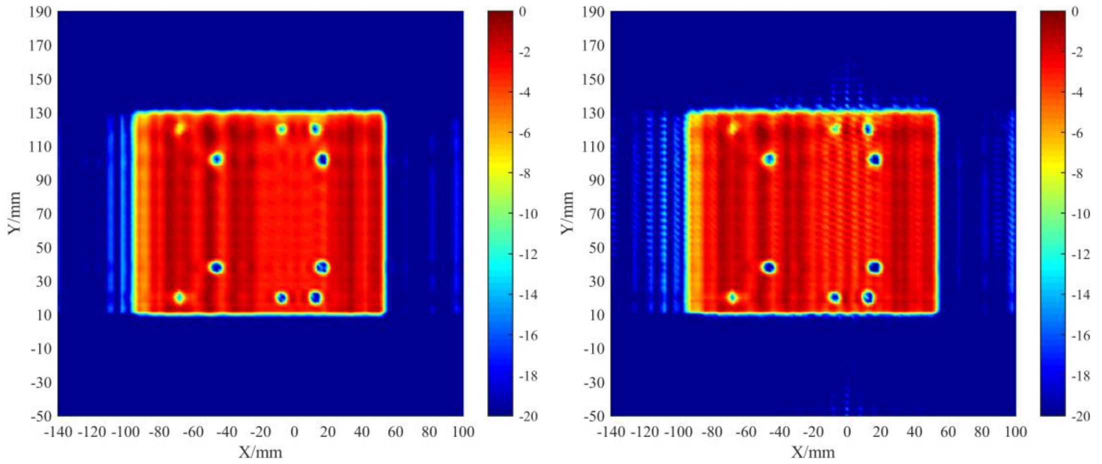

(e) (f)

Figure 5- 5. Reconstructed images with 20-dB dynamic range of scheme III in Table. 3- 1. The target placed at the centre A(0,0) of the SPA with Tx and Rx (a) lined up (b) separated vertically by 181 mm. The target palced at B(0,70) of the SPA with Tx and Rx (c) lined up (d) separated vertically by 181 mm. The target palced at C(-20,70) of the SPA with Tx and Rx (e) lined up (f) separated vertically by 181 mm

Similarly, the reconstructed images of the testing target locating in the B and C of the scanning area, illustrated in Figure 5- 6, are compared in Figure 5- 5 (c), (d) and (e), (f), respectively. The results has indicated that different target positions within the FOV will affect the image quality slightly. The vertical separation (S_{TR}) of 181 mm between Tx and Rx will not affect the simulated images much, only adding a few artificial shades, which agrees with the analysis in Figure 5- 3.

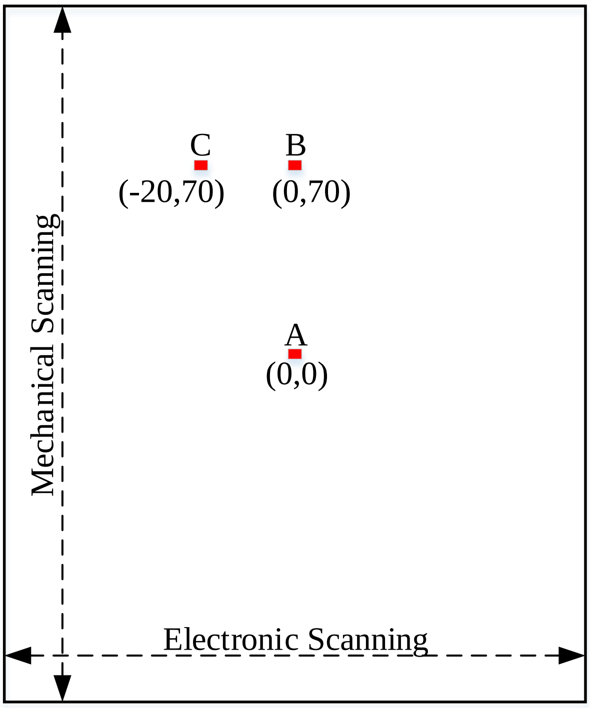

Figure 5- 6. Target center locates at positions A, B and C of the scanning area

II. Results of Imaging on Pure Metallic Target Using the Experimental Set-up

In order to investigate the effects caused by the beam properties, a WR3 band standard pyramidal horn having a peak gain of 23.68 dB and about 12° HPBW at 220 GHz has been used as the SPA element in imaging simulation study, which is the same as the one used in the experiment. Therefore, four configurations indicated in Table. 5-2 have been simulated, and the reconstructed images are compared in Figure 5- 7. Comparing Figure 5- 7 (a) with Figure 5- 5 (b) in different beam properties, we can see that the sharp beam has a deteriorated image quality in the central part of the image that corresponds to the SPA centre, which is caused by a narrower Tx illuminating area. This has been further verified when compared Figure 5- 7 (a) and Figure 5- 7 (c), the image quality in the central part has been improved at a longer object distance with widening of the beam-width. Besides, it demonstrates that the image always has the best quality in the centre of scanning area if comparing Figure 5- 7 (a) with Figure 5- 7 (b) in which the target is placed at (-30,-20) [4]. Finally, when comparing Figure 5- 7 (c) and Figure 5- 7 (d) in different mechanical scanning interval of dv, we have not seen an obvious improvement when the interval dv is reduced from 4 mm to 2.5 mm. That is because the 4 mm mechanical scanning interval has already reached to a theoretical interval of 4.12 mm derived by equation (2- 22), for an acceptable resolution [5, 6].

Table. 5- 2. Comparison between simulated and experimental results with a 0.3 m mechanical scanning length and the SPA referring to Figure 5- 2(b) consisting of WR3 pyramidal standard horns

Cases	Target Position/mm	dv/mm	Identified holes
Config.S1 in Figure 5- 7 **(a)**	(0,0) at 1.1 m	4	10
Config.S2 in Figure 5- 7 **(b)**	(-30,-20) at 1.1 m	4	10
Config.S3 in Figure 5- 7 **(c)**	(0,0) at 1.4 m	4	10
Config.S4 in Figure 5- 7 **(d)**	(0,0) at 1.4 m	2.5	10
Config.M1 in Figure 5- 9**(a)**	at 1.1 m	4	8
Config.M2 in Figure 5- 9**(b)**	at 1.1 m	4	9
Config.M3 in Figure 5- 9**(c)**	at 1.4 m	4	10
Config.M4 in Figure 5- 9**(d)**	at 1.4 m	2.5	10

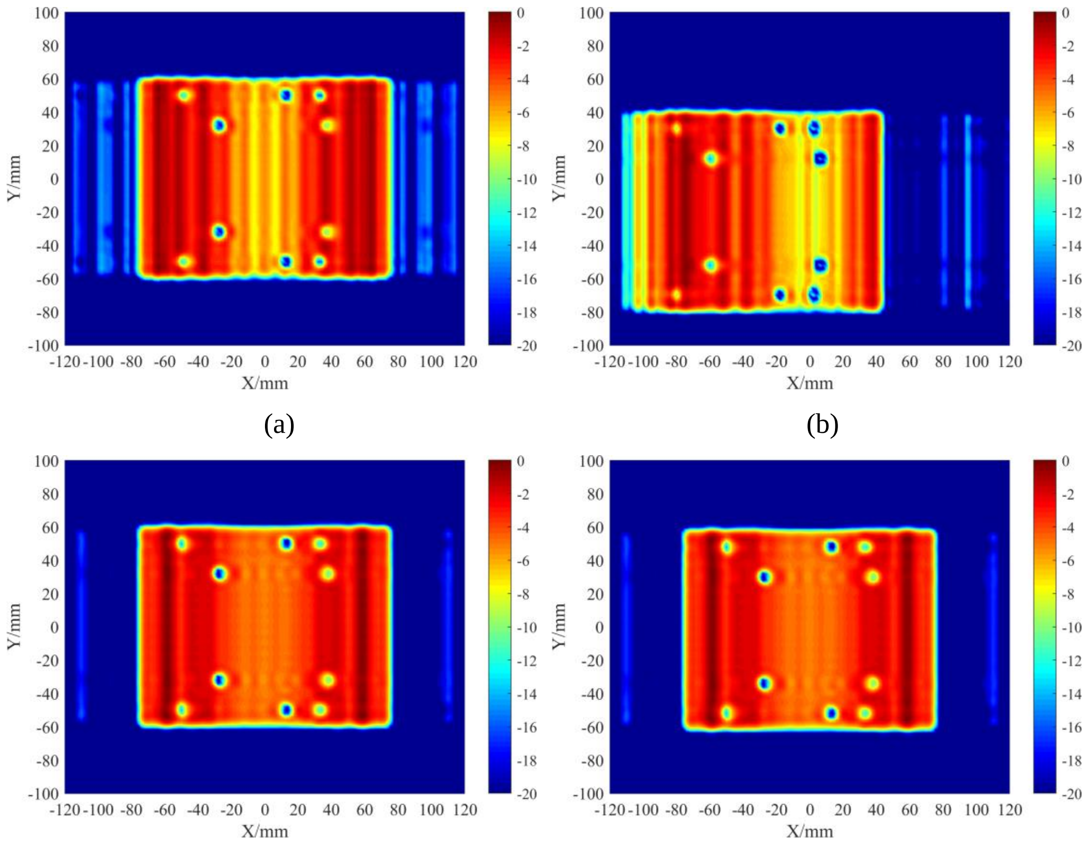

(a) (b)

(c) (d)

Figure 5- 7. Images with 20-dB dynamic range reconstructed by using simulated data in various configurations in Table. 5- 2. (a) Configuration S1 (b) Configuration S2 (c) Configuration S3 and (d) Configuration S4

Figure 5- 8 (a), (b) and (c) show the photographs of experimental set-up of the whole system, the close view of the linear scanning stages that imitates the sparse periodic array, and the NSI 2000 scanning system [1] with the mounted target whose movement inversely imitates the mechanical scanning of the array to the target in practice. The horns utilized in the experiment are WR3 (220 – 325 GHz) standard pyramidal horns with a peak gain of about 23.81 dB at 220 GHz, and the typical output power from the THz mixer head at 220 GHz is -13 dBm (0.05 mW).

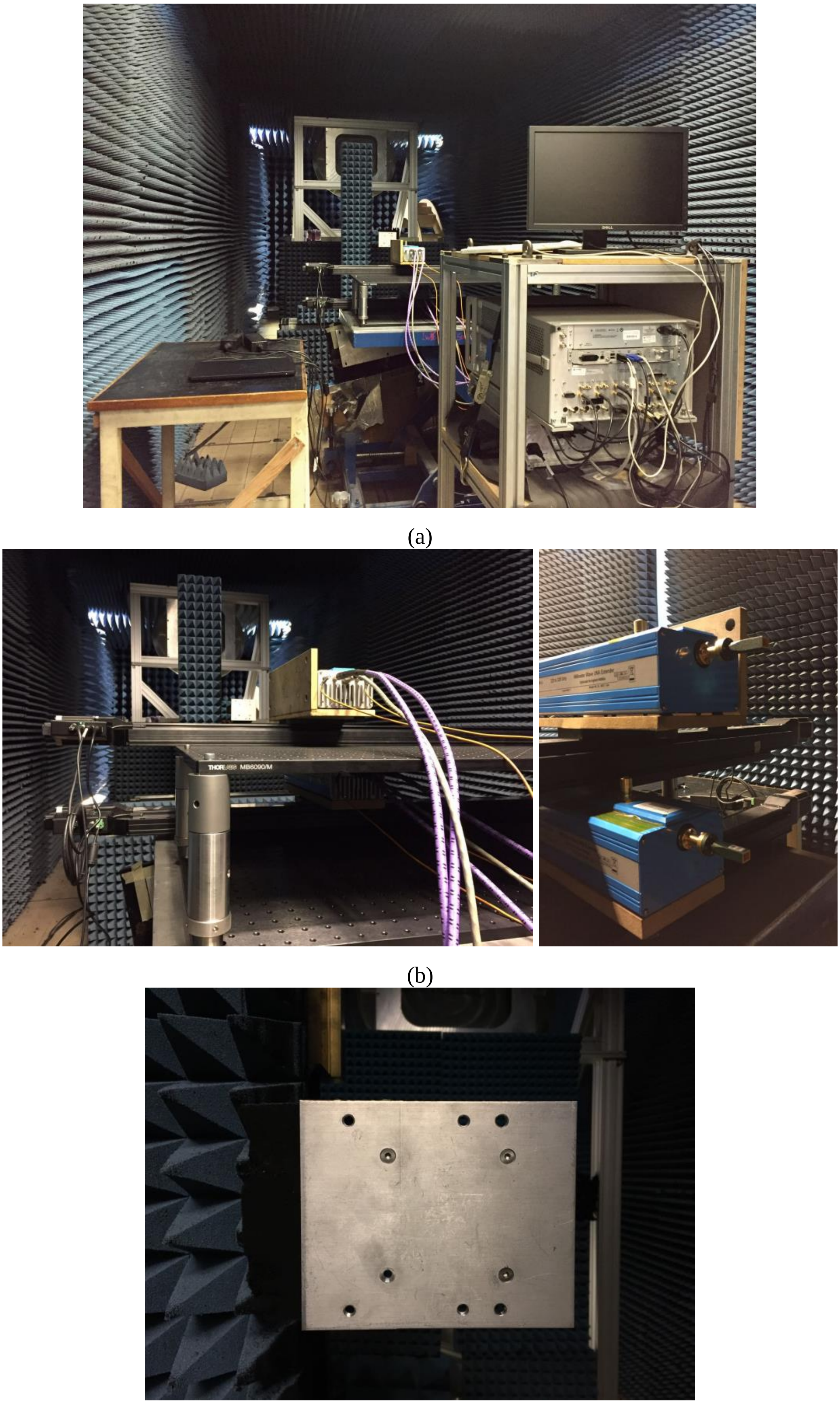

(a)

(b)

(c)

Figure 5- 8. The photographs of the experimental set-up. (a) Full view of the system, close view of (b) the horizontal linear scanning stages and (c) target mounted on the NSI 2000 vertical scanning system

The experimental images of this metallic plate target properly placed at the distance of 1.1 m and 1.4 m are reconstructed in Figure 5- 9 (a), (c) and (d). The target position in Figure 5- 9 (b) moves 40 mm at x-axis compared to Figure 5- 9 (a). It is out of the FOV, so the left edge of target cannot be imagined. In addition, the simulated results in Figure 5- 7 have shown that a little farther target distance can help to improve the image quality when the sharp beam is used. This has been experimentally verified again by comparing Figure 5- 9 (a) and Figure 5- 9 (c) with different target distance. In addition, the vertical mechanical scanning intervals of 4 mm and 2.5 mm with a same scanning length of 0.3 m at a target distance of 1.4 m are reconstructed in Figure 5- 9 (c) and (d) as well. Theoretically, a finer scanning interval can provide a higher image SNR based on equation (2- 25) [5, 7]. Accordingly, the image SNRs in Figure 5- 9 (c) and (d) are 20.49 dB and 22.27 dB, respectively. There is only 1.78 dB improvement because this improvement is becoming less with the increase in sampling interval and the 4.0 mm sampling interval has already reached to the theoretical sampling interval threshold of 4.12 mm derived by equation (2- 22) [5, 6].

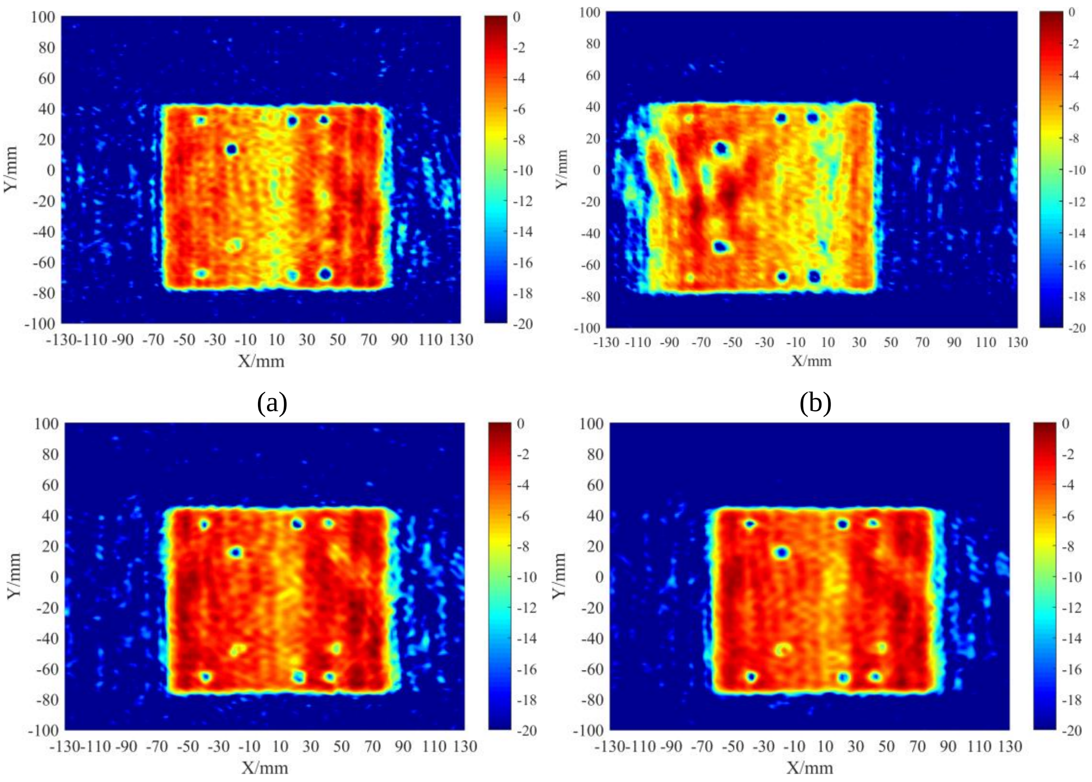

(a) (b)

(c) (d)

Figure 5- 9. Images with 20-dB dynamic range reconstructed by using experimental data in various configurations in Table. 5- 2. (a) Configuration M1 (b) Configuration M2 (c) Configuration M3 (d) Configuration M4

Therefore, the experimental results are summarized in Table. 5- 2 in comparison with the simulated results. The number of holes that can be identified are used to be a rough measure of imaging performance. It is worth mentioning that there are three fixing screws in the experiments that fill the holes, which make them barely visible in the reconstructed images. Therefore, taken account of the target lateral position along x-axis, the experimental results have already shown an excellent consistency with the simulated results in Figure 5- 7. Therefore, the feasibility of the proposed THz imaging scheme is verified in experiment.

In addition to above single-pass synthetic aperture imaging, the proposed SPA imaging system can work in a multi-pass interferometric synthetic aperture imaging mode, as introduced in 2.3.3.I. This mode allows the SPA to move the positions along the electronic scanning direction, collecting datasets of several single-pass synthetic aperture image to synthesize a multi-pass interferometric synthetic aperture image, as depicted in equation (2- 15) based on traditional GSAFT.

We have also tested this imaging mode in the experiment using the proposed experimental set-up and same configurations referring to Figure 5- 9 (a) and (c). Since we have used 1 Tx and 1 Rx moving along the electronic scanning direction to imitate the SPA, we can use the movement of target along the electronic scanning direction to realize this interferometric measurement. In chapter 3.2.1, we have demonstrated in simulation that the target needs to be placed within the FOV of $0.5 \cdot dt \cdot Nt \cdot Nr$ in order to reconstruct the image completely (FOV edge is at ±96 mm in this configuration). This has been further verified by the reconstructed single-pass synthetic aperture imaging results in Figure 5- 10 and Figure 5- 11 where the target is placed at 1.1 m and 1.4 m from the array, respectively. And the target movement interval at x-axis is 20 mm. Accordingly, when the target moves out of the FOV along x-axis, the part of the target cannot be imagined. Furthermore, the difference caused by different target positions has also been revealed in simulated results in Figure 5- 7 (a), (b) and experimental results in Figure 5- 9 (a), (b). However, this impact will become relatively slight when the target moves within the FOV as demonstrated in Figure 5- 5, Figure 5- 10 (c), (d) and Figure 5- 11 (b), (c).

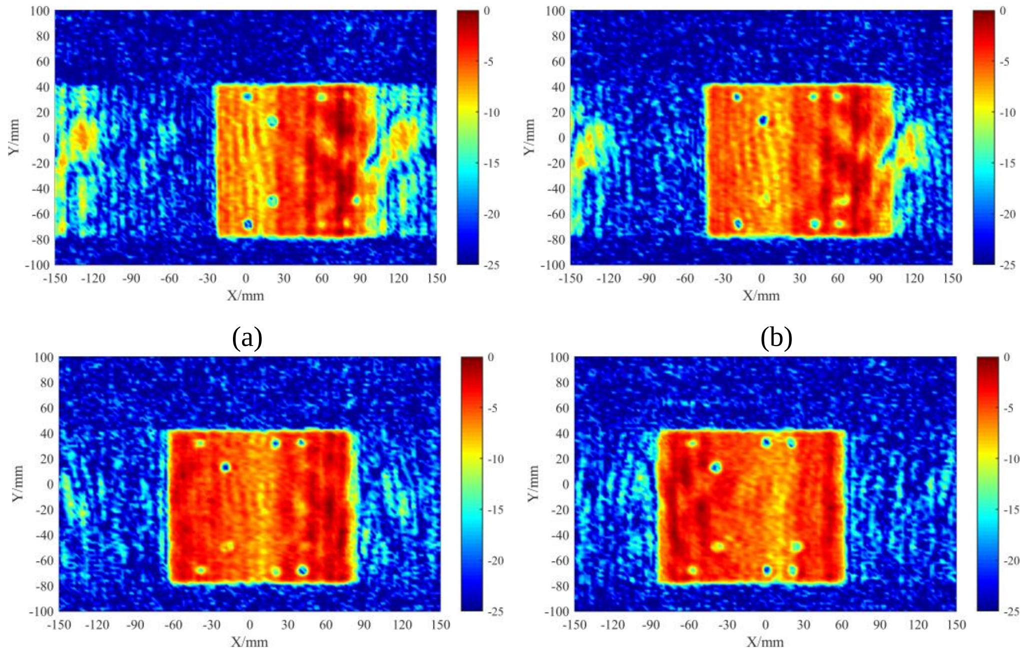

(a) (b)

(c) (d)

Figure 5- 10. Reconstructed single-pass synthetic aperture images with 25-dB dynamic range of target at different x-axis positions. (a) Position x1 (b) Position x2 (c) Position x3: Figure 5- 9(a) (d) Position x4. (Mechanical scanning length is 0.3 m with an interval of 4 mm, target distance = 1.10 m)

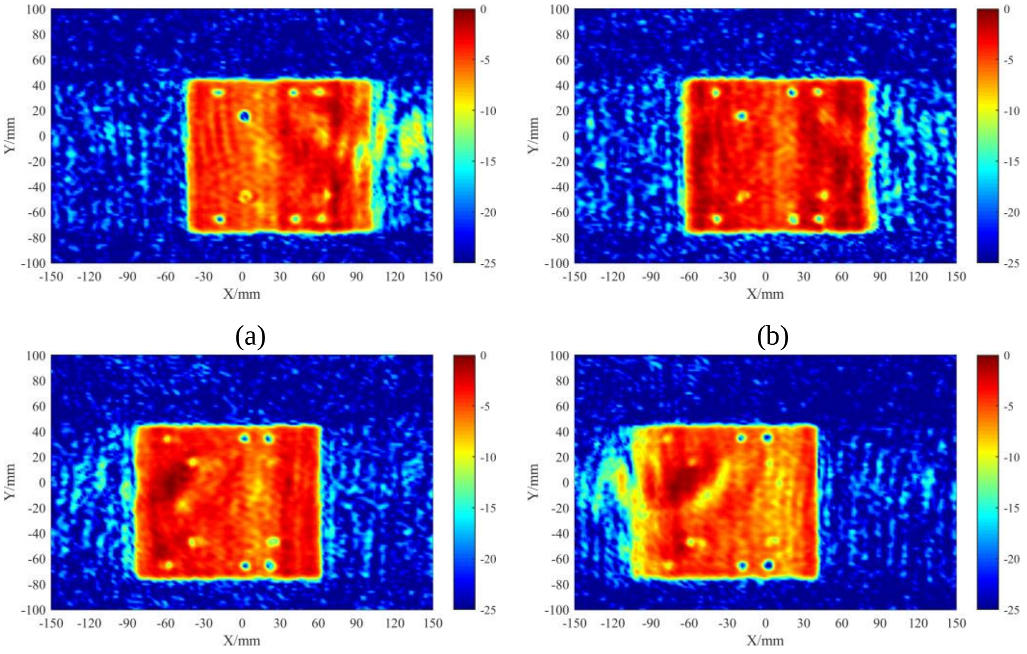

(a) (b)

(c) (d)

Figure 5- 11. Reconstructed single-pass synthetic aperture images with 25-dB dynamic range of target at different x-axis positions. (a) Position x1 (b) Position x2: Figure 5- 9(c) (c) Position x3 (d) Position x4. (Mechanical scanning length: 0.3 m, interval: 4 mm, target distance: 1.40 m)

Two images reconstructed by equation (2- 15) using multi-pass interferometric synthetic aperture focusing technique have been shown in Figure 5- 12 (a) and (b), corresponding to Figure 5- 10 and Figure 5- 11. The corresponding image signal to noise ratios (SNRs) defined as the ratio of difference in brightness between bright and dark areas to the standard deviation of the dark area in equation (2- 25) are compared in Figure 5- 13. Comparing to the single-pass synthetic aperture imaging results, the multi-pass interferometric synthetic aperture technique has improved image quality significantly including image contrast and SNR. In Figure 5- 12 (a), there are 9 holes that can be identified which is more than any image in Figure 5- 10. In addition, the artifacts in background (blue area) are less while the target image (red area) is uniform, so the contrast is improved, leading SNR increases by about 2.76 dB. Similarly, the image SNR increases by about 4.60 dB after using multi-pass interferometric synthetic aperture technique in Figure 5- 12 (b). In addition, because the target image has been reconstructed more completely, the image SNRs in Figure 5- 11 and Figure 5- 12 (b) are higher than Figure 5- 10 and Figure 5- 12 (a).

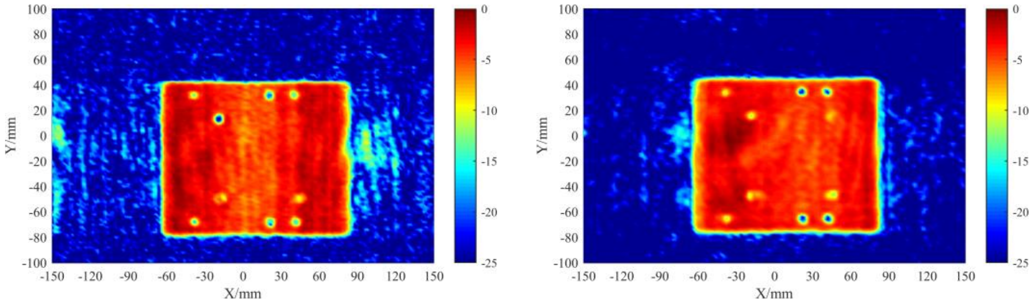

(a) (b)

Figure 5- 12. Reconstructed multi-pass interferometric synthetic aperture images with 25-dB dynamic range based on (a) Figure 5- 10 (b) Figure 5- 11

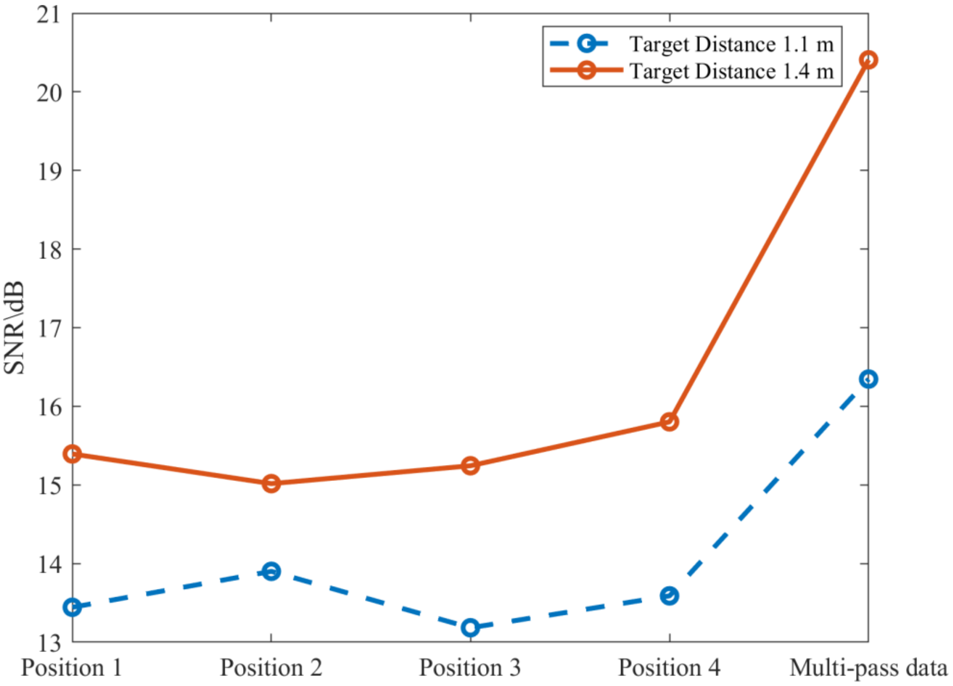

Figure 5- 13. Image signal to noise ratios (SNRs) of Figure 5- 10, Figure 5- 11 using single-pass synthetic aperture technique and Figure 5- 12 using multi-pass interferometric synthetic aperture technique

III. Experimental Results of Imaging on Simplified Body Chunk

In addition to the pure metallic target, the target of patches etched on the dielectric substrate (260 mm × 180 mm × 1.6 mm) imitating the mannequin as shown Figure 5- 14 have been tested in the experiment. The SPA consists of 8 Tx and 8 Rx with WR3 standard pyramidal horns operating at 220 GHz and the Tx element spacing is 6 mm. The target distance is 1.40 m and mechanical scanning length is 0.5 m with a step of 2.5 mm, so the theoretical resolutions are 3.20 mm and 1.90 mm along horizontal and vertical directions according to equation (2- 22).

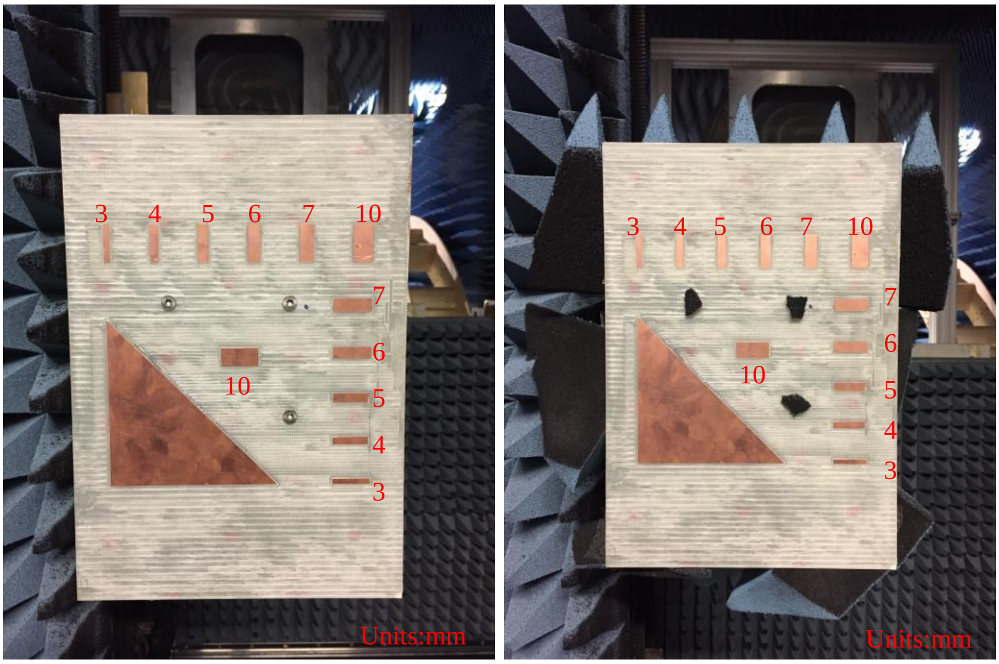

(a) (b)

Figure 5- 14. The photograph of target under test (a) without and (b) with some absorbers

The reconstructed single-pass images of the target in Figure 5- 14 (a) have been shown in Figure 5- 15 (a) to (c) with a 10 mm position variation along the electronic scanning direction and the multi-pass interferometric synthetic aperture image has been shown in Figure 5- 15 (d). Similarly, the reconstructed single-pass images of the target in Figure 5- 14 (b) have been shown in Figure 5- 16 (a) to (e) and the multi-pass interferometric synthetic aperture image has been shown in Figure 5- 16 (f). The corresponding image SNRs are compared in Figure 5- 17. The single-pass synthetic aperture images show that the artifacts in the background are high while high power (red area) spreads on the non-metallic surface, which degrades image contrast indicated as low SNRs. It is because of deteriorating focusing caused by much more scattering from the unsmoothed surface of dielectric substrate. As a result, this should be significantly improved by using multi-pass interferometric synthetic aperture technique and more datasets, which has been verified successfully in Figure 5- 15 (d) and Figure 5- 16 (f) where the image SNRs improve by about 4.10 dB and 8.50 dB indicated in Figure 5- 17.

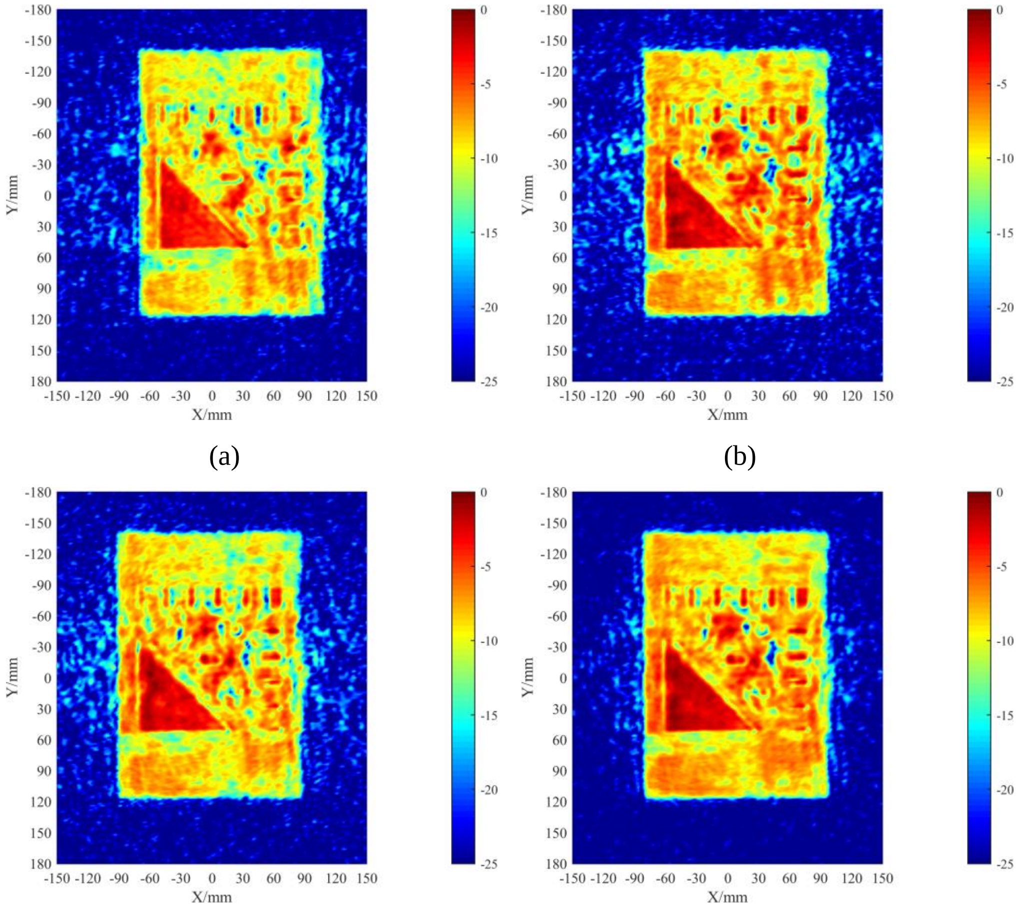

(a) (b)

(c) (d)

Figure 5- 15.(a)-(c) Single-pass synthetic aperture images of the target shown in Figure 5- 14(a) placed differently with an interval of 10 mm along the electronic scanning direction and (d) the corresponding multi-pass interferometric synthetic aperture image(25-dB dynamic range)

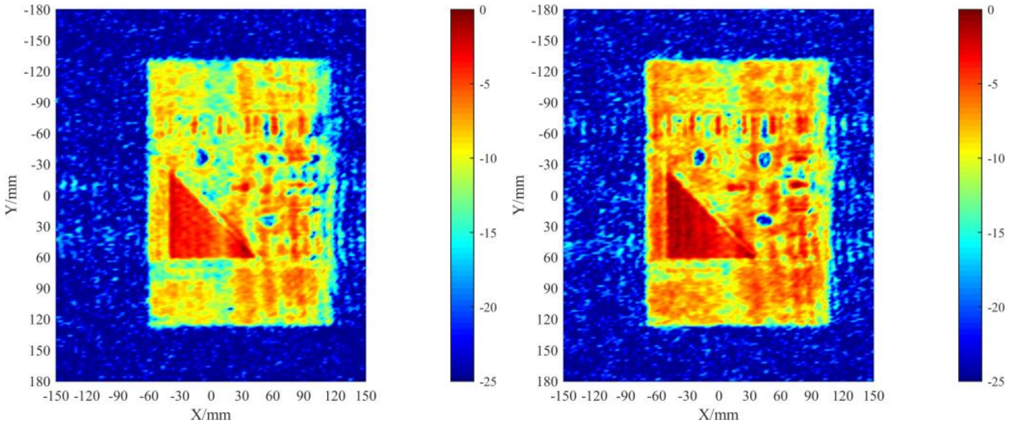

(a) (b)

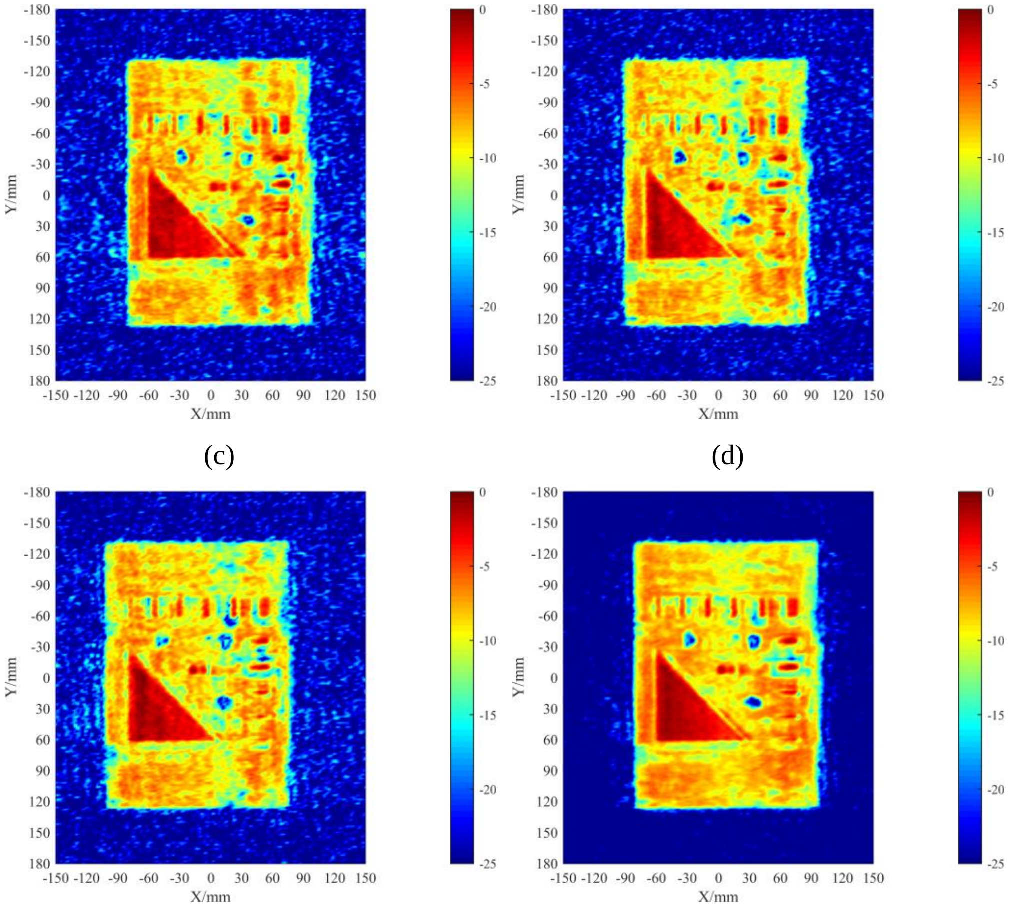

(c) (d)

(e) (f)

Figure 5- 16. (a)-(e) Single-pass synthetic aperture images of the target shown in Figure 5- 14(b) placed differently with an interval of 10 mm along the electronic scanning direction and (f) the corresponding multi-pass interferometric synthetic aperture image (25-dB dynamic range)

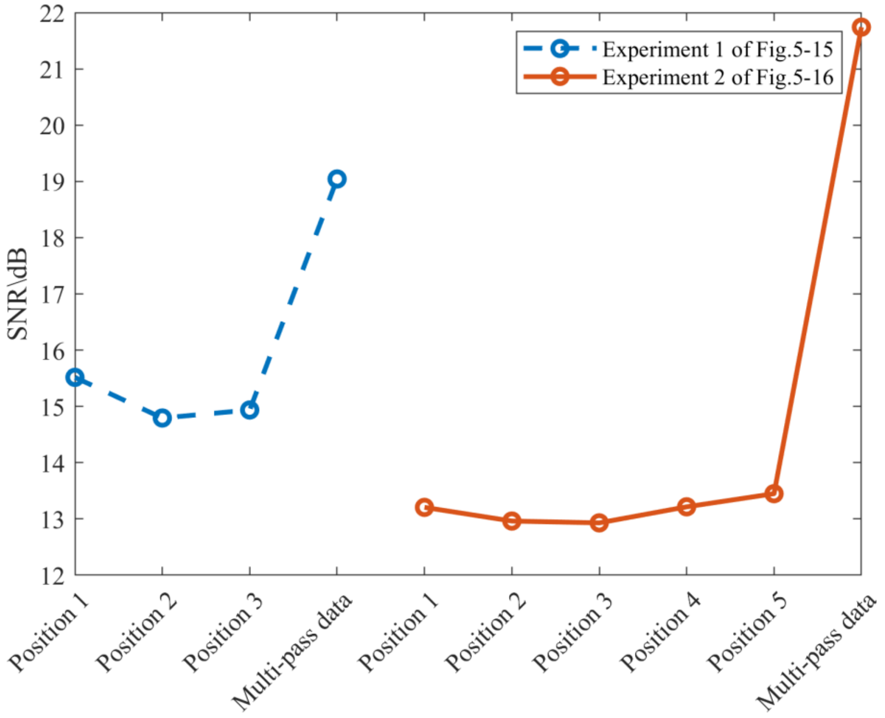

Figure 5- 17. Image signal to noise ratios (SNRs) of Figure 5- 15 and Figure 5- 16

Therefore, the multi-pass interferometric synthetic aperture imaging technique can be used in the proposed THz-SPA imaging system to improve the imaging performance. This can be simply deployed by allowing the SPA to move the position along the electronic scanning direction. Since the scanning aperture is not increased too much while the sampling data is dense, the image contrast and SNR can be improved more obvious. However, this approach will cost more time on data acquisition. Therefore, this kind of system in practice can normally operate in single-pass synthetic aperture mode one by one and produce each corresponding image simultaneously. When the single-pass synthetic aperture image is clear to identify, the imaging is finished early. If not, it continues scanning next pass and the improved multi-pass interferometric synthetic aperture image can be finally produced to deal with complex circumstance.

5.2.2. 94 GHz Imaging Performance

In comparison, we have investigated the imaging at 94 GHz using the traditional GSAFT imaging algorithm on three configurations as illustrated in Figure 5- 18 and the parameters are listed in Table. 5- 3. The experimental set-up is same with Figure 5-2. Both configurations 1 and 2 have 10 Tx elements and 10 Rx elements but with different Tx element spacing, so the effective length of configuration 2 is twice as long as configuration 1. In contrast, we keep the Tx element spacing in configuration 1 and 3 same but double the number of Rx elements in configuration 3, so the effective length is doubled as well, same as configuration 2. Besides, we made the last left-side Tx element denoted by letter **A** as a reference whose positions in three configurations are same. Meanwhile, the target has been placed slightly to the left side, closing to the referenced Tx element to assure a good illumination and the corrugated horns utilized in the experiments as shown in Figure 5- 19 have a measured peak gain of about 17.19 dB and a HPBW at H plane of about 13°. Therefore, the practical resolution taking account of this narrow beam-width can be calculated by equation (2- 15) [6, 8], as shown in Table. 5- 3. The simulations were conducted in the commercial software of FEKO^{TM} by using a horn with a similar HPBW at H plane in comparison with the experiments. So the simulated pattern of the horns used in the imaging simulation and the measured H plane pattern of the horns used in the experiments are compared in Figure 5- 19 in which the operation frequency is 94 GHz.

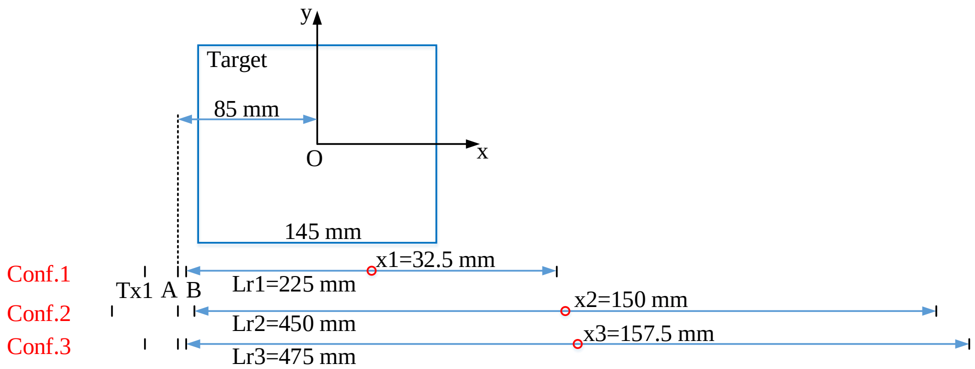

Figure 5- 18. Positions of three SPA configurations in simulation

Table. 5- 3. The parameters in three SPA configurations and practical resolutions calculated by equation (2- 22) (Units: mm)

Configuration	**Tx & Rx**	**Lt**	θ_b	**HPBW**	**Practical Resolutions at 1.3 m**
1 (dt=5)	10 & 10	275	12.075°	13°	7.586 mm
2(dt=10)	10 & 10	550	23.888°	13°	7.048 mm
3(dt=5)	10 & 20	525	22.832°	13°	7.048 mm

Consequently, the images based on the simulated and measured data have been compared in (a) and (b) of Figure 5- 20, Figure 5- 21 and Figure 5- 22, respectively. As shown in the simulated results, three configurations have shown similar resolutions of around 7.0 mm, as indicated in Table. 5- 3. It indicates that the resolution is improving toward to the array centre since the phase shift between sampling points is decreasing while the image quality is deteriorating (here, this means to increasing contrast) since the illumination from the Tx elements placed at two ends is becoming weaker. Therefore, the reconstructed image of configuration 1 has shown the best resolution and image quality since its target is close to both the Tx elements and array centre due to its compact array size. In addition, the resolution in configuration 2 and 3 deteriorates a little since the target is far away from the array centre and the contrast at right edge of the target is worse since the illumination from Tx elements becomes weaker. In contrast, the experimental images have already shown a consistent resolution with the simulated ones except that the image quality (contrast) in a small part in image of configuration 1 deteriorates a little. That is because, in addition to the difference in illumination power at the centre and two edges of the target, the sampling by this SPA technique has one central sampling point missed, as one example of 8 Tx and 8 Rx illustrated in Figure 5- 23. This effect has already been indicated in the simulated image in configuration 1 where the centre position of the array corresponds to the axis x = 32.5 mm in the image. Furthermore, it has also been verified in our simulation and experimental studies at 220 GHz that this issue will become more obvious when the beam width is relatively narrow to the target distance or element spacing. As shown in Figure 5- 19 (b), the pattern (out of HPBW) of the horns used in the experiments is already little bit narrower than the ones in simulation. In addition, the practical sensitivity of the imaging system is not as ideal as the simulated one, which is equivalent to further reducing the beam width. Fortunately, this issue can be solved by reducing the element spacing, using wider beam-width or increasing the target distance.

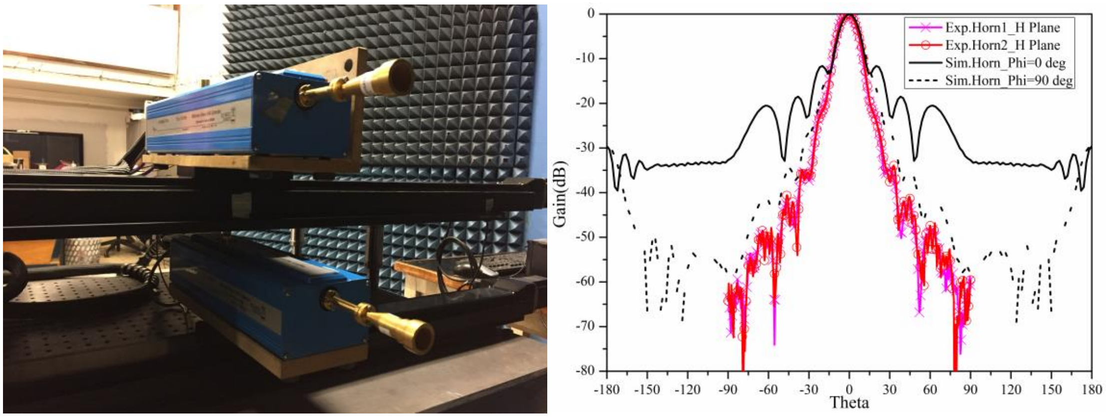

(a) (b)

Figure 5- 19. (a) Linear SPA scanning stages in the experiment with corrugated horns operating at 94 GHz (b) Comparison between the measured H plane pattern of the horns used in the experiments and the simulated pattern in configurations study (f = 94 GHz)

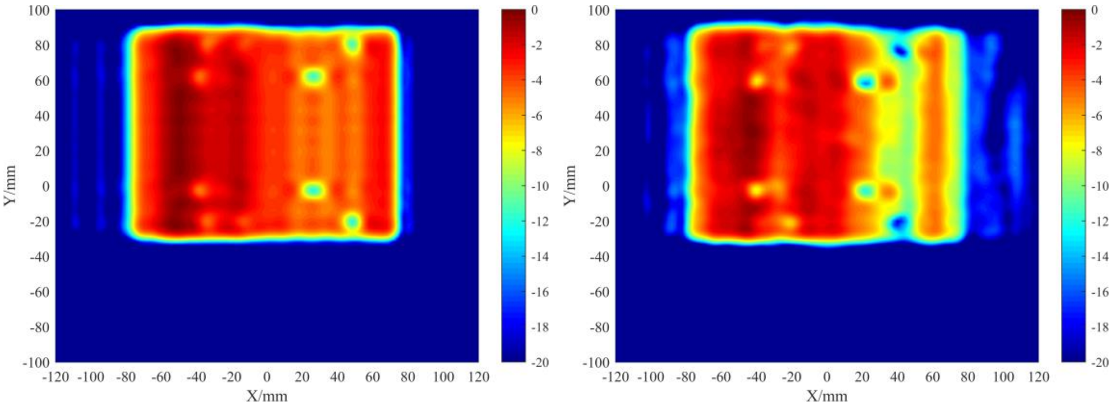

(a) (b)

Figure 5- 20. Reconstructed images of the configuration 1 in Table. 5- 3. (a) Simulated data (b) Measured data (20-dB dynamic range)

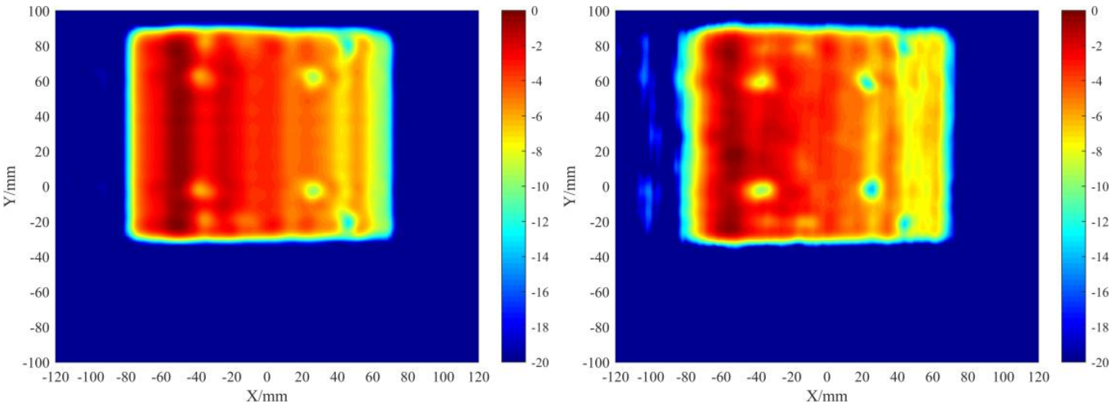

(a) (b)

Figure 5- 21. Reconstructed images of the configuration 2 in Table. 5- 3. (a) Simulated data (b) Measured data (20-dB dynamic range)

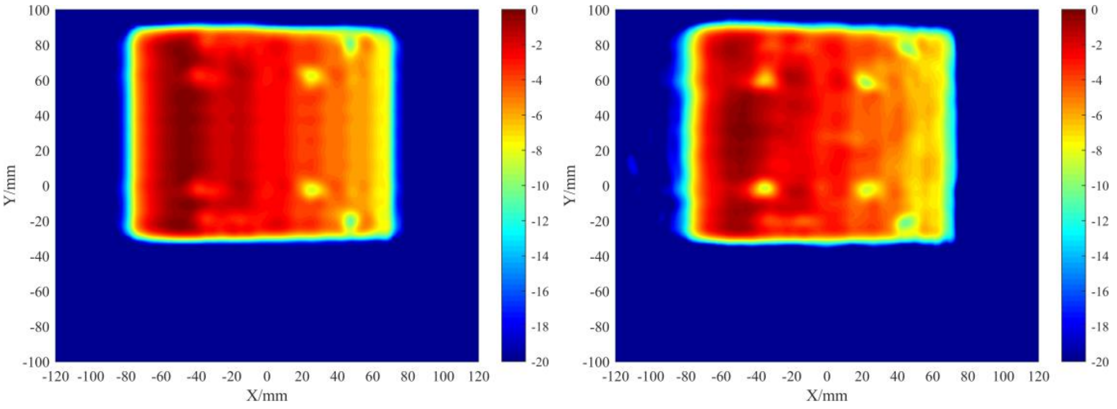

(a) (b)

Figure 5- 22. Reconstructed images of the configuration 3 in Table. 5- 3. (a) Simulated data (b) Measured data (20-dB dynamic range)

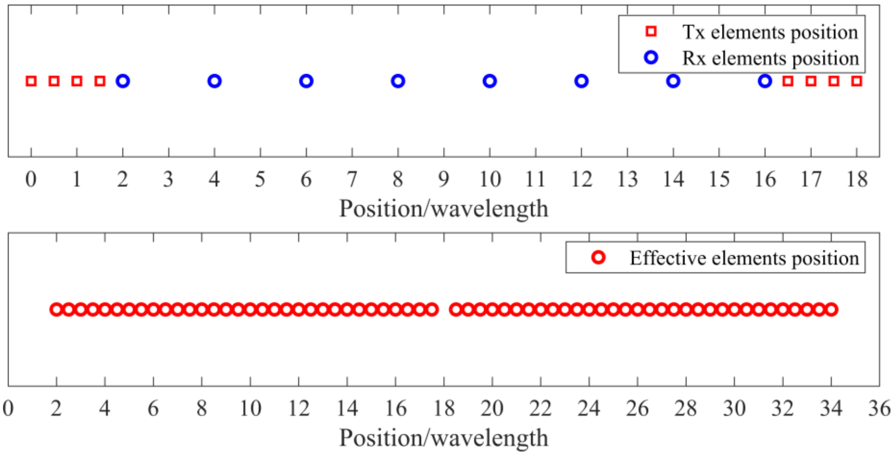

Figure 5- 23. Illustration of a SPA with 8 Tx & 8 Rx and its 64 positions in the effective aperture

5.3. Analysis between the Measured GSAFT and CS Imaging Results

5.3.1. 220 GHz Imaging Performance

We firstly use the simulated echo data of Figure 5- 7 (a) to verify the proposed CS reconstruction approach at THz band [9]. Theoretically, it provides a resolution of 3.906 mm in the X-horizontal direction and 2.50 mm in the Y-vertical direction at target plane, respectively , which corresponds to the first nulls of point spread functions (PSF) in Figure 5- 24. In order to investigate the performance of CS reconstruction, the images reconstructed by GSAFT and CS approaches with 100%, 80%, 50%, 30% simulated sampling data are compared in Figure 5- 25, respectively. The results indicate that the GSAFT reconstruction fails to reconstruct the target image if the full sampling data is not used while the CS approach can still provide a high quality image. Specifically, the image reconstructed by the CS approach with only 50% sampling data can gain almost the same image quality as the GSAFT approach using the full data, only inducing a little more artifacts in the background. In addition, even though the proportion of sampling data used drops to 30%, the target and holes can still be recognized in the CS reconstruction [9].

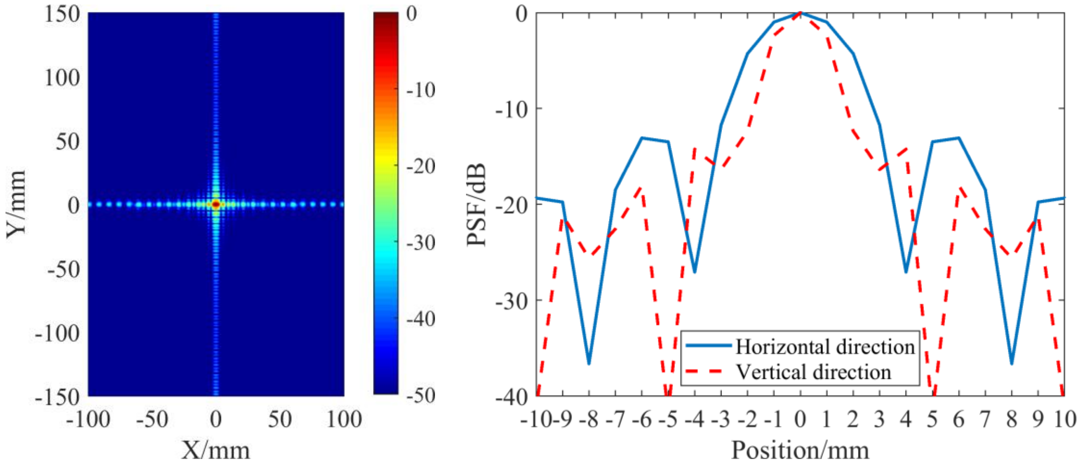

(a) (b)

Figure 5- 24. Point spread function. (a) Planar (b) X = 0 mm (vertical direction) and Y = 0 mm (horizontal direction)

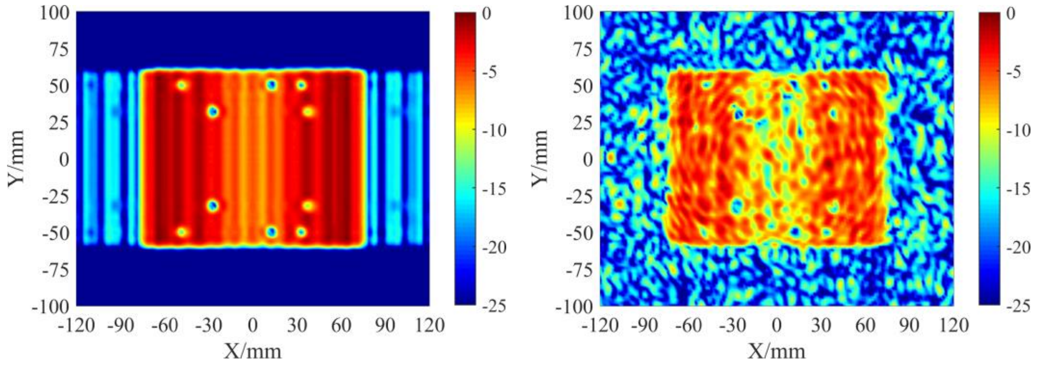

(a) (b)

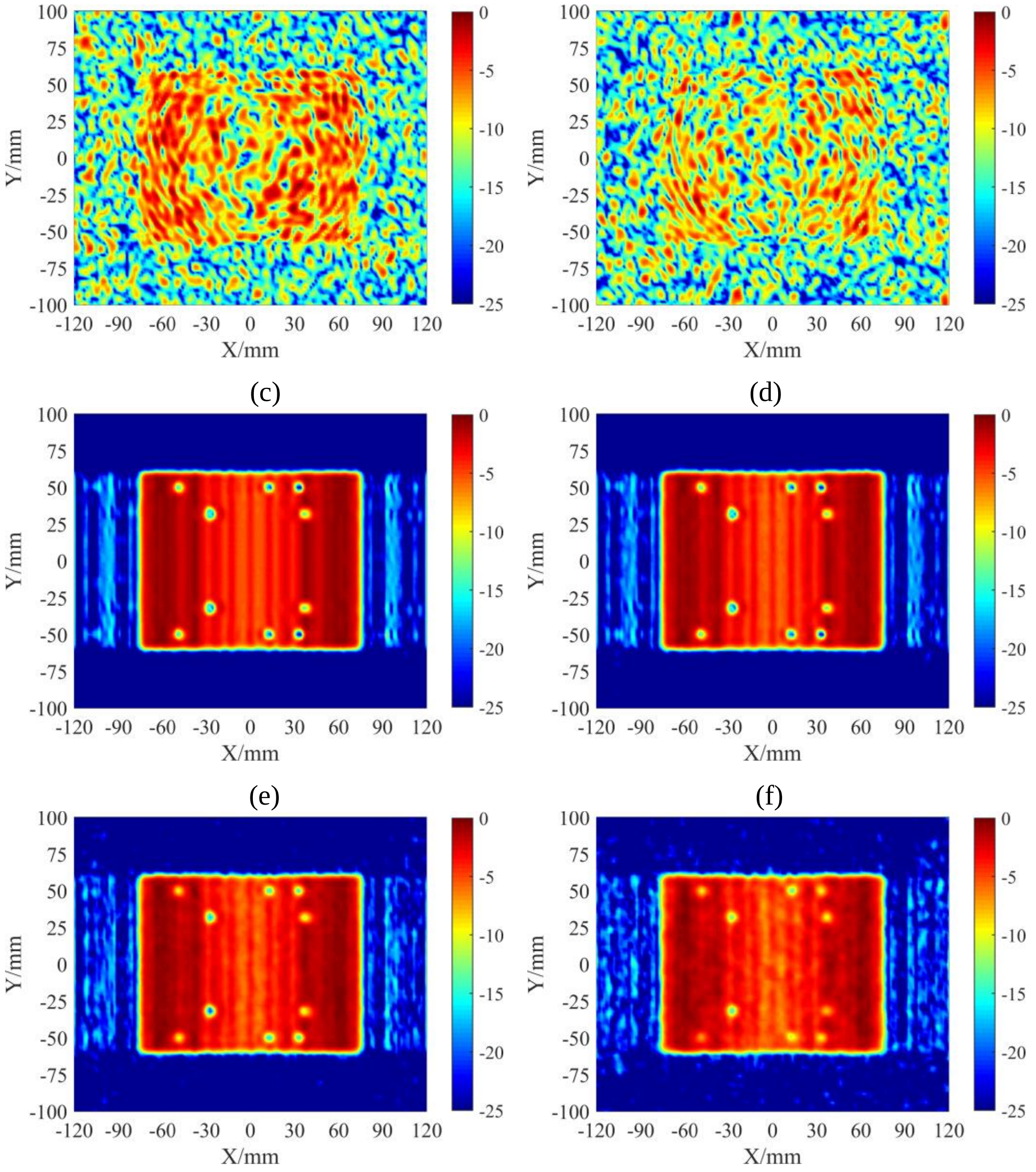

(c) (d)

(e) (f)

(g) (h)

Figure 5- 25. Images with 25-dB dynamic range reconstructed by the GSAFT approach with (a) 100% (b) 80% (c) 50% (d) 30% simulated sampling data; and the CS approach with (e)100% (f) 80% (g) 50% (h) 30% simulated sampling data

To verify it in the experiment, the images reconstructed by GSAFT and CS approaches with 100%, 80%, 50%, 30% measured echo data of Figure 5- 10 (d) are compared in Figure 5- 26, respectively. It is found that the measured results do not look as good as the simulated ones. The resolution is getting poorer and more artifacts appear on the measured images due to the noise and multiple reflections. The smallest holes on the target can still be identified when the image is constructed using CS approach with 80% measured data as shown in Figure 5- 26 (f). However, it is hard to tell the smallest holes when the images are constructed using CS approach with less measured data as shown in Figure 5- 26 (g) (50%) and Figure 5- 26 (h) (30%), respectively. Therefore, one needs to strike a balance between the image quality and reducing sampling data in the practical application.

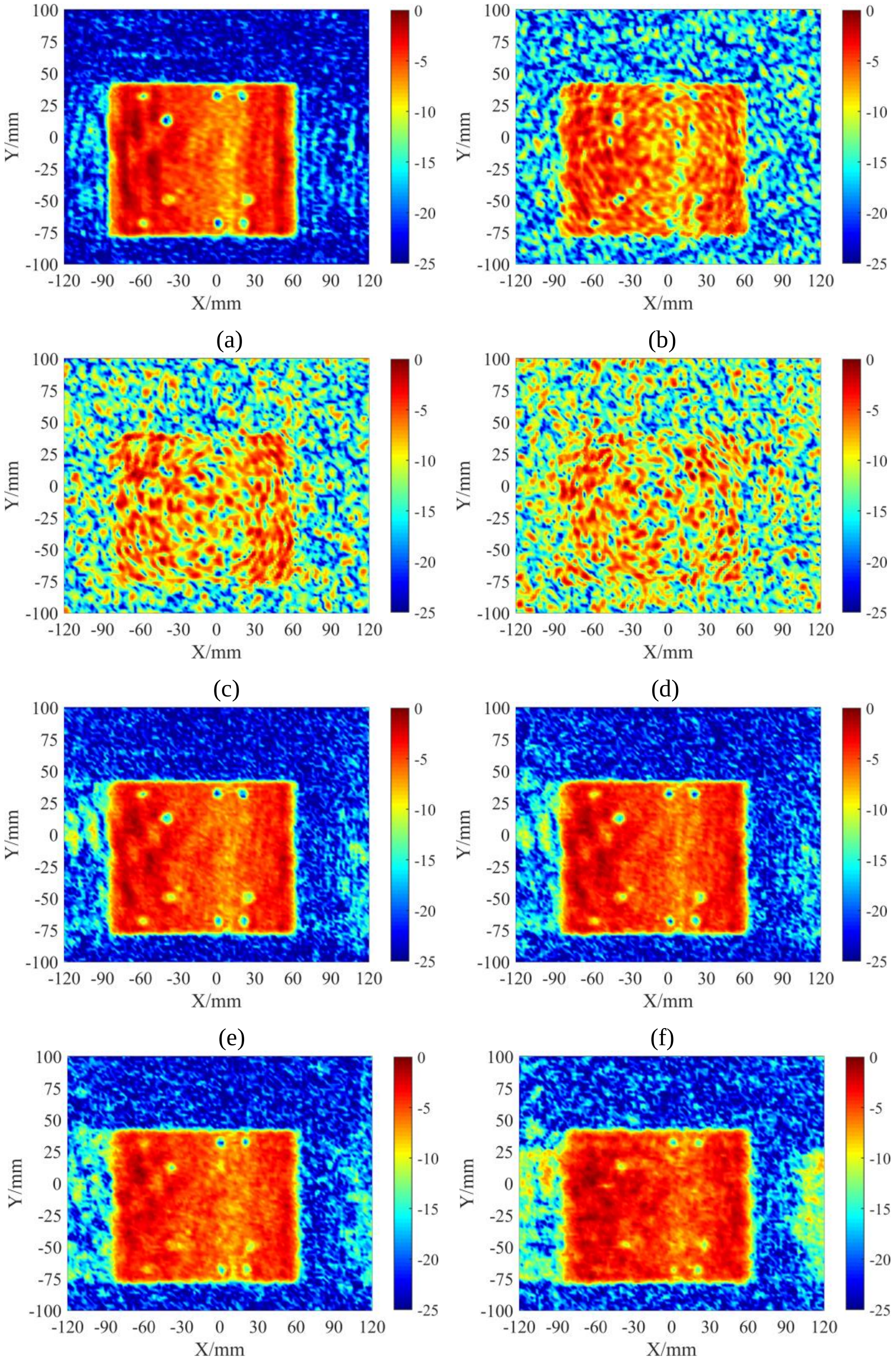

Figure 5- 26. Experimental images with 25-dB dynamic range reconstructed by the GSAFT approach with (a) 100% (b) 80% (c) 50% (d) 30% measured sampling data; and the CS approach with (e) 100% (f) 80% (g) 50% (h) 30% measured sampling data

5.3.2. 94GHz Imaging Performance

As shown above, it has been demonstrated in simulation and experiments that CS can alleviate the aliasing/artifacts and reconstruct images successfully with much less data. Next, we have investigated the CS reconstruction at 94 GHz based on the experimental data of the configurations in Table. 5- 3 [10]. Therefore, the experimental images of the configuration 1 reconstructed by the traditional GSAFT approach and the proposed CS approach with 100%, 80%, 60%, 40%, 20% sampling data are shown in Figure 5- 27. Similarly, the experimental images of the configuration 2 and 3 are shown in Figure 5- 28 and Figure 5- 29, respectively. It is shown that the traditional GSAFT approach is not capable of reconstructing the target properly when the data randomly redundancy is large (>20%). On the contrary, the proposed CS approach is capable of achieving the image reconstruction even when the data randomly redundancy is as large as 80%. The proposed CS approach is capable of reconstructing a good quality image with only 40% sampling data, compared to 100% data using the traditional GSAFT approach [10].

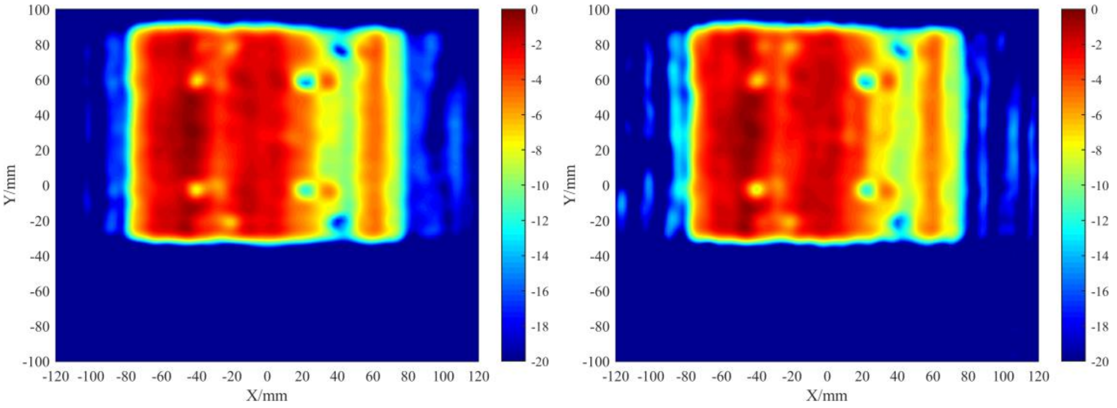

(a) (b)

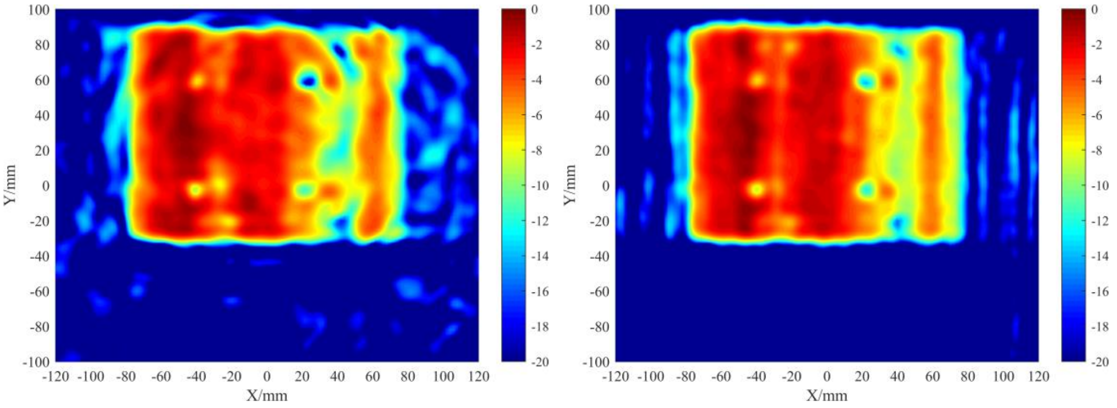

(c) (d)

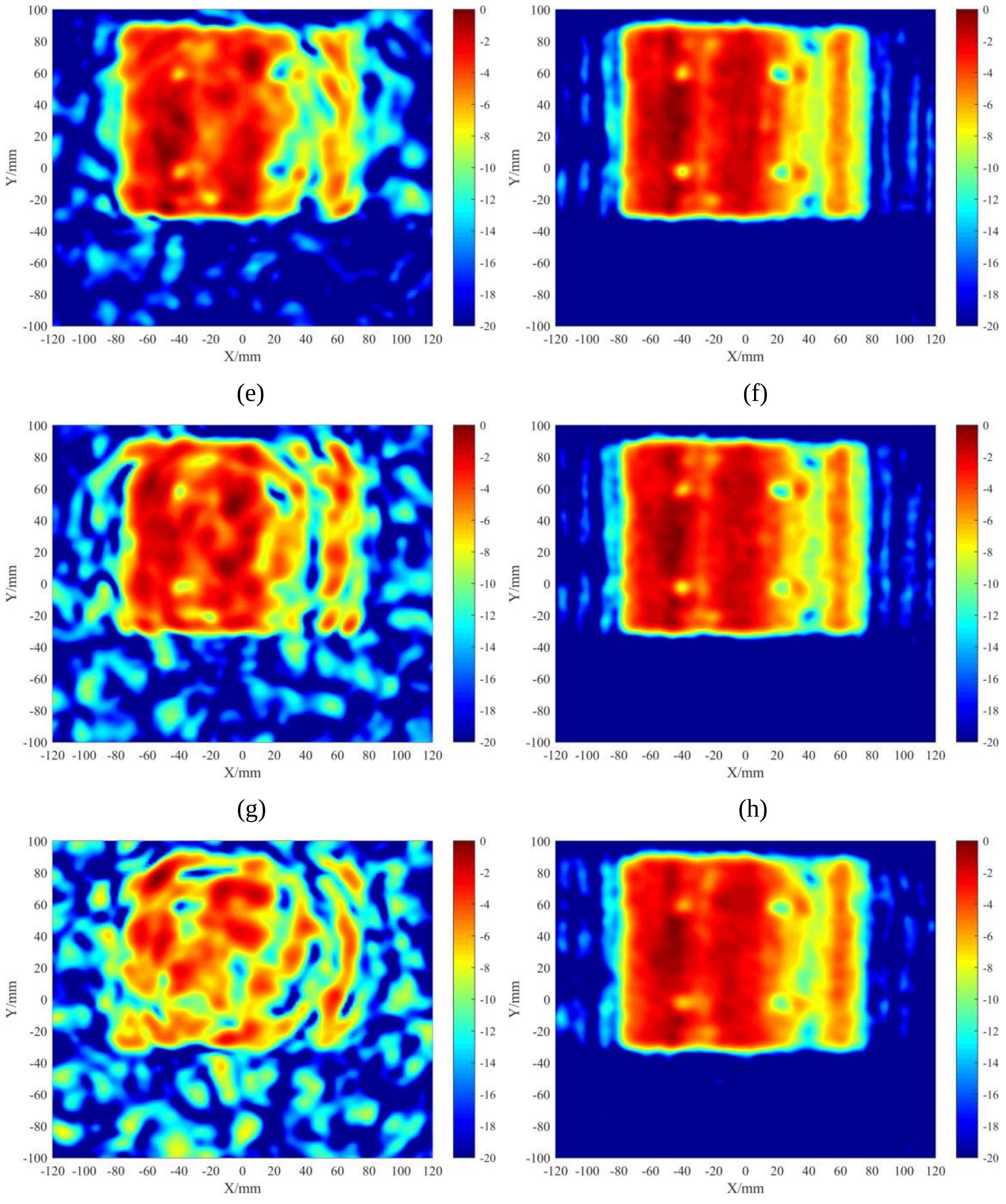

(e) (f)

(g) (h)

(i) (j)

Figure 5- 27. Reconstructed images in configuration 1 with 100% experimental data by (a) GSAFT approach (b) CS approach; 80% experimental data by (c) GSAFT approach (d) CS approach; 60% experimental data by (e) GSAFT approach (f) CS approach; 40% experimental data by (g) GSAFT approach (h) CS approach; 20% experimental data by (i) GSAFT approach (j) CS approach (20-dB dynamic range)

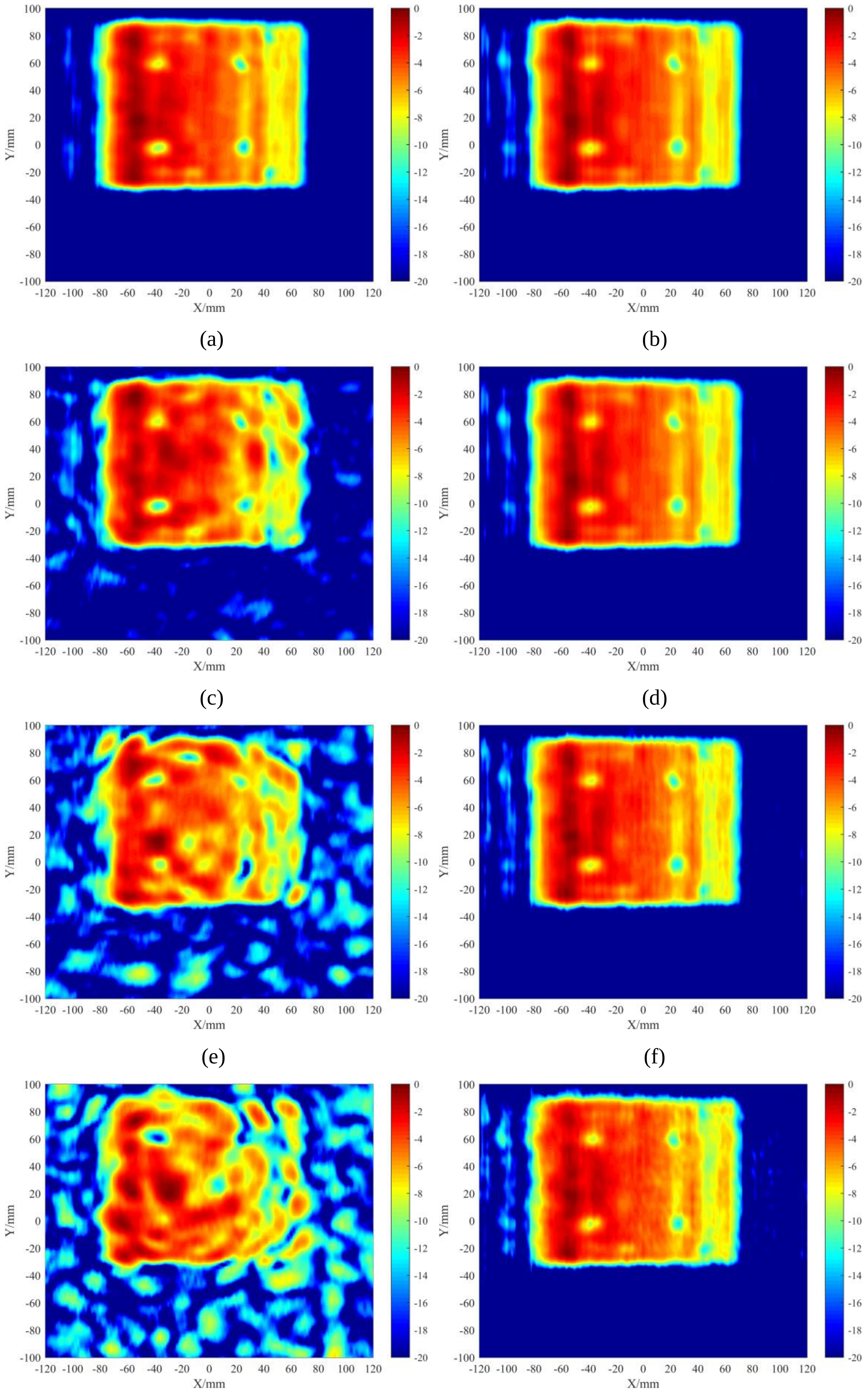
Y/mm
X/mm
100
80
60
40
20
0
-20
-40
-60
-80
-100
-120
-100
-80
-60
-40
-20
0
20
40
60
80
100
120
0
-2
-4
-6
-8
-10
-12
-14
-16
-18
-20

(a) (b) (c) (d) (e) (f) (g) (h)

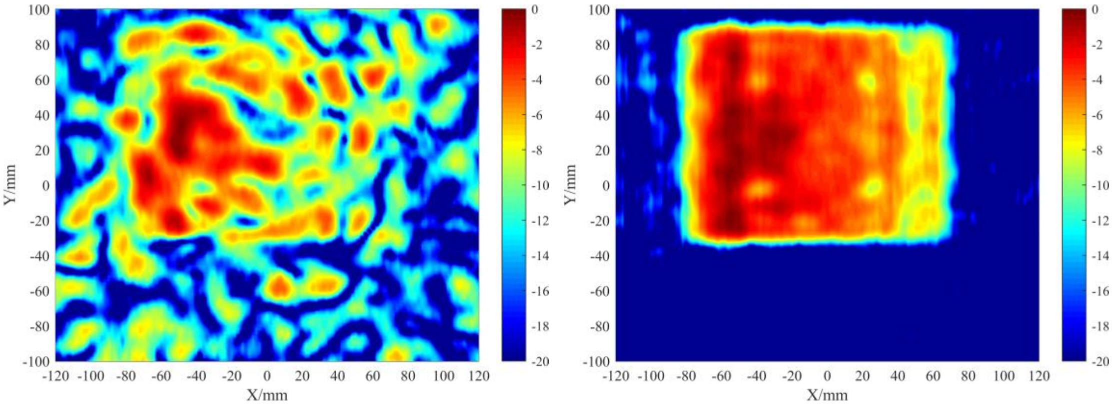

(i) (j)

Figure 5- 28. Reconstructed images in configuration 2 with 100% experimental data by (a) GSAFT approach (b) CS approach; 80% experimental data by (c) GSAFT approach (d) CS approach; 60% experimental data by (e) GSAFT approach (f) CS approach; 40% experimental data by (g) GSAFT approach (h) CS approach; 20% experimental data by (i) GSAFT approach (j) CS approach (20-dB dynamic range)

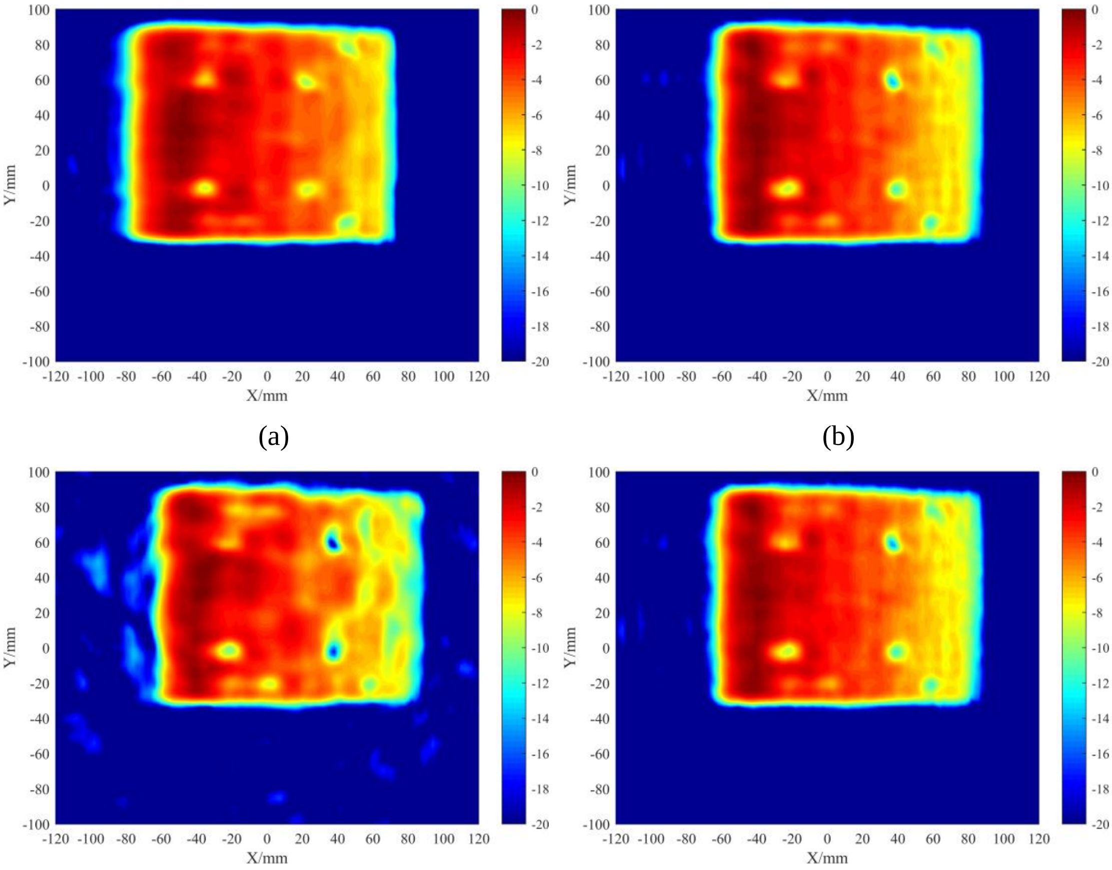

(a) (b)

(c) (d)

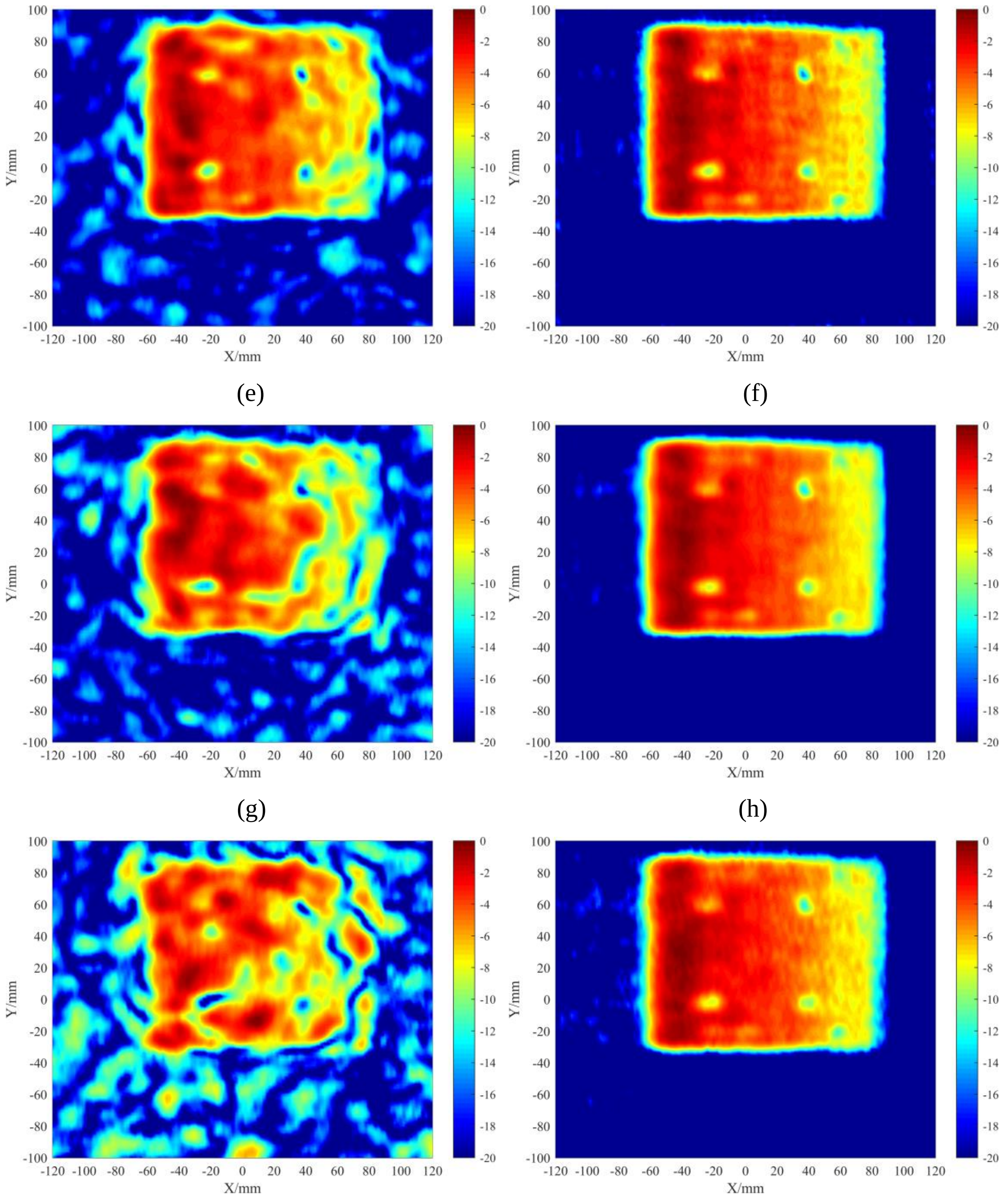

(e) (f)

(g) (h)

(i) (j)

Figure 5- 29. Reconstructed images in configuration 3 with 100% experimental data by (a) GSAFT approach (b) CS approach; 80% experimental data by (c) GSAFT approach (d) CS approach; 60% experimental data by (e) GSAFT approach (f) CS approach; 40% experimental data by (g) GSAFT approach (h) CS approach; 20% experimental data by (i) GSAFT approach (j) CS approach (20-dB dynamic range)

Finally, we have assessed the effect of signal noise on this CS reconstruction scheme using the simulated data in configuration 1 with the added Gaussian noise of 3 different grades of signal to noise ratio (SNR): 5 dB, 10 dB and 15 dB, respectively. The images are constructed based on 80% of the data chosen randomly and compared in Figure 5- 30. It is shown that the obvious artifacts will appear when the SNR is lower than 10 dB, leading to the degradation of the image quality. When the SNR being increased to 15 dB, the noise almost has no effect on the constructed image. Therefore, we should always keep the SNR higher than 15 dB in the Rx channel in the experiment [10].

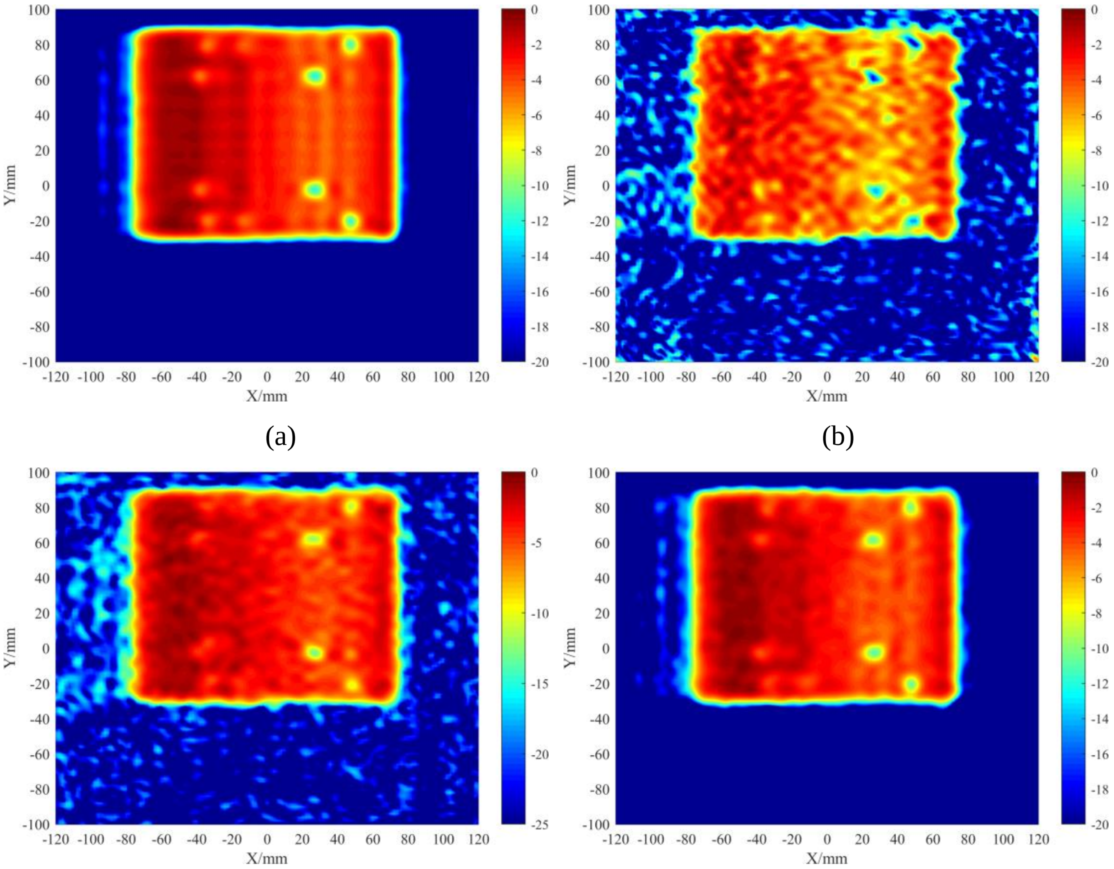

(a) (b)

(c) (d)

Figure 5- 30. The images with 20-dB dynamic range reconstructed by the proposed CS approach with 80% of the simulated data of the Configuration 1. (a) No added noise, and added Gaussian noise in (b) 5 dB SNR (c) 10 dB SNR and (d) 15 dB SNR

5.4. Summary

This chapter has mainly evaluated the proposed SPA imaging system working at 220 GHz and 94 GHz in simulation and experiment, respectively. Firstly, the experimental set-up has been proposed that only uses 1 Tx and 1 Rx channels to imitate the electronic scanning of a SPA. Besides, the effect of separation between Tx and Rx has been analyzed by the simulated PSF in MATLAB, which shows that the separation in practice has little impact on the imaging performance. It has also been verified in the following reconstructed images using the simulated and measured data. Secondly, a good consistency between the images reconstructed using the realistic simulated data and measured data has verified the proposed scanning scheme and the imaging system using a SPA. Thus, the desired resolution and contrast have been achieved in the experimental imaging system. Besides, we have experimentally verified the multi-pass interferometric synthetic aperture imaging performance that can be deployed in the proposed THz-SPA imaging system as a complementary mode to improve the image quality. Finally, the proposed CS THz-SPA reconstruction model has also been evaluated by using the simulated and measured data. The consistent results between the simulation and experiment have proved that the CS technique can be used to reduce the sampling points and hence save the data acquisition time.

5.5. References

[1] Q. M. U. o. London. *NSI Planar Near-field Antenna Measurement Scanner*. Available:https://antennas.eecs.qmul.ac.uk/facilities/antenna-measurement-laboratory/nsi-planar-near-field-beam-pattern-scanner/

[2] D. M. Sheen and T. E. Hall, "Reconstruction techniques for sparse multistatic linear array microwave imaging," in *Proc. SPIE 9078, Passive and Active Millimeter-Wave Imaging XVII,* vol. 9078, pp. 90780I-90780I-12, 2014.

[3] S. Hu, M. Zhou, X. Chen, and Y. Alfadhl, "Suppressing Ghost Images for Synthetic Aperture THz Imaging With Large Sampling Spacing," in *12th European Conference on Antennas and Propogation*, London, 2018.

[4] X. Zhuge and A. G. Yarovoy, "A Sparse Aperture MIMO-SAR-Based UWB Imaging System for Concealed Weapon Detection," *IEEE Transactions on Geoscience and Remote Sensing,* vol. 49, no. 1, pp. 509-518, 2011.

[5] M. Zhou, Y. Alfadhl, and X. Chen, "Optimal Spatial Sampling Criterion in a 2D THz Holographic Imaging System," *IEEE Access,* vol. 6, pp. 8173-8177, 2018.

[6] Q. Cheng, A. Alomainy, and Y. Hao, "On the performance of compressed sensing-based methods for millimeter-wave holographic imaging," *Applied Optics,* vol. 55, no. 4, pp. 728-738, 2016.

[7] A. Tamminen, J. Ala-Laurinaho, and A. V. Räisänen, "Indirect holographic imaging: evaluation of image quality at 310 GHz," in *SPIE Defense, Security, and Sensing*, vol. 7670, p. 11: SPIE, 2010.

[8] S. Hu, C. Shu, Y. Alfadhl, and X. Chen, "A THz Imaging System Using Linear Sparse Periodic Array," *IEEE Sensors Journal,* vol. 20, no. 6, pp. 3285-3292, 2020.

[9] S. Hu, C. Shu, Y. Alfadhl, and X. Chen, "THz sparse periodic array imaging system using compressed sensing," *IET Microwaves, Antennas & Propagation,* vol. 14, no. 11, pp. 1157-1161, 2020.

[10] S. Q. Hu, C. Shu, Y. Alfadhl, and X. D. Chen, "W Band Imaging System Using Linear Sparse Periodic Antenna Array and Compressive Sensing for Personnel Screening," *IEEE Access*, vol. 7, pp. 173603-173611, 2019.

Chapter 6 **Summary and Future Work**

6.1. Summary

THz imaging is a promising technique for concealed threats detection for personnel screening due to its merits of short wavelength and strong penetrating ability. The passive THz imaging system has a poor resolution and difficulties in long-time operation constrained by the cooling system. Therefore, the active imaging system has become a popular solution, but it is still facing challenges in achieving the low cost and high frame rate. Both challenges are usually in conflict with the high image quality, so a proper imaging system is desired to balance the imaging performance and the system cost. Therefore, the THz imaging system using electronic scanning scheme of an array has been proposed. It is capable of achieving the fast scanning and high resolution due to the synthetic aperture technique used. However, the traditional THz imaging system using a uniform array demands a large number of elements/channels in order to form a large aperture that is the prerequisite for achieving the high resolution, leading to a high cost. Therefore, the linear sparse periodic array (SPA) properly designed by using the effective aperture concept has been proposed, which is feasible to provide a high imaging performance with fewer elements because of lengthened aperture of the effective array. However, the element spacing used in the current publications needs to be smaller than one wavelength. It is either impractical to place THz antenna elements or costly when a large number of elements are used. Therefore, we have investigated the linear sparse periodic array with large element spacing in two different configurations operating at 0.22 THz and 94 GHz, respectively. Besides, we have conducted a wide range of simulation studies on various targets that gradually approach to the realistic target in practice. The simulation studies have revealed the knowledge in relationship between SPA configuration and corresponding imaging performance including FOV, resolution and effect of dielectric permittivity. This leads to the design guideline for such a THz imaging system with a SPA. In addition, we have improved the traditional reconstruction algorithm of Generalized Synthetic Aperture Focusing Technique (GSAFT) particularly for suppressing the ghost images. This improved GSAFT approach allows us to use a large element spacing in the SPA. It has achieved the comparable performance to the reconstruction using the traditional GSAFT. Meanwhile, in order to deal with complex circumstances, we have proposed to use the multi-pass interferometric synthetic aperture mode where different datasets are collected with different SPA positions to reconstruct a quality-improved image.

Bedsides, we have also investigated the reconstruction approach based on the compressive sensing technique and proposed the discrete SPA-THz CS reconstruction model for the proposed SPA-THz imaging system. It integrates the CS technique with the system response of the proposed SPA-THz imaging system. The images reconstructed by this approach with the simulated data have successfully verified the proposed model, demonstrating its advantage of reducing the sampling points but maintaining the high image quality simultaneously.

Finally, we have experimentally verified the proposed SPA-THz imaging system, the improved GSAFT reconstruction approach and the proposed CS reconstruction approach. We have firstly investigated the effect caused by the separation of Tx and Rx arrays in MATLAB simulation, revealing it acceptable to separate Tx and Rx arrays in the traditional SPA into two lines. Therefore, we have proposed the simplified experimental set-up that only uses 1 Tx and 1 Rx scanning along two separated linear tracks to imitate the electronic scanning of the linear sparse periodic array. This set-up is practical and economical for the implementation. The images reconstructed with the measured data have achieved the desired image quality, showing the great consistency with the simulated results. Besides, we have performed multi-pass interferometric synthetic aperture imaging with the measured data, showing its improvement on the image contrast, SNR and resolution. This can be deployed in the proposed SPA-THz imaging system as a complementary mode to provide a finer image when necessary. Therefore, the derived design guidelines and the proposed SPA-THz imaging system in this thesis have been fully verified and evaluated.

6.2. Key Contributions

My key contributions in this thesis are summarized as follows.

1. Literature on the imaging system for security detection has been fully reviewed, especially focusing on the application of THz imaging technique. This provides readers with a full knowledge in the state-of-the-art research.

2. An improved Generalized Synthetic Aperture Focusing Technique has been proposed to suppress the ghost images so that the larger element spacing in Linear Sparse Periodic Array (SPA) can be used.

3. Comprehensive simulation has been conducted to investigate the SPA-THz imaging system for security detection, revealing the knowledge of estimating imaging performance such as FOV and resolution. This leads to the design guideline for such a kind of SPA-THz imaging system.

4. The CS imaging algorithm for reducing the sampling data has been explored. So discrete CS reconstruction model particularly for such a multi-static SPA-THz imaging system has been proposed and verified.

5. The effect of TR separated on two scanning tracks has been investigated, revealing its negligible impact. Thus, a practical experimental set-up for testing the proposed SPA imaging system has been designed, only using 1 Tx and 1 Rx channels separated on two linear stages to imitate the electronic scanning of SPA.

6. Numerical and experimental verification of the proposed SPA imaging scheme have been compared. The experimental results agree well with the numerical simulated results, further verifying the proposed SPA-THz imaging system and the proposed CS reconstruction approach. Besides, I have demonstrated the multi-pass interferometric synthetic aperture imaging as a complementary mode feasible to improve the image quality for dealing with complex circumstance when necessary.

6.3. Future Work

Although the CS technique can save the data acquisition time, its reconstruction is time-consuming due to the iterations needed in solving the equation set, so this should be improved by exploring new imaging algorithm. Besides, the computer vision techniques such as deep learning are anticipated to be applied to improve the efficiency and accuracy of target identification. But this requires large amount of data to train the model.

In addition, low side-lobe level is helpful to suppress the ambiguities in the reconstructed image, so it is desired to optimize the traditional linear sparse periodic array (SPA) to gain a lower side lobe level. The goal can be achieved by adjusting the positions of Tx elements and increasing the number of Tx elements in the traditional SPA. Furthermore, it is desired to keep exploring other kinds of arrays potential for high-quality imaging application.

Regarding the experimental test, on the one hand, more experiments on imaging of dielectric board with printed metallic strips are desired. Moreover, the scenario of imaging of a wood board stuck with kinds of realistic targets such as knife, scissor and plastic items can be tested in next stage. On the other hand, the wideband imaging operation, circular scanning scheme and polarimatric imaging technique can also be tested in the future when the conditions permit.

List of Publications in PhD Period

Journal Papers

[1]. Shaoqing Hu, Chao Shu, Yasir Alfadhl and Xiaodong Chen, "THz Imaging System Using Compressed Sensing", ***IET Microwaves Antennas & Propagation***, Vol.14, No.11, pp.1157-1161, September, 2020.

[2]. Chao Shu, Shaoqing Hu, Yuan Yao, Yasir Alfadhl and Xiaodong Chen, "W-band Grooved-Wall Circularly Polarized Horn Antenna", ***IET Microwaves Antennas & Propagation,*** Vol.14, No.11,pp.1171-1174, September, 2020.

[3]. Shaoqing Hu, Chao Shu, Yasir Alfadhl and Xiaodong Chen," A THz Imaging System Using Linear Sparse Periodic Array", ***IEEE Sensors Journal***, Vol.20, No. 6, March 15, 2020.

[4]. Shaoqing Hu, Chao Shu, Yasir Alfadhl and Xiaodong Chen," W Band Imaging System Using Sparse Periodic Linear Antenna Array and Compressive Sensing", ***IEEE Access***, Vol.7, pp. 173603-17611, December, 2019.

[5]. Chao Shu, Junbo Wang, Shaoqing Hu, Yuan Yao, Junsheng Yu, Yasir Alfadhl and Xiaodong Chen, "A Wideband Dual Circular Polarization Horn Antenna for mmWave Wireless Communications", ***IEEE Antennas and Wireless Propagation Letters***, Vol.18, No.9, pp. 1726-1730, July, 2019.

[6]. S.Hu, X.Chen, D.Zhao, Y.Yao, "Wideband Circularly Polarized Cavity Backed Monopole Antenna for Global Navigation Satellite Systems", ***IET Microwaves Antennas & Propagation***, Vol.11, No.4, 2016, pp.503-512, April, 2017.

Conference Papers

[7]. Shaoqing Hu, Chao Shu, Xiaodong Chen and Kai Wang, "THz Personnel Screening System with Multi-pass Interferometric Synthetic Aperture Technique", The 13th UK-Europe-China Workshop on Millimeter-Waves and Terahertz Technologies (UCMMT 2020), Tianjin, China, August, 2020. **(First Prize of Best Student Paper Award)**

[8]. Chao Shu, Shaoqing Hu, Yuan Yao and Xiaodong Chen, "Deep-Learning-based Inverse Modelling with CMA-ES as Applied to the Design of A Wideband High-isolation Septum Polarizer", *2020 IEEE International Symposium on Antennas and Propagation/USNC-URSI Radio Science Meeting (APS/URSI 2020)*, Montreal, Canada, July, 2020.

[9]. Shaoqing Hu, Chao Shu, Xiaodong Chen and Kai Wang, "Element Mutual Coupling Effect in a Wideband Planar Aperiodic Sparse Phased Array", *The 14th European Conference on Antennas and Propagation(EuCAP 2020)*, Copenhagen, Denmark, March, 2020.

[10]. Shaoqing Hu, Chao Shu, Yasir Alfadhl, Xiaodong Chen and Kai Wang, "Design

of Wideband Planar Aperiodic Sparse Phased Array", *2019 International Symposium on Antennas and Propagation (ISAP 2019)*, Xi'an, China, October, 2019.

[11]. Shaoqing Hu, Chao Shu and Xiaodong Chen, "Experimental Verification of a THz SPA Imaging System Using Compressive Sensing", The 12th UK-Europe-China Workshop on Millimeter-Waves and Terahertz Technologies (UCMMT 2019), London, United Kingdom, August, 2019.

[12]. Shaoqing Hu, Chao Shu, Xiaodong Chen and Kai Wang, "Optimization of A Wideband Planar Sparse Array Based on Danzer Aperiodic Tiling", *2019 IEEE International Symposium on Antennas and Propagation and USNC-URSI Radio Science Meeting (AP-S/URSI 2019)*, Atlanta, United States, July, 2019.

[13]. Shaoqing Hu, Xiaodong Chen and Yasir Alfadhl, "Study on 94GHz Imaging System Using Sparse Periodic Linear Antenna Array and Compressive Sensing", The 11th UK-Europe-China Workshop on Millimeter-Waves and Terahertz Technologies (UCMMT 2018), Hangzhou, China, September, 2018.

[14]. Shaoqing Hu, Xiaodong Chen and Yasir Alfadhl, "A THz Imaging System Using Sparse Antenna Array", The 43rd International Conference on Infrared, Millimeter and Terahertz Waves (IRMMW-THz 2018), Nagoya, Japan, September, 2018.

[15]. Shaoqing Hu, Min Zhou, Xiaodong Chen and Yasir Alfadhl, "Suppressing Ghost Images for Synthetic Aperture THz Imaging with Large Sampling Spacing", *The 12th European Conference on Antennas and Propagation(EuCAP 2018)*, London, United Kingdom, April, 2018.

[16]. Shaoqing Hu, Min Zhou, Xiaodong Chen and Yasir Alfadhl, "Study on a Sparse Antenna Array for Terahertz Imaging", *The 10th UK-Europe-China Workshop on Millimeter-Waves and Terahertz Technologies (UCMMT 2017)*, Liverpool, United Kingdom, September, 2017.

[17]. Chao Shu, Shaoqing Hu, Yuan Yao and Xiaodong Chen, "High-gain Reflector Antenna with Beam Steering for Terahertz Wireless Communications", *The 10th UK-Europe-China Workshop on Millimeter-Waves and Terahertz Technologies (UCMMT 2017)* , Liverpool, United Kingdom, September, 2017.

[18]. Min Zhou, Shaoqing Hu, Yasir Alfadhl and Xiaodong Chen, "Investigation of THz Image Reconstruction by Inverse Convolution Algorithm", *The 10th UK-Europe-China Workshop on Millimeter-Waves and Terahertz Technologies (UCMMT 2017)*, Liverpool, United Kingdom, September, 2017.

Appendix I: FFT-Based Back Propogation Reconsctruction Algorithm

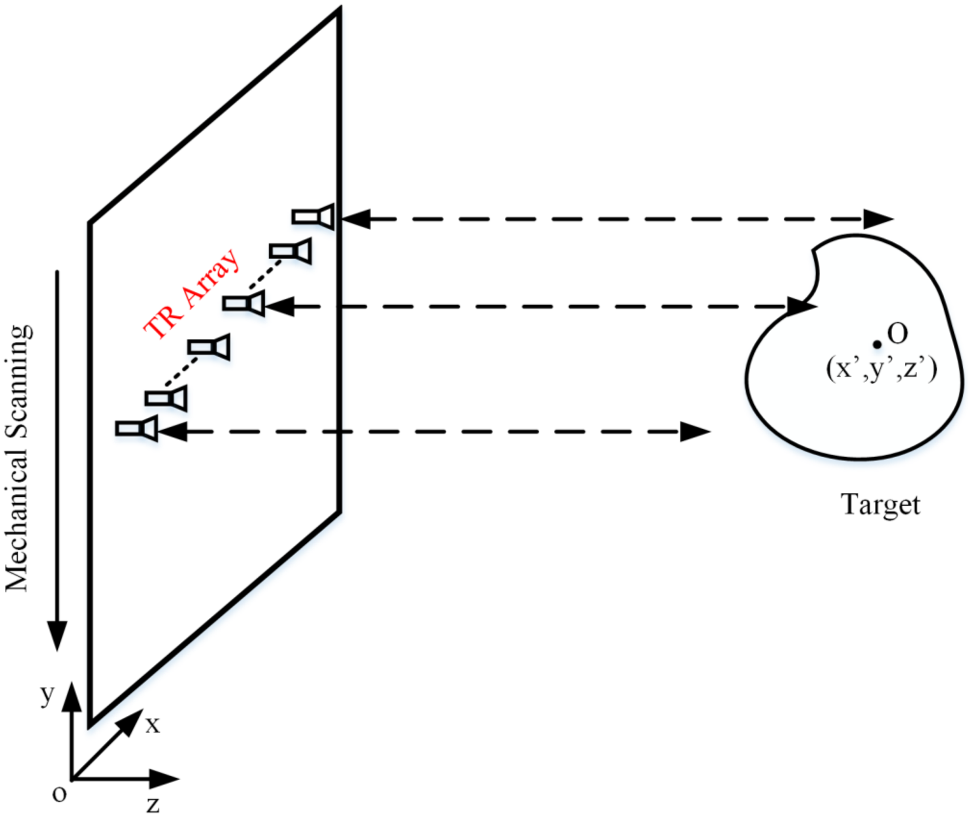

Figure I-1. Monostatic scanning scheme

For the monostatic scanning scenario including the raster scanning scheme or the electronic scanning scheme with an array, its separation between Tx and Rx is very small when compared to the target distance so that both of them can be replaced by their central point to calculate the phase in the image reconstruction. Consequently, the high efficient reconstruction based on back propagation algorithm and Fast Fourier Transform can be employed, the derivation is shown in (I- 1) ~ (I- 10). As shown in Figure I-1, the response $S(x, y)$ at the transceiver will simply be the superposition of each point on the target $Sg(x', y', z_o)$ multiplied by the roundtrip phase to that point or

$$S(x,y)=\iint Sg(x',y',z_o)e^{-j2k\sqrt{(x-x')^2+(y-y')^2+z_o^2}}dx'dy' \qquad \text{(I- 1)}$$

where *k* is wavenumber. The exponential term in (I- 1) denotes a spherical wave emanating from (*x*, *y*), which can be decomposed into a superposition of plane-wave components

$$e^{-j2k\sqrt{(x-x')^2+(y-y')^2+z_o^2}} = \iint e^{jk_x(x-x')+jk_y(y-y')+jk_z z_0} dk_x dk_y \qquad \text{(I- 2)}$$

where k_x and k_y are the Fourier-transform variables corresponding to *x* and *y*, respectively. The spatial wavenumbers will range from -2*k* to 2*k* for propagating waves.

Submitting the relation (I- 2) into the equation (I- 1), we can get

$$S(x,y) = \iint [\underbrace{\iint Sg(x',y',z_o) e^{-j(k_x x'+k_y y')} dx'dy']}_{\text{2D Fourier Transform of Sg(x',y',z}_o\text{)}} \times e^{jk_x x+k_y y+k_z z_o} dk_x dk_y \qquad \text{(I- 3)}$$

Using the 2-D Fourier transform definition described in the Appendix III

$$F(k_{x'},k_{y'}) = FT_{2D}\left\{Sg(x',y')\right\} \qquad \text{(I- 4)}$$

Submitting the Fourier-transform relation (I- 4) into (I- 3) and using the Fourier transform definitions in the Appendix III, we can get

$$\begin{aligned} S(x,y) &= \iint F(k_{x'},k_{y'}) e^{jk_z z_o} e^{j(k_x x+k_y y)} dk_x dk_y \\ &= FT_{2D}^{-1}[F(k_{x'},k_{y'}) e^{jk_z z_o}] \end{aligned} \qquad \text{(I- 5)}$$

$$F(k_{x'},k_{y'}) = FT_{2D}[S(x,y)] e^{-jk_z z_o} \qquad \text{(I- 6)}$$

Therefore, the inversion for the image yields

$$Sg(x',y') = FT_{2D}^{-1}[FT_{2D}[S(x,y)] e^{-jk_z z_o}] \qquad \text{(I- 7)}$$

From the dispersion relation for electromagnetic plane waves

$$k_x^2 + k_y^2 + k_z^2 = 4k^2 \qquad \text{(I- 8)}$$

$$k_z = \sqrt{4k^2 - k_x^2 - k_y^2} \qquad \text{(I- 9)}$$

Thus, the reconstruction algorithm is summarized by

$$Sg(x', y') = FT_{2D}^{-1}[FT_{2D}[S(x,y)]e^{-j(\sqrt{4k^2 - k_x^2 - k_y^2})z_o}] \qquad \text{(I- 10)}$$

Appendix II: L_p Norms and Compressive Sensing Reconstruction

Firstly, we need to introduce the definitions of l_p-norm involved in the CS reconstruction. Let $p \geq 1$ be a real number. The p-norm (also called l_p-norm) of vector $\boldsymbol{x}=[x_1, x_2, x_3 \dots, x_n]$ is

$$\|x\|_p = (\sum_{i=1}^{n} |x_i|^p)^{1/p} \tag{II- 1}$$

When p =1, we get the taxicab norm or Manhattan norm. When p = 2, we get the Euclidean norm, and as p approaches ∞, the p-norm approaches the infinity norm or maximum norm:

$$\|x\|_\infty = \max_i |x_i| \tag{II- 2}$$

The p-norm is related to the generalized mean or power mean.

Another function is named l_0 "norm" by David Donoho. The quotation marks warn that this function is not a proper norm. For example, scaling the vector x by a positive constant does not change the "norm". Defining $0^0 = 0$, the zero "norm" of x is equal to

$$|x_1|^0 + |x_2|^0 + \cdots + |x_n|^0 \tag{II- 3}$$

So it is the number of non-zero entries of the vector x. This is not a norm because it is not homogeneous. Despite these defects as a mathematical norm, the non-zero counting "norm" is useful in scientific computing, information theory, and statistics–notably in compressive sensing in signal processing and computational harmonic analysis.

Let y be the under-sampled data and Θ the measurement matrix, the CS model can be written as

$$y = \Theta x \tag{II- 4}$$

As (II- 4) is an underdetermined system, it has infinite solutions. CS theory offers an alternative way to solve this by enforcing a sparsity constraint on the solution:

$$\min_{x} \|x\|_0 \text{ subject to } y = \Theta x \tag{II- 5}$$

Unfortunately, (II- 5) is computationally difficult to solve. A more general approach is to relax the l_0 norm to l_1 norm:

$$\min_{x} \|x\|_1 \text{ subject to } y = \Theta x \tag{II- 6}$$

This minimization problem is often known as Basis Pursuit (BP). Considering the imaging system is always accompanied with noise, (II- 6) is commonly solved by rewriting it as a Basis Pursuit De-Noise (BPDN) problem:

$$\min_{x} \|x\|_1 \text{ subject to } \|y - \Theta x\|_2 \leq \sigma \tag{II- 7}$$

and σ is a nonnegative real parameter that defines the noise level.

Appendix III: Spatial Fourier-Transform Definitions

Fourier transform is helpful to convert a function not only between time-domain and frequency-domain, but also between space-domain and spatial-frequency domain. Typically, the time or space function will be denoted with a lower case letter while the frequency-domain function will be denoted with a capital letter. All versions of the Fourier-transform operator will often be denoted by FT. The inverse Fourier transform operator will often be denoted by FT^{-1}. A function f and its Fourier transform F are defined as a Fourier-transform pair denoted by

$$f \Leftrightarrow F \tag{III- 1}$$

The temporal Fourier transform and its inverse are defined by

$$F(\omega) = \int f(t) e^{-j\omega t} dt = \mathrm{FT}\{f(t)\} \tag{III- 2}$$

$$f(t) = \frac{1}{2\pi} \int F(\omega) e^{j\omega t} d\omega = FT^{-1}\{F(\omega)\} \tag{III- 3}$$

The 1-D spatial Fourier transform and its inverse are defined as

$$F(k_x) = \int f(x) e^{-jk_x x} dx = FT_{1D}\{f(x)\} \tag{III- 4}$$

$$f(x) = \frac{1}{2\pi} \int F(k_x) e^{jk_x x} dk_x = FT_{1D}^{-1}\{F(k_x)\} \tag{III- 5}$$

The 2-D spatial Fourier transform and its inverse are defined as

$$F(k_x, k_y) = \int f(x, y) e^{-j(k_x x + k_y y)} dx dy = FT_{2D}\{f(x, y)\} \tag{III- 6}$$

$$\begin{aligned} f(x,y) &= \frac{1}{(2\pi)^2}\int F(k_x,k_y)e^{j(k_x x+k_y y)}dk_x dk_y \\ &= FT_{2D}^{-1}\{F(k_x,k_y)\} \end{aligned} \qquad \text{(III- 7)}$$

The 3-D spatial Fourier transform and its inverse are defined as

$$\begin{aligned} F(k_x,k_y,k_z) &= \int f(x,y,z)e^{-j(k_x x+k_y y+k_z z)}dxdydz \\ &= FT_{3D}\{f(x,y,z)\} \end{aligned} \qquad \text{(III- 8)}$$

$$\begin{aligned} f(x,y,z) &= \frac{1}{(2\pi)^3}\int F(k_x,k_y,k_z)e^{j(k_x x+k_y y+k_z z)}dk_x dk_y dk_z \\ &= FT_{3D}^{-1}\{F(k_x,k_y,k_z)\} \end{aligned} \qquad \text{(III- 9)}$$